

High-speed Shape and Displacement Measurements by Holography and Applications in Middle Ear Research

A Dissertation
submitted to the faculty of the

Worcester Polytechnic Institute

as a partial fulfillment of the requirements for the
Degree of Doctor of Philosophy
in
Mechanical Engineering

By

Haimi Tang

March 15th 2022

Approved:

Prof. Cosme Furlong, Advisor

Prof. John J. Rosowski, Co-advisor, Mass. Eye and Ear

Prof. Jeffrey T. Cheng, Co-advisor, Mass. Eye and Ear

Prof. Kristen Billiar, Member, Dissertation Committee

Prof. John M. Sullivan, Member, Dissertation Committee

Prof. Yihao Zheng, Graduate Committee Representative

Copyright © 2022

By

CHSLT – Center for Holographic Studies and Laser micro-mechaTronics

Massachusetts Eye and Ear

Mechanical Engineering Department

Worcester Polytechnic Institute

Worcester, MA 01609-2280

All rights reserved

Abstract

The human ear has three main parts: the outer ear, the middle ear, and the inner ear. The middle ear is an air-filled space separated from the outer ear by the tympanic membrane; it includes a chain of three ossicular bones (malleus, incus, and stapes) that connect the tympanic membrane to the inner ear. The primary function of the middle ear is to effectively transfer acoustic energy from compression waves in the air to fluid membrane waves in the cochlea. The mechanical response of the TM to sound is complex in space and time. The complexity of these responses can be attributed to various features, including, but not limited to, the tympanic membrane's complicated shape, spatially varying thickness, the presence of different fiber populations with different orientations, and the middle and inner ear load. A method that can simultaneously gather relevant data from the entire sample is necessary to characterize these spatiotemporal responses, where simultaneity ensures the tympanic membrane is in a similar state throughout the measurement.

This work describes the development of a holographic system capable of measuring shape and sound-induced motions of the mammalian tympanic membranes with high-speed image acquisition. The shapes of the mammalian tympanic membranes are in the millimeters range, whereas sound-induced motions of such membranes are in the nanometers range. Three shape measurement modalities have been implemented into the holographic setups as follows: (1) A multi-wavelength method with a wavelength-tunable laser; (2) A multi-angle illumination method with a single wavelength laser; (3) A miniaturized fringe projection system with a microelectromechanical systems (MEMS) mirror. Moreover, the processing algorithm of the holographic high-speed displacement measurement is substantially optimized to allow near real-

time examination of data quality during the experiment, thereby making live animal measurements practical.

The frequency response function (FRF) was calculated at each measured pixel of the entire TM surface to understand the large dataset obtained from the holographic measurement. The middle-ear system's complex modal indicator function (CMIF) and spatially-averaged frequency response functions are derived from FRFs. Furthermore, motion parameters-based impulse analyses of the FRFs are spatially-averaged by the tympanic membrane surface's quadrants to characterize the tympanic membrane's mechanical properties.

This work provides a complete description of tympanic membrane mechanics, including the 3D shape information and full-field tympanic membrane surface normal vibration in both the time and frequency domains. The hardware and software developments in the methodologies described in this work enable the in-vivo animal experiments, allowing near-real time examination of the quality of the experimental results and measurement on naturally semi-transparent samples. The proposed optical phase filtering and unwrapping strategies reduce the various noises from the experimental data further improve the practicality of the animal experiments. To understand the large dataset gathered from the holographic data, the quadrated average motion parameters of the impulse response are proposed, and these parameters show certain levels of statistical significance in differentiating pathological middle ear condition from the normal condition. The developed measurement and methodologies for analysis were applied to study six live chinchillas with otitis media with effusion. The left ear of each animal was injected with lipopolysaccharide to induce middle ear infection, while the right ear served as the control ear. The holographic measurement results were compared to the auditory brainstem response (ABR) and distortion product otoacoustic emissions (DPOAE) results. The results show significant changes in the TM's

mechanical parameters and impulse responses in the OME-infected ear, consistent with the ABR and DPOAE measurements, correlating to hearing losses in these ears.

Acknowledgements

Foremost, I would like to express my sincere gratitude and appreciation to my advisors, Professors Cosme Furlong (Worcester Polytechnic Institute), Jeffrey T. Cheng and John J. Rosowski (Harvard Medical School) for allowing me to carry out this study and for their invaluable guidance and continuous support throughout.

I would like to thank my Ph.D. dissertation committee members for their continuous assistance and support. Additionally, I want to thank all the members of the Center for Holographic Studies and Laser micro-mechaTronics (CHSLT) at the Mechanical Engineering Department of WPI and Eaton-Peabody Laboratory (EPL) at Massachusetts Eye and ear Infirmary (MEEI). I would like to thank Payam Razavi and Pavel Psota, for their constant support.

This work has been funded by the National Institutes of Health (NIH), the National Institute of Deafness and other Communication Disorders (NIDCD), and the Massachusetts Eye and Ear Infirmary (MEEI).

Last but not least, I would like to thank my family for their patience, supports and encouragement.

Table of Contents

Abstract	3
Acknowledgements	6
List of Figures	10
Nomenclature	30
Objectives	31
Impact of this work	32
<u>Chapter 1</u> Introduction	33
1.1 Problem Statement	33
1.2 Significance of the Problem	33
1.3 Dissertation Outline	34
<u>Chapter 2</u> Physiology of the Human Ear	37
2.1 Human Middle Ear	37
2.2 Anatomy and Microstructure of the Tympanic Membrane	38
2.3 Function of the Tympanic Membrane	41
2.4 Available Tympanic Membrane Measurements	42
2.5 Available Tympanic Membrane Models	48
Chapter 3 Tympanic Membrane Measurement Needs and Challenges	51
3.1 Full Field of View of TM Transient Response and Shape Measurements	51
3.2 Tympanic Membrane Measurement Challenges	52
Chapter 4 Digital Holographic Interferometry and Fringe Projection	56
4.1 Light Interference in Holography	56
4.2 High-Speed Displacement Measurements using Phase Correlation Interferometry ..	59

4.3 High-Speed Holographic Shape Measurements	64
4.4 High-Speed Fringe Projection Shape Measurement	67
4.5 Applications of Holographic Interferometry and Fringe Projection in Hearing Research.....	69
Chapter 5 New Developments in Analyzing Digital Holographic Interferometry for TM Investigation.....	
5.1 Complex Field Filtering of the Optical Phase	71
5.2 Temporal Phase Unwrapping.....	78
5.3 Frequency and Impulse Response Analysis	81
Chapter 6 Paper A: Ultra-high Speed Holographic Shape and Displacement Measurements in the Hearing Sciences	
Chapter 7 Paper B: High-speed Holographic Shape and Full-field Displacement Measurements of the Tympanic Membrane in Normal and Experimentally Simulated Pathological Ears	102
Chapter 8 Paper C: Analyses of the Tympanic Membrane Impulse Response Measured with High-Speed Holography	
Chapter 9 Frequency and Impulse Response analyses of the Tympanic Membrane Response in Human Middle Ear with Pathologies from High-speed Holographic Measurement	135
Chapter 10 Tympanic Membrane Shape and Impulse Response Measured with High-Speed Holography in Live Chinchilla Ear with Otitis Media with Effusion	
10.1 Background and method of animal study.....	165
10.2 Measurement results.....	168
10.3 Discussion and Conclusion.....	174

Chapter 11 Conclusions and Future Work	185
References	190

List of Figures

- Fig. 1.1. Schematic of the outer ear, middle ear, and inner ear (adapted from Hearing excellence, 2021).
- Fig. 1.2. Orientation and location of the cone-shaped human Tympanic Membrane (TM) within the ear canal. The TM is located at the end of the ear canal with an inclination angle of approximately 60 degrees relative to the center line of the ear canal (adapted from Mayo clinic, 2021).
- Fig. 1.3. Terminology for different components of the TM. The landmarks of a right TM are shown here (adapted from Medicoapps,2021)
- Fig. 1.4. The internal structure of the TM tissue showing different categories of fibers and layers (adapted from Lim, 1970).
- Fig. 1.5. Fibrous structure of a guinea pig TM imaged with scanning electron microscope in: (a) the anterior superior quadrant of the TM (magnification: 300x); (b) the posterior superior quadrant of the TM (magnification: 300x); PF: Parabolic Fibers, RF: Radial Fibers, CF: Circular Fibers (adapted from Kawabata and Ishii, 1971).
- Fig. 1.6. The three human ossicles: the malleus (M), incus (I) and stapes(S) (adapted from Louis Hofmeyr,2021)
- Fig. 2.7. Visual inspection of the outer ear (ear canal and eardrum) by qualitative otoscopy. The schematic (a) shows a conventional otoscope illuminating the surface of the eardrum, and (b) Digital video-otoscopy that allows enlargement of the area being examined.

- Fig. 2.8. Time-averaged holograms of the vibrational patterns of a live cat TM at different tonal frequencies: (a) 2000 Hz; (b) 4000 Hz; and (c) 5000 Hz (adapted from Khanna and Tonndorf 1972).
- Fig. 2.9. Time-averaged holograms were measured in cadaveric humans, live chinchilla, and cadaveric cats at three different excitations frequencies (adapted from Rosowski et al., 2009).
- Fig. 2.10. Magnitudes and phases maps of sound-induced motion of a cadaveric human TM at four different excitation frequencies normalized by the sound pressure (adapted from Cheng et al., 2013).
- Fig. 2.11. View of an electrical lumped model of the intact chinchilla middle ear as a series of interconnected circuit elements: (a) middle-ear cavity, (b) ossicle-uncoupled TM, (c) ossicle coupled TM and malleus-incus complex, (d) Incudostapedial joint, and (e) stapes, cochlea, and cochlear windows (adapted from Bowers and Rosowski, 2019)
- Fig. 2.12. Finite element model of a chinchilla tympanic membrane. (a) Lateral view of the FE model with the tympanic membrane (TM), malleus-incus (M-I) complex, anterior malleal ligament (AML), posterior incudal ligament (PIL), and TM annulus (TMA). (b) Posterior view of the FE model with manubrium, PIL, tensor tympani tendon (TTT), stapes, stapedia annual ligament (SAL), and cochlear load. The FEA results: the distributions of the equivalent von Mises stress (c) and the displacement (d) in the open case and the distributions of the equivalent von Mises stress (e) and the

displacement (f) in the shielded case. All the results are relative to the time when the maximum stress was reached (adapted from Gan et al., 2016).

Fig. 4.1. An electromagnetic wave with wavelength λ . The electric-field component e_x and the magnetic-field component h_y oscillate in phase but orthogonally to each other and to the direction of propagation. This wave is linearly polarized along the x -direction (adapted from Matthew Schwartz, 2021)

Fig. 4.2. An example of preparation of a kernel at (x,y) location of image matrix I for Pearson correlation calculation in the vectorized algorithm. I is the original matrix and $AI-3$, $BI-3$ and $CI-3$ are translated matrices.

Fig. 4.3. 2D Holographic shape measurement schematics: (a) Multi-wavelength method, (b) Multi-angle wavelength method. PB is the observation unit vector and SP is the illumination unit vector. S_1 and S_2 are the illumination point before (x_1, y_1) and after (x_2, y_2) changing of the illumination angle in the multi-angle method.

Fig. 4.4. Optical geometry for fringe projection (adapted from Jia Yang, 2014)

Fig. 5.1 Example of moving window average filter: (a) unfiltered optical phase; (b) results of filtering direct from the optical phase and (c) results of filtering in the reconstructed optical complex field.

Fig. 5.2 Example of phase unwrapping of moving window average filter: (a) unwrapping of unfiltered optical phase; (b) unwrapping of results of filtering direct from the optical phase and (c) unwrapping of results of filtering in the reconstructed optical complex field.

- Fig. 5.3 Comparison of the unwrapped results from Figs 5.2(a) and (c). The profile of the vertical line is a black line shown in the subpanel across the center of the sample.
- Fig. 5.4. Artificial noise is added to the optical phase: (a) artificial random noise; (b) optical phase without artificial noise; and (c) the optical phase with artificial noise added.
- Fig. 5.5 Compression of unwrapping results: (a) the unwrapping results of the optical phase with the artificial noise; (b) the unwrapping results of the complex field filtered optical phase with the artificial noise; and (c) the comparison of the unwrapped results from unfiltered and filtered results. The profile of the vertical line is a black line, as shown in the subpanel across the center of the sample.
- Fig. 5.6 (a) Wrapped optical phase from the first and last phase samplings. (b) Spatial phase unwrapping results.
- Fig. 5.7 The 49 consecutive optical phases changes defined from the 50-phase samplings acquired during the tuning of the wavelength
- Fig. 5.8 (a) Temporal phase unwrapping results and (b) Optical phase of the back line marked in (a).
- Fig. 5.9. (a) Wrapped optical phase between the first and last phase samplings. (b) Eleven consecutive phase differences from a total of twelve phase samplings during the change of the illumination angle. (c) Temporal phase unwrapping result and (d) Unwrapped optical phase of the black line marked (c).

- Fig. 5.10. FRF magnitude of a single pixel of the TM (TB7).
- Fig. 5.11. Reconstructed IRF(x, y, t) (in blue) of a single point at the center of the umbo in TB1. The yellow arrows at the top left of the plot describe the rising time, the time to the first peak of the IRF. The orange line is the absolute value of the IRF. The peaks of the orange line (marked in orange diamonds) are fit by an exponential decay function. The green triangle and line mark the time constant of the fitted exponential decay (the exponential decay time of the IRF).
- Fig. 5.12. Measured displacements of TB1. The 2D map (a) shows the RMS value of the raw displacements during the first 3 ms. Panel (b) illustrates the microphone measurement of the stimulus, and panel (c) illustrates the measured surface normal displacement at 5 points on the TM during the 3 ms after stimulus initiation.
- Fig. 5.13 Example of moving window average filter: (a) unfiltered optical phase; (b) results of filtering direct from the optical phase and (c) results of filtering in the reconstructed optical complex field.
- Fig. 5.14 Example of phase unwrapping of moving window average filter: (a) unwrapping of unfiltered optical phase; (b) unwrapping of results of filtering direct from the optical phase and (c) unwrapping of results of filtering in the reconstructed optical complex field.
- Fig. 5.15 Comparison of the unwrapped results from Fig.s 5.2(a) and (c). The profile of the vertical line is a black line shown in the subpanel across the center of the sample

Fig. 5.16. Artificial noise is added to the optical phase: (a) artificial random noise; (b) optical phase without artificial noise; and (c) the optical phase with artificial noise added.

Fig. 5.17 Compression of unwrapping results: (a) the unwrapping results of the optical phase with the artificial noise; (b) the unwrapping results of the complex field filtered optical phase with the artificial noise; and (c) the comparison of the unwrapped results from unfiltered and filtered results. The profile of the vertical line is a black line, as shown in the subpanel across the center of the sample.

Fig. 5.18 (a) Wrapped optical phase from the first and last phase samplings. (b) Spatial phase unwrapping results.

Fig. 5.19 The 49 consecutive optical phases changes defined from the 50-phase samplings acquired during the tuning of the wavelength

Fig. 5.20 (a) Temporal phase unwrapping results and (b) Optical phase of the back line marked in (a).

Fig. 5.21. (a) Wrapped optical phase between the first and last phase samplings. (b) Eleven consecutive phase differences from a total of twelve phase samplings during the change of the illumination angle. (c) Temporal phase unwrapping result and (d) Unwrapped optical phase of the black line marked (c).

Fig. 5.22. FRF magnitude of a single pixel of the TM (TB7).

Fig. 5.23. Reconstructed IRF(x, y, t) (in blue) of a single point at the center of the umbo in TB1. The yellow arrows at the top left of the plot describe the

rising time, the time to the first peak of the IRF. The orange line is the absolute value of the IRF. The peaks of the orange line (marked in orange diamonds) are fit by an exponential decay function. The green triangle and line mark the time constant of the fitted exponential decay (the exponential decay time of the IRF).

Fig. 5.24. Measured displacements of TB1. The 2D map (a) shows the RMS value of the raw displacements during the first 3 ms. Panel (b) illustrates the microphone measurement of the stimulus, and panel (c) illustrates the measured surface normal displacement at 5 points on the TM during the 3 ms after stimulus initiation

Fig. 6.1. Schematic of the outer ear, middle ear, and inner ear.

Fig. 6.2. Schematic of high-speed fringe projection and holographic displacement configuration. The MEMS mirror scans the sample's surface with a single fringe generated by the cylindrical and expansion lens for shape measurement. The PZT (piezoelectric ceramic material) mounted mirror is used to change the optical path for phase-shifting during displacement measurement. The middle ear sample is excited by transient click-like sounds produced by the loudspeaker. The sound wave near the surface of the TM is measured simultaneously by a calibrated broad range microphone.

Fig. 6.3. Fringe projection measurement of a flat surface. (a) Raw single fringe images captured by a high-speed camera, where m indicates the phase-shifting order and q indicates the fringe order. (b) Reconstruction of four-

step phase-shifted images; each multi-fringe image is the summation of the same phase order. (c) Optical phase of the flat surface obtained by the four-step phase-shifting method.

Fig. 6.4. Measurements of a NIST traceable gauge by three methods. (a) NIST gauge dimensions. (b) The reconstructed optical phase image and the 3D shape measurement result of NIST gauge by fringe projection method. (c) The optical phase and the 3D shape measurement of NIST gauge by the multi-angle method. (d) The optical phase and the 3D shape measurement result of NIST gauge by the multi-wavelength method. Z is the average height, and " σ " is the standard deviation of the given segment of each red line. All the Z_2 are aligned to the zero position of the Z direction.

Fig. 6.5. Representative shape measurement results: Panel (a) is the shape result of TM1 measured by the high-speed fringe projection method, (b) is the TM2 shape measurement result by the multi-angle method, and panel (c) shows the shape measurement result of TM3 using the multi-wavelength method. The top panels (i) show optical phase maps and the bottom panels (ii) show 3D surface plots of the shape. The resolution in terms of standard deviation (" σ ") for the three shape measurement results is 0.11, 0.15, and 0.13 mm, respectively.

Fig. 6.6. High-speed displacement measurement results of a latex drum membrane and its comparison with the LDV result. The drum membrane is excited by a short acoustic click. The surface displacement of the membrane is captured by the high-speed holographic method, while the displacement of

the center of the membrane is measured by an LDV. (a) The wrapped optical phase of the surface displacement at 4.16 ms after excitation. (b) Comparison of the displacement at the membrane center [P1 in (c)] measured by the LDV and the high-speed holographic method. (c) Root-Mean-Square (RMS) of the displacement 3.5 to 7.5 ms after excitation. The RMS is calculated based on the holographic displacement measurements along the temporal axis (d) Three individual displacement waveforms are marked in (c) from the holographic measurement results. The first 3 ms of the experiment is for the PZT phase shifter to scan the optical path to provide a 90-degree phase-shifted image, while the excitation starts at the 3.72ms [30]

Fig. 6.7. Comparison of Pearson's correlation coefficient calculation of Optical Phase(OP) from a TM's High-Speed Displacement (HSD) measurement. (a) The OP of HSD measurement was obtained by the Nested Loop Algorithm (NLA) and the Vectorization Algorithm(VA). (b) the comparison of the computational speed shows the NLA takes 3.54s and the VA takes 0.17s to calculate the same OP.

Fig. 6.8. High-speed holographic surface normal displacement results of a cadaveric TM. (a) The 3D shape measurement used in the calculation of surface normal vector. (b) The excitation signal to deform the TM is an acoustic click generated by a 50 μ s impulse. (c) The RMS map of the first 3 ms of vibration normal to the TM surface after the excitation. The RMS is calculated based on the holographic displacement measurements along the

temporal axis from 0 to 3 ms after the TM is excited by the acoustic wave.

(d) Time-domain and frequency-domain wavefronts of the five individual points. The locations of these selected points are marked in (c).

Fig. 6.9. 2D Holographic schematic for shape measurements: (a) multi-wavelength experimental setup; (b) multi-angle wavelength experimental setup. The observation unit vectors are PB and the illumination vectors are SP for the two methods. S₁ and S₂ are the illumination points before and after changing the illumination angle in the multi-angle method.

Fig. 6.10. The repeatability of the MEMS mirror is examined by checking the repeatability of the fringe position projected by the MEMS mirror during 5 consecutive TM measurements. (a) One fringe image with the Fringe position determined by averaged pixel position of the intensity image of each row. (b) the fringe position of 5 consecutive measurements and its averaged standard deviation is ± 0.63 pixels with averaged fringe width of 100 pixels. The reposition error introduced by the MEMS mirror is less than 1% of the fringe width and is assumed to be negligible.

Fig. 7.1. Schematic of high-speed digital holographic (HDH) system [4]. The 532 nm laser is used for measurements, and the 770–780 nm tunable laser is used for shape measurements. The two lasers are coupled into the same optical path to ensure the shape and displacement measurements are in the same coordinate system avoiding the need for image registration.

Fig. 7.2. (a) Shows the setup, measuring instrumentations, and the sample; and (b) is a photograph of the human postmortem tympanic membrane (TM) with half

level saline injected. The yellow contour shows the level of fluid. (c) Shows the incudo-stapedial (IS) joint. The red dash shows where the IS joint is interrupted.

Fig. 7.3. (a):TB3 shape when the middle-ear cavity is closed; (b):TB4 shape when the middle-ear cavity is closed;(c): TB5 shape when the middle-ear cavity is closed; Comparison of TM shape along the black solid line marked in the left panel in TB 3~5 (d): between open and closed cavity condition; (e): between half fluid injection and closed cavity condition; (f): between full fluid injection and closed cavity condition; (g): between Stapes fixation and closed cavity condition;

Fig. 7.4. Root mean square (RMS) of TB3 displacement under different conditions. (a) Open cavity; (b) closed cavity; (c) half fluid in contact; (d) full fluid in contact; (e) stapes immobilization; and (f) IS joint interruption. (h): between IS joint interruption and closed cavity condition.

Fig. 7.5. RMS of TB4 displacement under different conditions. (a) Open cavity; (b) closed cavity; (c) half fluid in contact; (d) full fluid in contact; (e) stapes immobilization; and (f) IS joint interruption.

Fig. 7.6. RMS of TB5 displacement under different conditions. (a) Open cavity; (b) closed cavity; (c) half fluid in contact; (d) full fluid in contact; (e) stapes immobilization; and (f) IS joint interruption

Fig. 7.7. Umbo displacement of TB3 under different cases (umbo location is marked as the intersection of the solid black and dashed black lines in Fig. 3a).

- Fig. 7.8. Umbo displacement of TB4 under different cases (umbo location is marked as the intersection of the solid black and dashed black lines in Fig. 3b).
- Fig. 7.9. Umbo displacement of TB5 under different cases (umbo location is marked as the intersection of the solid black and dashed black lines in Fig. 3c).
- Fig. 7.10. Waveforms of six points of the surface of the TM of TB3 when the middle-ear cavity is open. (a) Wrapped optical phase 0.56 ms after excitation; (b) TM surface normal displacement 0.56 ms after excitation; and (c) time waveforms of six points marked in part (c).
- Fig. 7.11. The complex model indicator function of TB3–5 under different conditions.
- Fig. 7.12. The complex model indicator function subtracted by the closed cavity case of TB3–5.
- Fig. 8.1. Schematic of the high-speed digital holographic multi-angle shape and vibration measurement system. During the shape measurement, the illumination angle θ is altered by the motorized rotation mirror. The PZT (piezoelectric ceramic material) positioned mirror is used to shift the phase of the reference beam for shape and displacement measurement (Khaleghi et al., 2016). The middle ear sample is excited by transient click-like sounds produced by the speaker, and the resultant sound pressure near the surface of the TM is recorded by a calibrated microphone sensitive to a broad range of frequencies.
- Fig. 8.2. The timing of a multi-angle shape measurement. Ten interference patterns are defined during a 500 ms duration 1.5° mirror rotation. Each pattern is the result of 200 camera frames captured within 3 ms when the PZT

mounted mirror in the reference beam is moved from 0 to 5 μm . The motion of the PZT supplies the controlled shift in the optical phase necessary to define the interference pattern at each of the 10 instances (Dobrev et al., 2013).

Fig. 8.3 The timing of a multi-angle shape measurement. Ten interference patterns are defined during a 500 ms duration 1.5° mirror rotation. Each pattern is the result of 200 camera frames captured within 3 ms when the PZT mounted mirror in the reference beam is moved from 0 to 5 μm . The motion of the PZT supplies the controlled shift in the optical phase necessary to define the interference pattern at each of the 10 instances (Dobrev et al., 2013).

Fig. 8.4 The FRF magnitude of a single pixel of the TM (TB7).

Fig. 8.5 Reconstructed $\text{IRF}(x,y,t)$ (in blue) of a single point at the center of the umbo in TB1. The yellow arrows at the top left of the plot describe the rising time t_R , the time to the first peak of the IRF. The orange line is the absolute value of the IRF. The peaks of the orange line (marked in orange diamonds) are fit by an exponential decay function. The green triangle and line mark the time constant of the fitted exponential decay (the exponential decay time t_D of the IRF).

Fig. 8.6 Shape measurement from 8 TMs. Manubrium and umbo are outlined by the solid black line. Within each TM, a red line is plotted along the manubrial axis and a blue line perpendicular to the manubrial axis at the center of the umbo. The TM shape profiles along these two lines are compared in Fig. 7.

- Fig. 8. 7. The relative depth $z(x,y)$ along and perpendicular to the manubrial axis of 8 measured TBs (a) The manubrial axis from superior to inferior. (b) The anterior to the posterior axis. The center of the umbo is at position 0 on both axes.
- Fig. 8. 8. Measured displacements of TB1 and TB7. The 2D maps on the left show the RMS value of the raw displacements during the first 3 ms. Panels i.b and ii.b illustrate the microphone measurement of the stimulus, and panels i.c and ii.c illustrate the measured surface normal displacement at 5 points on the TM during the 3 ms after stimulus initiation.
- Fig. 8. 9. Magnitude of the surface averaged FRF of 8 TMs. The median of the 8 measurements is plotted in black.
- Fig. 8. 10. Frequency and impulse analysis results of TB1:(a) dominant frequency map, (b) impulse RMS response map, the RMS values of the impulse response are normalized by their umbo value, and the colorbars show the ratio to the umbo value, (c) individual impulse responses of selected six points on the TM surface (marked by points in each of the maps). P1 is the umbo, and the other points are placed in each of the four quadrants of the TM. The dots on the IRFs mark the time to the first response maximum t_R . (d) rising time map, (e) decay time map, and (f) correlation coefficient of the decay time.
- Fig. 8. 11. (a) Dominant frequency maps of TB1 to TB8. (b) the four quadrants and umbo averaged value and their median value.

- Fig. 8. 12. (a) Amplitude ratio of the RMS of first 3 ms of the calculated impulse response. The IRMS maps are normalized by the value at the umbo, and the colorbar shows the ratio to the umbo value. (b) The four quadrant averaged values and their median.
- Fig. 8. 13. (a) Maps of the rising time t_R of the reconstructed impulse response of TB1 to TB8, (b) the av
- Fig. 8. 14. (a) Maps of the decay time t_D of the impulse response, (b) the quadrant and umbo spatial averages and their median values. Averaged quadrants and umbo value and their median value.
- Fig. 8. 14. (a) Maps of the decay time t_D of the impulse response, (b) the quadrant and umbo spatial averages and their median values.
- Fig. 8. 15. Mean (\pm STD) position along and perpendicular to the manubrial axis of painted specimens (TB1 to TB5) and unpainted specimens (TB6 to TB8).
- Fig. 8. 16. Median and range of the surface averaged magnitude of FRF of painted specimens (TB1 to TB5) and unpainted specimens (TB6 to TB8).
- Fig. 8. 17. Comparison of averaged umbo and surface FRFs (normalized by sound pressure) with the pressure normalized umbo motion from Gan et al. 2004 (Gan et al., 2004). Mean(\pm SE) magnitudes are plotted and compared.
- Fig. 8. 18. Plots the mean and standard deviation of the frequency dependence of the damping ratio from all locations on the 8 individual specimens. Each plotted point is an average of the damping ratio at all (x,y) locations with identical dominant frequency in individual TBs, where the number of (x,y) locations that contribute to each plotted plot varies from a few thousand to tens of thousands.

Fig. 9.1. A complete data set of TB1: (a) Averaged FRF of the Normal, half-fluid, full-fluid, Stapes fixation and IS joint interruption cases; (b) Dominant frequencies and RMS of the IRF maps of the Normal, half-fluid, full-fluid, Stapes fixation and IS joint interruption cases; (c) Rising time and decaying time maps of the Normal, Stapes fixation and IS joint cases; and (d) the outlines of the quadrants and umbo and manubrium

Fig. 9.2. A complete data set of TB7: (a) Averaged FRF of the Normal, half-fluid, full-fluid, Stapes fixation and IS joint interruption cases; (b) Dominant frequencies and RMS of the IRF maps of the normal, half-fluid, full-fluid, Stapes fixation and IS joint interruption cases; (c) Rising time and decaying time maps of the Normal, Stapes fixation and IS joint cases; and (d) the outlines of the quadrants and umbo and manubrium

Fig. 9.3. The averaged Frequency Response Function (FRF) amplitude spectrum with standard error. The averaged FRF for each condition was averaged spatially for each measurement and then averaged among different specimens. Manipulation-induced differences from Normal with 5% or better statistical significance are marked with asterisks.

Fig. 9.4. Mean quadrant and umbo averages of FRF dominant frequency and IR RMS amplitude with standard errors for different middle ear conditions. N=8 for Normal, ST and IS. N=7 for the fluid-filled conditions.

Fig. 9.5. Mean quadrants and umbo averaged rising time and decaying time with standard errors for Normal, stapes fixation and IS joint interruption conditions.

- Fig. 9.6 Mean quadrant and umbo averaged damping ratio with standard error for Normal, stapes fixation and IS joint interruption conditions.
- Fig. 9.7 Comparison of the dB change in the RMS: (a) ratio between stapes fixation and Normal condition; (b) ratio between IS joint and Normal condition. (c) ratio between half-fluid and Normal condition. Changes from Normal with statistical significance level of 5% are marked with an asterisk, and two asterisks mark 1% significance.
- Fig. 9.8 Comparison of the dB change in the dominant frequencies: (a) ratio between stapes fixation and Normal condition; (b) ratio between IS joint and Normal condition. (c) ratio between half-fluid and Normal condition. Changes from Normal with statistical significance level of 5% are marked with an asterisk, and two asterisks mark 1% significance.
- Fig. 9.9. Comparison of the dB change in rising time: (a) ratio between stapes fixation and Normal condition; (b) ratio between IS joint and Normal. Data points with statistical significance from Normal conditions are marked asterisk. (c) ratio between half-fluid and Normal condition. One asterisk marks 5% significance, and two asterisks mark 1% significance
- Fig. 9.10 Comparison of the dB change in decaying time: (a) ratio between stapes fixation and Normal condition; (b) ratio between IS joint and Normal condition. (c) ratio between half-fluid and Normal condition.
- Fig. 9.11 Comparison of the dB change in damping ratio: (a) ratio between stapes fixation and Normal condition; (b) ratio between IS joint and Normal condition. (c) ratio between half-fluid and Normal condition.

Fig. 10.1. Endoscopic images of the TM in six animals. The images were gathered 5 days after inoculation of the left middle ear. The left side of each panel shows the TM of the LPS injected ear; the right side of each panel shows the TM of the control ear. The manubrium and umbo are oriented in the 12 o'clock direction. The LPS injected ears contain yellow or reddish fluid behind the drum (usually behind the posterior TM) with bubbles sometimes visible (e.g. animal 4 & 6). The TMs of the controlled ears are free of fluid, and the definition of the manubrium and umbo is clear.

Fig. 10.2. Manubrial length (M-length) and Perpendicular length (P-length) comparison between LPS injected ears and controlled ears for Animal #1 to #6. The Manubrial position (M-position) and its Perpendicular position (P-position) of the LPS injected ears and controlled ears are compared, respectively. S marks the superior side of the TM and P marks the posterior side of the TM.

Fig. 10.3. The averaged frequency response functions (AFRF) of LPS injection ears are shown in red and controlled (normal) ears are shown in black. Different line type indicates the measurements were taken with different excitation levels.

Fig. 10. 4. The maps of IRMS, the RMS of the impulse response. The LPS injected ears are on the left of each panel, and the normal ears are on the right. In each ear the manubrium is aligned in the 12 o'clock direction with the umbo at the bottom of the manubrium.

Fig. 10.5. (a) the change of the ABR and (b) DPOAE thresholds before and after 5 days of LPS injection of left ear and right ear. The LPS was only injected into the left ear, and the right ear remained untouched as a control measurement.

Fig. 10.6. Maps of the dominant frequencies of OME with LPS injected ears and normal ears. The left ears are injected with the LPS, and the right ears are measured as a control. The dominant frequencies are determined by locating the frequency with the maximum FRF amplitude in the frequency domain. The dominant frequency maps show a large variation between 500 Hz to 3 kHz.

Fig. 10.7. Maps of the Rising time of the OME with LPS injected ears (left) and normal (right) ears. The manubrium are aligned in the 12 o'clock direction, and the posterior directions are marked respectively for each side of the ears. The rising time is calculated from the impulse response function, and it is the time for each TM point to travel to its maximum displacement.

Fig. 10.8. Maps of the Decaying time of the OME with LPS injected ears (left) and normal (right) ears with manubrium orientated at 12 o'clock. The decaying time suggests how fast the TM surface will damp out the surface vibration, and it is related to the estimation of the damping of the mechanical properties.

Fig. 10.9. Maps of the damping ratio of the LPS injected ears in the left panel and normal ear in the right panel. The damping ratio is estimated based on the dominant frequencies and decaying time of each measured point on the TM.

The damping ratio calculated here is the middle ear's system damping, including the effect from the middle cavity and the loads from the inner ear.

Fig. 10.10. The areas averaged motion parameters for anterior, posterior, and manubrium areas: (a) dominant frequencies, (b) RMS of the impulse response, (c) rising time, (d) decaying time, and (e) damping ratio. The averaged motion parameters of LPS injected (OME) ears, and their standard deviations are shown in black, while the control ears(normal) data are red.

Fig. 11.1 Proposed schematic of the holographic system to measure larger deformations of the TM under blast-like excitation. Two lasers are used as coherent light sources. The wavelength of each laser should be carefully chosen to generate a desired synthetic wavelength. At least one wavelength-tunable laser is preferred to increase the flexibility of the synthetic wavelength range.

Nomenclature

TM	Tympanic Membrane
HDH	High-speed Digital Holography
CCD	Charge-Coupled Device
dB	Decibels
BS	Beam splitter
λ	Laser Wavelength
e_x	Electric-field
h_y	Magnetic-field
k	Wavenumber
S	Illumination point
B	Observation Point
LDV	Laser Doppler Vibrometry
MEMS	Micro-Electro-Mechanical Systems
d	optical path difference
SPL	Sound Pressure Level
\mathbf{K}	Sensitivity vector
Λ	Synthetic wavelength
φ	Optical phase of the hologram
$\Delta\phi$	Interference phase
ω	Angular frequency
ζ	Damping ratio
RMS	Root Mean Square
PZT	Piezoelectric or lead (Pb) zirconate (Zr) titanate (Ti)
FRF	Frequency Response Function
IRF	Impulse Response Function
FFT	Fast Fourier Transform

Objectives

The primary objective of this work is to improve a full-field high-speed holographic system for live animal experimentations to characterize the mechanics of Tympanic membranes (TM) associated with different pathologies for hearing research. The development includes:

1. Implementing shape and displacement measurement methods in live animal experiments.
2. Carrying out post-analysis procedures to understand the complex spatiotemporal transient response of tympanic membrane (TM).
3. Providing a systemic matrix to differentiate pathological middle ear conditions from the normal condition.
4. The long-term objective is to develop a high-speed endoscopic shape and motion measurement system for in-vivo holographic measurements for clinical application.

The techniques described in this dissertation are as follows:

1. Implementation of software and hardware for high-speed shape and displacement acquisition
2. Validation of measuring accuracy
3. Optimization of the processing algorithm
4. Frequency and impulse analysis of TM motion
5. Quadrant analysis of the TM motion parameter from impulse analysis.

Impact of this work

The prevalence of hearing loss increases with age. It has been reported that 30.0 million or 12.7% of Americans aged 12 years and above had bilateral hearing loss from 2001 through 2008. This estimate increases to 48.1 million or 20.3% when including individuals with unilateral hearing loss (Lin et al. 2001). Early diagnosis can help prevent the progression of hearing loss, especially in speech frequencies. On the other hand, the lack of an early diagnosis may lead to permanent hearing loss. The present screening methods include otoscopic examination, auditory brain stem response (ABR), and Otoacoustic emissions (OAE). However, Those methods often cannot accurately distinguish between the types of hearing loss and are time-consuming procedures. The efficient, fast-paced, quantitative motion measurement methods with a large field of view of the TM developed in this dissertation could help diagnose middle-ear hearing losses.

Chapter 1 Introduction

1.1 Problem Statement

In the hearing process, sound-induced motions on the Tympanic Membrane (TM) are the first mechanical event in the transduction of sound in air to the vibrations of the ossicles within the middle ear and the hair cells within the inner ear. Understanding the sound-induced spatio-temporal displacements of the TM will provide significant clinically relevant and basic-science information about the performance and health of the middle ear. Accurate measurements of these displacements are challenging because of the need to measure nanometer level displacements with micron spatial resolution over centimeter sized structures with 25 microsecond temporal resolution all at the end of the narrow ear canal. Furthermore, submillimeter scale physiological movements, due to respiration, tremor and heartbeat, can significantly affect the measurements of TM motion in live ears. A high-speed holographic system to measure the TM's transient full-field acoustically induced motions is being developed to tackle these measurement challenges. The combination of high-speed temporal sampling with high spatial resolution and relatively large fields of view lead to large datasets that require new analyses that maximize the speed of computation and identify common features in normal ears and variations in diseased ears.

1.2 Significance of the Problem

As per the 2017 Centers for Disease Control and Prevention (CDC), Early Hearing Detection and Intervention Hearing Screening & Follow-up Survey ([CDC, 2021](#)), infant hearing screening has revealed that 1.7 per 1,000 babies have hearing loss. Early diagnosis of hearing loss is beneficial in the course of treatment. However, present screening methods (Otosopic Examination, Auditory Brain Stem Response (ABR) and Otoacoustic Emissions (OAE)) do not

accurately identify different types of hearing loss making it difficult to prescribe treatment. Furthermore, these methods can be challenging in newborns, due to the small size of the ear and the necessity for the infant to remain quite during the tests. An efficient, fast paced quantitative large field of view TM motion measurement tool could help separate middle-ear hearing losses from those due to pathology in the inner ear. Such a tool would also be useful in applications in patients of all ages, such as: (1) the development of new surgical procedures to repair damaged TMs and ossicles, (2) the additive manufacture of artificial and biological grafts for surgical repairs, (3) the development of new hearing devices (i.e., hearing aids and devices for hearing protection), (4) the refinement of existing Finite Element Models (FEMs) of the middle ear.

1.3 Dissertation Outline

This dissertation is organized into two main parts, with each split into several chapters.

The first part, *Background*, is a summary of previous work, and principles of holographic displacement and shape measurement.

Chapter 2 is a brief description of the physiology of the human ear. The functions of the Tympanic Membrane (TM) and the ossicles (malleus, incus, and stapes) are reviewed. The challenges of performing quantitative TM measures are also discussed.

Chapter 3 is a statement of the needs and challenges that provide the performance specifications of the imaging system we develop and use.

Chapter 4 explicates the principles and mathematics of light interference and introduces the methodologies for measurements of TM displacement and shapes using holography and fringe projection for the investigations of middle ear function and their applications.

Chapter 5 describes newly developed image analysis methods that improve the quality of the shape and displacement measurement results, and the frequency and impulse analysis methods to interpret the displacement results.

The second part, *Developments*, describes the progress made as part of this work, and consists of several in press and in preparation publications.

Chapter 6 describes the application of Ultra-high-speed holographic shape and displacement measurements in the investigation of the tympanic membrane. The development of a miniaturized fringe projection system based on a scanning MEMS mirror and optimization of Pearson's correlation calculation algorithm is also described.

Chapter 7 elucidates applications of high-speed holographic shape and displacement measurement system in the study of TM function in normal and experimentally simulated pathological ears. Preliminary descriptions of the frequency and impulsive analyses we used to describe the TM's transient response are presented. The results demonstrate our measurement system and analysis methods have the potential of differentiating different middle ear pathologies.

Chapter 8 describes a systematic study of cadaveric human tympanic membrane impulse response measured with high-speed holography. Spatially-varying TM motion parameters like dominant frequencies, rising time, decaying time, and damping ratio derived from the impulse analysis are presented. A statistical analysis of those parameters on different quadrants of the TM is also included.

Chapter 9 describes frequency and impulse response analyses of the tympanic membrane response based on high-speed holographic measurement in cadaveric human middle ears with simulated pathologies. This chapter also includes a statistical analysis of how different pathologies

affect the motion parameters derived from the impulse and frequency response analyses of transient responses from TMs with pathological middle ear conditions.

Chapter 10 describes the application of high-speed holographic displacement and shape measurement to live normal chinchilla ears, and ears with OME (Otitis Media with Effusion). The frequency and impulse analysis on the live data reveals significant differences between the healthy middle ears and those with OME.

Chapter 2 Physiology of the Human Ear

2.1 Human Middle Ear

The human ear has three main parts: the outer ear, the middle ear, and the inner ear (Figure 2.1). The outer ear is comprised of the auricle and external auditory canal; the middle ear is an air-filled space that is separated from the outer ear by the tympanic membrane (TM), or the eardrum. The middle ear includes a chain of three ossicular bones (malleus, incus, and stapes) that connect the TM to the inner ear. The hollow, air-filled space within the middle ear is also known as the tympanic cavity; it is surrounded by the bony walls of the temporal bone. The auditory tube, or the Eustachian Tube connects the tympanic cavity with the nasal cavity and allows pressure to equalize between the middle ear and the throat. The primary function of the middle ear is to effectively transfer acoustic energy from compression waves in the air to fluid–membrane waves in the cochlea.

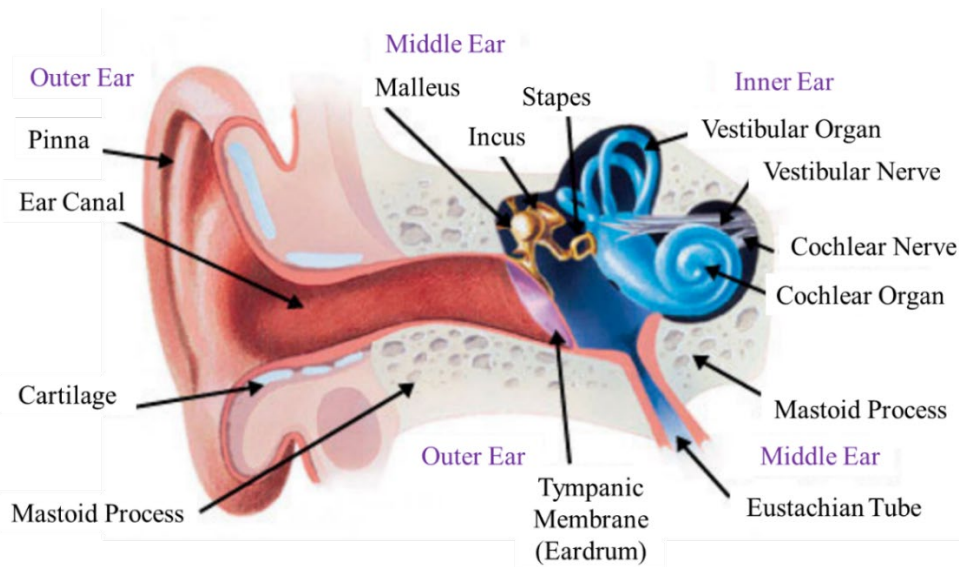


Figure 2.1. Schematic of the outer ear, middle ear, and inner ear (adapted from Hearing excellence, 2021).

2.2 Anatomy and Microstructure of the Tympanic Membrane

The TM in adult humans is conical in shape with a ~8–10 mm diameter and 2–3 mm depth. Typically, the TM is situated at the end of the ear canal at an acute angle. Figure 2.2 shows the conical TM inclined to the long-axis of the tube-like external auditory canal.

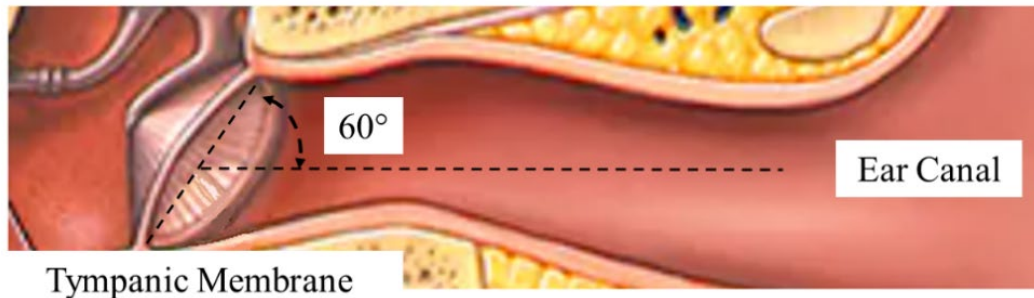


Figure 2.2. Orientation and location of the cone-shaped human Tympanic Membrane (TM) within the ear canal. The TM is located at the end of the ear canal with an inclination angle of approximately 60 degrees relative to the center line of the ear canal (adapted from Mayo clinic, 2021).

The TM can be broken into several components (**Figure 2.3.**). They are (1) the *Pars tensa*, the tense and stiff membrane which includes about 80% of the TM area in humans; (2) the *Pars flaccida*, a membrane component in the superior TM region that takes up about 20% of the TM area; (3) the manubrium of the malleus (the lateral most ossicle), which is embedded in the TM; and (4) the umbo, the spoon-shaped inferior tip of the manubrium which is located near the center of the TM at the tip of the cone. The TM's exterior edge (annulus or annular ring) consists of fibrous and cartilaginous tissue that is thicker and stiffer than the remaining parts of the membrane.

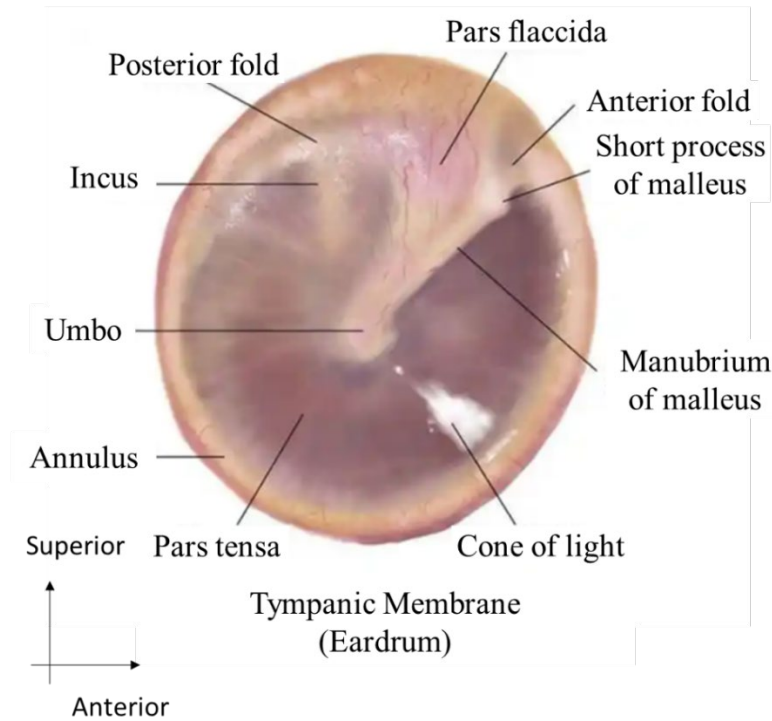


Figure 2.3. Terminology for different components of the TM. The landmarks of a right TM are shown here (adapted from Medicoapps,2021)

The microstructure of the mammalian TMs, particularly human TMs, is that of a multi-layered fibrous structure consisting of a lateral epidermal layer, a middle lamina propria, and a medial mucosal epithelial layer (Lim, 1970). **Figure 2.4.** presents an image of these layers and fibers in the TM tissue, showing collagen fibers within the lamina propria that are oriented along radial and circumferential directions. **Figure 2.5.** displays pictures of the fibrous structure of the TM in a guinea pig captured using an electron microscope (Kawabata and Ishii, 1971).



Lateral side of the Tympanic membrane

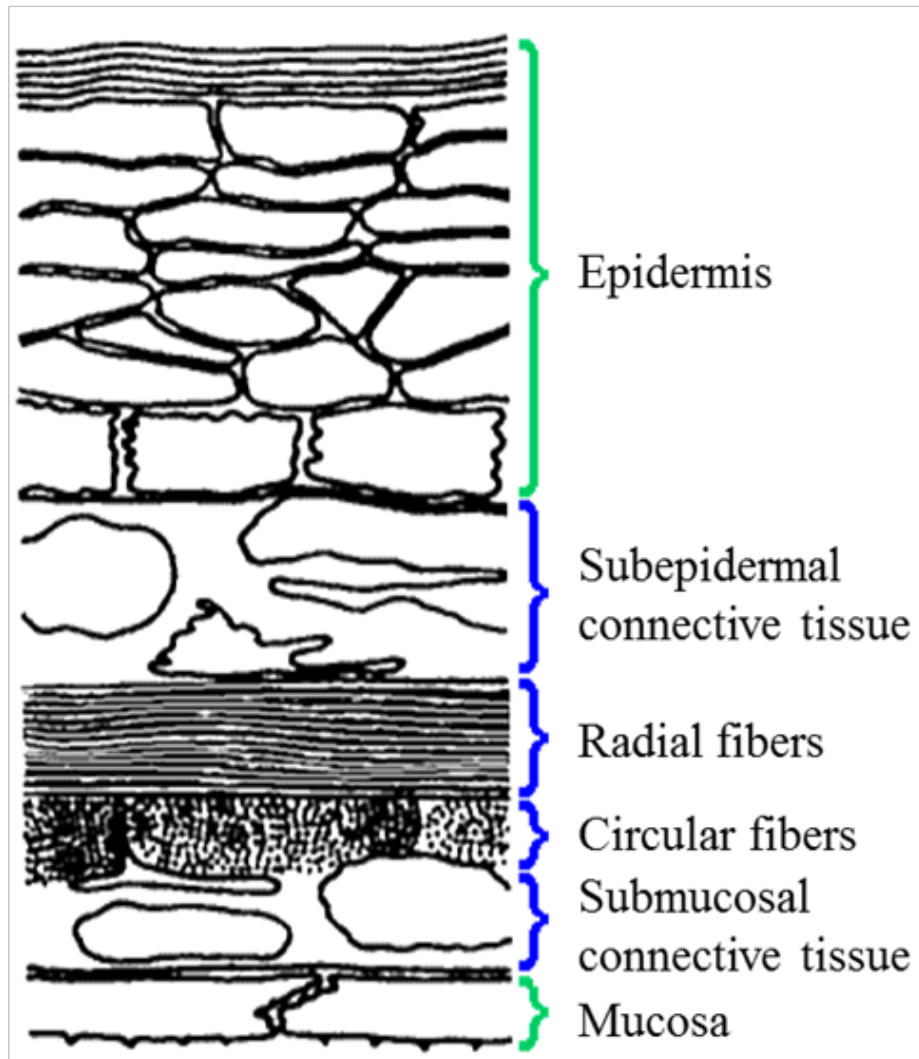


Figure 2.4. The internal structure of the TM tissue showing different categories of fibers and layers (adapted from Lim, 1970).

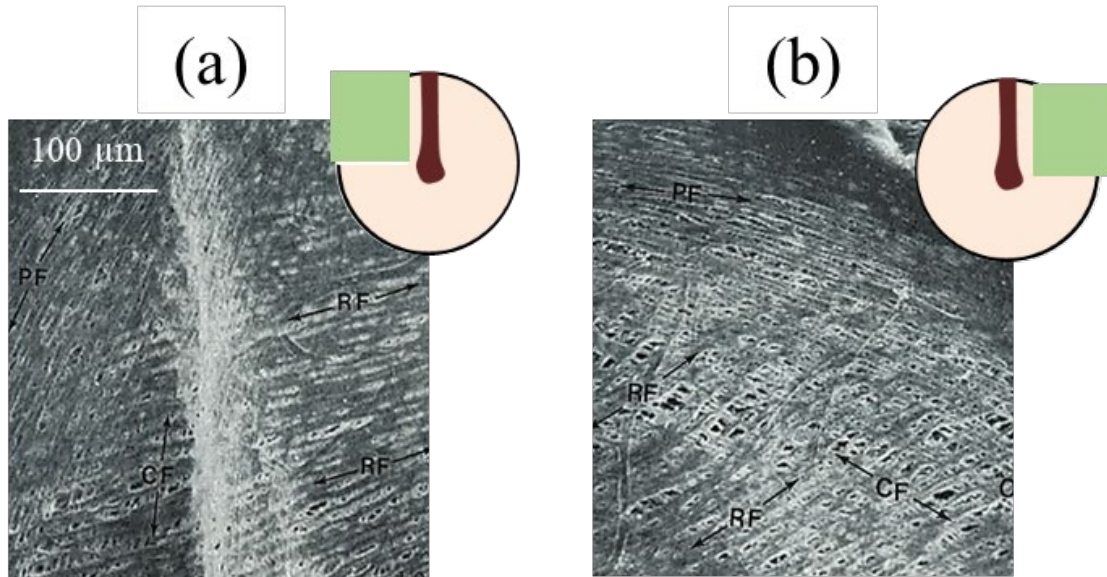


Figure 2.5. Fibrous structure of a guinea pig TM imaged with scanning electron microscope in: (a) the anterior superior quadrant of the TM (magnification: 300x); (b) the posterior superior quadrant of the TM (magnification: 300x); PF: Parabolic Fibers, RF: Radial Fibers, CF: Circular Fibers (adapted from Kawabata and Ishii, 1971).

2.3 Function of the Tympanic Membrane

The middle ear is responsible for the transfer of sound from the air to the cochlea fluids through the TM's vibration and the three ossicular bones. Normally, when sound waves in the air strike a liquid, most of the energy is reflected from the fluid surface. The Tympanic Membrane helps to match the impedance of sound in the air to the acoustic waves travelling in fluids in the inner ear.

The impedance matching function is accomplished via several mechanisms. The vibratory area of the TM (eardrum) is larger than the surface area of the stapes' footplate (**Figure 2.6**). The accumulated force from the sound pressure acting on the TM is concentrated over the smaller area of the footplate, which increases the sound pressure at the inner ear but a decrease in the volume velocity, the hall marks of a hydro-mechanical transformer. Furthermore, the articulated ossicular

chain is shaped like a lever—the malleus is the long arm, the fulcrum is the body of the incus, and the lenticular process of the incus is at the end of the short arm.

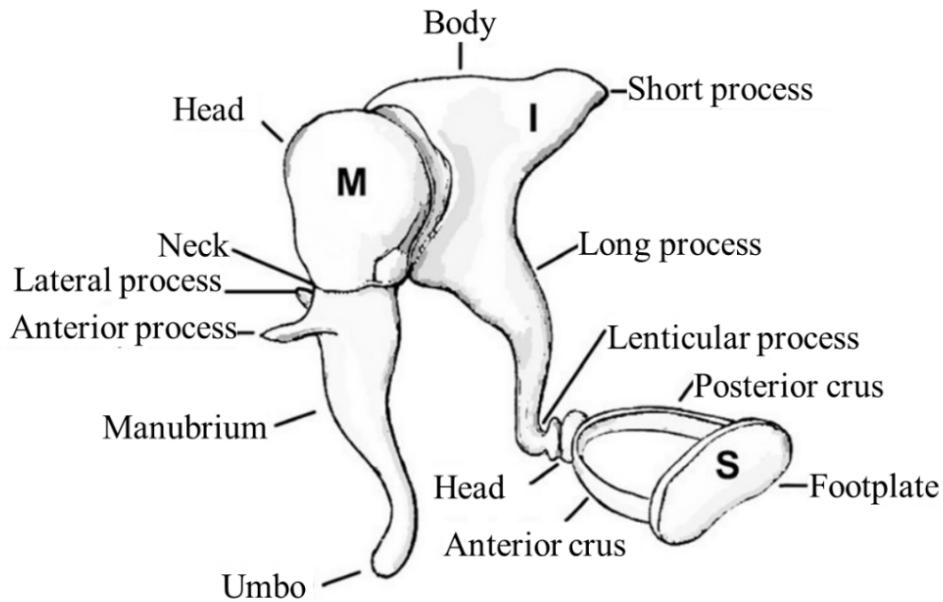


Figure 2.6. The three human ossicles: the malleus (M), incus (I) and stapes(S) (adapted from Louis Hofmeyr,2021)

2.4 Available Tympanic Membrane Measurements

2.4.1 Otoscopy and Endoscopy

Otoscopy is the qualitative examination of the outer ear and TM using an otoscope (**Figure 2.7.**). While techniques can evaluate gross pathology of the external and middle ear, they cannot quantitatively examine the shape and sound-induced motion of the TM.

An endoscope is an illuminated optical fiber (a type of borescope) typically slender and used to examine structures within the human body. Endoscopes use mm thick optical fibers that transfer illumination in one direction and live, high-resolution images in the other direction. When

used in the ear canal, the endoscope's distal tip can be angled so that a wider view of the eardrum can be achieved as compared to using an otoscope. An endoscope can be used to carry out middle-ear surgical procedures such as tympanoplasty to repair a tear in the TM. Such repairs can improve the patient's hearing and stop the incidence of frequent ear infections. The endoscope is also useful in removing ear wax that is impacted in the ear canal. The endoscope helps visualize the ear wax as it is removed via a low-pressure, gentle suction and fine sterile probes.

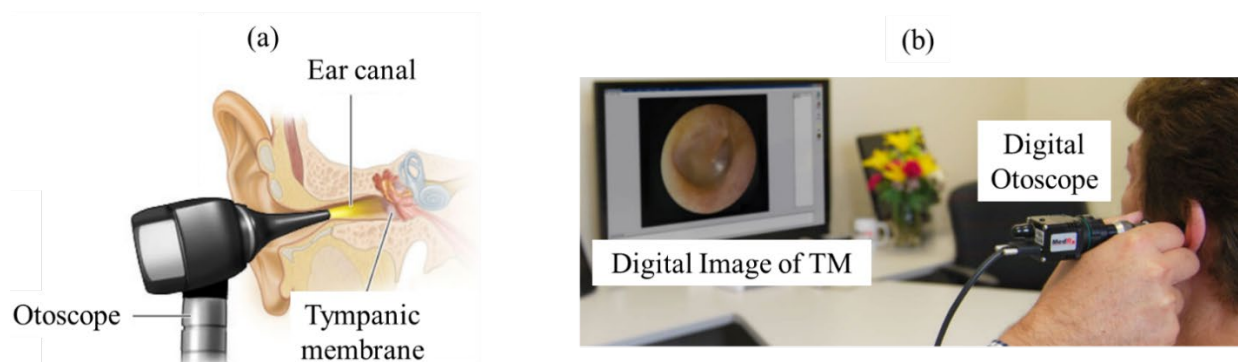


Figure 2.7. Visual inspection of the outer ear (ear canal and eardrum) by qualitative otoscopy. The schematic (a) shows a conventional otoscope illuminating the surface of the eardrum, and (b) Digital video-otoscopy that allows enlargement of the area being examined (adapted from <https://www.intelcrew.com,2021>).

2.4.2 Acoustic Admittance and Reflectance

Acoustic admittance and reflectance describe a number of acoustic techniques that depend on measurements of the sound pressure produced in the ear canal by a calibrated sound source (Rosowski et al. 2013). These techniques describe the average motion or sound energy absorbance of the entire TM. While these techniques can help distinguish different middle ear pathologies, they are not sensitive nor selective enough to be used by themselves (Hunter et al. 2013; Nakajima et al. 2013); neither can they localize the pathology to specific regions of the TM.

2.4.3 Laser Doppler Vibrometry (LDV)

Laser Doppler Vibrometry (LDV) is used in the clinic and various hearing research applications. LDV provides non-contact measurements of the vibrations of points on a surface. The laser beam of the vibrometer is directed onto the moving surface, and the time-varying vibration amplitude of the target is collected based on the Doppler shift of the reflected laser beam. Usually, an LDV's output is a continuous analogue voltage that is directly proportional to the target velocity component along the laser beam's direction. LDV measurements are used to qualify the transfer function of the manubrium and the umbo (Foth et al., 1996; de La Rochefoucauld and Olson, 2010; Rosowski et al., 2003). It is also used to characterize the vibration of the mammalian ossicles, in ears with open middle-ear cavities where measurements at multiple points on the ossicles have been used to quantify the rotation of the ossicles (Decraemer et al., 2014).

A scanning laser Doppler vibrometer is an LDV system with the laser beam quickly moving from measurement point to measurement point while quantifying the motion at each point. The use of a scanning LDV for the investigations of the human TM motion in the presence of middle ear liquid was reported in 2014 (Zhang et al., 2014). Another special configuration of LDV is continuous-scan laser Doppler vibrometry (CSLDV), where the laser beam is swept across the surface of the test subject to simultaneously capture the motion of many points of a surface (Salman, Muhammad, 2012). However, the vibration measurement with this method is limited to several hundred Hertz. Thus, CSLDV is not suitable for use in hearing research as human hearing is sensitive to a wide range of higher frequencies (0.1 to 20 kHz). While the LDV is not FDA-approved for clinical use, it has been used as an experimental tool to assist in the diagnosis of ossicular disorders (Huber et al. 2001; Whittemore et al. 2004).

2.4.4 Laser Holography

In cats, Khanna and Tonndorf (1972) reported the first laser holography study of sound-induced TM motions using time-averaged holographic interferometry. The holograms were recorded using a high-resolution photographic plate with an electromagnetic shutter for exposure control. Figure 2.8 shows time-averaged holograms corresponding to vibrational patterns stimulated with different frequencies. A digital time-averaged holographic system was described by Rosowski et al. (2009) to investigate the sound-induced motion of mammalian TM. The researchers were able to capture and display time-averaged holograms corresponding to sound-induced motion of the TMs of postmortem human, cat, and chinchilla using tones of frequencies as high as 25 kHz (Figure 2.9).

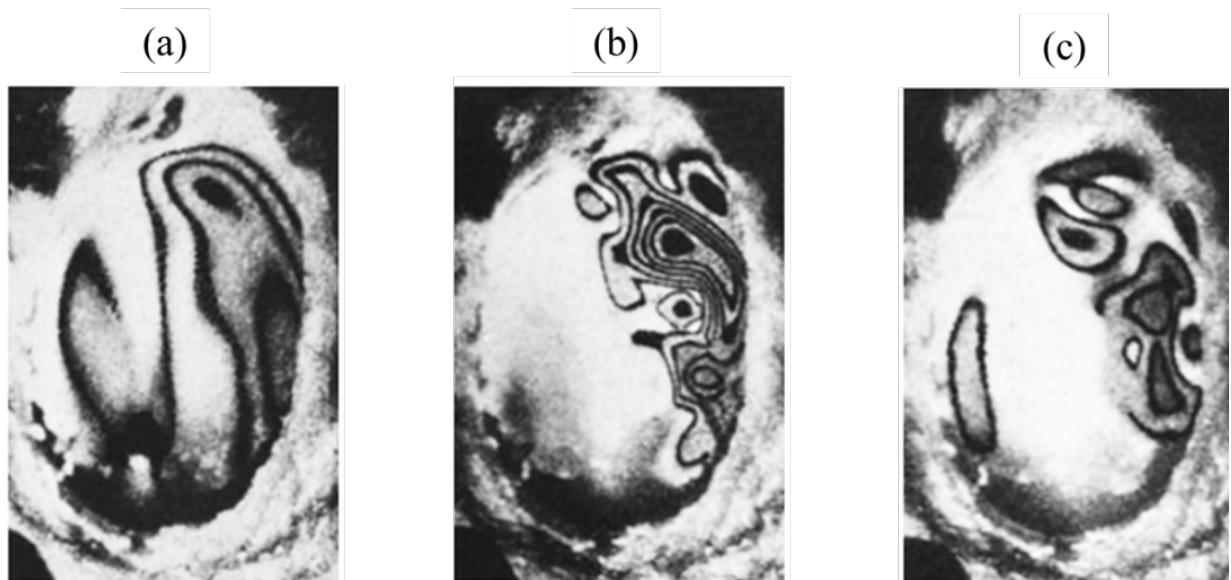


Figure 2.8. Time-averaged holograms of the vibrational patterns of a live cat TM at different tonal frequencies: (a) 2000 Hz; (b) 4000 Hz; and (c) 5000 Hz (adapted from Khanna and Tonndorf 1972).

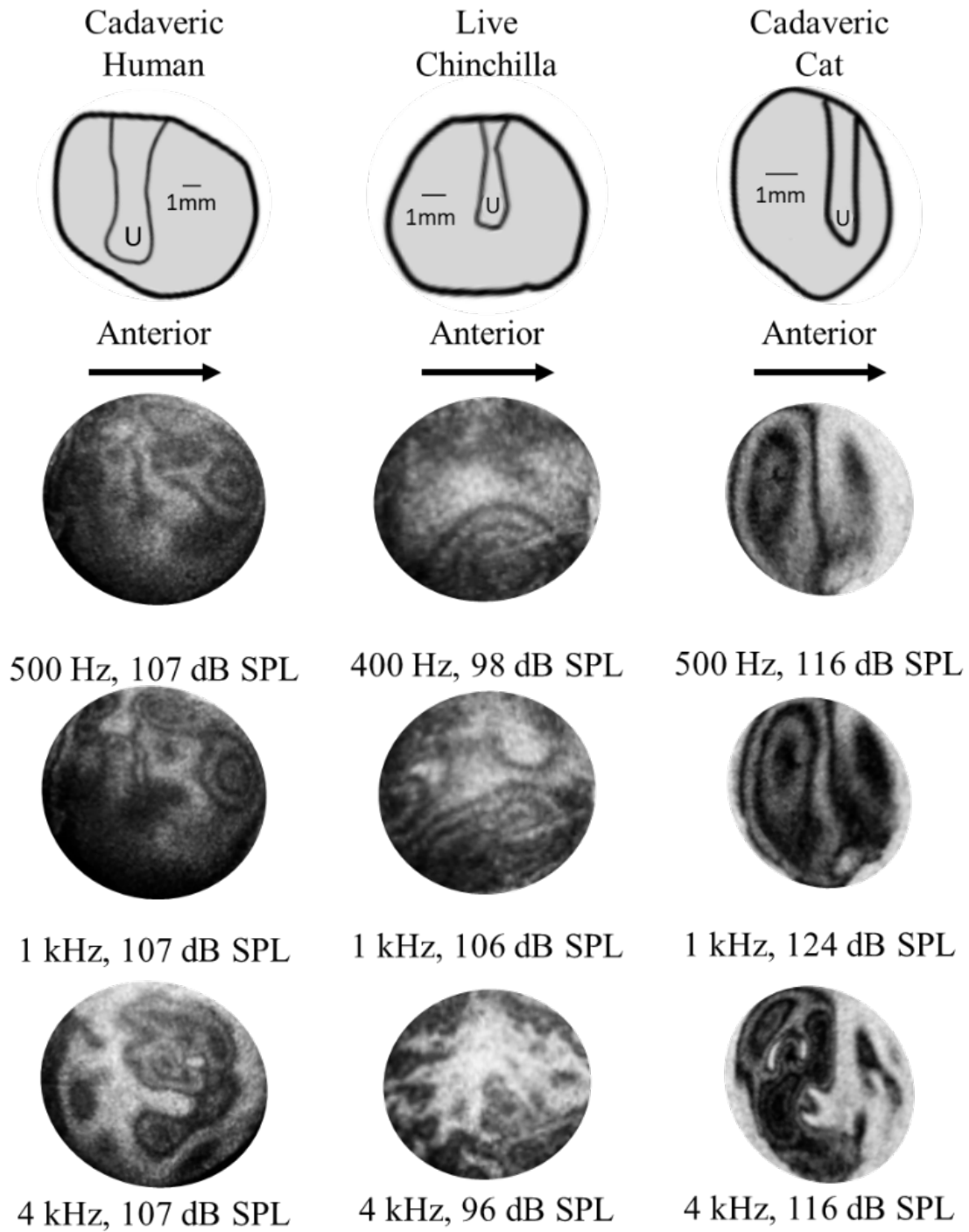


Figure 2.9. Time-averaged holograms were measured in cadaveric humans, live chinchilla, and cadaveric cats at three different excitations frequencies (adapted from Rosowski et al., 2009).

To assess the magnitude and phase of TM motions with various tonal stimuli, stroboscopic holographic interferometry was used. This tool quantifies the sound-induced motion of the TM at fixed instances during sinusoidal stimulation (Hernández-Montes et al., 2009; Furlong et al., 2009; Cheng et al., 2010; 2013). The optical path length between the TM and the recording camera is affected by the sound-triggered vibrations of the TM surface. The change of the optical path length produces time-dependent variations of the intensity of the interference pattern at each camera pixel. In stroboscopic measurements, the camera records holographic images with the object illuminated by a series of short laser pulses that are synchronized with the acoustic stimulus. Two holograms illuminated at two different stimulus phases are used to compute the deformation of the TM across the phases. Figure presents the magnitudes and phases of sound-induced vibrations of a human TM at different tonal frequencies captured using stroboscopic holographic interferometry (Cheng et al., 2013).

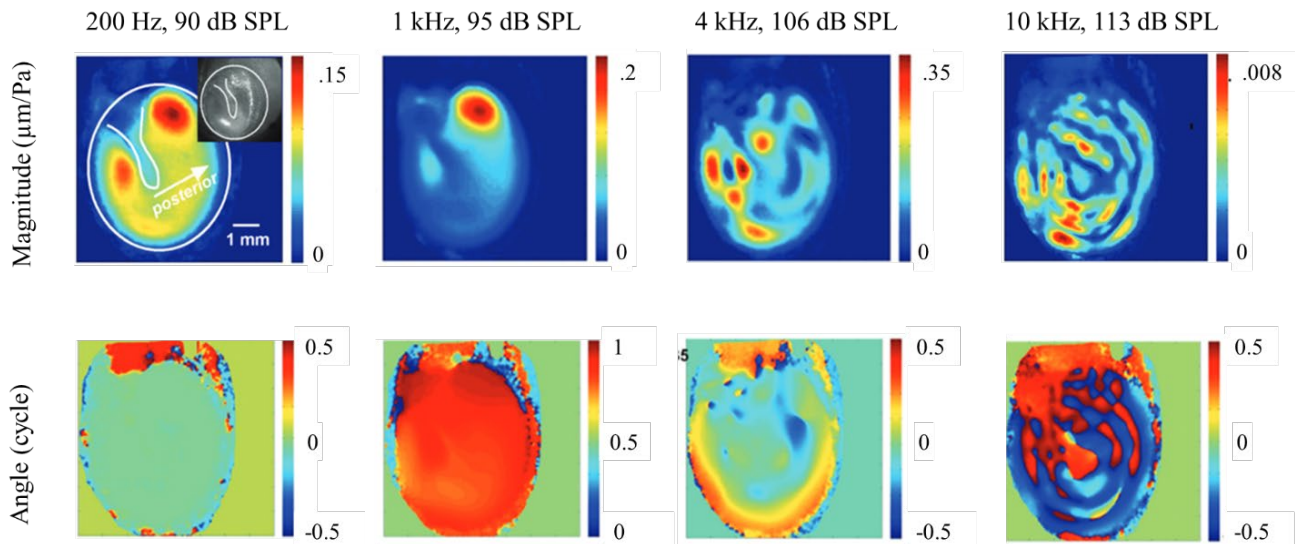


Figure 2.10. Magnitudes and phases maps of sound-induced motion of a cadaveric human TM at four different excitation frequencies normalized by the sound pressure (adapted from Cheng et al., 2013).

2.5 Available Tympanic Membrane Models

Models of the human TM and middle ear codify our knowledge of the structure and function of the TM and middle ear. They also serve to help planing rehabilitative strategies (e.g., surgical reconstruction of the TM and the production of better TM and ossicular replacement grafts), help diagnosis by predicting the effect of particular middle-ear pathologies, and aid the optimization of hearing aids (Cheng et al., 2007; Danti et al., 2015; Deng et al., 2009; Fay et al., 2005; Kozin et al., 2016). Available middle models can be broadly classified into two main categories: lumped-parameter (Feng & Gan, 2004; Zwislocki, 1962) and distributed or finite element models (Fay et al. 2006; De Greef et al., 2015; Funnell & Laszlo, 1978).

Lumped-parameter models are based on well-known electrical analogues of acoustical and mechanical systems. Each part of the ear is modeled as a lumped linear/non-linear time-invariant system in which the output of one connected element is the input of the others. To create a model of the hearing process, the parameters of each part of the model are adjusted based on experimental data. These models find extensive use in the determination of the performance quality of various hearing devices, predictions of the consequences of different hearing pathologies (Rosowski and Merchant 1995; Voss et al. 2001) and the effect of non-linear middle-ear responses with high-intensity sounds (Price and Kalb 1998; Zagadou et al. 2016). Figure 2.10 shows one of the lumped models used to model the complete chinchilla peripheral auditory system.

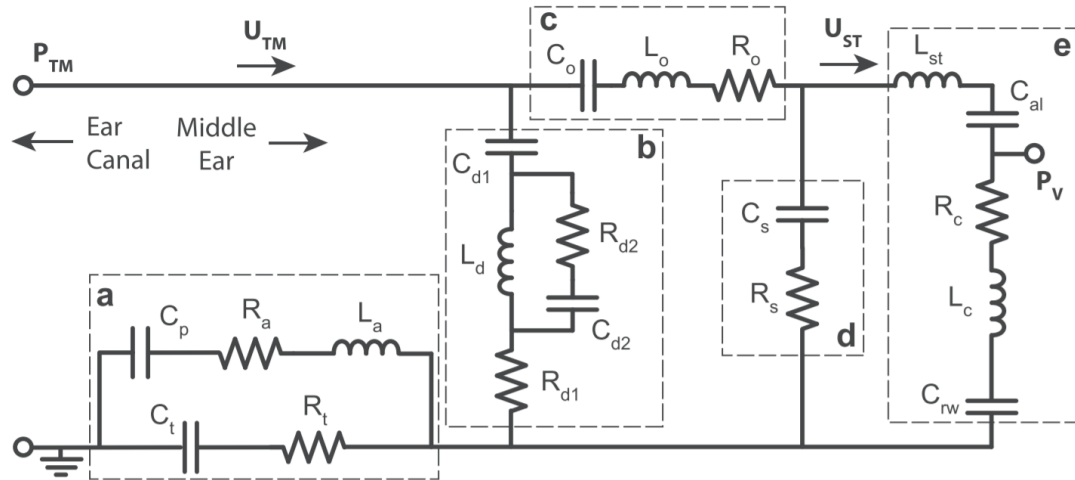


Figure 2.11. View of an electrical lumped model of the intact chinchilla middle ear as a series of interconnected circuit elements: (a) middle-ear cavity, (b) ossicle-uncoupled TM, (c) ossicle-coupled TM and malleus-incus complex, (d) Incudostapedial joint, and (e) stapes, cochlea, and cochlear windows (adapted from Bowers and Rosowski, 2019)

On the other hand, distributed models use finite elements (FE) (De Greef et al., 2015; Funnell & Laszlo, 1978; Rong Z. Gan et al., 2016b) and continuum mechanics (Rabbitt & Holmes, 1986) to include more parameters for modeling complex TM behaviors. For instance, TM FE and distributed models can imitate the shape, thickness, ultrastructure, pre-stress, ligaments forces, etc. for the simulation of the hearing process (Fay et al. 2005). Figure presents Von Mises stress distribution in a chinchilla TM responding to tonal stimuli as predicted by an FE model. The shape of all the middle ear components is determined through micro-CT scanning (Gan et al., 2016a).

While lumped-parameter models are suitable for easy analysis and prediction of the lower hearing frequency range (i.e., < 2 kHz), distributed models provide a greater amount of fundamental information regarding the possible dynamic behavior of TM at higher frequencies. A common problem with FE models is the limited information pertaining to the mechanical properties of the TM for material characterization.

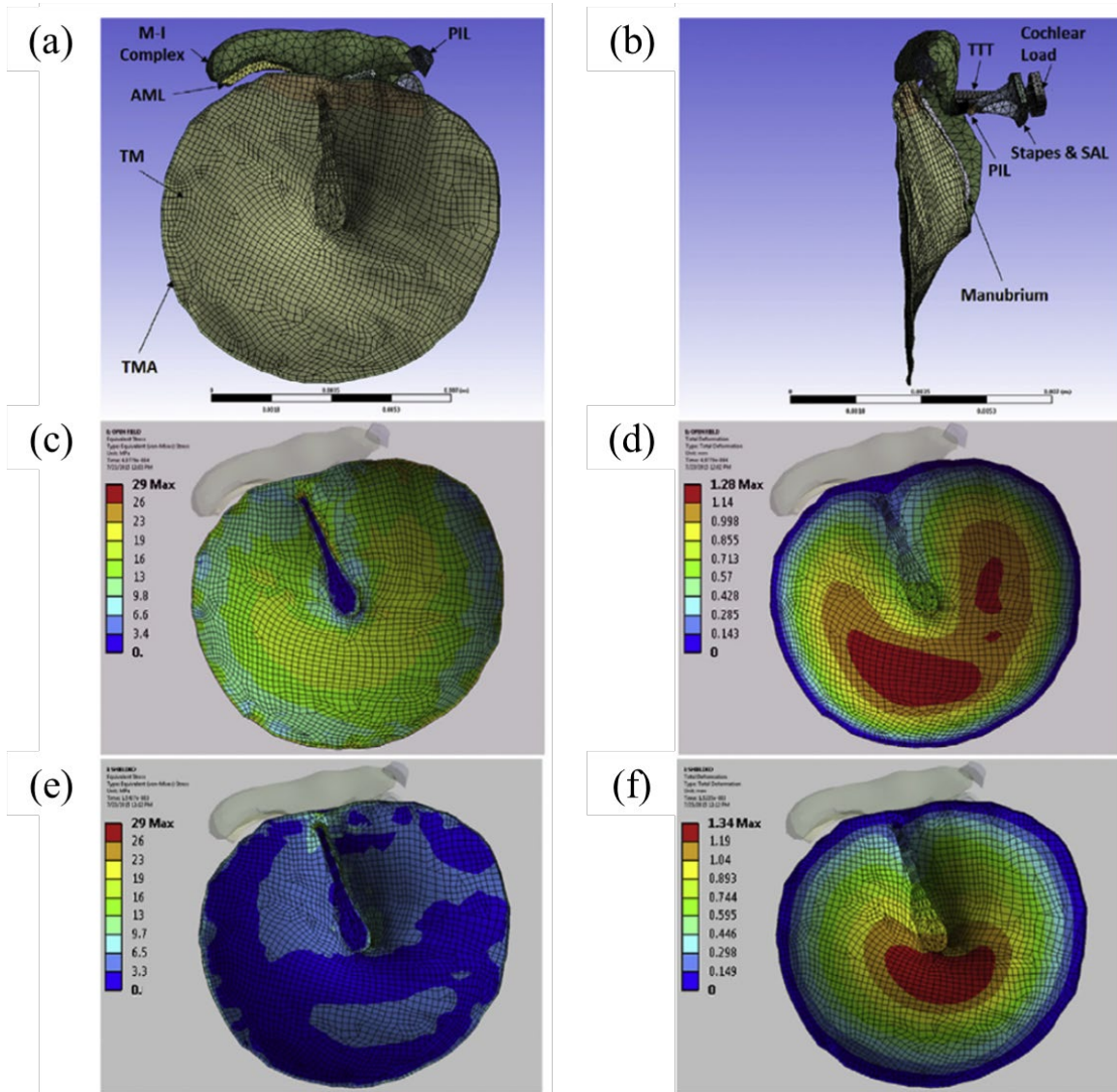


Figure 2.12. Finite element model of a chinchilla tympanic membrane. (a) Lateral view of the FE model with the tympanic membrane (TM), malleus-incus (M-I) complex, anterior malleal ligament (AML), posterior incudal ligament (PIL), and TM annulus (TMA). (b) Posterior view of the FE model with manubrium, PIL, tensor tympani tendon (TTT), stapes, stapedia annual ligament (SAL), and cochlear load. The FEA results: the distributions of the equivalent von Mises stress (c) and the displacement (d) in the open case and the distributions of the equivalent von Mises stress (e) and the displacement (f) in the shielded case. All the results are relative to the time when the maximum stress was reached (adapted from Gan et al., 2016).

Chapter 3 Tympanic Membrane Measurement Needs and Challenges

3.1 Full Field of View of TM Transient Response and Shape Measurements

The mechanical response of the TM to sound is complex in space and time. The complexity of these responses can be attributed to various features including, but not limited to, the TM's complicated shape, spatially varied thickness, the presence of different fiber populations with different orientations, and the middle and inner ear load (e.g. Fay et al. 2006). Two-dimensional LDV measurement needs to scan the sample point by point which is not applicable for periodic motion. Acoustic measurements or brain response measurements are limited to measure the average effect of the TM response and also requires the measurement to be repeated to increase the signal to noise ratio. Therefore, those measurements are not suitable to measure the transient full-field responses of the TM for clinical applications.

To characterize the transient spatiotemporal responses of the tympanic membrane, a method is required that simultaneously gathers relevant data from the entire sample, where simultaneity ensures the TM is in a similar state throughout the measurement.

For the spatial characterization of the different TM regions, full field of view measurements are needed to investigate the responses at the pars tensa, pars flaccida, and manubrium. Such full-field measurements would simultaneously measure the motion of the sample's entire spatial domain without the need to scan its surface.

Measurements of the temporally varying transient acoustic response is acquired by measuring a 3 ms in duration full-field TM displacement response to an impulsive acoustic click (click duration of 50 microseconds) with a camera frame rate of over 20,000 frames a second. A single full-field transient response simultaneously measures the response of the entire TM to a

broad range of excitation frequencies (0.333 to 10 kHz). The 3 ms duration of the transient response measurement reduces the effects of low-frequency environmental and physiological noise that can complicate in-vivo measurements. These short transient responses are also less affected by any time dependence in the mechanical properties of biological samples (Dobrev et al., 2014). However, the transient response, compared to a steady-state sinusoidal response, requires more analytic effort, where we first quantify the frequency response and impulse response of each point on the TM surface.

Near synchronous measurement of the TM shape and displacement response allows us to compensate the measured displacements for shape-related spatial variations in the holographic sensitivity vector and quantify surface normal displacements (Khaleghi et al., 2016). Accurate TM shape measurements may also provide useful clinical information related to the presence or absence of pathology, the effects of TM reconstructions, as well as the manufacture of personalized grafts adapted for the TM shape.

3.2 Tympanic Membrane Measurement Challenges

Accurate TM displacement and shape measurements are important to clinical and research applications; the performance criteria needed for accuracy are described here.

3.2.1 Anatomical and Physiological challenges

The first challenge arises from the size and shape of the TM. The human TM is about 8 mm in diameter, and the acoustically induced displacements, in normal hearing conditions (< 90 dB SPL), range from a sub-nanometer to hundreds of nanometers. The measurement tool must be capable of observing and measuring nanometer-scale motions from a field of view with a diameter of approximately 10 mm. Furthermore, the conical human TM is about 2–3 mm deep; it is aligned

at an angle relative to the ear canal, resulting in a required depth of field greater than 5 mm. The confined location of the TM at the end of the ear canal, along with its fragile structure, demands endoscopic and non-destructive measurements.

Second, in in-vivo measurements, the live sample moves due to the animal's heartbeat, muscle tremor, or respiration that cause comparatively slow (relative to sound frequencies) millimeter to sub-millimeter displacements. These motions can complicate holographic measurements of sound-induced motions making in vivo measurements even more challenging (Razavi et al., 2017).

Lastly, to fulfill the Nyquist criterion for the entire hearing frequency range (up to 20 kHz), the measurements should have a temporal resolution of at least 40 kHz (i.e., $< 25 \mu\text{s}$ sampling period). Oversampling can be helpful in improving resolution and signal-to-noise ratio in practical measurements.

3.2.2 Methodological Challenges

The number of techniques capable of measuring nanometer-scale displacement resolution over a large field of view (i.e., $> 10,000$ points) in hearing research are limited. Sound-induced sub-nanometer to micrometer-scale displacements on the TM are measured using LDV (Buunen & Vlaming, 1981) and Optical Coherence Tomography (OCT) Vibrometry (Chang et al., 2011). However, both LDV and OCT require the scanning of multiple points to achieve full field measurements; thus, they are limited to measurements of repeated motions. There are particular LDV setups that allow simultaneous measurements on many points on a surface, such as the multi-point differential laser Doppler velocimeter (Maru et al., 2010) or Continuous-Scan Laser Doppler Vibrometry (Ehrhard et al., 2017). However, their low spatial or frequency resolution makes them unsuitable for measurements of the in-vivo TM responses. Typically for a scanning LDV, a

complete scan requires seconds to minutes depending on the desired spatial resolution and type of scan. Such scanning systems for repeated measurements are also more susceptible to random physiological motions and other uncontrollable disturbances. By contrast, holography is an optical-metrology approach that can meet various TM measuring requirements, including non-destructive testing, nanometer-scale precision, and a full field of view. It is capable of determining the phase and intensity of the scattered light containing information pertaining to the shape of the sample on a nanometer scale. Holographic interferometry is sensitive to various physical factors such as uncontrolled displacements, temperature, etc. as it measures the optical phase caused by the changes in the length of the optical path or the refractive index associated with these physical parameters; however, uncontrolled variations in these factors can be limited by rapid data acquisition.

3.2.3 Development of Holographic Methods for TM Measurements

The time-averaged holographic study of Khanna and Tonndorf (1972) was the first to make use of holography to perform TM measurements. The contributions of these researchers opened up new avenues in hearing research for others (Dancer et al., 1975; Lokberg, 1980; Tonndorf & Khanna, 1972). Rosowski et al. (2009) demonstrated the use of significantly improved digital holographic methods. Further improvements for extracting the shape and acoustically induced one-dimensional and three-dimensional displacements of the TM in response to continuous sinusoids sounds were made later (Cheng et al., 2010; Hernández-Montes et al., 2009; Dobrev et al., 2015; Khaleghi et al., 2015). The majority of these later reports used stroboscopic imaging to attain high-temporal resolution (either transient or continuous sinusoidal stimulation) and depended on the repeatability of the motions. Dobrev et al. (2014) introduced high-speed digital holography (HDH) that used the latest high-speed digital imaging technologies to extract transient

full-field measurements of the TM. One of the main advantages of using HDH is its ability to measure a broad-band transient response of the TM with sufficient temporal resolution but without excitation repetitions. Khaleghi et al. (2015) developed a holographic system that is capable of measuring the three-dimensional sound-induced displacements of TM and its shape based on the dual-wavelength holographic contouring technique. Khaleghi and his coworker demonstrated that the TM's primary displacement is along the normal direction of the surface. Razavi et al. (2018) further a holographic system that is capable of measuring the three-dimensional sound-induced displacements of TM and its shape based on Khaleghi et al.'s (2015) dual-wavelength holographic contouring technique. The shape data are then exploited to measure the surface normal displacement of the transient response of the TM.

Chapter 4 Digital Holographic Interferometry and Fringe Projection

Holographic interferometry allows the measurement of static and dynamic displacements of objects on optically diffusive surfaces with precision up to fractions of a wavelength of light. It can be used in stress, strain, and vibration analysis and for non-destructive testing. It can be used to detect variations in optical path length on a transparent material, enabling, for example, fluid flow to be observed and evaluated. It can also be used to describe the shape of the target surface. Holography is a two-step method that involves (1) recording the interference between a diffracted light field scattered from the object beam and a reference beam and (2) reconstructing images to extract a measured quantity. Both steps can be achieved using traditional photographic plates or a digital sensor array (digital camera). The resulting interference fringe pattern is sensitive to changes in the optical path length or the refractive index of the medium through which light travels. Based on the design, holographic interferometry can monitor surface displacement, 3D shape, fluid flow, thermal fluctuations, and other physical factors associated with refractive index change (i.e., the change of the air density).

Instead of allowing light to build an interference pattern, the Fringe Projection approach projects a structured light pattern directly onto the surface of the sample. When viewed from different angles, the pattern appears geometrically distorted as a result of the shape of the surface of the object, allowing shape or shape variation measurements.

4.1 Light Interference in Holography

This section will briefly introduce the basics of light interference, which is the working principle of any holographic setups. In holography, light acts as a transverse electromagnetic wave with a time-varying electromagnetic field (Figure 4.1), with wavelength λ , an electric-field

component e_x , and a magnetic-field component h_y . Within the propagating wave e_x and h_y oscillate in phase but are orthogonal to each other and to the direction of propagation. The propagation of the electric field of light (E) in scalar form of a polarized light propagating in the z -direction can be described by a sinusoid:

$$E(z, t) = E_0 \cos(kz - \omega t + \phi) , \quad (4.1)$$

where E_0 is the amplitude of the wave; the $kz - \omega t + \phi$ term is the phase of the wave, ϕ is the initial phase offset, k is the wavenumber, and ω is the angular frequency of the light wave.

$$\omega = 2\pi f = \frac{2\pi c}{\lambda} \quad \text{and} \quad k = \frac{2\pi}{\lambda} , \quad (4.2)$$

where f and λ are the frequency and corresponding wavelength of the light wave. Using Euler's formula, light propagation can be expressed as follows:

$$E(z, t) = \frac{1}{2} E_0 e^{i(kz - \omega t + \phi)} , \quad (4.3)$$

The interference of two superimposed coherent light waves can be described by the superposition of two coherent, linearly polarized plane waves of the same frequency ω propagating in the z -direction, with wavenumber k_1 and k_2 , phases ϕ_1 and ϕ_2 , and amplitudes E_{o1} and E_{o2} . The electric fields E_1 and E_2 can be described:

$$E_1(z, t) = E_{o1} e^{i(\omega t - k_1 \cdot z + \phi_1)} , \text{ and} \quad (4.4)$$

$$E_2(z, t) = E_{o2} e^{i(\omega t - k_2 \cdot z + \phi_2)} . \quad (4.5)$$

The superposition of the two waves shown in Equations 4.4 and 4.5 is:

$$E(z, t) = E_1(z, t) + E_2(z, t) . \quad (4.6)$$

The intensity of light is measured by light sensors such as photographic film, photodiodes, and CCDs (Schnars et al., 2015). The light intensity is proportional to the square of the electrical

field and is independent of the temporal term t . The intensity I can be obtained by the following equation (Kreis, 2002):

$$I(z) \propto E^2. \quad (47)$$

Plugging Equation (4.6) into equation (4.7) and simplifying leads to:

$$I(z) \propto E_{01}^2 + E_{02}^2 + E_{01}E_{02} \cos(k_1 \cdot z - k_2 \cdot z + \phi_1 - \phi_2) \quad (48)$$

Equation **Error! Reference source not found.** can also be written as the intensities of the two waves:

$$I(z) = I_1 + I_2 + 2\sqrt{I_1 I_2} \cos(K \cdot z + \phi), \quad (49)$$

where $K = k_1 - k_2$ and $\phi = \phi_1 - \phi_2$. The resultant interference pattern $I(z)$ between two waves of equal frequency does not depend on the temporal variation of their electromagnetic field but is a function of the difference between the wavenumbers k_1 and k_2 and the difference between the initial phase offsets ϕ_1 and ϕ_2 (Kreis, 2002).

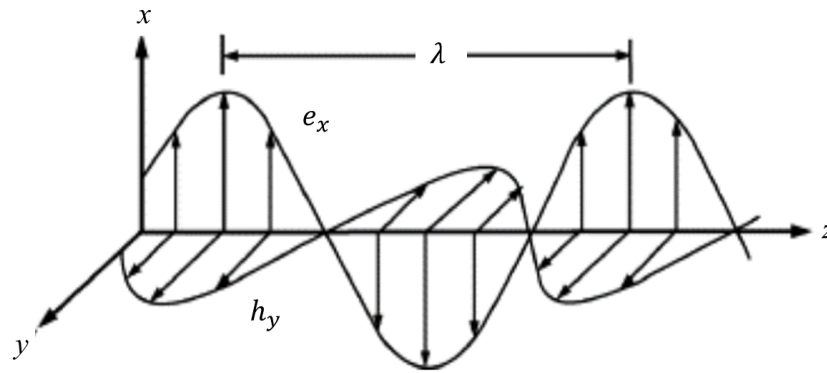


Figure 4.1. An electromagnetic wave with wavelength λ . The electric-field component e_x and the magnetic-field component h_y oscillate in phase but orthogonally to each other and to the direction of propagation. This wave is linearly polarized along the x -direction (adapted from Matthew Schwartz, 2021)

4.2 High-Speed Displacement Measurements using Phase Correlation Interferometry

Phase correlation (Payam, 2018) is used to extract the optical phase difference of a pair of holograms. The interference of the object beam and the reference beam forms a speckle pattern which can be captured by digital optical sensors (cameras). A statistical analysis of such speckle pattern will provide information about the optical phase difference between the two beams. Such speckle pattern is formed by the constructive (bright area) and destructive (dark area) superposition of multiple spherical wavefronts from diffuse reflections of monochromatic light. The bright and dark areas vary in the spatial domain of the sample's surface as the optical path length varies.

Statistical analysis of speckle patterns using Pearson's correlations reveals a correlation near one when the object and reference beams are in phase and a near-zero correlation when they are out of phase. Despite the fact that the speckles are spatially random, the relationship between variations of the speckle pattern and the interference phase ($\Delta\phi$) is consistent (Jones & Wykes, 1983). If sample displacements are spatially continuous in a spatially discrete digital hologram, phase variations along a small group of pixels centered at a pixel of interest are negligible. As a result, the superposition of a reference and object beam at the pixel of interest (x, y) is defined as follows:

$$I_{ref}(x, y) = I_r(x, y) + I_o(x, y) + 2\sqrt{I_r(x, y)I_o(x, y)} \cos(\phi), \quad (4.10)$$

where I_r and I_o represent the reference and object beam intensities, respectively, and ϕ is the random phase difference between the two interfered wavefronts. After displacement (or deformation) of the sample, the optical path length between the two beams changes, producing a phase difference $\Delta\phi$ in the deformed image, which can be expressed as follows:

$$I_{def}(x, y) = I_r(x, y) + I_o(x, y) + 2\sqrt{I_r(x, y)I_o(x, y)} \cos(\phi + \Delta\phi) \quad (4.11)$$

Before and after sample deformation, the Pearson's product-moment coefficient, ρ , between a tiny kernel around the point of interest is calculated (Jones & Wykes, 1983; Schmitt & Hunt, 1997).

$$\rho(I_{ref}(x, y), I_{def}(x, y)) = \frac{(r + 1)^2 + 4r \cos(\Delta\phi)}{(r + 1)^2 + 4r} \quad (4.12)$$

where $r = \frac{I_o}{I_r}$ is the intensity ratio of the object and reference beams.

In practice, PZT calibration can be used to remove the DC terms in 4.11, $I_r(x, y) + I_o(x, y)$ for easier post-processing of holograms. PZTs can be mounted in either the object beam or reference beam path and used to generate a fixed optical path difference equal to the laser's wavelength when there is no excitation on the sample. The DC term is equal to the integration of the interference pattern during the movement of the PZT. Therefore, after removing the DC term. Equation 4.12 can be simplified into the following equation:

$$\rho(I_{ref}(x, y), I_{def}(x, y)) = \cos(\Delta\phi). \quad (4.13)$$

By definition, the Pearson's product-moment coefficient of two images, I_{ref} and I_{def} , before and after sample deformation may be determined using the following equation:

$$\rho(I_{ref}, I_{def}) = \frac{\langle I_{ref}I_{def} \rangle - \langle I_{ref} \rangle \langle I_{def} \rangle}{\left[\langle I_{ref}^2 \rangle - \langle I_{ref} \rangle^2 \right]^{\frac{1}{2}} \left[\langle I_{def}^2 \rangle - \langle I_{def} \rangle^2 \right]^{\frac{1}{2}}} \quad (4.14)$$

where the operator $\langle \rangle$ describes the expected value, and I_{ref} and I_{def} are the grayscale pixel values in matrix form.

The Pearson correlation coefficient is calculated using a sliding window technique on each pair of captured images. Moving a sliding window (e.g., 3 x 3 pixels) from point to point in the horizontal and vertical directions is all that is required for the calculation. However, calculating the Pearson's coefficient of two 512 by 512-pixel images with the sliding window approach requires more than 250,000 iterations with two levels of nested loops, and takes roughly 3.5 seconds on a modern computer. More than 1000 pictures are collected for a typical displacement measurement, which takes around an hour to process. Accessing the measurement quality during the measurement is problematic due to the considerable processing time. To improve the computational speed and save experimental time, I have optimized the Pearson correlation algorithm. The optimized approach allows us a near 'real-time' presentation of the optical phase of the displacement data. The near 'real-time' processing of the results enables access to the data quality during the measurement to expedite the studies. The simplified technique allows measurements on postmortem human middle ears with experimentally produced diseases or measurements on live animal samples to be completed in a short period of time, minimizing time-related changes in biological samples.

A vectorization approach is used to optimize the program by removing nested loops and improving computational performance. Vectorization is the process of transforming an algorithm from acting on a single value at a time to working on a collection of values (vector or matrix) at once by exploiting modern CPU vector operation capabilities.

For example, consider calculating the Pearson's coefficient of two images of 512 by 512 pixels using a kernel of 3 by 3 pixels: the nested loop approach will calculate the Pearson's coefficient of the window at one pixel and then repeat this process 262,144 (512 x 512) times, whereas the vectorization approach will perform all the calculations simultaneously. To

accomplish the vectorization, the original photos are turned into two matrix sets of gray scale values. The 3 by 3 kernel at (x, y) coordinates of the original image matrix I is shown in Figure 4.2. The center element of the kernel of each modified matrix (A1–C3) is translated to the original kernel's surrounding elements. These nine matrices (A1–C3) can be used directly in Eq. (4.14) to compute the Pearson's correlation coefficient calculation.

To increase the vectorization to n by n kernel size, the original image matrix I must be turned into a n^2 matrix in the same manner as described previously. The Pearson's correlation coefficient is determined using these n^2 matrices. To generalize the Pearson correlation coefficient computation for n by n kernel size ($n=3, 5, 7, \dots$), defining $I'(i, j)$ are the n^2 translated matrices of the original image matrix I , where $i= 1, 2, 3, \dots, n$ and $j = 1, 2, 3, \dots, n$, and $I_{x,y}$ is the matrix element at (x, y) coordinate; $I'(i, j)$ is related to $I_{x,y}$ by the following equation:

$$I'(i, j) = I_{(x-\frac{n-1}{2}+i-1),(y-\frac{n-1}{2}+j-1)}, \quad (4.15)$$

$$i= 1, 2, 3 \dots n \text{ and } j = 1, 2, 3, \dots, n.$$

This is valid for both the undeformed frame I_{ref} and deformed frame I_{def} . Plug Equation 4.15 for I_{ref} and I_{def} into Equation 4.14 and simplify:

$$I' \rho(I_{ref}, I_{def}) = \frac{\sum_i^n \sum_j^n X \cdot Y}{[\sum_i^n \sum_j^n X^2 \cdot \sum_i^n \sum_j^n Y^2]^{\frac{1}{2}}}, \quad (4.16)$$

Where $X = I_{ref}'(i, j) - \frac{1}{n^2} \sum_i^n \sum_j^n [I_{ref}'(i, j)]$, and $Y = I_{def}'(i, j) - \frac{1}{n^2} \sum_i^n \sum_j^n [I_{def}'(i, j)]$. As a result, the $\rho(I_{ref}, I_{def})$ may be determined in terms of $I_{ref}'(i, j)$ and $I_{def}'(i, j)$ without any loops. The fastest calculation is the 3 x 3 pixel-kernel version, which uses the fewest modified matrices and takes roughly 0.15s to complete on a modern computer(AMD Opteron 2384 2.70 GHz). This Pearson's coefficient kernel of 3 by 3 pixels is suitable for displaying the findings immediately

after the measurement to access the optical phase quality and assess whether the measurement has to be repeated.

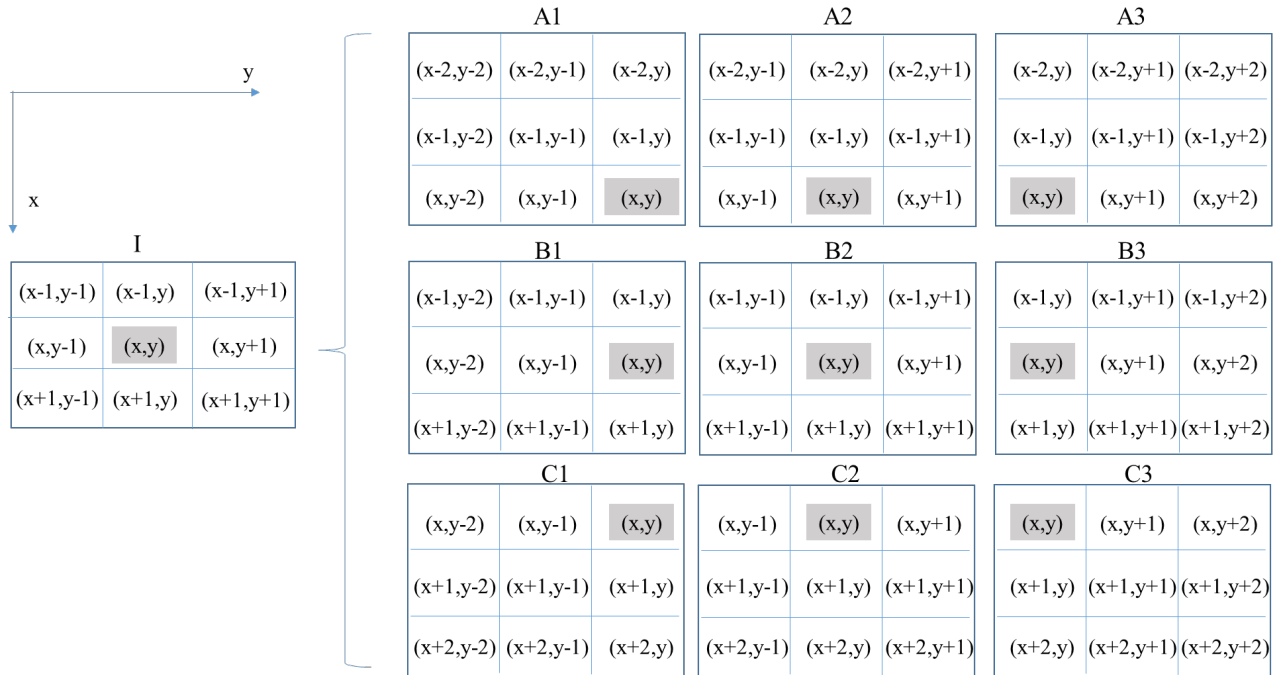


Figure 4.2. An example of preparation of a kernel at (x,y) location of image matrix I for Pearson correlation calculation in the vectorized algorithm. I is the original matrix and $A1-3$, $B1-3$ and $C1-3$ are translated matrices.

4.3 High-Speed Holographic Shape Measurements

By comparing the optical path difference of the reference and object beams collected by an optical sensor, digital holography (DH) may record and reconstruct an optical wavefield (amplitude and phase). The fringe locus function gives the measured optical phase $\Delta\phi$ for a general holographic interference setup (Kreis, 2002):

$$\Delta\phi = \mathbf{d} \cdot \mathbf{e}, \quad (4.17)$$

where \mathbf{d} is the optical path difference vector, and \mathbf{e} is the sensitivity vector defined as:

$$\mathbf{e} = \frac{2\pi}{\lambda} [\mathbf{b} - \mathbf{s}], \quad (4.18)$$

Where λ is the wavelength of the laser, \mathbf{b} is the observation unit vector, and \mathbf{s} is the illumination unit vector. In general, the object beam is reflected by a diffusive scattering object, and the measured optical phase contains a large amount of spatially variable speckle noise. As a result, the optical path difference cannot be calculated using a single optical wavefield. However, the difference in the detected optical phase change ($\Delta\phi_2 - \Delta\phi_1$) from two camera exposures can be expressed as:

$$\Delta\phi_2 - \Delta\phi_1 = \mathbf{d} \cdot \mathbf{e}_2 - \mathbf{d} \cdot \mathbf{e}_1 \quad (4.19)$$

where \mathbf{e}_1 and \mathbf{e}_2 are the sensitivity vectors at the two camera exposures. The optical phase change ($\Delta\phi_2 - \Delta\phi_1$) in **Equation 4.19** can be retrieved if the speckle distributions at the two exposures correlate, which is the foundation of digital holographic shape measurement (Kreis, 2005; Jones, 1989).

Assuming no object deformation occurs during the measurement, the height information (i.e., shape) of the measured subject can be acquired by varying the sensitivity vector's magnitude

or direction. The magnitude of the sensitivity vector can be altered by adjusting the wavelength of the laser source, resulting in the multi-wavelength approach. The multi-angle shape measuring method, on the other hand, varies the direction of the sensitivity vector by changing the angle of the object beam.

4.3.1 Multiple wavelength Holographic Interferometry

A tunable laser can be used to change the magnitude of the sensitivity vector by altering the wavelength of the laser source (Razavi et.al., 2018). Razavi implemented this shape measurement into the high-speed system, this dissertation includes improvements of the post analysis of the holographic data (more details are available in **chapter 5**). The optical phase difference $\Delta\phi_2 - \Delta\phi_1$ of a holographic measurement of an object with two different wavelengths gives the following equation:

$$\Delta\phi_2 - \Delta\phi_1 = \mathbf{d} \cdot \mathbf{e}_2 - \mathbf{d} \cdot \mathbf{e}_1 = \mathbf{d} \cdot \left[\frac{2\pi}{\lambda_2} (\mathbf{b} - \mathbf{s}) - \frac{2\pi}{\lambda_1} (\mathbf{b} - \mathbf{s}) \right] \quad (4.20)$$

The left-hand side of Equation 4.20 is the optical phase difference, which is determined from the interference pattern captured by the camera. The wavelengths λ_1 and λ_2 are known experimental parameters, \mathbf{b} and \mathbf{s} are the observation and illumination vectors, respectively, which can be measured directly or obtained using calibration. The optical path difference vector \mathbf{d} can be solved to extract shape information. In the simplified 2D case shown in Fig. 4.3a, \mathbf{P} is a random point on the subject, \mathbf{B} is the observation point, and \mathbf{S} is the illumination point. In this case, the optical path difference vector \mathbf{d} is as follows:

$$\begin{aligned}
|\mathbf{d}| &= |\mathbf{PB} - \mathbf{SP}| \\
&= \sqrt{(\mathbf{P}_x - \mathbf{S}_x)^2 + (\mathbf{P}_y - \mathbf{S}_y)^2} \\
&\quad + \sqrt{(\mathbf{B}_x - \mathbf{P}_x)^2 + (\mathbf{B}_y - \mathbf{P}_y)^2}
\end{aligned} \tag{4.21}$$

where P_y is the user-defined pixel coordinates in the y -direction. P_x containing the shape information in the x -direction is the only unknown variable in **Equation 4.21**. According to Equation 4.20, the sensitivity of the measurement is proportional to the wavelength.

4.3.2 Multiple-Angle Holographic Interferometry

The shape can also be measured by mechanically changing the direction of the illumination vector \mathbf{s} thereby changing the sensitivity vector (Figure 4.3b). From Eq. (4.19), we get the following equation:

$$\begin{aligned}
\Delta\phi_2 - \Delta\phi_1 &= \mathbf{d} \cdot \mathbf{e}_2 - \mathbf{d} \cdot \mathbf{e}_1 = \\
&\quad \mathbf{d} \cdot \left[\frac{2\pi}{\lambda} (\mathbf{b} - \mathbf{s}_2) - \frac{2\pi}{\lambda} (\mathbf{b} - \mathbf{s}_1) \right]
\end{aligned} \tag{4.22}$$

where \mathbf{s}_1 and \mathbf{s}_2 are the observation vectors at two camera exposures, which can be measured or calibrated (Psota et al.,2020). The shape information is obtained by solving the optical phase difference from Equation 4.22. By introducing a known angle change $d\theta$ to the illumination vector in the experimental arrangement shown in Figure 4.3 (b), the shape information in the x -direction may be obtained by the following relation (Psota et. al., 2020):

$$x = (\Delta\phi_2 - \Delta\phi_1) \left(\frac{2\pi}{\lambda} \sin \theta \, d\theta \right)^{-1} \tag{4.23}$$

The method's sensitivity grows as the angle change increases, and it is also dependent on a non-zero illumination angle θ .

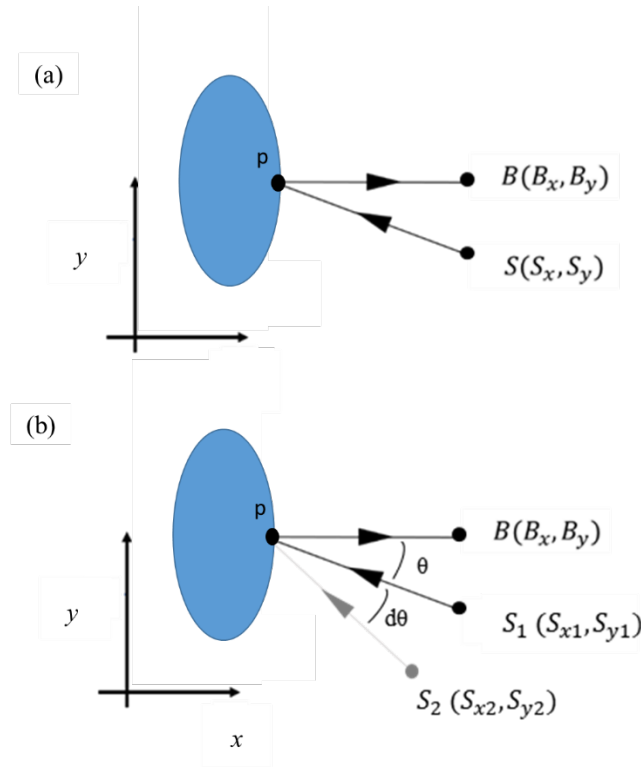


Figure 4.3. 2D Holographic shape measurement schematics: (a) Multi-wavelength method, (b) Multi-angle wavelength method. \mathbf{PB} is the observation unit vector and \mathbf{SP} is the illumination unit vector. \mathbf{S}_1 and \mathbf{S}_2 are the illumination point before (x_1, y_1) and after (x_2, y_2) changing of the illumination angle in the multi-angle method.

4.4 High-Speed Fringe Projection Shape Measurement

The fringe projection shape measuring method is based on projecting well-defined fringe patterns onto the sample. The optical geometry of a general projection and imaging system is depicted in Figure 4.4. Points P and E represent the locations of projection and imaging optics, respectively. Under normal viewing conditions, if the distance between the sensor and the

reference plane is large in comparison to the spacing (or pitch) between the projected fringes, the phase and height are related using the triangulation method (Su et al., 2007).

$$h(x, y) = \frac{L}{d} |AC| = \frac{L}{Dd} \frac{\Delta\phi}{2\pi f} \quad (4.24)$$

where L is the distance between the sensor and the reference plane; d is the distance between the sensor and projector; $|AC|$ is the distance between points A and C ; f is the spatial frequency of the projected fringes in the reference plane, and $\Delta\phi$ is the phase of the projected fringe between points A and C . Thus, the height information $h(x, y)$ is only a function of phase $\Delta\phi$, whereas the other parameters in Equation 4.24 are fixed based on the configuration of the optical measuring system.

The phase-shifting technique is commonly used in interferometry to improve contour resolution and quantify measured phase by removing sign ambiguity. Consider four sinusoidal fringe patterns I_1 , I_2 , I_3 and I_4 with phase shifts of 0° , 90° , 180° , and 270° within one period of the fringe. The phase $\Delta\phi$ of the image can be obtained by the following equation:

$$\Delta\phi = \arctan \frac{I_4 - I_2}{I_1 - I_3} \quad (4.25)$$

Due to the constraints of high-speed imaging and power limitations, the system is configured to scan a single fringe across the sample and take a sequence of high-speed images. Once a sequence of images of single fringe projections to different locations on the sample have been recorded, they are numerically summed to form a fringe image with phase-shifting for shape measurement. In this high-speed fringe projection configuration, the high-speed camera captures the $4n$ single fringe images sequentially: $I_1^1, I_1^2, I_1^3, I_1^4, I_2^1, I_2^2, I_2^3, I_2^4 \dots I_n^1, I_n^2, I_n^3, I_n^4$, and the pitch between each projected fringe is $\frac{W}{4}$, where W is the width of the single fringe. Numerical

summations $(I_1^1 + I_2^1 \dots I_n^1)$, $(I_1^2 + I_2^2 \dots I_n^2)$, $(I_1^3 + I_2^3 \dots I_n^3)$, and $(I_1^4 + I_2^4 \dots I_n^4)$ are calculated to reconstruct the completed four-phase shifted fringe images, and the optical phase $\Delta\phi$ is obtained via Equation 4.26:

$$\Delta\phi = \arctan \frac{(I_1^4 + I_2^4 \dots I_n^4) - (I_1^2 + I_2^2 \dots I_n^2)}{(I_1^1 + I_2^1 \dots I_n^1) - (I_1^3 + I_2^3 \dots I_n^3)} \quad (4.26)$$

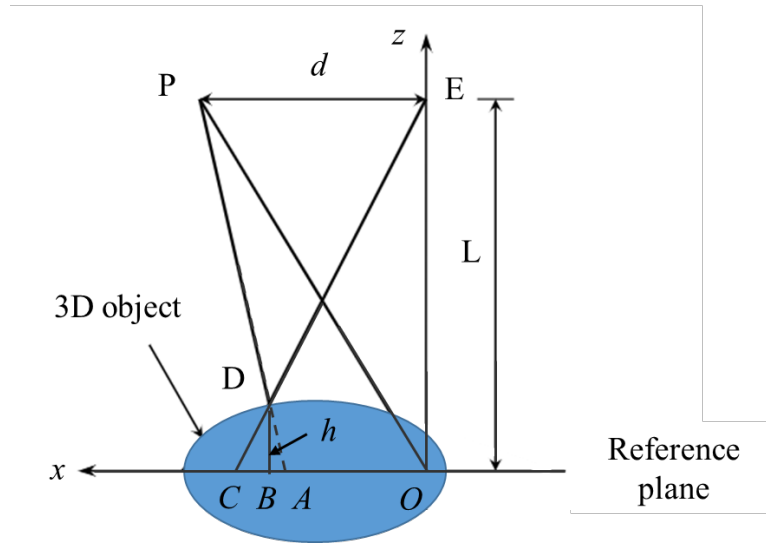


Figure 4.4. Optical geometry for fringe projection (adapted from Jia Yang, 2014)

4.5 Applications of Holographic Interferometry and Fringe Projection in Hearing Research

Many researchers are interested in studying the sound-induced vibrational patterns of various mammalian TMs. Previous research on the use of holographic interferometry in the study of the middle ear can be classified into the following categories: (1) qualitative investigations of the sound-induced vibrational patterns of the TM using conventional time-averaged and double exposure holography (Khanna & Tonndorf, 1972; von Bally, 1978; Uyemura et al., 1979; von Bally & Greguss, 1987; Ogura et al., 1979; 1983); (2) quantitative one-dimensional measurements

of the sound-induced motions of the TMs (Wada et al., 2002; Rosowski et al., 2009; Cheng et al., 2010; Chang et al., 2013; Cheng et al., 2013; Dobrev et al., 2014); (3) measurements of 3D shapes of the TMs (Decraemer et al., 1991; Solís et al., 2012, Khaleghi et al., 2015, Psota et al., 2020). and (4) high-speed measurement of the impulse response of the TM normalized by its form (Razavi et al., 2018).

Fringe projection was used to investigate the shape and static pressure induced changes in shape of TMs. Dirckx et al. (1997) studied the shape and static-pressure-induced deformation of the gerbil tympanic membrane in real-time using the Moire projection method. Liang et al. (2016, 2018) used a micro-fringe projection with Ronchi rulings to analyze the shape change of chinchilla tympanic membrane before and after pressure change and the mechanical properties of baboon tympanic membrane.

Chapter 5 New developments in analyzing digital holographic interferometry for TM investigation

This chapter discusses the new developments in the shape and displacement analysis methodologies, including the complex field filtering strategy to improve the measurement quality, the temporal phase unwrapping method for shape measurement to increase the measurement resolution and frequency and impulse analysis to understand tympanic membrane mechanisms under different middle ear conditions.

5.1 Complex Field Filtering of the Optical Phase

The optical phase quality from experimental data is often affected by various noises which often come from:

- Low reflection from the sample,
- Inaccurate beam ratio
- Sensor noise from the camera
- Uncertainty from the phase shifting procedures

This section proposes a filtering strategy to post process the optical phase to alleviate the affects of abovementioned noises in the measurement results. First of all, the image directly obtained from the high-speed holographic displacement measurement system is a speckle image. Pearson's correlation is used to extract the optical phase from the speckle images, as described in the previous chapter. Once the optical phase is obtained, a phase unwrapping algorithm can be applied to demodulate the optical phase. Phase unwrapping is the process to reconstruct the physically continuous phase variation which can be done by adding or subtracting multiples the phase jumps to eventually remove any phase discontinuities. Filtering is an essential process to improve the signal-to-noise ratio of a given measurement system. However, directly applying a filter on the

optical phase obtained from the high-speed holographic measurement is not applicable and will result in failure of the phase unwrapping process. This section will discuss an approach to apply filtering in the complex field of the optical phase image to improve the phase quality.

5.1.1 Reconstruct the Complex Field Using Optical Phase

The optical phase image is an image of the measured target, which shows the phase difference between the illumination beam and reference beam of the holography setup ranging from $-\pi$ to π . Assuming the optical phase image is I , the following equation is used to reconstruct the complex field of I :

$$C_I = \exp(I \cdot j) = \cos I + j \sin I \quad (5.1)$$

where j is imaginary unit. Equation (5.1) satisfies the following relationship between the complex field C_I and the optical phase I :

$$\text{angle}(C_I) = \arctan\left(\frac{\sin I}{\cos I}\right) = I \quad (5.2)$$

C_I is referred to as the complex field of the optical phase. The amplitude of the C_I is not of interest here and has been retained as a unit.

5.1.2 Moving Window Average Filtering of the Complex Field Versus Filtering of the Optical Phase

The two-dimensional (2D) moving window average filtering process is used to reduce the noise within the collected images. It operates by replacing the value of each pixel with the averaged value of the given size of a window of pixels. In the case of an image matrix M , the 2D moving window averaging of a k by k window at (x, y) pixel location is calculated by the following equation:

$$2D_{mean(M_{x,y})} = \frac{1}{k^2} \sum_{j=y-k}^{y+k} \sum_{i=x-k}^{x+k} M_{i,j} \quad (5.3)$$

If such a filter is applied to the optical phase I , then *the* $2D_{mean(I)}$ will have a smaller range compared to its unfiltered value. This reduction depends on the window size k and the gradient of the optical phase. As the range of filtered optical phase is no longer from $-\pi$ to π . Unwrapping algorithms that depend on detecting the $-\pi$ to π jump will not work on such an optical phase. If this 2D moving window averaging is applied to the reconstructed complex field C_I by averaging the real part and imaginary part separately, then the filtered $2D_{mean(C_I)}$ is

$$\begin{aligned} 2D_{mean(C_I)} &= \frac{1}{k^2} \sum_{j=y-k}^{y+k} \sum_{i=x-k}^{x+k} \text{real}(C_I) \\ &\quad + \frac{1}{k^2} \sum_{j=y-k}^{y+k} \sum_{i=x-k}^{x+k} \text{img}(C_I) \\ &= \frac{1}{k^2} \sum_{j=y-k}^{y+k} \sum_{i=x-k}^{x+k} \cos I + \frac{1}{k^2} \sum_{j=y-k}^{y+k} \sum_{i=x-k}^{x+k} j \sin I \end{aligned} \quad (5.4)$$

And the angle of the complex field is as follows:

$$\begin{aligned} \text{angle}(2D_{mean(C_I)}) &= \text{artan} \left(\frac{\frac{1}{k^2} \sum_{j=y-k}^{y+k} \sum_{i=x-k}^{x+k} \sin I}{\frac{1}{k^2} \sum_{j=y-k}^{y+k} \sum_{i=x-k}^{x+k} \cos I} \right) \\ &= \text{arctan} \left(\frac{\sum_{j=y-k}^{y+k} \sum_{i=x-k}^{x+k} \sin I}{\sum_{j=y-k}^{y+k} \sum_{i=x-k}^{x+k} \cos I} \right) \end{aligned} \quad (5.5)$$

$$\begin{aligned} \text{angle}(2D_{mean(C_I)}) &= \text{artan} \left(\frac{\frac{1}{k^2} \sum_{j=y-k}^{y+k} \sum_{i=x-k}^{x+k} \sin I}{\frac{1}{k^2} \sum_{j=y-k}^{y+k} \sum_{i=x-k}^{x+k} \cos I} \right) \\ &= \text{arctan} \left(\frac{\sum_{j=y-k}^{y+k} \sum_{i=x-k}^{x+k} \sin I}{\sum_{j=y-k}^{y+k} \sum_{i=x-k}^{x+k} \cos I} \right) \end{aligned} \quad (5.5)$$

And equation (5.5) is an arctangent function that inherently ranges from $-\pi$ to π , which ensures a $-\pi$ to π jump exists for detection by unwrapping algorithms. An example of a high-speed displacement measurement is shown in the Figure 5.1. Figure 5.1 shows a wrapped optical phase gathered during the transient displacement of a latex membrane produced by an impulsive click-like sound. Figure 5.1(a) is the unfiltered optical phase derived from Pearson's correlation; (b) is the filtered optical phase obtained by directly applying the moving averaging filter on the optical phase; and (c) is the optical phase after applying the same moving averaging filter on the reconstructed complex field.

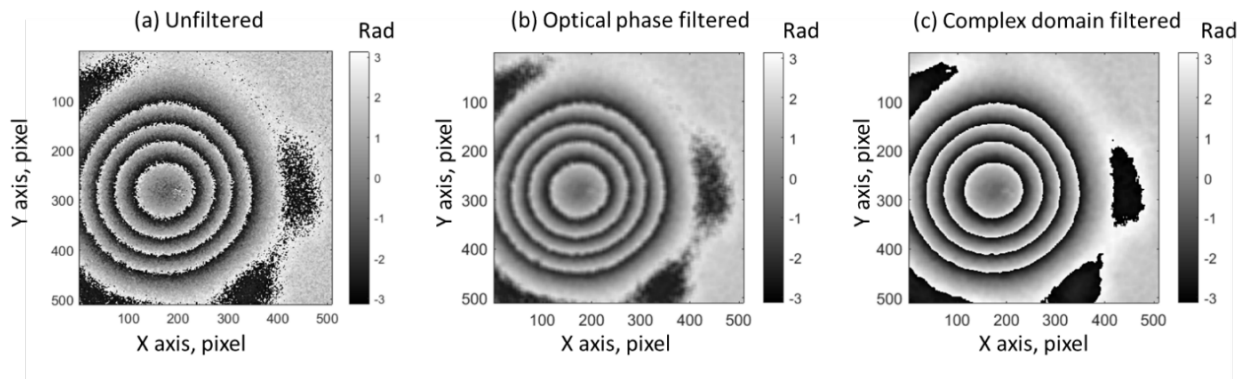


Figure 5.1 Example of moving window average filter, images show the optical phase of a high-speed holographic displacement of a vibrate latex drum: (a) unfiltered optical phase; (b) results of filtering direct from the optical phase and (c) results of filtering from the complex field

The 2D Goldstein branch cut phase unwrapping algorithm (Estrada et al., 2012) is applied to the three optical phases, and the results are shown in Figure 5.2. Figure 5.2 (a) is the unwrapped unfiltered optical phase. (b) is the unwrapped results from Figure 5.1 (b). Figure 5.2 (c) illustrates the unwrapped results after filtering in the complex field. Figure 5.1 (c). Both (a) and (c) are successfully unwrapped, but (b) is not, as the $-\pi$ to π jumps lost in the filtering.

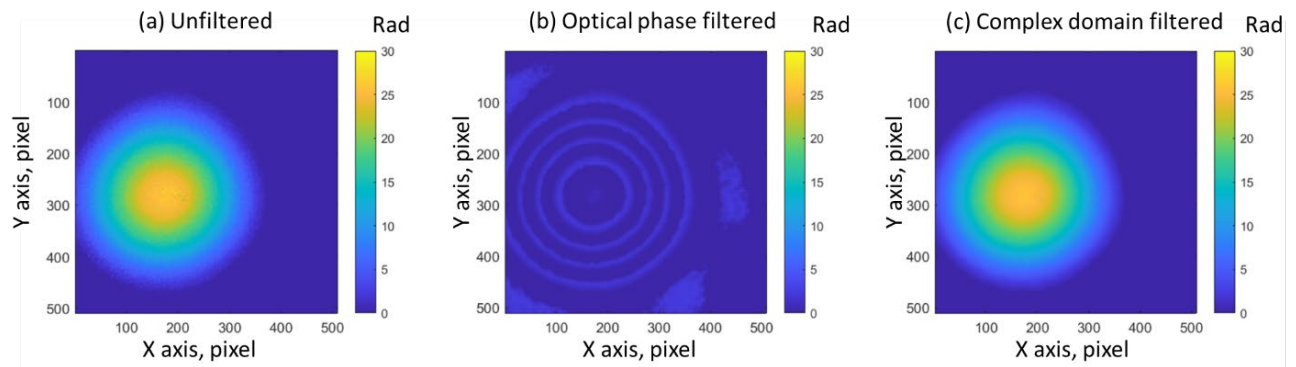


Figure 5.2 Example of phase unwrapping of moving window average filter: (a) unwrapping of unfiltered optical phase; (b) unwrapping of results of filtering direct from the optical phase and (c) unwrapping of results of filtering in the reconstructed optical complex field. (a) and (c) have a similar unwrapping results, the detailed comparison is available in **Figure 5.3**.

To compare the unwrapped results from Figure 5.2(a) and (c), the phase profile along a vertical diameter (the black line shown in the subpanel in Figure 5.3) is plotted in Figure 5.3. The unwrapped complex field filtered optical phase (the orange line) smoothly varies along the diameter, especially when compared to the unwrapped optical phase without any filtering (the blue line). Next we add a 2D map of artificial random phase noise (Figure 5.4 (a)) with a range from -2.3 to 2.3 radian to the raw optical phase (Figures 5.4 (b) and 5.4 (c)). The range of this noise is large enough to generate unwrapping failures. The unwrapped optical phases of the measured profile with added noise are shown in Figure 5.5. Figure 5.5 (a) depicts the unwrapped optical phase without any filtering, and it has many areas with unwrapping errors. Figure 5.5(b) showcases the unwrapped optical phase after filtering in the complex field, and no unwrapping errors are observed. Clearly, filtering of the reconstructed complex field of a noisy optical phase can improve the unwrapping quality. The unwrapping results of direct filtering of the optical phase are not shown, as it has been demonstrated that such filtering does not lead to proper unwrapping.

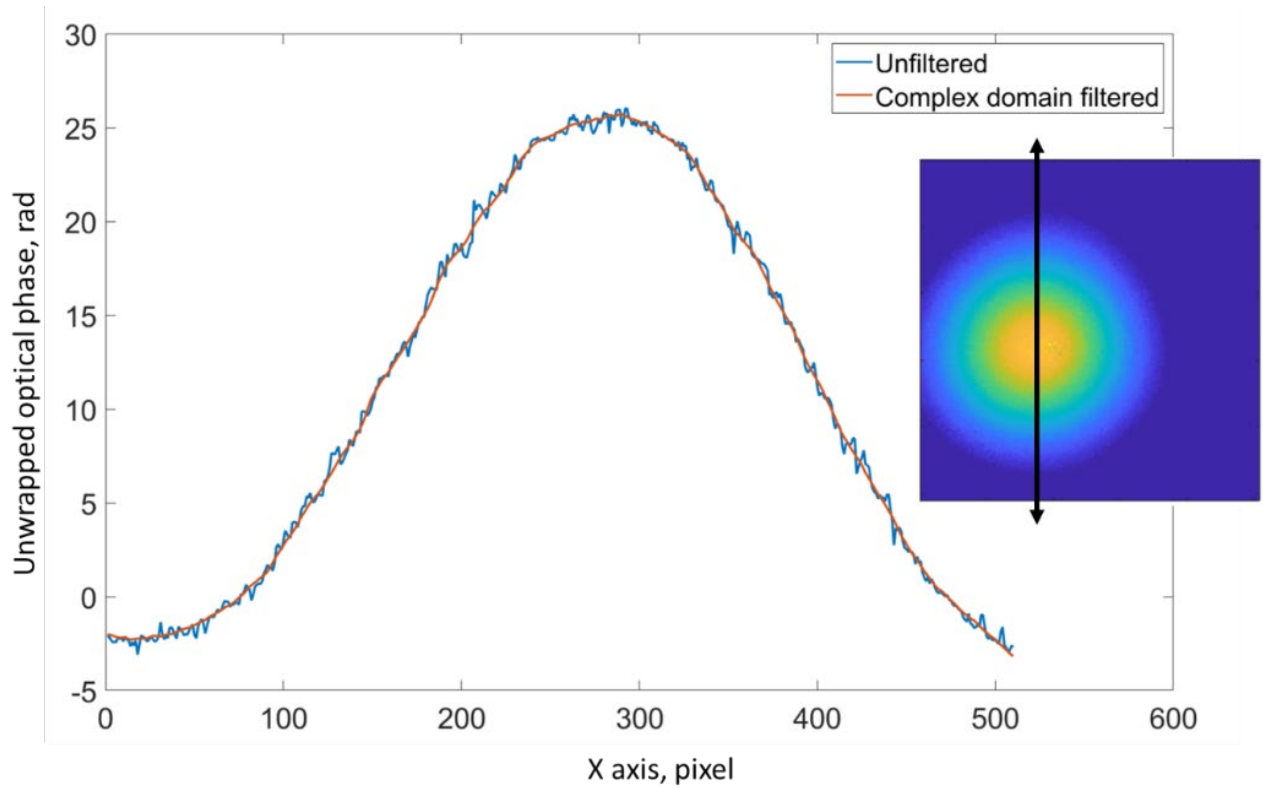


Figure 5.3 Comparison of the unwrapped results from Figures 5.2(a) and (c). The profile of the vertical line is a black line shown in the subpanel across the center of the sample.

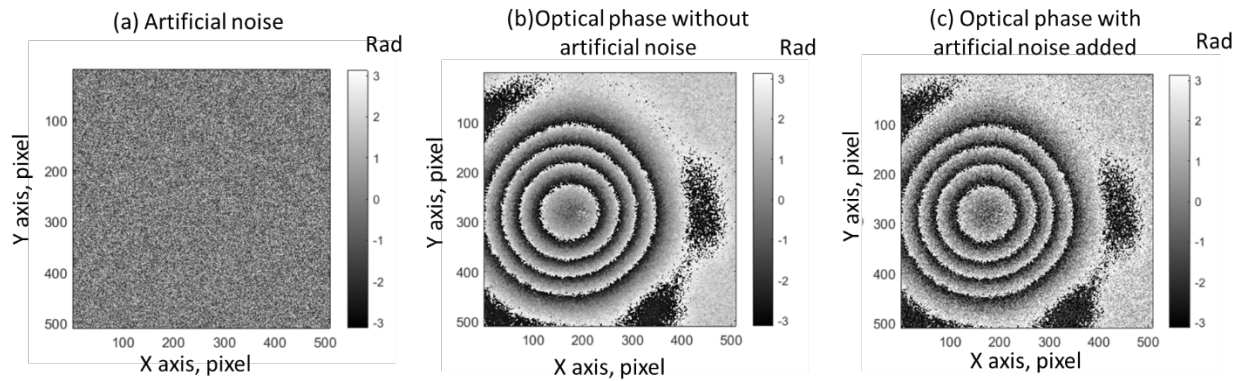


Figure 5.4. Artificial noise is added to the optical phase: (a) artificial random noise; (b) optical phase without artificial noise; and (c) the optical phase with artificial noise added.

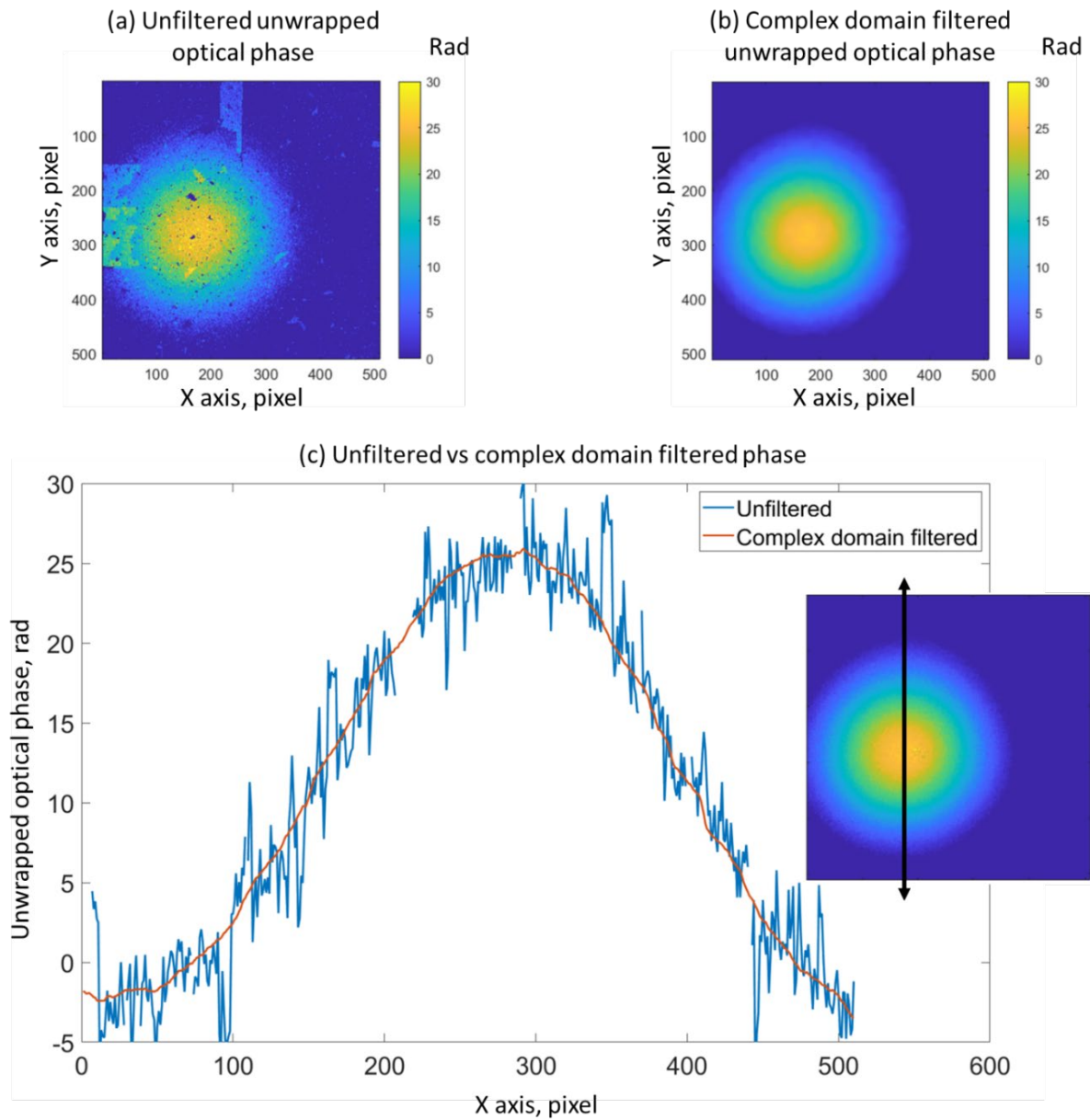


Figure 5.5 Compression of unwrapping results: (a) the unwrapping results of the optical phase with the artificial noise; (b) the unwrapping results of the complex field filtered optical phase with the artificial noise; and (c) the comparison of the unwrapped results from unfiltered and filtered results. The profile of the vertical line is a black line, as shown in the subpanel across the center of the sample.

5.2 Temporal Phase Unwrapping

Shape measurements using multi-angle and multi-wavelength techniques have been described in detail in the previous chapter. In this section a temporal phase unwrapping method is compared to the 2D surface unwrapping algorithm described above. First, wrapped optical phase patterns are calculated for consecutive phase differences ($d\phi$) produced by a continuous changing wavelength or illumination angle. Second, spatial unwrapping is applied to each phase difference ($d\phi$). Due to the small change in phase between the consecutive images, the spatial unwrapping algorithm can successfully unwrap the unfiltered optical phase. Lastly, all of the unwrapped consecutive phase differences are summed to obtain the total optical phase (ϕ_{total}) of the shape measurement:

$$\phi_{total} = \sum \text{unwrap}(d\phi) \quad (5.6)$$

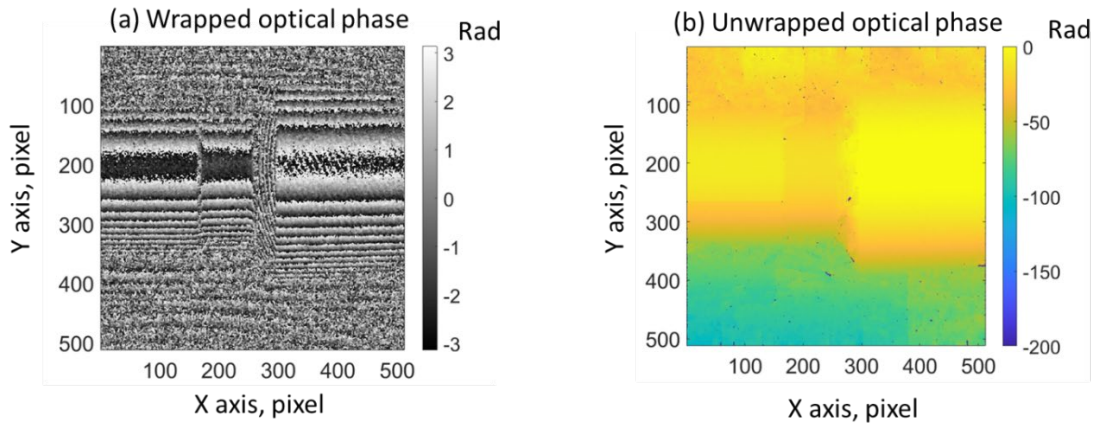


Figure 5.6 (a) Wrapped optical phase from the first and last phase samplings. (b) Spatial phase unwrapping results.

The shape of a NIST traceable cylinder gauge was obtained using the multi-wavelength shape measurement method. A total of 50 optical phase sampling instances were completed during the wavelength tuning of 3.7 nm. The optical phase difference between the first and last phase sampling is shown in Figure 5.6(a), and the spatially unwrapped phase from this difference is

shown in Figure 5.6(b). Because the difference in optical between the first and last phase samplings is large, the raw phase difference in Figure 5.6(a) contains many discontinuities and the unwrapped phase of Figure 5.6(b) is muddy. In contrast, the 49 consecutive optical phases differences are shown in Figure 5.7. In each optical phase, the number of phase discontinuities (the number of times the colors change from white to black) are small, and they can be successfully unwrapped using the spatial phase unwrapping algorithm.

By summing all 49 of the the unwrapped consecutive optical phases together, another estimation of the total optical phase is obtained and shown in Figure 5.8. Note the clarity of the temporally unwrapped phase image (Figure 5.8(a)) and the clearly defined shape of the NIST sample (Figure 5.8(b)).

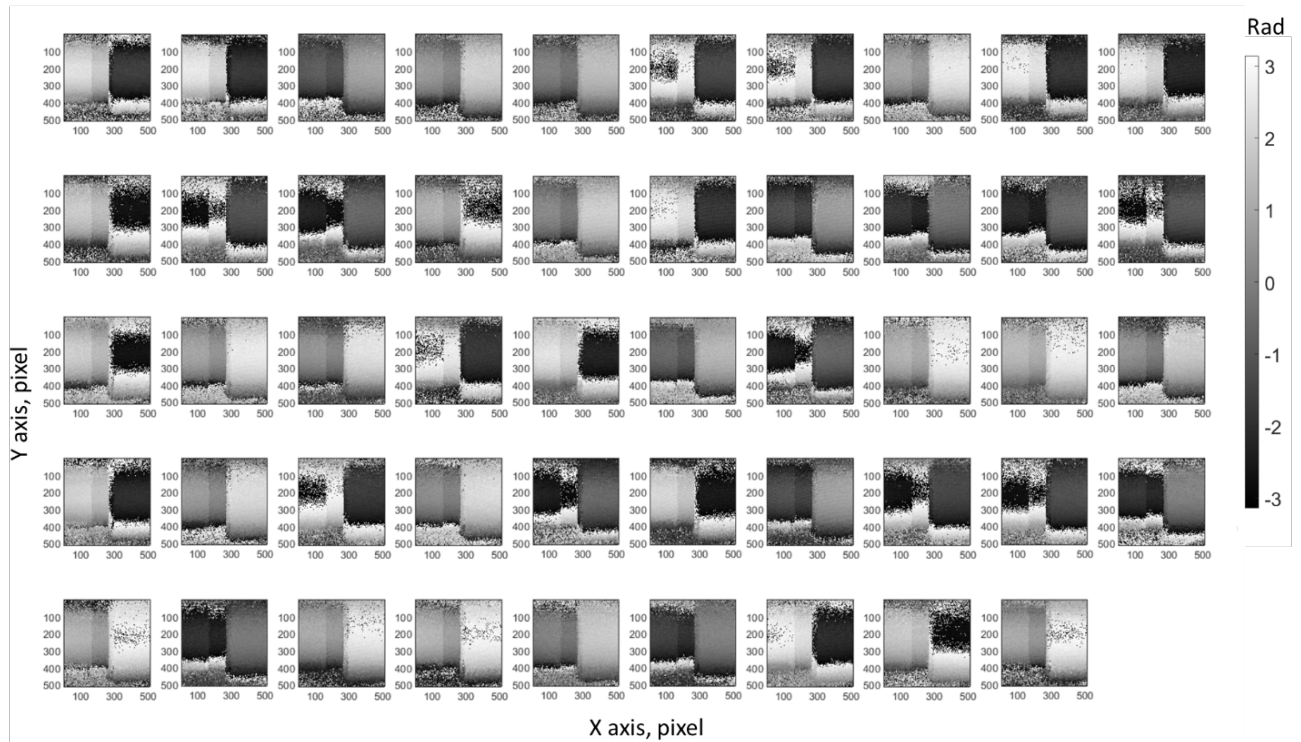


Figure 5.7 The 49 consecutive optical phases changes defined from the 50-phase samplings acquired during the tuning of the wavelength

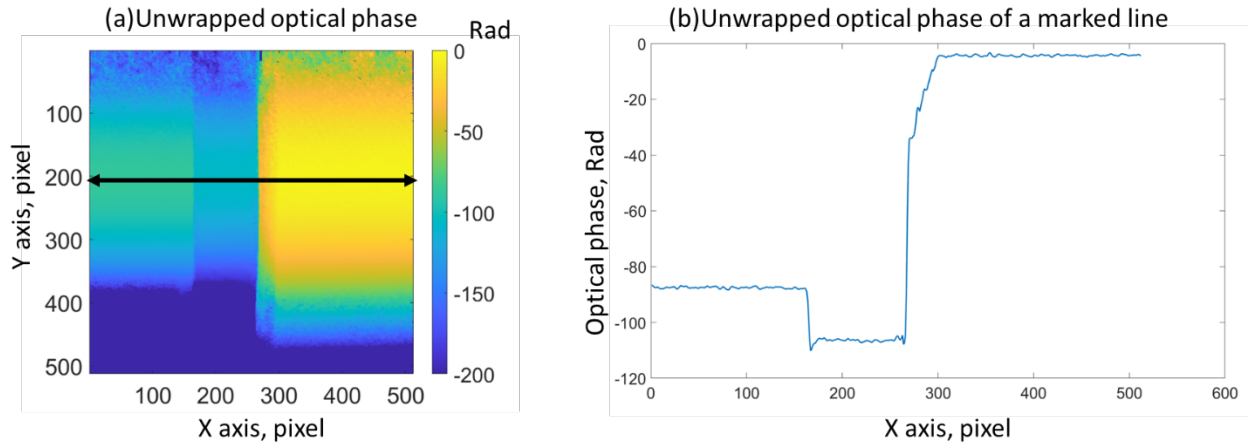


Figure 5.8 (a) Temporal phase unwrapping results and (b) Optical phase of the back line marked in (a).

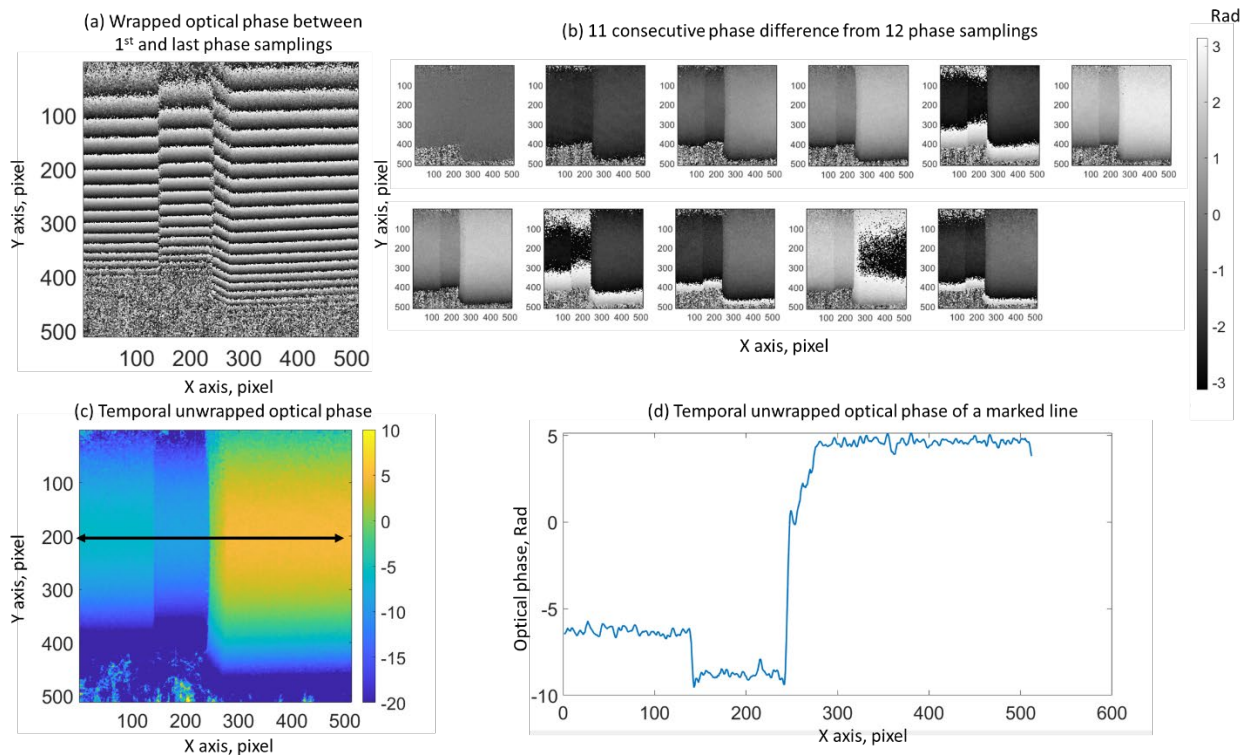


Figure 5.9. (a) Wrapped optical phase between the first and last phase samplings. (b) Eleven consecutive phase differences from a total of twelve phase samplings during the change of the illumination angle. (c) Temporal phase unwrapping result and (d) Unwrapped optical phase of the black line marked (c).

The same temporal unwrapping approach can be applied to a series of images captured during a continuous change in illumination angle. Figure 5.9 shows the NIST shape measured by the multi-angle method with temporal phase unwrapping. Figure 5.9(a) depicts the wrapped optical phase between the first and last phase samplings. Figure 5.9(b) illustrates 11 consecutive phase differences from a total of twelve phase samplings during the ramped change in the illumination angle. Figure 5.9(c) showcases the temporal phase unwrapping results and Figure 5.9(d) presents the unwrapped optical phase of the black line in Figure 5.9(c).

5.3 Frequency and Impulse Response Analysis

In the previous chapter, the process of obtaining the displacement along the surface normal direction of the TM from the high-speed holographic measurement has been described. The analysis method used to interpret the displacement results will be explained herein.

5.3.1 Frequency Response Function

A Frequency Response Function (FRF) describes the ratio of the frequency content of a measured output to the frequency content of the excitatory input. In the case of the TM, the frequency response function (FRF) is a quantitative representation of the output spectrum of the TM's motion driven by a broad-band acoustic stimulus. In our work, we use a click as a broad band stimulus. In this case of the high-speed holographic measurement of TM, instead of having the response to the excitation of one point, the system provides FRFs of all the measured surfaces of the TM. In our measurement, we measured the full-field transient displacement of the entire surface of the TM S, which, in turn, allowed us to compute the FRF at all measured (x, y) points. At each point, the FRF was calculated by the ratio of Fourier transforms of the surface-normalized

displacements S , and the stimulus sound pressure p measured at a single point near the TM, as follows:

$$FRF(x, y, f) = \frac{FFT_S(x,y)}{FFT_P} \quad (5.7)$$

The averaged frequency response function is introduced to visualize the average frequency response of this complex 3D matrix (x , y and f) of FRF function.

1.3.1.1. Averaged Frequency Response Function

The spatial averages of the measured parameters are computed to help perform quantitative comparisons of the complex 2D patterns of TM motion parameters that we observed. To compare the total stimulus-induced motion of different TM samples, Equation 5.8 is used to define the spatially averaged magnitude of the FRF at each of the spectral frequencies as follows:

$$\text{Spatially average magnitude}(f) = 2d_{\text{mean}}[\text{abs}(FRF)] \quad (5.8)$$

where the *abs* function describes the magnitude of a complex argument and $2d_{\text{mean}}$ denotes the 2D averaging operator. Only points determined to be on the TM surface were included in the average. As this is a full field of view measurement, it is possible to apply 2D-averaging to different fractions of the TM area. For example, we have defined the average of parameters in different quadrants of the TM and over the umbo and manubrium (more details are included in the development section).

1.3.1.2. Dominant Frequency

The dominant frequency of the frequency response at each location on the TM is defined as the highest magnitude component of the $FRF(x,y)$. Figure 5.10 shows an example of the frequency-dependent magnitude of an FRF at a single point on the TM surface in TB7(fresh

cadaveric human temporal bone). The magnitude is scaled in $\mu\text{m}/\text{Pa}$. The red dot marks the dominant frequency, 3.4 kHz, where the magnitude of the *FRF* is maximum.

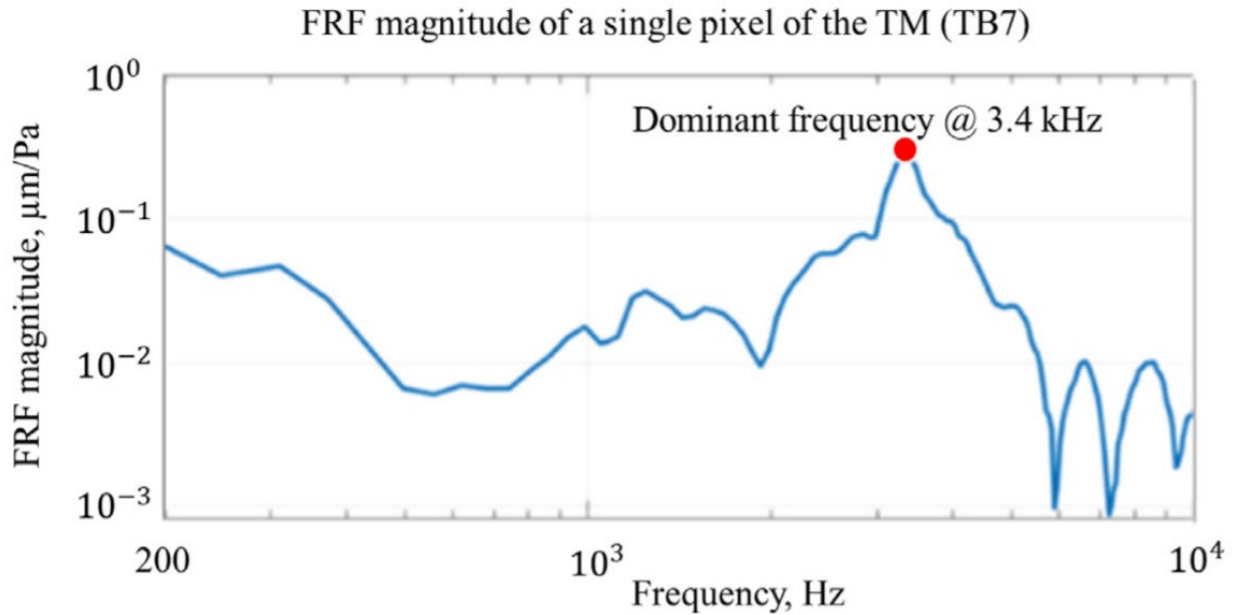


Figure 5.10. FRF magnitude of a single pixel of the TM (TB7).

5.3.2 Impulse Response Function

The impulse response function (IRF) of the TM is obtained by taking the Inverse Fast Fourier Transformation (IFFT) of the FRF measured at each point on the TM:

An example of an IRF is illustrated in Figure 5.11. Based on the IRFs of the TM, we developed the following quantitative analyses to gain insights into TM mechanics.

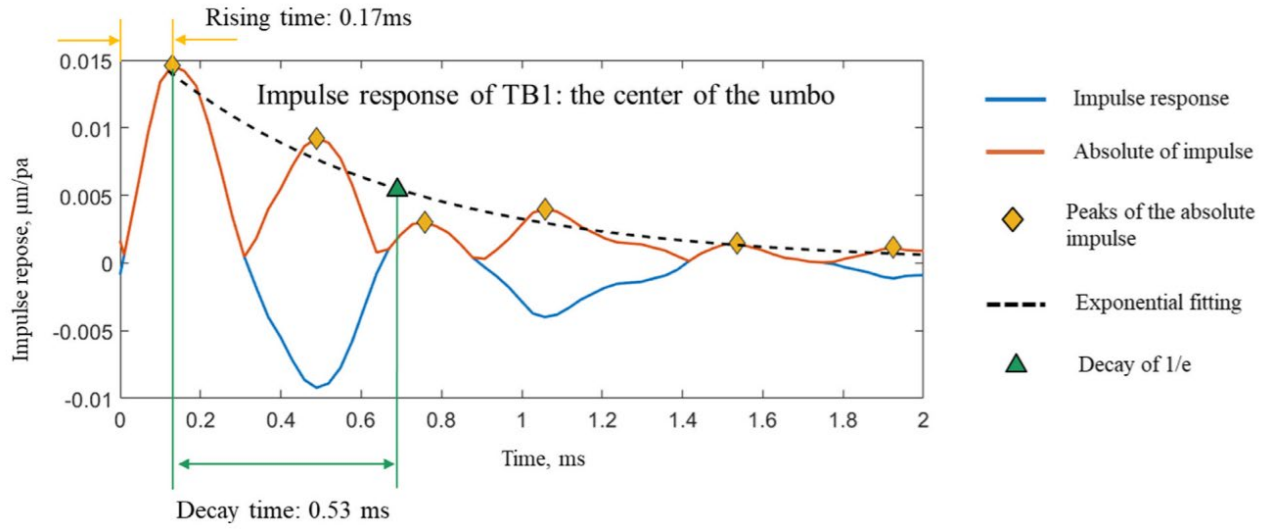


Figure 5.11. Reconstructed $\text{IRF}(x, y, t)$ (in blue) of a single point at the center of the umbo in TB1. The yellow arrows at the top left of the plot describe the rising time, the time to the first peak of the IRF. The orange line is the absolute value of the IRF. The peaks of the orange line (marked in orange diamonds) are fit by an exponential decay function. The green triangle and line mark the time constant of the fitted exponential decay (the exponential decay time of the IRF).

5.3.2.1. Root Mean Square of the Impulse Response

The root-mean square of the $\text{IRF}(x, y, t)$ at each TM location, $\text{IRMS}(x, y)$, is derived by calculating the RMS of the first 3 ms of the IRF at each location. The 3 ms threshold is based on the observation that the TM impulse response converges to zero before 3 ms in most cases.

The rising time at each TM location $t_r(x, y)$ is the time required for the $\text{IRF}(x, y, t)$ to reach the first peak (marked by the yellow arrows in Figure 5.11).

5.3.2.3. Exponential Decay Time

The exponential decay time at each TM location $t_d(x, y)$ was based on a fit of the exponential function ae^{bt} to the series of points in time described by the successive peaks (the yellow diamonds in Figure 5.11) of the first 2 ms of the absolute value of the IRF(x, y, t). The first peak in the series was the maximum in the IRF(x, y, t). The decay time is the time ($t_d = -\frac{1}{b}$) when the fitted exponential reaches $1/e$ (~36.8%) of the maximum displacement.

5.3.2.4. Damping Ratio

If we assume a simple second-order mass-spring-damping system, with the measured dominant frequency as the natural frequency of the system, then the damping ratio ζ can be estimated from the following equation:

$$\zeta = \frac{\alpha}{\omega_n} \quad (5.10)$$

The exponential decay rate (α) is the reciprocal of the decay time, and the natural frequency (ω_n) can be approximated by our estimation of dominant frequency. Given those definitions, ζ varies across the TM's surface as an inverse function of both the dominant frequency and decay time.

5.3.3. Two-Dimensional Maps of Motion Parameters

The basic analysis results comprise 2D maps of the measured and computed motion parameters. The map of the RMS value of the raw displacements at each x and y position on a TM are illustrated on the left in Figure 5.12(a).

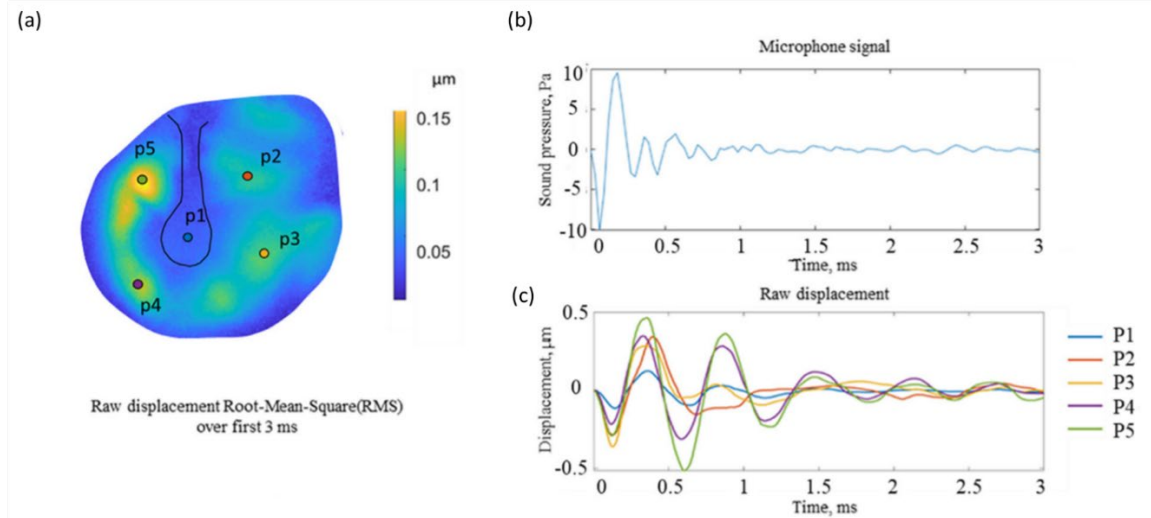


Figure 5.12. Measured displacements of TB1. The 2D map (a) shows the RMS value of the raw displacements during the first 3 ms. Panel (b) illustrates the microphone measurement of the stimulus, and panel (c) illustrates the measured surface normal displacement at 5 points on the TM during the 3 ms after stimulus initiation.

As the high-speed camera records a square of 512×512 pixels, which included the elliptical TM area, it is needed to define the edges of the TM and identify the location of the umbo and manubrium within the square of pixels. This is done with the aid of the raw RMS displacement maps. As the bony ear canal outside the TM surface has zero motion, the edges of the TM can be defined by the sudden drop of the RMS displacement value. Also, the umbo and manubrium are known to have smaller motions compared to most of the TM surface (Rosowski et al., 2009, Khanna & Tonndorf, 1972, Khaleghi et al., 2014, Khaleghi et al., 2016), and the outline of the umbo and manubrium can be identified by lower RMS values. Once the edges were determined and the umbo and manubrium were identified, the various measured parameters described above were then quantified on each TM surface map with a color-coded magnitude scale. The maps of all abovementioned parameters can be obtained and will be discussed in the development section of this dissertation.

Chapter 6 Paper A: Ultra-high speed holographic shape and displacement measurements in the hearing sciences

Overview

This paper was accepted to published in the “Light: Advanced Manufacturing” in 2022, describes the development of a holographic system capable of measurements of shape and sound-induced motions of the mammalian tympanic membranes with high-speed image acquisition. The shapes of the mammalian TMs are in millimeters range, whereas sound-induced motions of such membranes are in nanometers range. Two shape measurement modalities have been implemented into our holographic setups: (1) multi-wavelength method with a wavelength tunable laser; and (2) multi-angle of illumination method with a single wavelength laser. In this paper a third method using a miniaturized fringe projection system with a Microelectromechanical systems (MEMS) mirror is presented with the comparison of the three methods on the measurement of the shapes of human eardrums. Processing time of the high-speed holographic displacement analysis algorithm is optimized. Shape and displacement measurements methodologies are validated with a NIST traceable gauge and a latex drum and applied to measure human eardrums. For the shape measurement. The multi-wavelength method performs best on measuring the NIST target, while the measurement quality decreases on measuring the human TM due to the lower power of the tunable laser. The fringe projection method and multi-angle method can measure the human TM without painting the surface. The fringe projection method requires fewer images to be captured than the multi-angle methods, making it a more practical shape measurement for live animal study. However, the fringe projection method and multi-angle method require triangulation volume, which is not suitable for measuring TM with an intact ear canal.

ARTICLE

Open Access

Ultra-high speed holographic shape and displacement measurements in the hearing sciences

Haimi Tang^{1,2,4,*}, Pavel Psota³, John J. Rosowski^{4,5}, Cosme Furlong^{1,2,4,5} and Jeffrey Tao Cheng^{4,5}

Abstract

The auditory system of mammals enables the perception of sound from our surrounding world. Containing some of the smallest bones in the body, the ear transduces complex acoustic signals with high-temporal sensitivity to complex mechanical vibrations with magnitudes as small as tens of picometers. Measurements of the shape and acoustically induced motions of different components of the ear are essential if we are to expand our understanding of hearing mechanisms, and also provide quantitative information for the development of numerical ear models that can be used to improve hearing protection, clinical diagnosis, and repair of damaged or diseased ears.

We are developing digital holographic methods and instrumentation using an ultra-high speed camera to measure shape and acoustically-induced motions in the middle ear. Specifically we study the eardrum, the first structure of the middle ear which initializes the acoustic-mechanical transduction of sound for hearing. Our measurement system is capable of performing holographic measurement at rates up to 2.1 M frames per second. Two shape measurement modalities had previously been implemented into our holographic systems: (1) a multi-wavelength method with a wavelength tunable laser; and (2) a multi-angle illumination method with a single wavelength laser. In this paper, we present a third method using a miniaturized fringe projection system with a microelectromechanical system (MEMS) mirror. Further, we optimize the processing of large data sets of holographic displacement measurements using a vectorized Pearson's correlation algorithm. We validate and compare the shape and displacement measurements of our methodologies using a National Institute of Standards and Technology (NIST) traceable gauge and sound-activated latex membranes and human eardrums.

Keywords: Ultra-high speed digital holography, Microelectromechanical systems (MEMS), Miniaturized Fringe Projection, Middle-ear mechanics, Shape and displacement measurements.

Introduction

The human ear is normally sectioned into three parts: the

Correspondence: Haimi Tang (htang3@wpi.edu)

¹Center for Holographic Studies and Laser micro-mechaTronics, Worcester Polytechnic Institute, Worcester, MA USA, 01609

²Mechanical Engineering Department, Worcester Polytechnic Institute, Worcester, MA USA, 01609

Full list of author information is available at the end of the article.

outer, middle, and inner ear, **Fig. 1**. The outer ear contains the auricle and external auditory canal. The middle ear is an air-filled space separated from the outer ear by the tympanic membrane (TM), or eardrum, with three ossicular bones (malleus, incus, and stapes) connecting the TM to the inner ear (cochlea). The cochlea is a fluid-filled structure that transduces acousto-mechanical motions into

© The Author(s) 2022



Open Access This article is licensed under a Creative Commons Attribution 4.0 International License, which permits use, sharing, adaptation, distribution and reproduction in any medium or format, as long as you give appropriate credit to the original author(s) and the source, provide a link to the Creative Commons license, and indicate if changes were made. The images or other third party material in this article are included in the article's Creative Commons license, unless indicated otherwise in a credit line to the material. If material is not included in the article's Creative Commons license and your intended use is not permitted by statutory regulation or exceeds the permitted use, you will need to obtain permission directly from the copyright holder. To view a copy of this license, visit <http://creativecommons.org/licenses/by/4.0/>.

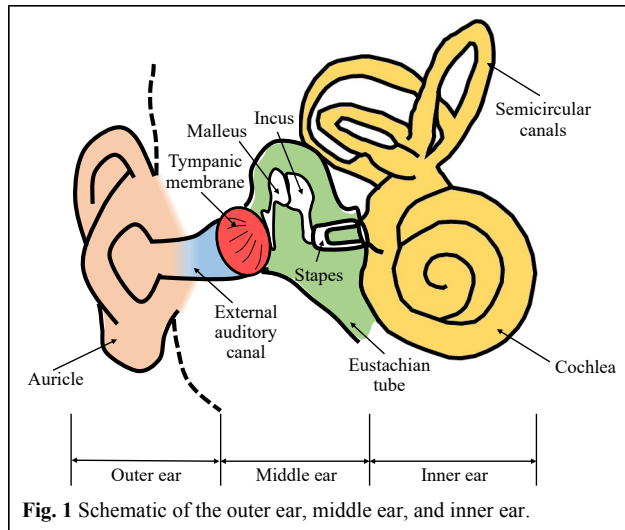


Fig. 1 Schematic of the outer ear, middle ear, and inner ear.

neural signals to the brain¹. During normal hearing, sound travels in the form of acoustic wave in the air and enters the external auditory ear canal to vibrate the TM². The vibration is then transmitted to the cochlea through the ossicles. Inside the cochlea, the sensory hair cells are set in motion to trigger nerve signals that are then received by the brain³.

The thin semitransparent TM has unique anatomical and physical features that are critical to the hearing process^{4,5}. In particular, the adult human TM has an elliptical shape, measuring 9–10 mm horizontally and 8–9 mm vertically, with inhomogeneous, multi-layered, and anisotropic material characteristics⁶. It also has a flattened conical shape 2–3 mm in depth with apex directed inward towards the middle ear cavity. Characterization of the TM's morphology and vibration induced by acoustic excitation is essential to understand middle-ear structure and function in normal ears and in ears with pathologies such as otitis media with effusion, traumatic TM perforation, formation of retraction pocket and tympanosclerosis^{7–18}.

We have been developing holographic methodologies utilizing ultra-high speed cameras up to 2.1 million frames per second^{19,20} to quantitatively study the structure and function of the TM under different excitation conditions^{21–27}. As the frame rate of the camera is inversely related to the pixel density, in this study, we choose to run the camera at 67,200 frames per second to provide a field of view of the TM with a resolution of 512 pixels by 512 pixels. The 67,200 frames per second meets the Nyquist criterion for measuring the typical hearing frequency range from 20 Hz to 20 kHz^{28,29}. We have developed two high-speed techniques for TM shape measurements: the multi-wavelength technique³⁰ and the multi-angle technique³¹. The multi-wavelength technique uses a tunable laser source

(to resolve optical phase differences to identify the shape) from a fixed angle of illumination³⁰; whereas the multi-angle technique uses a single wavelength laser source but with a dynamically changing angle of illumination (to introduce optical phase changes)³¹.

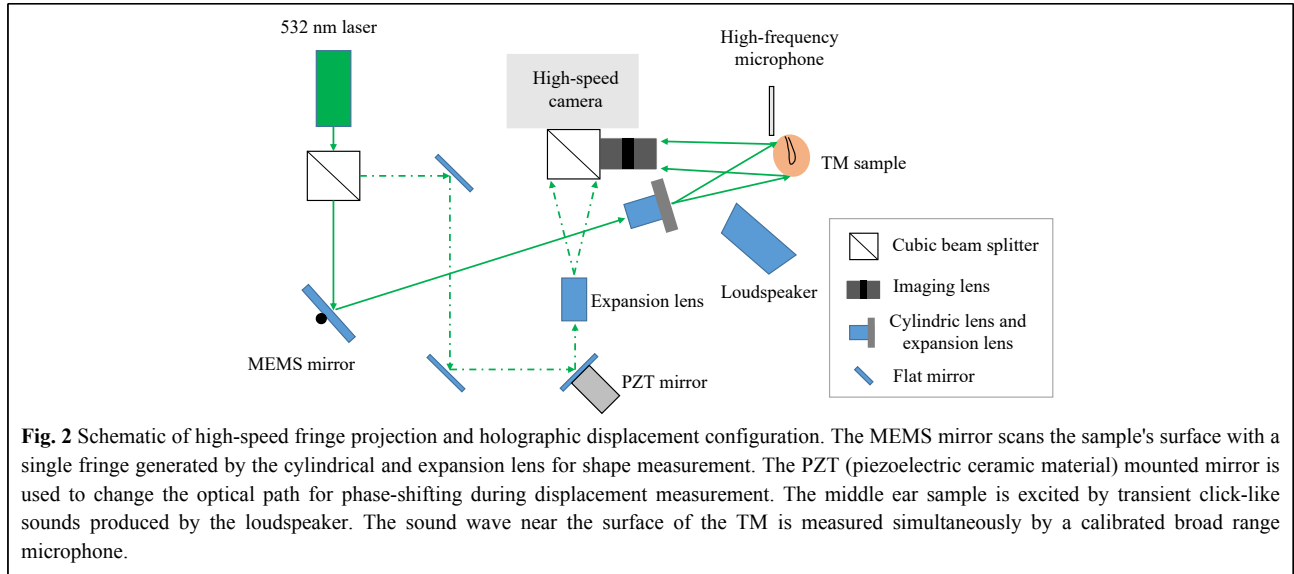
In this paper, we report our development of a new high-speed shape measurement approach that is based on fringe projection techniques to improve the optical efficiency and image quality during high-speed image acquisition for TM measurements. Also, because of the large amount of data that are collected during measurements, we report improved approaches to evaluate the optical phase. Our multi-wavelength and multi-angle techniques calculate the optical phase change during high-speed image acquisition using Pearson's correlation coefficient. Our previous coefficient calculations^{30–33} included two levels of nested loops, which took a significant amount of the processing time. In this paper we report an optimized vectorized algorithm that removes the nested loops, greatly speeding up the Pearson's coefficient calculation.

This paper consists of introduction, results, discussion, methods and conclusion and future works sections. The physiology of the middle ear and the past developments of holography techniques on shape and vibration measurements for the middle ear research are discussed in the introduction section. The results section shows preliminary results of shape and vibration measurements of human TM, as well as National Institute of Standards and Technology (NIST) shape measurement comparison of the three shape measurement techniques. The methods section presents the principles of holographic vibration measurement utilizing Person phase correlation and shape measurement based on multi-angle and multi-wavelength configurations. Moreover, a miniaturized fringe projection is also discussed in the methods section and its schematics of the optical setups. The merits of different shape measurement techniques in applications for high-speed TM shape measurement are discussed in the discussion section. At last, the conclusion and future work are discussed.

Results

Representative shape measurements

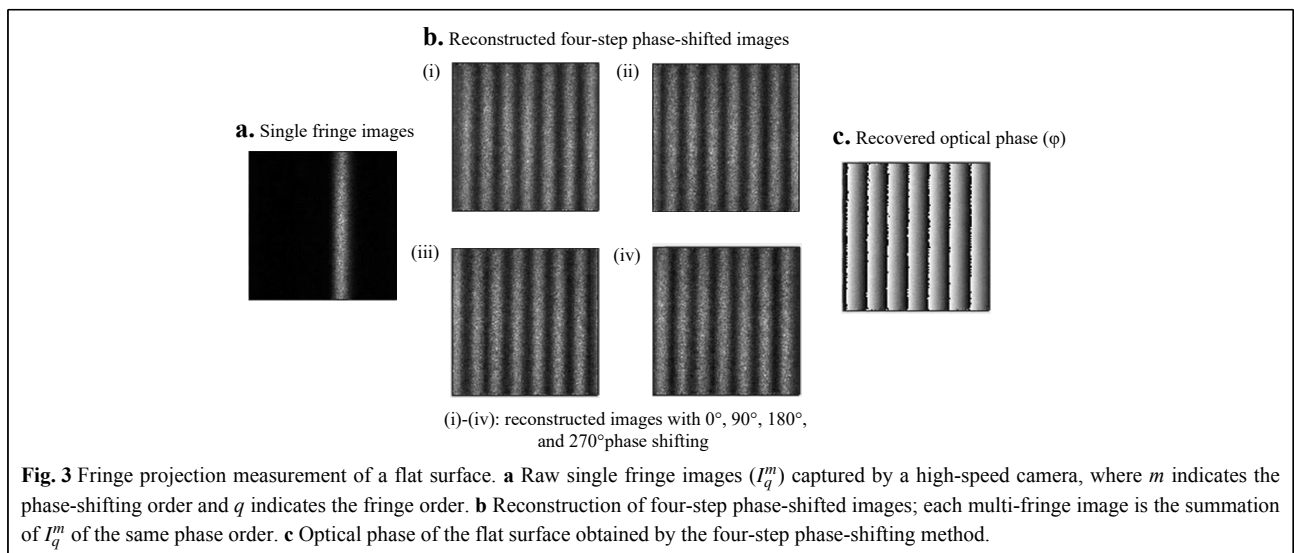
The surface of a NIST traceable gauge was analyzed using high-speed fringe projection (HSFP) to demonstrate its working principle. A single fringe was projected and scanned across the sample's surface by the scanning MEMS (Micro-ElectroMechanical System) mirror during image acquisition. Fig. 2 shows the experiment setup combining the HSFP with the high-speed digital holography (HDH) system. More details will be presented

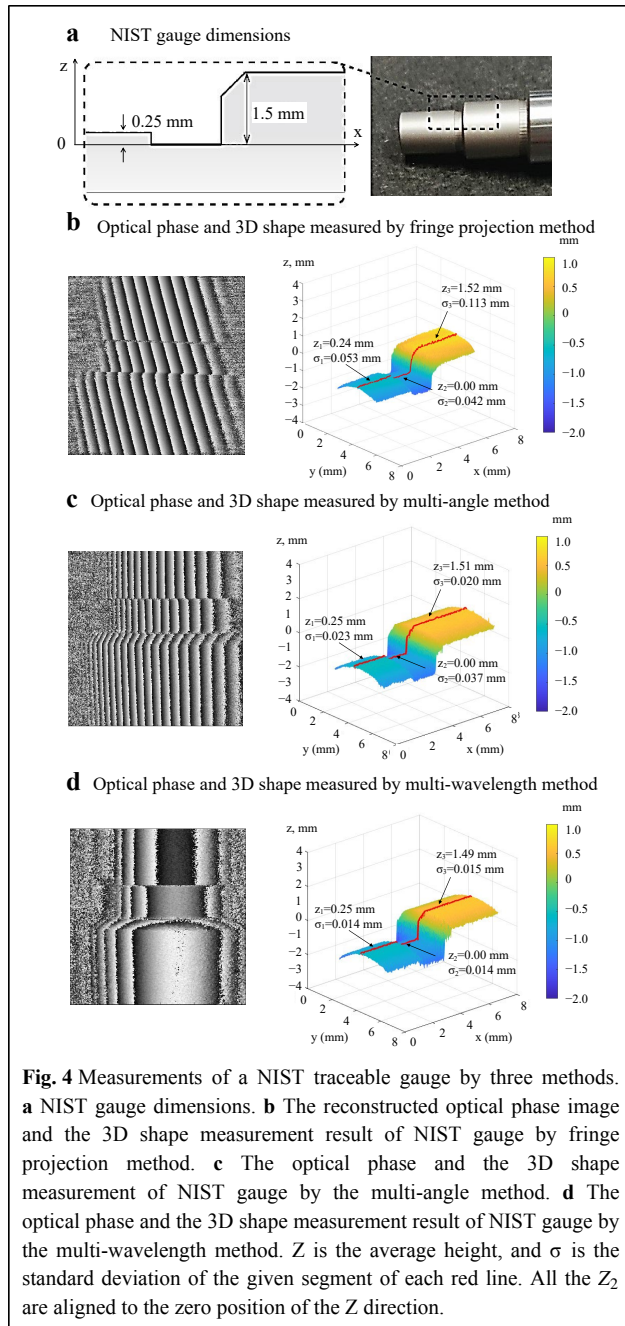


in the method section. Fig. 3a shows a single projected fringe. The single fringe images were grouped to form the four-step phase-shifted images based on the phase-shifting orders, as shown in Fig. 3b. Fig. 3b also shows multiple raw fringe images ($I_1^1, I_1^2, I_1^3, I_1^4, \dots, I_q^m$) at different MEMS mirror positions, where m is the phase-shifting order and q is the fringe order. Finally, the optical phase of the sample's shape, as shown in Fig. 3c, was obtained from the four reconstructed phase-shifted images.

The dimensions of a NIST gauge are shown in Fig. 4a. The optical phase and 3D reconstructed shape measured by the Fringe Projection method is shown in Fig. 4b; Fig. 4c is the optical phase and 3d reconstructed shape measured by the multi-angle method. Fig. 4c depicts the optical phase and 3d reconstructed shape measured by the multi-

wavelength method. In all 3D reconstructed shapes, the red line traces the height (in z-axis) of the middle section of the sample, where the lowest middle segment of NIST gauge is aligned to zero ($z = 0$). The average measured height profiles of the two end segments of the NIST gauge measured by three methods are 0.24 mm, 0.25 mm, 0.25 mm and 1.52 mm, 1.51 mm, 1.49 mm respectively. The standard deviations (σ) for the three segments are 0.042 mm, 0.037 mm, 0.014 mm; 0.053 mm, 0.023 mm, 0.014 mm; and 0.113 mm, 0.020 mm, 0.014 mm. The mean results agree with the dimensions provided by the manufacture of 0.25 mm and 1.50 mm, respectively, but for each position the standard deviations are smaller for the multi-wavelength method. The fringe-projection technique produced the largest σ s.





The three abovementioned shape measurement methods were used to measure the shape of one of three tympanic membranes (TM 1-3) from three cadaveric human temporal bones. Fig. 5 shows the three TM shapes measured using the HSFP, multi-angle, and multi-wavelength techniques, respectively. To assess variability within these measurement methods, a smoothing filter based on a moving kernel of 5x5 pixels size was applied and the standard deviation between the raw and the smoothed shape results were computed. Fig. 5a(i) shows

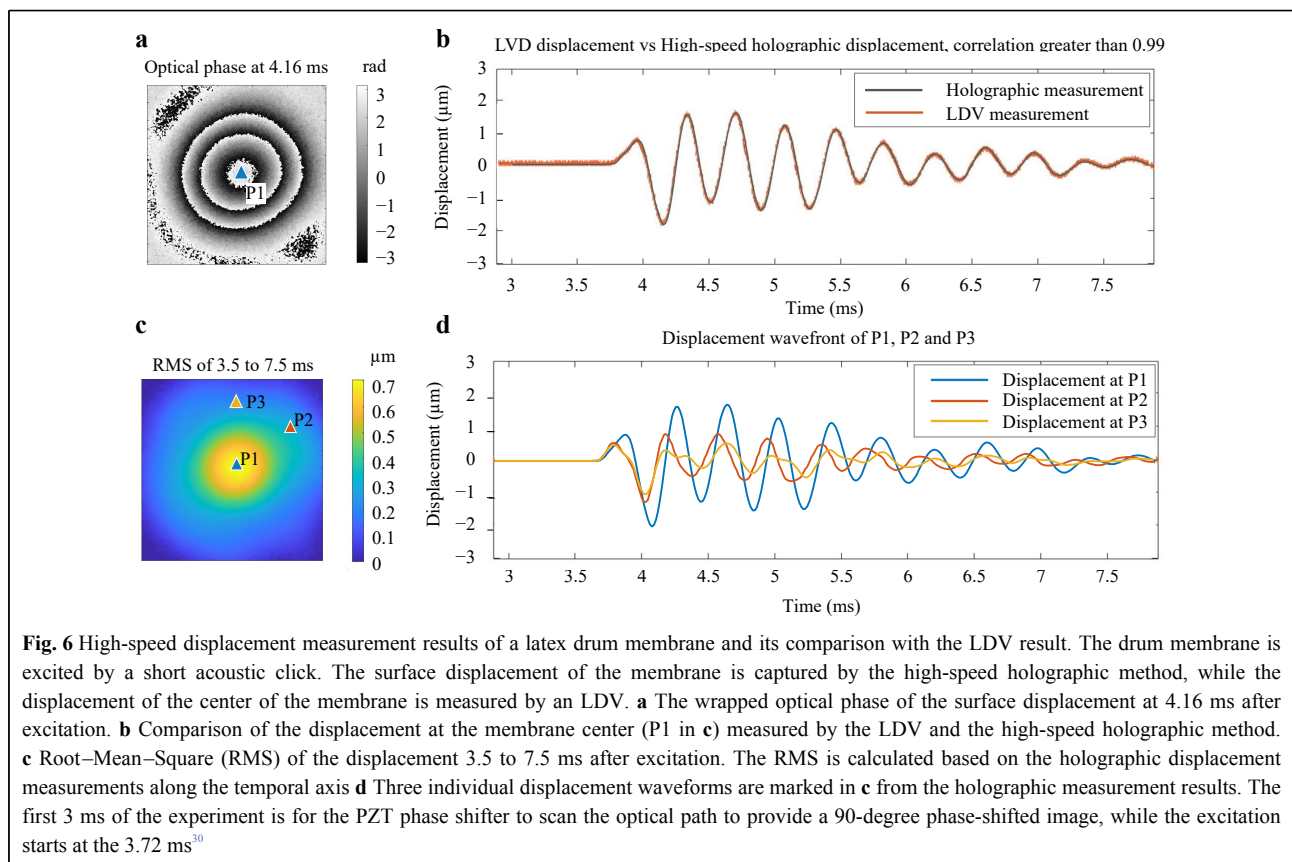
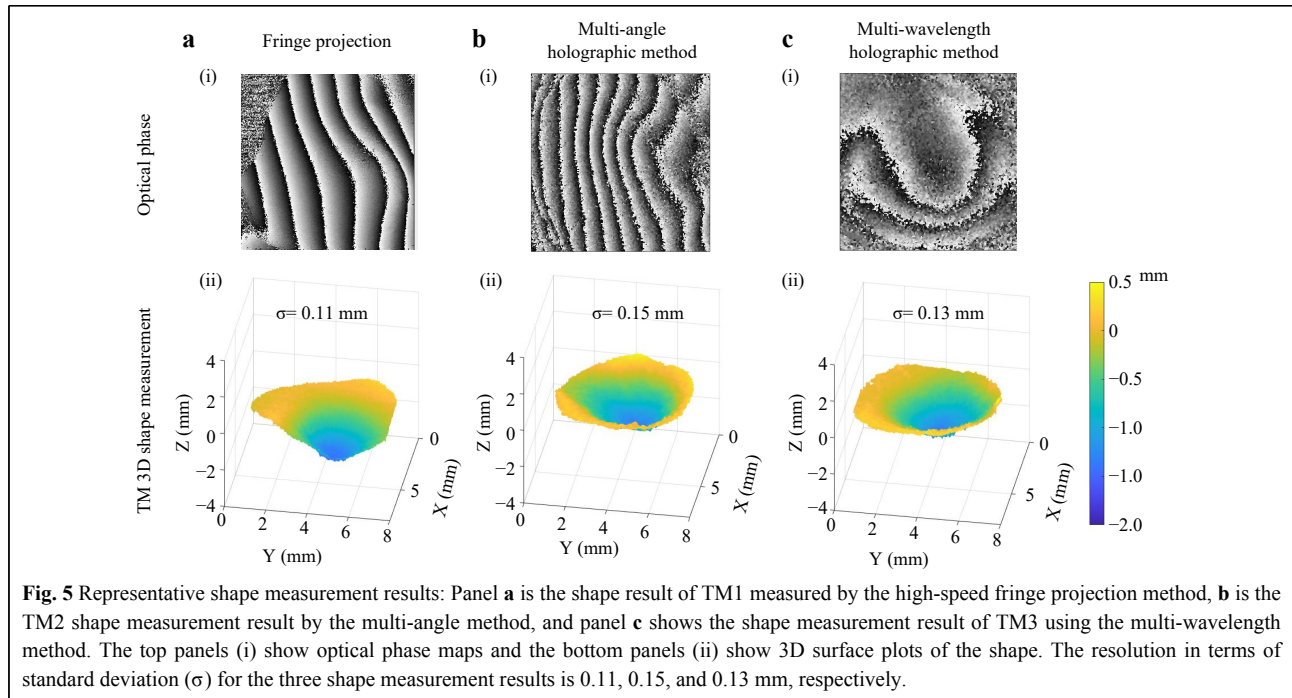
the wrapped optical phase of TM1 obtained by the HSFP, and Fig. 5a(ii) depicts the smoothed 3D shape profile. The standard deviation between the raw and smoothed shapes obtained with HSFP is 0.11 mm, and the measurement was done by capturing 72 images in 25 ms. Fig. 5b(i, ii) shows the shape of TM2 measured by the multi-angle shape measurement method. The standard deviation is 0.15 mm, and the measurement was performed by capturing 1200 images in about 18 ms. Two pairs of four-phase-shifted images (total of 8 images) out of the 1200 images were chosen to reconstruct the shape at the optimal fringe density for phase unwrapping. Finally, Fig. 5c(i, ii) shows the shape measurement results of TM3 obtained with the multi-wavelength method, with a standard deviation of 0.13 mm. The measurement took about 150 ms due to the limitation of the wavelength tuning speed.

Representative displacement measurements

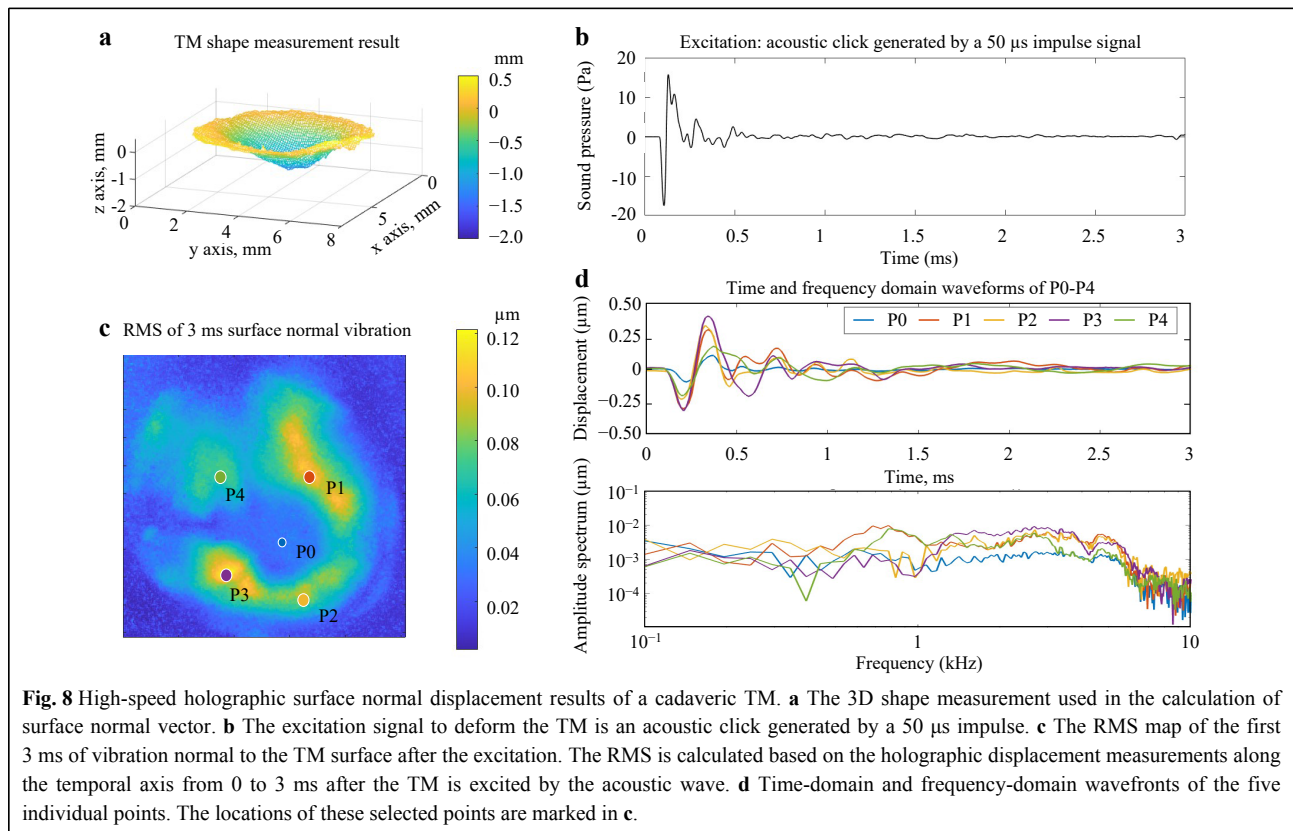
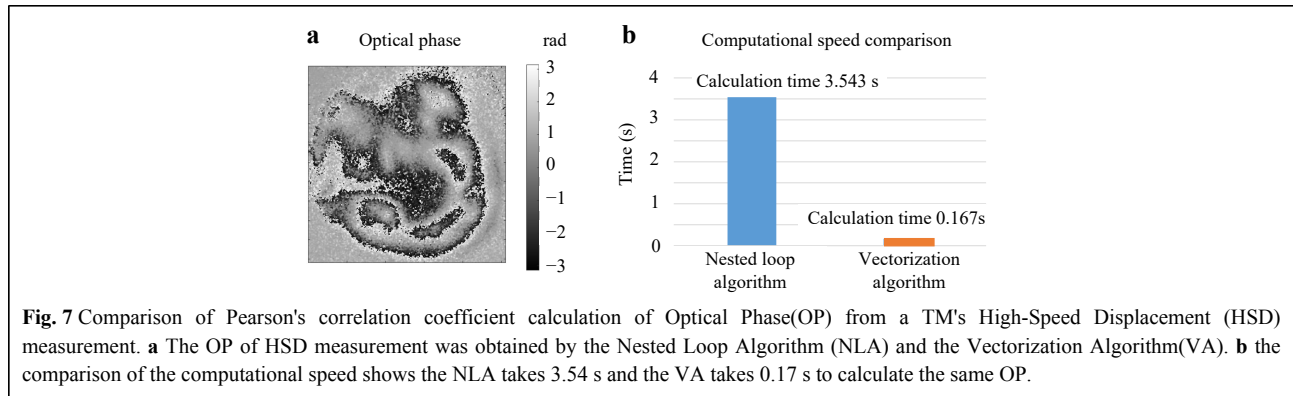
To demonstrate the accuracy of the HDH displacement measurement, the surface displacements of a latex drum head of diameter 5 mm were measured with the HDH and compared with the displacement at the center of the drum (P1 in Fig. 6) simultaneously obtained by an LDV (Polytec VFX-1-140). The latex drum head was excited using an impulsive sound generated from a loudspeaker. Fig. 6a shows a representative optical phase at 4.16 ms after the excitation. Fig. 6b compares the time-waveform of the displacement at P1 measured using the LDV and the HDH, showing a large overlap. The correlation between the two methods was found to be greater than 99%. Fig. 6c shows the Root-Mean-Square (RMS) pattern of the vibration from 3.5 ms to 7.5 ms after the excitation, with three markers: P1 is at the center of the drum where the LDV measures the displacement; P2 and P3 were chosen arbitrarily to show the lead and lag of the individual displacement on the sample's surface. Fig. 6d depicts the temporal evolution of the wavefronts of the three markers (P1 to P3) obtained using the HDH.

Once validated, the HDH measured the displacements of a human cadaveric TM (TM1) induced by an acoustic click. The optical phase of the displacement was calculated using the vectorized Pearson's correlation coefficient algorithm to speed up the data processing. The vectorized algorithm's performance was compared with the previous nested-loop algorithm. Both algorithms generated the same optical phase shown in Fig. 7a. However, the vectorized algorithm took 0.17 s, whereas the nested loop algorithm took 3.54 s, using the same kernel size of 3 by 3 pixels (Fig. 7b). Clearly the vectorized algorithm outperformed the nested loop algorithm.

A previous study demonstrated that the dominant



displacement of the TM is perpendicular to its surface³². Therefore, the TM shape information was used to calculate the TM's surface normal vectors, which were combined with the holographic displacement measurements to determine the surface normal displacement. As a representative example, Fig. 8 shows the normal



displacement component of a human TM sample when it was under an acoustic click excitation. Fig. 8a shows the 3D TM shape measurement results used to calculate the TM's surface normal vectors. Fig. 8b depicts the excitation signal, the click-like sound pressure near the TM produced by a loudspeaker. The RMS map of the surface normal displacement of the TM is shown in Fig. 8c. P_0 is marked at the center of the ossicular attachment to the TM, and P_1 to P_4 mark the maximum RMS value in each quadrant. The individual wavefronts of P_0 to P_4 are shown at the top of Fig. 8d, while the bottom of the figure illustrates the magnitude of the computed frequency response at each

location. These figures demonstrate that the amplitudes, cycles of vibrations, the leading and the lagging of the initial vibrations, and the time for each point to settle down are all different at different locations of the TM. The frequency and impulse responses computed from the stimulus and local displacements characterize location dependent TM mechanical properties and help differentiate various middle ear conditions corresponding to middle ear pathologies^{34–36}.

Discussion

The discussion section compares the three-shape

measurements based on their performance on a NIST gauge and applications on real TM samples, followed by discussion of the practicability of the three methods in TM measurements.

Table 1 compares the three shape measurement methods based on the results reported in this paper. The optical setup for the NIST gauge measurements was configured to mimic that used in the TM measurements, which met constraints like magnification requirements, the limited volume for triangulation, and available spatial resolution for the high-speed camera. The computed resolution is better (of lower value) in the NIST gauge measurements compared to the TM measurements because the NIST gauge is more reflective and does not need the higher illumination power required by the TM. Within the NIST gauge measurements, the resolution of the multi-wavelength method is better than the multi-angle, which is better than HSFP.

Performing high-speed imaging on semi-transparent samples such as TM requires a large illumination density, which significantly affects the optical phase quality of the results. The HSFP and multi-wavelength methods use the same 210 mW power laser light source, whereas the tunable laser output is 10 mW. Furthermore, the HSFP focuses all the available optical power on a single fringe, and can achieve the highest illumination power density of the three methods. In contrast, the multi-wavelength method has the lowest optical phase quality due to the tunable laser's lower illumination power. The image acquisition times for the fringe projection and multi-angle

method are limited by the scanning speed of the MEMS mirror, and they have a similar measurement time of about 20–30 ms. The measurement time for the multi-wavelength method is limited by the wavelength tuning time of 150 ms. The processing time of the fringe projection method is much less than the multi-angle and multi-wavelength methods because the latter two need more computational power to track the four-step phase-shifted frames at each illumination position or wavelength.

The resolution of the shape measurement method is related to the optical phase quality as well as the sensitivity of the method's configuration. A comparison of factors that affect the sensitivity of the shape measurements is presented in **Table 2**. The sensitivity of the fringe projection method depends upon the projected fringe density and the triangulation of the illumination and observation direction. The sensitivity of the multi-angle method depends upon the illumination power as well as the illumination and observation direction and the angle difference of the illumination tuning. The multi-wavelength method's sensitivity depends upon the illumination and observation direction and the wavelength change. The fringe projection method has the highest resolution in terms of standard deviation among the TM measurement results and the lowest resolution among the NIST measurements. This may be because the fringe projection method can use the higher available illumination power when measuring the semi-transparent TM, whereas the additional power is not needed when measuring the NIST.

Table 1 Comparison of the three high-speed shape measurement methods based on TM and NIST measurement

	Fringe projection		Multi-angle		Multi-wavelength	
Illumination density	High		Moderate		Low to moderate	
Acquisition time for the entire measurement (multiple images were taken)	18 ms		26 ms		150 ms	
Processing time	Fast		Moderate		Moderate	
Temporal phase unwrapping	Not compatible		Compatible		Compatible	
Triangulation volume	Needed		Needed		Not needed	
Resolution	TM	NIST	TM	NIST	TM	NIST
	0.11 mm	0.11 mm	0.15 mm	0.04 mm	0.13 mm	0.01 mm

Table 2 Comparison of factors that affect the sensitivity of the three high-speed shape measurement methods

Method	Factors that affect the sensitivity	
Fringe projection method	Illumination and observation direction	Fringe density
Multi-angle method	Illumination and observation direction	Angle difference
Multi-wavelength method	Illumination and observation direction	Wavelength difference

The HSFP method used in this paper is not compatible with temporal phase unwrapping, which requires a series of fringe images, where the fringe width gradually decreases to increase the fringe density. In HSFP the diameter of the laser beam determines the width of the fringe, and it cannot be changed automatically during the measurement in the current configuration. The multi-angle and multi-wavelength methods are suitable for temporal phase unwrapping since the spatial frequency of the optical phase of both methods changes gradually as the tuning of the illumination or the wavelength changes. By introducing temporal phase unwrapping, the resolution of the measurement results can be further improved³⁶.

The HSFP and multi-angle method require triangulation volume. Fringes projected perpendicular to the sample's surface are not sensitive to the shape of the sample along the projection direction. Thus, for both methods, there must be a triangulation volume to allow the scanning of the illumination. The human eardrum is located at the end of an approximately 2.5 centimeter long and 0.7 centimeter diameter ear canal, and the limited space favors the multi-wavelength method. However, the use of a higher power multi-wavelength laser would be advisable. For measurement of the cadaveric human eardrum, the ear canal can be removed to expose widely the TM, so we propose the multi-angle and fringe projection methods using the high-power fixed wavelength laser to measure the deformation and shape of the cadaveric human eardrum.

The HSFP applies a phase-stepping algorithm that utilizes four phase-stepped images. However, the maximum MEMS mirror's scanning speed is 3 kHz which is not fast enough to scan more than three fringes onto the sample during image acquisition by the high-speed camera since the longest exposure time of the camera is 0.001 s (1 kHz). Therefore, the system cannot capture the completed multi-fringe image in one frame. To overcome this limitation, the completed multi-fringe images are reconstructed after the image acquisition by summing up a series of single fringe images. The number of single fringe images needed is related to the width of the projected fringe and the desired fringe density. In this paper, a total of 72 images are captured to measure the shape of the human eardrum. The processing time of these images for a modern computer is less than 1 second allowing rapid examination of measurement quality.

The multi-angle method measures the shape of a sample by scanning the illumination across the sample. A PZT actuator is used as the phase shifter for the four-step phase-shifting algorithm. Locating the correct frames for the four-step phase-shifting method at each scanning position is done by scanning the Pearson correlation computed for

each image to determine the shifted phase. This process for a total of 1200 images is more computationally expensive than the process of HSFP. Furthermore, with the multi-angle method, the illumination beam needs to be collimated and expanded to cover an area larger than the sample surface to maintain the illumination during the scanning and lowering the illumination density for high-speed imaging.

The multi-wavelength method utilizes a tunable laser for shape measurement. The wavelength is tuned during the high-speed image acquisition with a PZT actuator for phase shifting. A typical multi-wavelength shape measurement captures 50 high-speed images at 12 wavelengths. Within these 50 frames, four frames with 90-degree phase-shifted are selected via the calculation of the person correlation³⁷⁻⁴⁰ to calculate the optical phase at a given wavelength. Recording continuously while the phase shifter is moving linearly minimizes unwanted ringing within the phase shifter improving the accuracy of the phase shifting. It is possible to implement the method with 100 high-speed images at 12 wavelengths to improve the phase-shifting accuracy. The processing time of the multi-wavelength is similar to that of the multi-angle shape measurement. The output power and the tuning speed of the tunable laser limit the illumination power density and the measurement time. In our setup, the tunable laser only provides a minimal illumination power for the shape measurement, with a tuning time of 150 ms. A moving average filter has to be used to extract the optical phase due to the minimal illumination power reducing the spatial resolution of the shape measurement.

In summary, the multi-wavelength method does not require triangulation volume to measure the shape, but the optical power of these lasers are limited and the method generally requires painting of the TM. The Multi-angle method enables the shape measurement on the unpainted TM with more optical power, and the HSFP allows rapid shape measurement of the unpainted TM with the least post-processing time. However, both the Multi-angle and HSFP methods have constraints with the small triangulation volume. Therefore, the ideal approach to measure the TM through the intact ear canal in live ears will be to apply the Multi-wavelength method with a tunable laser with the desired optical power and tuning speed for high-speed imaging.

Materials and methods

Digital holography (DH) can record and reconstruct an optical wavefield (amplitude and phase) by comparing the optical path difference of the reference and object beams captured by an optical sensor (camera). For a general

holographic interference setup, the measured optical phase ϕ is given by the fringe locus function³⁶:

$$\phi = \mathbf{d} \cdot \mathbf{e} \quad (1)$$

where \mathbf{d} is the optical path difference vector and \mathbf{e} is the sensitivity vector defined as³⁸

$$\mathbf{e} = \frac{2\pi}{\lambda} [\mathbf{b} - \mathbf{s}] \quad (2)$$

where λ is the wavelength of the laser, \mathbf{b} is the observation unit vector, and \mathbf{s} is the illumination unit vector. Generally, the object beam is reflected by a diffusive scattering object, and the measured optical phase contains high spatial varying speckle noise. Therefore, the optical path difference cannot be retrieved from a single optical wavefield. However, the change in the measured optical phase ($\Delta\phi$) from the two camera exposures is expressed as

$$\Delta\phi = \mathbf{d} \cdot \mathbf{e}_2 - \mathbf{d} \cdot \mathbf{e}_1 \quad (3)$$

where \mathbf{e}_1 and \mathbf{e}_2 are the sensitivity vectors at two camera exposures. The optical phase change ($\Delta\phi$) can be retrieved if the speckle distributions at the two exposures correlate with each other. Eq. 3 is the foundation of digital holographic shape and deformation measurement^{36,37}.

For shape measurement, assuming there is no object deformation during the measurement, the height information (shape) of the measured subject can be obtained by modulating either the magnitude or the direction of the sensitivity vector. The magnitude of the sensitivity vector can be changed by tuning the wavelength of the laser source, which is basically the multi-wavelength method. On the other hand, it is possible to modulate the direction of the sensitivity vector by altering the angle of the object beam, which is the multi-angle shape measurement method. The details about the experimental setups for high-speed multi-wavelength shape and multi-angle shape measurement methods can be found in our previous publications^{29,30,34–36} and are briefly described below.

Gauges traceable to the National Institute of Standards and Technology (NIST) were used to validate the shape measurement capabilities of the methods presented in this paper. We then applied these methods to measure the shape of human TMs and compare the measurement results obtained by the three methods, including illumination density, image acquisition speed, optical phase quality, resolution, processing time, temporal phase unwrapping compatibility, and the need for triangulation volume.

To verify the accuracy of the displacement measurement, a latex drum head subjected to an impulsive sound stimulus was simultaneously measured by the High-speed Digital Holographic system (HDH) and a Laser

Doppler Vibrometer (LDV). The acoustically induced displacements of a human TM measured with HDH are presented in the results section to demonstrate the capability of the HDH system.

Multi-wavelength shape measurement method

A tunable laser can be used to change the magnitude of the sensitivity vector by changing the wavelength of the laser source, as described in²⁹. The optical phase difference ($\Delta\phi$) of a holographic measurement of an object with two different wavelengths results in

$$\Delta\phi = \mathbf{d} \cdot \mathbf{e}_2 - \mathbf{d} \cdot \mathbf{e}_1 = \mathbf{d} \cdot \left[\frac{2\pi}{\lambda_2} (\mathbf{b} - \mathbf{s}) - \frac{2\pi}{\lambda_1} (\mathbf{b} - \mathbf{s}) \right] \quad (4)$$

In Eq. 4, the optical phase ($\Delta\phi$) is the difference measured from the interference pattern captured by the camera. The wavelengths λ_1 and λ_2 are known experimental parameters for the tunable laser, and \mathbf{b} and \mathbf{s} are the observation and illumination vectors, respectively, which can be measured directly or obtained by calibration. The optical path difference vector \mathbf{d} can be solved to extract shape information. In the simplified 2D case shown in Fig. 9a, \mathbf{P} is a random point on the subject, \mathbf{B} is the observation point, and \mathbf{S} is the illumination point. In this case, the amplitude of the optical path difference vector \mathbf{d} can be expressed as:

$$|\mathbf{d}| = |\mathbf{PB} - \mathbf{SP}| = \sqrt{(\mathbf{P}_x - \mathbf{S}_x)^2 + (\mathbf{P}_y - \mathbf{S}_y)^2} + \sqrt{(\mathbf{B}_x - \mathbf{P}_x)^2 + (\mathbf{B}_y - \mathbf{P}_y)^2} \quad (5)$$

where P_y is the user-defined pixel coordinates in the y -direction. P_x , which contains the shape information in the x -direction, is the only unknown component of Equation (5) but can be solved for. Eqs. 4,5 show that as the wavelength change ($\lambda_1 - \lambda_2$) increases, the synthetic wavelength ($\lambda_1 \lambda_2 / (\lambda_1 - \lambda_2)$) increases, and thus uncertainty of the shape measurement decreases.

Multi-angle shape measurement method

The shape of the TM can also be measured by mechanically changing the direction of the illumination vector \mathbf{s} . From Eq. 3,

$$\Delta\phi = \mathbf{d} \cdot \mathbf{e}_2 - \mathbf{d} \cdot \mathbf{e}_1 = \mathbf{d} \cdot \left[\frac{2\pi}{\lambda} (\mathbf{b} - \mathbf{s}_2) - \frac{2\pi}{\lambda} (\mathbf{b} - \mathbf{s}_1) \right] \quad (6)$$

where \mathbf{s}_1 and \mathbf{s}_2 are the illumination vectors at two camera exposures that can be measured or calibrated³⁰. The shape information is obtained by solving the optical phase difference using Eq. 6.

For the experimental arrangement shown in Fig. 9b, by introducing a known angle change ($d\theta$) to the illumination

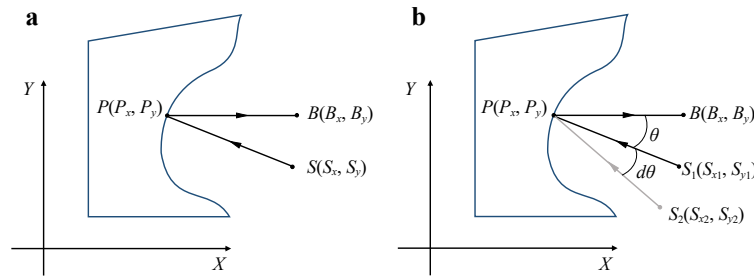


Fig. 9 2D Holographic schematic for shape measurements: **a** multi-wavelength experimental setup; **b** multi-angle wavelength experimental setup. The observation unit vectors are \mathbf{PB} and the illumination vectors are \mathbf{SP} for the two methods. S_1 and S_2 are the illumination points before and after changing the illumination angle in the multi-angle method.

vector, the height in the x direction can be determined by the following relation³⁶:

$$x = \Delta\phi \left(\frac{2\pi}{\lambda} \sin\theta d\theta \right)^{-1} \quad (7)$$

The sensitivity of the method increases as the angle change increases; moreover, it also depends on the non-zero illumination angle.

Digital fringe projection shape measurement method

In this paper a third shape measurement method called fringe projection method was also implemented in our setup, which has several advantages comparing with the other two methods as being discussed in the Results and Discussion sections. A MEMS mirror (Brand: Mirrorcle) with a cylindrical lens was used to project a single fringe onto the sample, which was set up at its maximum scan rate of 3 kHz, and the frame rate and exposure time of the high-speed camera (Brand: Photron Fastcam SAZ, with a resolution of 512 by 512 pixels) were set at 67, 200 frames per second and 1/67200 second, respectively. The camera was configured to be triggered by the position of the MEMS mirror to capture one image of a single fringe at each mirror position. All the single fringe images were summed up numerically to generate a synthesized, completed multi-fringe image after the high-speed acquisition.

The experimental setup for the high-speed fringe projection is previously shown in Fig. 2. The light source used is a 532-nm fixed wavelength laser (Oxxius). The laser beam is divided into a reference beam and an illumination beam. Two mirrors direct the reference beam to reach the expansion lens and are combined with the object beam at the beam splitter in front of the High-speed camera. The illumination beam first reaches the MEMS mirror, which has two rotation axes. The vertical axis rotation is used to switch the illumination to the cylindrical lens for fringe projection, and it is also used to switch the

expansion lens for displacement measurements. The cylindrical lens is used to generate a single vertical fringe onto the sample. The horizontal rotation of the MEMS mirror is used to scan the single fringe across the surface of the sample during the shape measurement. The mechanical shutter in the reference beam is activated to block the reference beam for fringe projection during the shape measurement. The mechanical shutter is deactivated during the high-speed displacement measurement, and the MEMS mirror fixes the illumination beam to the expansion lens. The reflected light from the sample interferes with the reference beam on the beam splitter in front of the camera. Finally, the resultant speckle pattern is recorded.

The position of the fringes was based on the size of the sample and the configuration of the optical setup. The first single fringe image was taken at the left-most side of the field of view. The second MEMS mirror position was programmed to be at 90° phase-shifted position of the first fringe, the third at the 180° phase-shifted position, and the fourth at the 270° phase-shifted position. (Four-phase shifting was chosen for its balance of shifting speed and overall accuracy; however, any phase shifting strategy can be implemented.) This process was repeated until the entire sample was scanned. The repeatability of the MEMS mirror is examined by investigating the signal fringe image. The MEMS is programmed to project a signal fringe to a fixed position (Fig. 10a) for high-speed imaging and move the fringe out of the field of view back to its zero position. This procedure is repeated five times. A Gaussian curve is horizontally fit to the intensity image row by row, and the peak of the Gaussian profile is used to determine the position of the projected fringe. The difference in fringe position of the five consecutive measurements is 0.63 pixels, and the averaged fringe width is 100 pixels. The error introduced by the MEMS mirror in repositioning the fringe is less than 1% of the fringe width, and is assumed to be negligible.

Once all the single fringe images were captured, they

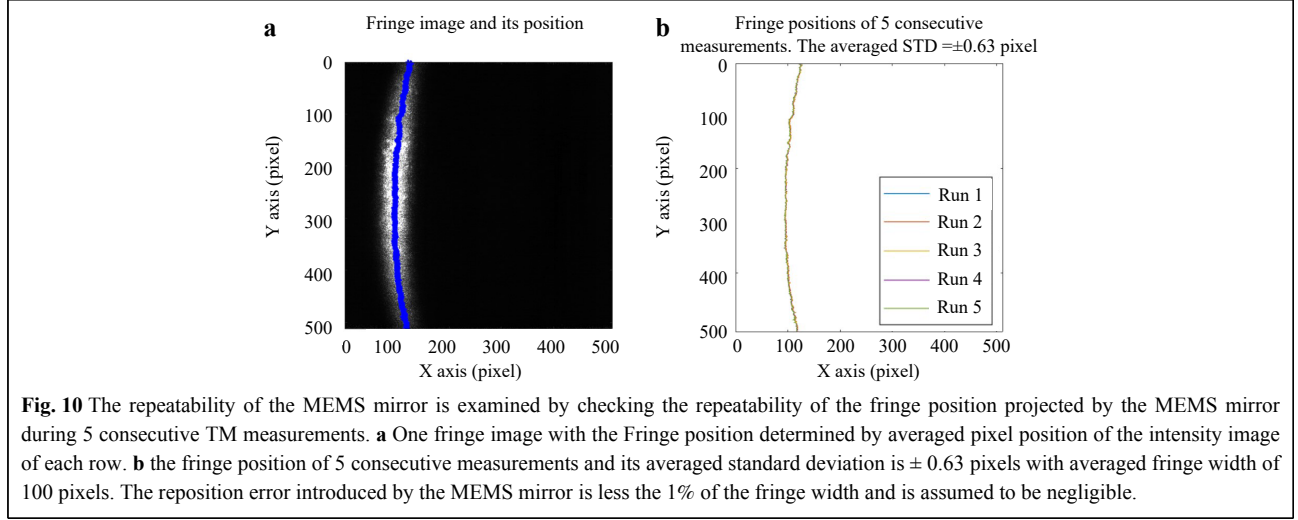


Fig. 10 The repeatability of the MEMS mirror is examined by checking the repeatability of the fringe position projected by the MEMS mirror during 5 consecutive TM measurements. **a** One fringe image with the Fringe position determined by averaged pixel position of the intensity image of each row. **b** the fringe position of 5 consecutive measurements and its averaged standard deviation is ± 0.63 pixels with averaged fringe width of 100 pixels. The reposition error introduced by the MEMS mirror is less the 1% of the fringe width and is assumed to be negligible.

were divided into four groups based on the angles of phase-shifting (0° , 90° , 180° , and 270°). The phase-shifting is calibrated based on the optical setup by making the distance between each projected fringe to be $W/4$, where W is the width of the single fringe. The four-step phase-shifted multi-fringe images represented the numerical summation of each image group. The optical phase of the shape of the sample was calculated using Eq. 8.

The fringe projection shape measurement method is based on the projection of well-defined fringe patterns onto the sample. In the high-speed fringe configuration, the high-speed camera captures the $4n$ single fringe images sequentially, $I_1^1, I_1^2, I_1^3, I_1^4, I_2^1, I_2^2, I_2^3, I_2^4, \dots, I_n^1, I_n^2, I_n^3, I_n^4$, where the superscript indicates the phase-shifting order and the subscript indicates the fringe order. Numerical summations $(I_1^1 + I_2^1 \dots I_n^1)$, $(I_1^2 + I_2^2 \dots I_n^2)$, $(I_1^3 + I_2^3 \dots I_n^3)$, and $(I_1^4 + I_2^4 \dots I_n^4)$ are calculated to reconstruct the completed multi-fringe images corresponding to the four-step phase-shifting frames. The optical phase ϕ of the shape of the sample is³⁷

$$\phi = \arctan \frac{(I_1^4 + I_2^4 \dots I_n^4) - (I_1^2 + I_2^2 \dots I_n^2)}{(I_1^1 + I_2^1 \dots I_n^1) - (I_1^3 + I_2^3 \dots I_n^3)} \quad (8)$$

High-speed digital holographic displacement measurement method

The displacement measurement method measures the full-field-of-view ($> 200,000$ points at 67,200 camera frame rate) transient displacements^{29,31,32–35}. The Pearson's correlation coefficients between the deformed frame and two undeformed reference frames with 0 and 90° phase-shifting are calculated to quantify the optical phase of the sample's displacement. Assuming I_r is the intensity of the reference beam and I_o is the intensity of the object beam, and ϕ is the optical phase difference between the object and

the reference beams. The interference patterns of the reference (undeformed) I_{ref} and deformed I_{def} states can be expressed as shown in Eqs. 9, 10^{29,38}, respectively:

$$I_{ref} = I_r + I_o + 2\sqrt{I_r I_o} \cos(\phi) \quad (9)$$

$$I_{def} = I_r + I_o + 2\sqrt{I_r I_o} \cos(\phi + \Delta\phi) \quad (10)$$

where $\Delta\phi$ is the optical phase change due to the sample's deformation. To extract $\Delta\phi$, we calculate the Pearson's correlation coefficient of a small window (e.g., 3 by 3 pixels) between the deformed and reference frames by using Eq. 11⁴⁰

$$\rho(I_{ref}, I_{def}) = \frac{\langle I_{ref} I_{def} \rangle - \langle I_{ref} \rangle \langle I_{def} \rangle}{\left[\langle I_{ref}^2 \rangle - \langle I_{ref} \rangle^2 \right]^{\frac{1}{2}} \left[\langle I_{def}^2 \rangle - \langle I_{def} \rangle^2 \right]^{\frac{1}{2}}} \quad (11)$$

where operator $\langle \rangle$ presents the expected value. Since the speckle pattern captured by the camera sensor is randomly distributed and the two same-sized matrices can be correlated, the expected value of the speckle pattern is equivalent to its numerical average³⁹. Assume ϕ is uniformly distributed and $\Delta\phi$ is constant within the small window, then the coefficient can be simplified in the following format by inserting (9) and (10) into (11)³²:

$$\rho = \frac{(r+1)^2 + 4r \cos(\Delta\phi)}{(r+1)^2 + 4r} \quad (12)$$

where $r = I_o/I_r$ is the intensity ratio of the object and reference beams. Therefore, the optical phase difference due to the deformation of the sample can be calculated by²⁹

$$\Delta\phi = \arctan \frac{\rho(I_{ref}, I_{def})}{\rho(I_{ref+\pi/2}, I_{def})} \quad (13)$$

where $(I_{ref+\pi/2})$ is the 90° phase-shifted reference frame of the undeformed frame. Khaleghi et al. have demonstrated that the dominant deformation of the TM is along the

surface normal direction⁴⁰. Razavi⁴⁰ demonstrated that the sensitivity vector of the holographic system varies when the sample is located close to the imaging lens; however, the magnitude of displacement (S) along the surface normal direction, can be compensated by the sensitivity vector variation $\mathbf{K}(x,y)$ and the surface normal vector of the sample $\mathbf{n}(x,y)$, can be measured as $\Delta\phi(x,y,t)$ ³⁴

$$S(x,y,t) = \frac{\Delta\phi(x,y,t)}{\mathbf{K}(x,y) \cdot \mathbf{n}(x,y)} \quad (14)$$

where x and y are the pixel coordinates of the camera and t is the time.

Pearson's correlation vectorization

Pearson's correlation coefficient was used to calculate the optical phase between two camera exposures. The previous algorithm used a sliding window technique on each recorded image. The process consists simply of moving a sliding window (e.g., 3 by 3 pixels) from point to point in the horizontal and vertical directions. Calculating the Pearson's coefficient of two of 512 by 512-pixel images requires more than 250,000 iterations, which takes about 3.5 seconds on a modern computer. For a typical displacement measurement, more than 1000 images are captured, which takes about one hour to finish the process. The long processing time makes accessing the measurement quality during the measurement impractical. The algorithm is optimized by a vectorization procedure to remove the nested loops to improve the computational performance. Vectorization is the process of converting an algorithm from operating on a single value at a time to operate on a set of vectors or matrices at one time utilizing the vector operation capabilities of modern CPUs.

To generalize the Pearson's correlation coefficient calculation for n by n kernel size ($n=3,5,7 \dots$), defining $I'(i,j)$ are n^2 translated matrices of the original image matrix I , where $i=1,2,3 \dots n$ and $j=1,2,3 \dots n$. and $I_{x,y}$ is the matrix element at (x,y) coordinate, $I'(i,j)$ is obtained by translating $I_{x,y}$ by the following Equation:

$$I'(i,j) = I_{(x-\frac{n-1}{2}+i-1),(y-\frac{n-1}{2}+j-1)}, \quad (15)$$

$$i = 1, 2, 3 \dots n \text{ and } j = 1, 2, 3 \dots n$$

Both the undeformed frame I_{ref} and deformed frame I_{def} are translated to $I'_{ref}(i,j)$ and $I'_{def}(i,j)$ by Eq. 15. The Pearson's correlation coefficient of I_{ref} and I_{def} can be calculated by Eq.11, and simplified expression is:

$$\rho(I_{ref}, I_{def}) = \frac{\sum_i \sum_j X \cdot Y}{[\sum_i \sum_j X^2 \cdot \sum_i \sum_j Y^2]^{\frac{1}{2}}} \quad (16)$$

where $X = I'_{ref}(i,j) - \frac{1}{n^2} \sum_i \sum_j [I'_{ref}(i,j)]$ and $Y = I'_{def}(i,j) - \frac{1}{n^2} \sum_i \sum_j [I'_{def}(i,j)]$. The fastest calculation is the 3 by 3

pixels kernel version because it requires the minimum number of translated matrices, which takes about 0.15 s to finish on a modern computer. This 3 by 3 pixel kernel of the Pearson's coefficient is suitable for displaying the results immediately after the measurement to assess the optical phase quality to determine if the measurement needs to be repeated.

The high-speed holographic displacement measurement method described in this paper utilizes the optimized Pearson's correlation algorithm to calculate the optical phase change introduced by the surface deformation of the sample. With the optimized algorithm, the calculation becomes 21 times faster using the same computation power. The improved processing speed makes it possible to display the optical phase of the high-speed image immediately after the acquisition for us to examine the measurement quality between the measurements, which streamlines the experiment process and makes measurements on live ears more practicable.

Conclusion and future work

This paper presents a newly developed shape measurement method using a miniaturized fringe projection system with a Microelectromechanical systems (MEMS) mirror. We compared this method to measure the shapes of a NIST target and human TMs with two previously developed methods: (1) multi-wavelength method and (2) multi-angle of illumination method. We also present vibration measurements of human TMs made with an upgraded holographic displacement system, which is validated by comparing the holographic results of a vibrating drum head to simultaneously measured LDV results. For the shape measurement, the multi-wavelength method performs best on measuring the NIST target, while the measurement quality decreases on measuring the human TM due to the lower power of the tunable laser. The fringe projection and multi-angle methods can measure the unpainted TM due to the adaptation of a higher power laser. The fringe projection method requires fewer captured images than the multi-angle methods, making it a more practical shape measurement for live animal study. However, the fringe projection method and multi-angle method require triangulation volume, posing challenges to measurements made through an intact ear canal.

In the future, we will continue developing the displacement and shape measurement in the direction of utilizing the multi-wavelength method by identifying a suitable high power tunable laser for this application. The future implementation will be combined with the HSH system with an endoscopic configuration to allow measurements of the eardrum shape and responses through

the intact ear canal in live ears. We have experimented with the Dynamic Time wrap algorithms to integrate the time series data for displacement pattern extraction from the holographic measurements. We will apply more artificial intelligence and data mining technologies to automate and streamline the data process.

Acknowledgements

Grant support from the US National Institute on Deafness and Other Communication Disorders (NIDCD R01 DC016079) is gratefully acknowledged. We would also like to acknowledge partial support by the Center for Holographic Studies and Laser micro-mechanics (CHSLT) at WPI. We also thank all of the reviewers of this manuscript for their insightful suggestions and input.

Author details

¹Center for Holographic Studies and Laser micro-mechanics, Worcester Polytechnic Institute, Worcester, MA USA, 01609. ²Mechanical Engineering Department, Worcester Polytechnic Institute, Worcester, MA USA, 01609. ³Faculty of Mechatronics, Informatics and Interdisciplinary Studies, Technical University of Liberec, Liberec, Czech Republic, 461 17. ⁴Eaton-Peabody Laboratory, Massachusetts Eye and Ear, Boston, MA USA, 02114. ⁵Department of Otolaryngology-Head and Neck Surgery, Harvard Medical School, Boston, MA, USA, 02115

Author contributions

Conceptualization, JJR, CF, JTC; methodology, HT, PP; software, HT, PP; validation, HT; formal analysis, HT; investigation, HT; resources, JJR, CF, JTC; data curation, HT, writing —original draft preparation, HT; writing —review and editing, HT, CF, JJR, JTC; visualization, HT; supervision, JJR, CF, JTC; project administration, JJR, CF, JTC; funding acquisition, JJR, CF, JTC.

Conflict of interest

The authors declare that they have no conflict of interest.

Received: 30 September 2021 Revised: 28 January 2022 Accepted: 15 February 2022

References

- Yost, W. A. *Fundamentals of Hearing: An Introduction*. 5th edn. (New York: Academic Press, 2006).
- Fastl, H. & Zwicker, E. Information processing in the auditory system. in *Psychoacoustics* (eds Fastl, H. & Zwicker, E.) (Berlin, Heidelberg: Springer, 2007). https://doi.org/10.1007/978-3-540-68888-4_3.
- Volandri, G. et al. Biomechanics of the tympanic membrane. *Journal of Biomechanics* **44**, 1219-1236 (2011).
- Rosowski, J. J. Outer and middle ears. in *Comparative Hearing: Mammals* (eds Fay, R. R. & Popper, A. N.) (New York: Springer, 1994), 172-247. https://doi.org/10.1007/978-1-4612-2700-7_6.
- Geisler, C. D. *From Sound to Synapse: Physiology of the Mammalian Ear*. (New York: Oxford University Press, 1998).
- Lim, D. J. Structure and function of the tympanic membrane: a review. *Acta Oto-Rhino-Laryngologica Belgica* **49**, 101-115 (1995).
- De Greef, D. et al. Details of human middle ear morphology based on micro-CT imaging of phosphotungstic acid stained samples. *Journal of Morphology* **276**, 1025-1046 (2015).
- van der Jeught, S. et al. Full-field thickness distribution of human tympanic membrane obtained with optical coherence tomography. *Journal of the Association for Research in Otolaryngology* **14**, 483-494 (2013).
- Aernouts, J., Aerts, J. R. M. & Dirckx, J. J. J. Mechanical properties of human tympanic membrane in the quasi-static regime from *in situ*, point indentation measurements. *Hearing Research* **290**, 45-54 (2012).
- Rosowski, J. J. et al. Computer-assisted time-averaged holograms of the motion of the surface of the mammalian tympanic membrane with sound stimuli of 0.4-25 kHz. *Hearing Research* **253**, 83-96 (2009).
- Rosowski, J. J. Models of external- and middle-ear function. in *Auditory Computation* (eds Hawkins H.L. et al.) (New York: Springer, 1996), 15-61.
- Lim, D. J. Human tympanic membrane: an ultrastructural observation. *Acta Oto-Laryngologica* **70**, 176-186 (1970).
- Wang, X. L. et al. Motion of tympanic membrane in guinea pig otitis media model measured by scanning laser Doppler vibrometry. *Hearing Research* **339**, 184-194 (2016).
- Fay, J. P., Puria, S. & Steele, C. R. The discordant eardrum. *Proceedings of the National Academy of Sciences of the United States of America* **103**, 19743-19748 (2006).
- Aernouts, J. et al. Elastic characterization of membranes with a complex shape using point indentation measurements and inverse modelling. *International Journal of Engineering Science* **48**, 6 (2010).
- Cheng, T. et al. Viscoelastic properties of human tympanic membrane. *Annals of Biomedical Engineering* **35**, 305-314 (2007).
- Fay, J. et al. Three approaches for estimating the elastic modulus of the tympanic membrane. *Journal of Biomechanics* **38**, 1807-1815 (2005).
- Milazzo, M. et al. The path of a click stimulus from ear canal to umbo. *Hearing Research* **346**, 1-13 (2017).
- Kakue, T. et al. High-speed phase imaging by parallel phase-shifting digital holography. *Optics Letters* **36**, 4131-4133 (2011).
- Fuller, P. W. W. An introduction to high speed photography and photonics. *The Imaging Science Journal* **57**, 293-302 (2009).
- Goode, R. L. et al. Laser Doppler Vibrometer (LDV)Ba new clinical tool for the otologist. *The American Journal of Otolaryngology* **17**, 813-822 (1996).
- Goode, R. L. et al. New knowledge about the function of the human middle ear: development of an improved analog model. *The American Journal of Otolaryngology* **15**, 145-154 (1994).
- Gan, R. Z., Wood, M. W. & Dormer, K. J. Human middle ear transfer function measured by double laser interferometry system. *Otology & Neurotology* **25**, 423-435 (2004).
- Rosowski, J. J., Nakajima, H. H. & Merchant, S. N. Clinical utility of laser-Doppler vibrometer measurements in live normal and pathologic human ears. *Ear and Hearing* **29**, 3-19 (2008).
- Decraemer, W. F., Khanna, S. M. & Funnell, W. R. J. Vibrations at a fine grid of points on the cat tympanic membrane measured with a heterodyne interferometer. *Proceedings of EOS/SPIE International Symposia on Industrial Lasers and Inspection, Conference on Biomedical Laser and Metrology and Applications*. Munchen: 1999, 1-4.
- de La Rochefoucauld, O. & Olson, E. S. A sum of simple and complex motions on the eardrum and manubrium in gerbil. *Hearing Research* **263**, 9-15 (2010).
- Cheng, J.T. et al. Motion of the surface of the human tympanic membrane measured with stroboscopic holography. *Hearing Research* **263**, 66-77 (2010).
- Kim, S. et al. Effect of age on binaural speech intelligibility in normal hearing adults. *Speech Communication* **48**, 591-597 (2006).
- Desoer, C. & Wang, Y.T. On the generalized Nyquist stability criterion. *IEEE Transactions on Automatic Control* **25**, 187-196 (1980).
- Razavi, P. et al. Combined high-speed holographic shape and full-field displacement measurements of tympanic membrane. *Journal of Biomedical Optics* **24**, 031008 (2018).
- Psota, P. et al. Multiple angle digital holography for the shape measurement of the unpainted tympanic membrane. *Optics Express*

- 28, 24614-24628 (2020).
32. Dobrev, I. et al. High-speed digital holography for transient response of the human tympanic membrane. in *Advancement of Optical Methods in Experimental Mechanics*, Volume 3 (eds Jin, H. et al.) (Cham: Springer, 2015). https://doi.org/10.1007/978-3-319-06986-9_39.
 33. Khaleghi, M. et al. In-plane and out-of-plane motions of the human tympanic membrane. *The Journal of the Acoustical Society of America* **139**, 104-117 (2016).
 34. Tang, H. M. et al. High-speed holographic shape and full-field displacement measurements of the tympanic membrane in normal and experimentally simulated pathological ears. *Applied Sciences* **9**, 2809 (2019).
 35. Tang, H. et al. Analyses of the tympanic membrane impulse response measured with high-speed holography. *Hearing Research* **410**, 108335 (2021).
 36. Tang, H. et al. High speed Holographic Shape and Vibration Measurement of the Semi-transparent Tympanic Membrane. *Mechanics of Biological Systems and Materials & Micro-and Nanomechanics & Research Applications*, Conference Proceedings of the Society for Experimental Mechanics Series. Springer, Cham. https://doi.org/10.1007/978-3-030-59765-8_12(2021).
 37. Jones, R. & Wykes, C. *Holographic and Speckle Interferometry*. 2nd edn. (Cambridge: Cambridge University Press, 1989).
 38. Kreis, T. *Handbook of Holographic Interferometry: Optical and Digital Methods*. (Weinheim: Wiley-VCH, 2005).
 39. Dobrev, I. T. Full-field vibrometry by high-speed digital holography for middle-ear mechanics. PhD thesis, Worcester Polytechnic Institute, Worcester, 2014.
 40. Razavi, P. Development of high-speed digital holographic shape and displacement measurement methods for middle-ear mechanics in-vivo. PhD thesis, Worcester Polytechnic Institute, Worcester, 2018.

Chapter 7 Paper B: High-speed holographic shape and full-field displacement measurements of the tympanic membrane in normal and experimentally simulated pathological ears

Overview

This paper was published on 13 July 2019 in Applied Sciences, volume 9, issue 14. This paper presents the measurements on cadaveric human ears with simulated common middle-ear pathologies. The frequency response function (FRF) was calculated at each measured pixel of the entire TM surface. The middle-ear system's complex modal indicator function (CMIF) is derived from FRFs to differentiate different middle-ear pathologies. Changes in the TM shape and the surface motion pattern before and after various middle-ear manipulations were observed from the results.

This paper provides a complete description of TM mechanics, including the 3D shape information and full-field TM surface normal vibration in both the time and frequency domains. The shape results show that the TM shape is affected by various middle-ear manipulations. Overall, the different manipulations introduce a maximum shape change of less than 0.3 mm. The fluid injection pushes the TM to deform towards the ear canal side, while the IS joint interruption seems to pull the TM toward the middle-ear cavity side. Displacements in the time domain show we can distinguish half fluid injection and full fluid injection by checking the RMS results and the open cavity case. Fluid injections will decrease the TM motion. Opening the cavity causes the TM surface to displace more than the normal middle-ear cavity condition.

Trends in different CMIFs associated with middle-ear conditions in the frequency domain were observed which indicating the potential of using the time-domain and frequency domain analysis results to separate various middle-ear pathologies.

Article

High-Speed Holographic Shape and Full-Field Displacement Measurements of the Tympanic Membrane in Normal and Experimentally Simulated Pathological Ears

Haimi Tang ^{1,2}, Payam Razavi ^{1,2} , Koohyar Pooladvand ^{1,2}, Pavel Psota ^{1,2,3}, Nima Maftoon ⁴, John J. Rosowski ^{5,6}, Cosme Furlong ^{1,2,5,6} and Jeffrey T. Cheng ^{5,6,*}

¹ Center for Holographic Studies and Laser Micro-mechanics (CHSLT), Worcester, MA 01609, USA

² Mechanical Engineering Department, Worcester Polytechnic Institute, Worcester, MA 01609, USA

³ Faculty of Mechatronics, Informatics and Interdisciplinary Studies, Technical University of Liberec, Liberec 46117, Czech Republic

⁴ Systems Design Engineering Department, University of Waterloo, Waterloo, ON N2L 3G1, Canada

⁵ Eaton-Peabody Laboratory, Massachusetts Eye and Ear Infirmary, Boston, MA 02114, USA

⁶ Department of Otolaryngology-Head and Neck Surgery, Harvard Medical School, Boston, MA 02114, USA

* Correspondence: tao_cheng@meei.harvard.edu; Tel.: +1-617-573-4128

Received: 15 June 2019; Accepted: 10 July 2019; Published: 13 July 2019



Abstract: To improve the understanding of the middle-ear hearing mechanism and assist in the diagnosis of middle-ear diseases, we are developing a high-speed digital holographic (HDH) system to measure the shape and acoustically-induced transient displacements of the tympanic membrane (TM). In this paper, we performed measurements on cadaveric human ears with simulated common middle-ear pathologies. The frequency response function (FRF) of the normalized displacement by the stimulus (sound pressure) at each measured pixel point of the entire TM surface was calculated and the complex modal indicator function (CMIF) of the middle-ear system based on FRFs of the entire TM surface motions was used to differentiate different middle-ear pathologies. We also observed changes in the TM shape and the surface motion pattern before and after various middle-ear manipulations. The observations of distinguishable TM shapes and motion patterns in both time and frequency domains between normal and experimentally simulated pathological ears support the development of a quantitative clinical holography-based apparatus for diagnosing middle-ear pathologies.

Keywords: frequency transfer functions; high-speed digital holography; human tympanic membrane; middle-ear pathologies

1. Introduction

The human middle ear, including the eardrum or the tympanic membrane (TM), transmits sound energy from the environment to the inner ear for hearing [1,2]. The mechanism of this energy transmission through the middle ear is intrinsically multifaceted and is affected by the TM's complex geometry (shape and thickness), spatially varied mechanical properties and microstructure (radial and circumferential fibers), as well as the load from the ossicular chain and inner ear [3–15]. Middle-ear pathologies such as TM perforation, otitis media with effusion, otosclerosis, and ossicular discontinuity can result in mild to severe conductive hearing loss. Currently, in otology and audiology clinics, there is no perfect objective diagnostic tool to differentiate middle-ear diseases, and the gold standard for the diagnosis of ossicular disorders is surgical exploration with an elevation of the eardrum to visualize the ossicular chain.

Over the past decade, various non-invasive optical methods, for example, holographic interferometric methods, were developed to quantify TM dynamics such as excitation-induced displacements, and physical characteristics such as shape and thickness [11,16–26]. However, a study on the live subject remains challenging due to the natural noise, such as motions due to respiration, heartbeat, muscle tremor, etc. and high sensitivity of the optical tools. Researchers utilized a high-speed digital holographic method to minimize these undesirable effects and made quantitative measurements on live subjects possible [24,27–30].

The high-speed digital holographic system we developed measures the TM's shape and transient acoustic-induced displacement nearly instantaneously (<200 ms) with a spatial shape resolution of 50–200 μm and a displacement resolution of 15 nm at an acquisition rate of 67,200 Hz [24,28,30–32]. This high-speed system takes into account the holographic-sensitivity vector variations due to the sample's shape and optical configuration to derive the true surface normal motion of the TM.

To investigate if such a high-speed digital holographic (HDH) system can be used as a diagnostic tool for middle-ear pathologies, this paper describes a study on the shape and displacement measurements on post-mortem temporal bones with different experimentally introduced middle-ear pathologies. We compared the full-field-of-view shape measurements and the time and frequency domain analysis of displacements under various middle-ear conditions (open and closed middle-ear cavity, two levels of fluid injection into the middle-ear cavity, stapes immobilization, and incudo-stapedial (IS) joint interruption) to identify TM motion patterns, and data trends associated with each middle-ear condition.

2. Materials and Methods

2.1. Principle of High-Speed Holographic for Shape and Displacement Measurements

2.1.1. Multiple Wavelength Holographic Interferometry (MWHI) Method for Shape Measurement

The multiple wavelength holographic interferometry (MWHI) shape measurements are based on the principle of variations in the wavelength of illumination with a constant optical path length (OPL) (i.e., a stationary sample) [33–37]. The relation between the interference phase $\Delta\gamma$, the constant OPL, and wavelengths λ_1 and λ_2 at two hologram exposures is described as follows:

$$\Delta\gamma = \frac{2\pi}{\lambda_1} OPL - \frac{2\pi}{\lambda_2} OPL = \frac{2\pi}{\Lambda} OPL, \quad (1)$$

where Λ is the synthetic wavelength:

$$\Lambda = \frac{\lambda_1\lambda_2}{\lambda_2 - \lambda_1}. \quad (2)$$

The synthetic wavelength Λ defines the sensitivity of the measurement. Assuming several synthetic wavelengths, the longest one determines the unambiguous measurement range, while the shortest synthetic wavelength gives the lowest uncertainty.

As described in [31], the MWHI method has been designed to sweep the synthetic wavelength allowing multiple measurements of shape in a short time. A tunable laser operating in open loop mode is used as a coherent light source, and continual wavelength tuning is achieved by changing the laser cavity length while keeping the number of waves in the cavity constant [38]. In this paper, a temporal unwrapping approach is applied to ensure that the measurement always yields the maximum resolution of a given wavelength tuning without spatial unwrapping errors.

During the wavelength tuning, N phase-shifted high-speed digital holograms are captured. The Pearson correlation of a 3 by 3 pixel kernel of the first image in the high-speed array and the rest are calculated, which gives information about optical phase change $\Delta\phi$ [32] as follows:

$$\rho(I_1(x, y), I_n(x, y)) = \frac{(r + 1)^2 + 4r \cos(\Delta\phi)}{(r + 1)^2 + 4r}, \tag{3}$$

where $\rho(\)$ is the Pearson correlation operator, I_1 is the first hologram, I_n is the n th holograms, and r is the object and reference beam ratio $r = I_o/I_r$.

Holograms with phase change $\Delta\phi$ of $\pi/2$, π , and $3\pi/2$ are identified from the image arrays to calculate the optical phase F of the measurement at each wavelength using the 4 step phase shifting equation [39]:

$$F = \arctan \frac{I_{3\pi/2} - I_{\pi/2}}{I_1 - I_\pi}, \tag{4}$$

where I_π , $I_{\pi/2}$, and $I_{3\pi/2}$ are the $\pi/2$, π , and $3\pi/2$ phase shifted holograms.

The optical phase difference ΔF_{N-1} of two consecutive high-speed phase measurements are calculated, and 2D Goldstein’s branch cut method [40] is applied to remove any phase jumps. The differential approach provides measurements with lower dynamic ranges, and therefore, the spatial unwrapping is more reliable. Moreover, if the number of phase sampling N is high enough, the optical phase difference has no 2π phase jumps, so the spatial unwrapping can be completely avoided.

The total phase change $\Delta\Upsilon$ of the entire wavelength tuning, ensuring the lowest uncertainty, is

$$\Delta\Upsilon = \sum_2^N \Delta\Phi_k. \tag{5}$$

Assuming perpendicular illumination and observation of the object, the surface z component of a point (x, y) on the sample is

$$z(x, y) = \frac{\Lambda}{4\pi} \Delta\Upsilon(x, y). \tag{6}$$

2.1.2. High-Speed Digital Holographic (HDH) Method for Displacement Measurement

We have previously developed and implemented the HDH method based on correlation interferometry that could “instantaneously” measure the full-field-of-view (>200,000 points at 67,200 camera frame rate) transient displacements of the TM in response to impulsive acoustical and mechanical excitations [24,28,30]. As described in [31], the HDH uses Pearson’s correlation to locate two reference frames I_{ref} and $I_{ref+\pi/2}$ with 0 and $\pi/2$ prior to the sample’s excitation based on Equation (3). The zero-order terms of all correlated kernels are removed by summation of reference frames that are within one period of optical phase shifts. The interference phase $\Delta\theta$ as a result of the sample’s motion of a small window centered at (x, y) is

$$\Delta\theta(t) = \arctan \frac{\rho(I_{ref}, I_{def}(t))}{\rho(I_{ref+\pi/2}, I_{def}(t))}. \tag{7}$$

Studies of in-plane and out-of-plane motions of the human tympanic membrane [41] confirm that TM has a thin-shell structure with the dominant displacement component along the surface normal. Using the information of the shape and the geometry of the experiment setup, the surface normal (n) of the TM surface and the sensitivity vectors (K) [28] of the holographic measurement are computed at each point of the TM surface. The magnitude of the displacement $s(t)$, therefore, can be expressed as

$$s(x, y, t) = \frac{\Delta\theta(x, y, t)}{K(x, y)\Delta n(x, y)}. \tag{8}$$

2.2. Experimental Setup and Procedures

The schematic diagram of the HDH system used in this study is shown in Figure 1. The details of the HDH system and acoustic measurement setups can be found in our previous publication [31]. Three

fresh non-fixed human postmortem temporal bones were used for the measurements. The cartilaginous and bony parts of the ear canal were removed to provide optical access to the TM. The middle-ear cavity was opened to check the health of the middle-ear ossicles, and then it was sealed using the sealing cement. A small metal tube was installed through the eustachian tube for injecting fluid into the middle-ear cavity. The TM surface was sprayed with a thin layer of HOLBEIN water soluble oil color (commercial trade name: TITANIUM WHITE) using a commercially available airbrush (MASTER® Model S68).

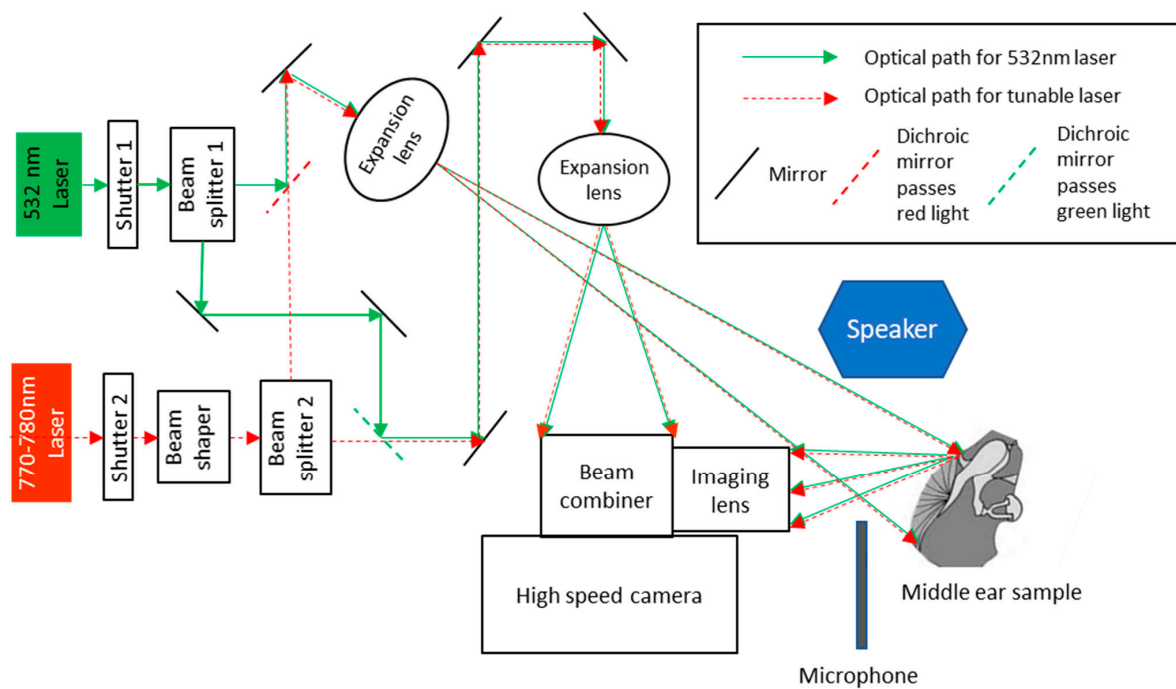


Figure 1. Schematic of high-speed digital holographic (HDH) system [4]. The 532 nm laser is used for displacement measurements, and the 770–780 nm tunable laser is used for shape measurements. The two lasers are coupled into the same optical path to ensure the shape and displacement measurements are in the same coordinate system avoiding the need for image registration.

Primary experiments measured the transient TM responses to a short acoustic click (i.e., a 50 μ s square pulse) generated by a speaker, as shown in Figure 1, and the TM shape information to calculate the true out-of-plane motion of the entire TM [4]. We also acquired the acoustic excitation profile using a high-frequency microphone situated close to the TM, as shown in Figure 1. After the control measurement on the normal ear (closed middle-ear cavity), the sample was subjected to a series of manipulations that simulated different middle-ear conditions and pathologies. The manipulations included: (i) open middle-ear cavity, (ii) closed middle-ear cavity, (iii) injecting saline into the middle-ear cavity to the level of half TM in contact with fluid, as shown in Figure 2b, (iv) injecting saline until the full TM was in contact with fluid, (v) removing the injected fluid, (vi) immobilizing the footplate of the stapes with super glue, and (vii) interrupting the incudo-stapedial (IS) joint, as shown in Figure 2c. The shape and transient acoustic-induced displacements were measured at each manipulation (experimental setup is shown in Figure 2a). The human temporal bone study was approved by the Institutional Review Board of the Massachusetts Eye and Ear Infirmary. The use of de-identified human cadaveric tissue (only age and gender information are available) does not require a human subject study protocol.

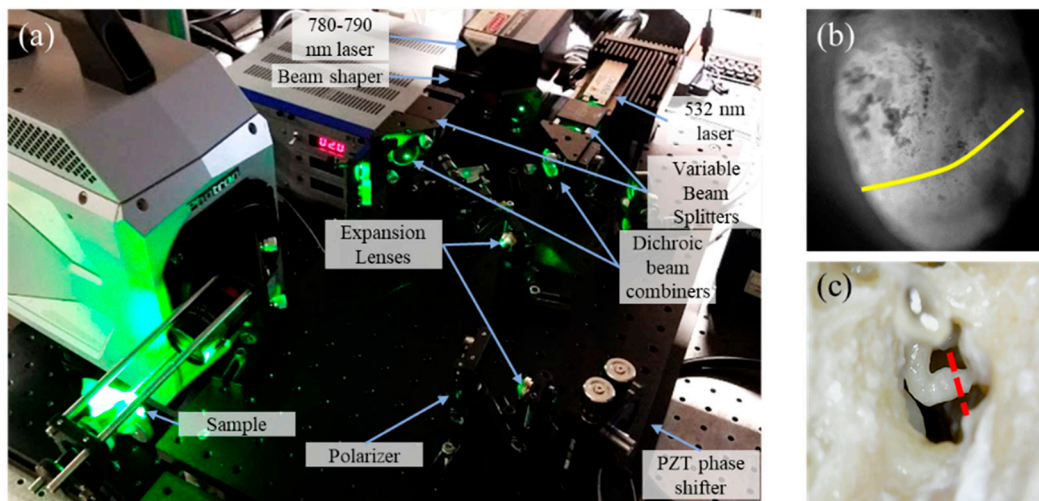


Figure 2. (a) Shows the setup, measuring instrumentations, and the sample; and (b) is a photograph of the human postmortem tympanic membrane (TM) with half level saline injected. The yellow contour shows the level of fluid. (c) Shows the incudo-stapedial (IS) joint. The red dash shows where the IS joint is interrupted.

2.3. Experimental Modal Analysis

Frequency response function (FRF) matrices computed from the ratio of the output displacements s and the input sound pressure p in the frequency domain were calculated for all the TM surface points with various middle-ear manipulations.

$$\text{FRF}(x, y, \omega) = \frac{\text{FFT}(s(x, y, t))}{\text{FFT}(p(t))}, \quad (9)$$

where x, y are the coordinates of TM points, t is time, and ω is the frequency.

FRF(x, y, ω) was then flattened into a 2D matrix $H(n, \omega)$ where n is the number of the nodes. FFT denotes fast Fourier transform.

Complex mode indicator functions (CMIFs) were calculated by taking singular value decomposition ([17], Equation (1)) of each FRF matrix,

$$[H] = [U][\Sigma][V]^H, \quad (10)$$

where $[H]$ is the flattened frequency response function matrix; $[U]$ is the left singular vector matrix (unitary); $[\Sigma]$ is the singular value matrix (diagonal); $[V]$ is the right singular vector matrix (unitary); and $[\cdot]^H$ marks the Hermitian (conjugate transpose) of matrix. The CMIF is defined as the main diagonal elements of the singular value matrix.

$$\text{CMIF} = \text{diag}[\Sigma] \quad (11)$$

3. Results

3.1. Representative Shape Measurement Results

The MWHI method has been verified to reach an accuracy of 0.045 mm and exhibited repeatable measurements with 17 μm accuracy on a (National Institute of Standards and Technology) traceable ball and artificial samples [31]. This paper presents the results of TM shape measurements from three post-mortem human temporal bones (TB3, TB4, and TB5) under different manipulations. The 3D shapes of the TM of the three samples measured with a closed middle-ear cavity are shown in Figure 3a–c with laser continuous wavelength tuning from 779 to 779.4 nm (i.e., maximum synthetic wavelength

1.7 mm), while N ($N = 17$) of phase samplings are performed to capture the optical phase at different wavelengths during wavelength tuning. The depth of the TM is rendered by color as shown in the color bar, where the TM annulus is set as zero (yellow), and the value increases negatively towards the middle-ear cavity side. In Figure 3d–h, the difference of the TM shape along the solid black line across the TM surface, as shown in Figure 3a, between the closed cavity (as reference) and different manipulations are shown. The comparison between the open cavity and the closed cavity shows no significant TM shape change in all three TBs (Figure 3d). The fluid injection induces more significant TM shape change where the fluid in contact with the TM pushes the TM surface outwards towards the ear canal side, yielding positive TM shape change values as shown in Figure 3e,f. Note in Figure 3e only half of the TM (to the right side of the plot) is in contact with the fluid. Stapes immobilization did not introduce significant TM shape change, as shown in Figure 3g. The IS joint interruption induced more significant changes to the TM shape which generally occurred at the posterior part of the TM, and the direction of the shape change was towards the middle-ear cavity (as shown in negative values in Figure 3h).

We used the shape information to derive TM transient surface-normal displacements. We investigated using the root mean square (RMS) of the motion of the entire TM surface to define an indicator to evaluate and distinguish different middle-ear manipulations. We also compared the umbo displacement in the time domain among different middle-ear manipulations. Figures 4–6 show the RMS of TM surface motions over the first 3 ms after the TM receives the acoustic excitation for three TBs—under different middle-ear conditions. Figures 7–9 show the umbo motion during the same time period under different manipulations for three bones. From the RMS results, we observed that an open cavity case always has a more complex distribution of the RMS than a closed cavity case. For half fluid injection cases, only the area not in contact with fluid shows significant RMS values of motion (right side of the TM in Figures 4c and 5c and left side of the TM in Figure 6c, the difference is caused by the different sides of the ear these specimens come from (TB3: 75 year old female, left ear; TB4: 61 year old male, left ear; TB5: 76 year old female, right ear)). When the middle-ear cavity is fully filled with fluid, the RMS value of TM motions is almost zero. Stapes immobilization and IS joint injection exhibit RMS motion patterns that are similar to those observed in the normal case.

The umbo displacement profiles with time show distinguishable differences among different middle-ear conditions for all three bones, as shown in Figures 7–9. In an open cavity case, the umbo undergoes more periods of motion compared to a closed cavity case, or umbo motion damps out faster in the closed cavity case. Half-fluid and full-fluid injections suppress umbo motion to very little or no sensible motion. The stapes immobilization and IS joint interruption alter the umbo motion in an analogous fashion with little distinguishable differences between the two cases.

Figure 10 shows the displacement of TB3 under an open middle-ear cavity. Figure 10a shows the measured optical phase at an arbitrary time, Figure 10b shows the unwrapped and scaled surface's normal displacement calculated from Figure 10a, and Figure 10c is the time waveform of the acoustic excitation signal (first row) and displacements of six discrete points marked in Figure 10b. The results show that different regions of the TM respond to the excitation differently, and that different regions of the TM reach displacement maximum and minimum at different times, and eventually settling at different times. The time of delay for each point to start the motion compared to the acoustic signal is also different point by point, suggesting that there are traveling waves forming on the surface of TM.

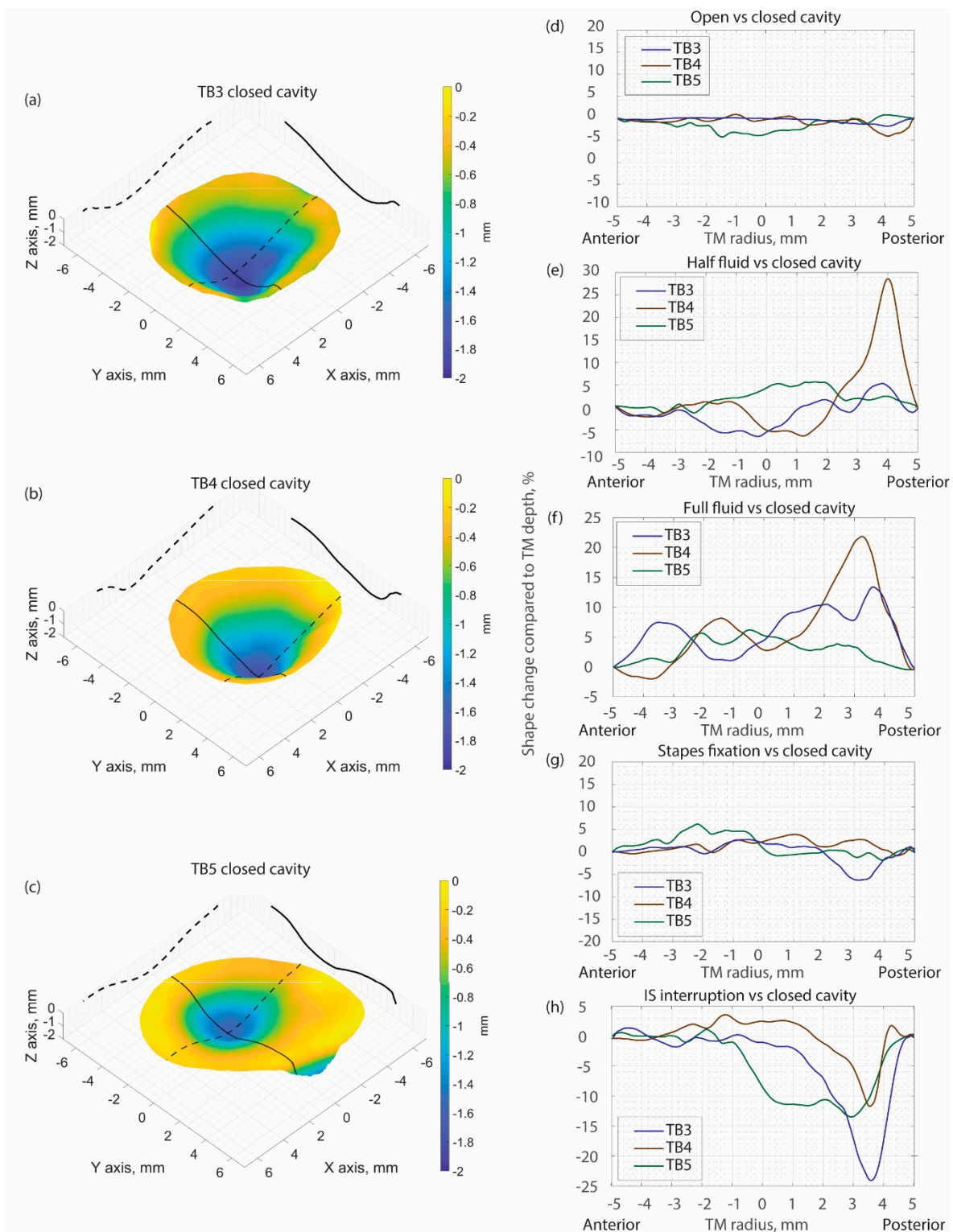


Figure 3. (a):TB3 shape when the middle-ear cavity is closed;(b):TB4 shape when the middle-ear cavity is closed;(c): TB5 shape when the middle-ear cavity is closed; Comparison of TM shape along the black solid line marked in the left panel in TB 3~5 (d): between open and closed cavity condition; (e): between half fluid injection and closed cavity condition; (f): between full fluid injection and closed cavity condition; (g): between Stapes fixation and closed cavity condition; (h): between IS joint interruption and closed cavity condition.3.2. Representative Displacement Measurement Results

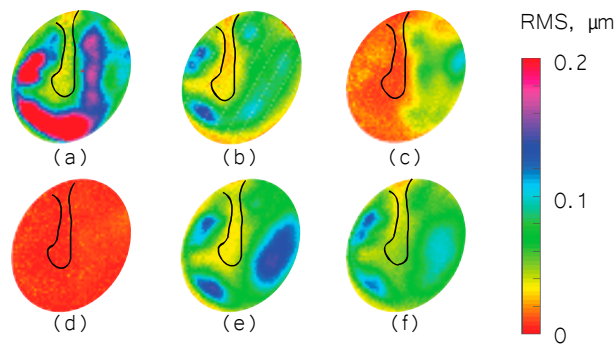


Figure 4. Root mean square (RMS) of TB3 displacement under different conditions. (a) Open cavity; (b) closed cavity; (c) half fluid in contact; (d) full fluid in contact; (e) stapes immobilization; and (f) IS joint interruption.

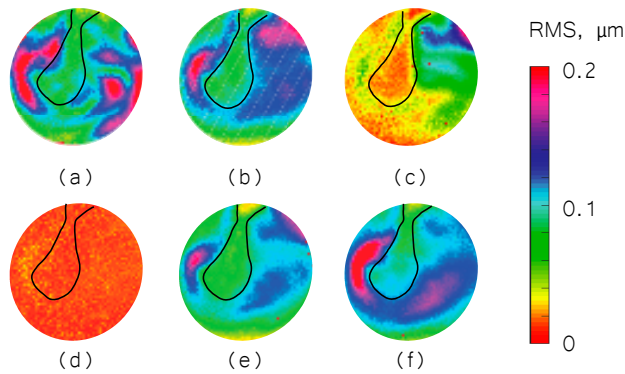


Figure 5. RMS of TB4 displacement under different conditions. (a) Open cavity; (b) closed cavity; (c) half fluid in contact; (d) full fluid in contact; (e) stapes immobilization; and (f) IS joint interruption.

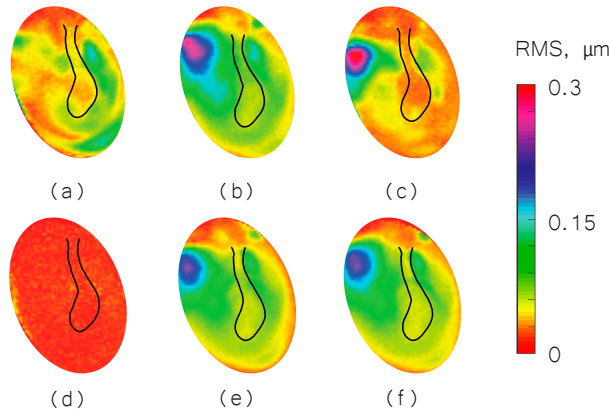


Figure 6. RMS of TB5 displacement under different conditions. (a) Open cavity; (b) closed cavity; (c) half fluid in contact; (d) full fluid in contact; (e) stapes immobilization; and (f) IS joint interruption.

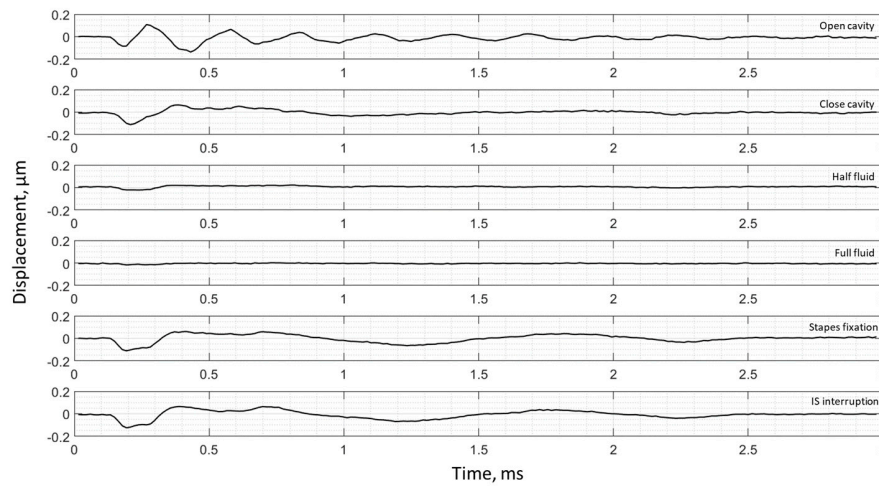


Figure 7. Umbo displacement of TB3 under different cases (umbo location is marked as the intersection of the solid black and dashed black lines in Figure 3a).

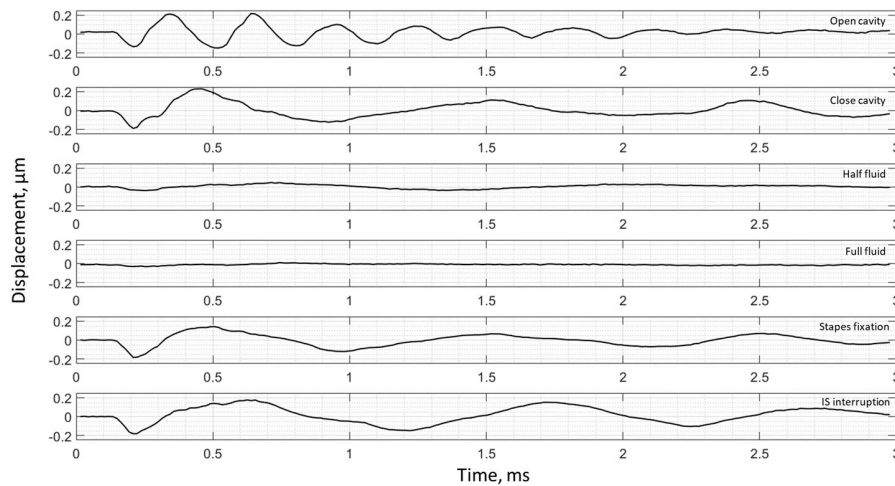


Figure 8. Umbo displacement of TB4 under different cases (umbo location is marked as the intersection of the solid black and dashed black lines in Figure 3b).

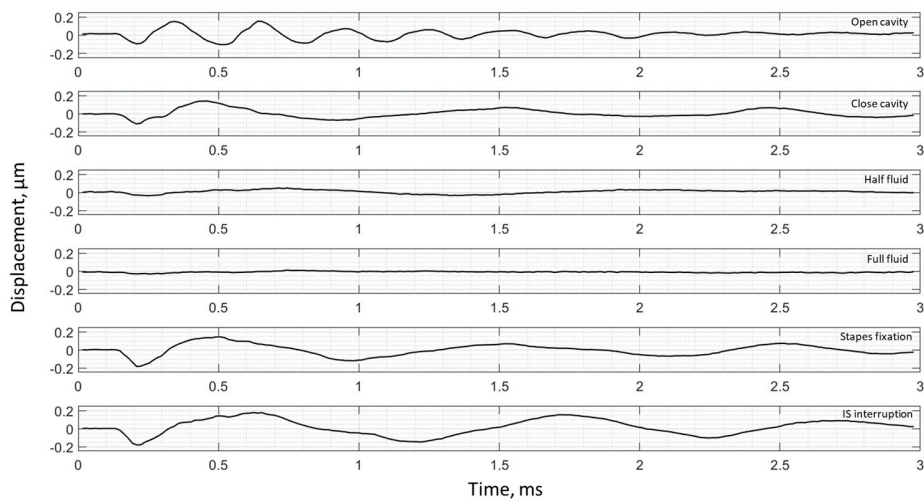


Figure 9. Umbo displacement of TB5 under different cases (umbo location is marked as the intersection of the solid black and dashed black lines in Figure 3c).

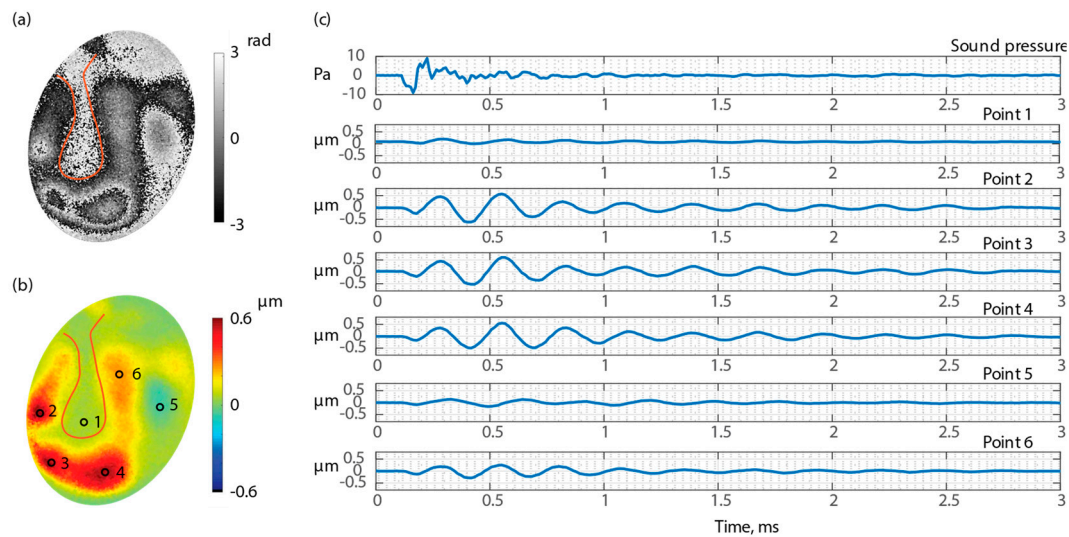


Figure 10. Waveforms of six points of the surface of the TM of TB3 when the middle-ear cavity is open. (a) Wrapped optical phase 0.56 ms after excitation; (b) TM surface normal displacement 0.56 ms after excitation; and (c) time waveforms of six points marked in part (c).

3.2. Frequency Analysis: Complex Mode Indicator Functions

To visualize and compare all the data of the entire surface of the TM across different manipulations, the complex mode indicator function (CMIF) was used as a generalized presentation of the membrane's frequency response. Figure 11 shows CMIFs computed from all three temporal bones with different middle-ear manipulations. The horizontal axis is the frequency in kHz (kilohertz), and the vertical axis is the singular value in decibels, which are the square root of the eigenvalues of the frequency response function (FRF) matrix. We observed that CMIF changes with different middle-ear conditions. We defined the closed cavity condition, as shown in the second row of Figure 11, as the baseline and subtracted other obtained CMIF data from this baseline for further comparison in Figure 12. The open cavity condition generally decreases CMIF amplitude at low frequencies around 1 kHz and induces a major peak at 3 to 5 kHz in all three TBs. A half fluid condition in TB3 and TB4 shows lower CMIF amplitude across the entire frequency spectrum compared to the baseline closed cavity case, although the decrease of CMIF in TB5 is relatively small. Also, for the full fluid case, all three samples have the lowest CMIF amplitudes, consistent with TM motions that are significantly reduced by fluid inside the middle-ear cavity. The CMIFs under the stapes immobilization condition at low-frequency ranges (0.5–2.5 kHz) for TB3 and TB4 are significantly reduced. However, this reduction is not obvious in TB5. Finally, the IS joint interruption condition introduces several additional peaks for CMIFs, particularly at mid- and high-frequency ranges.

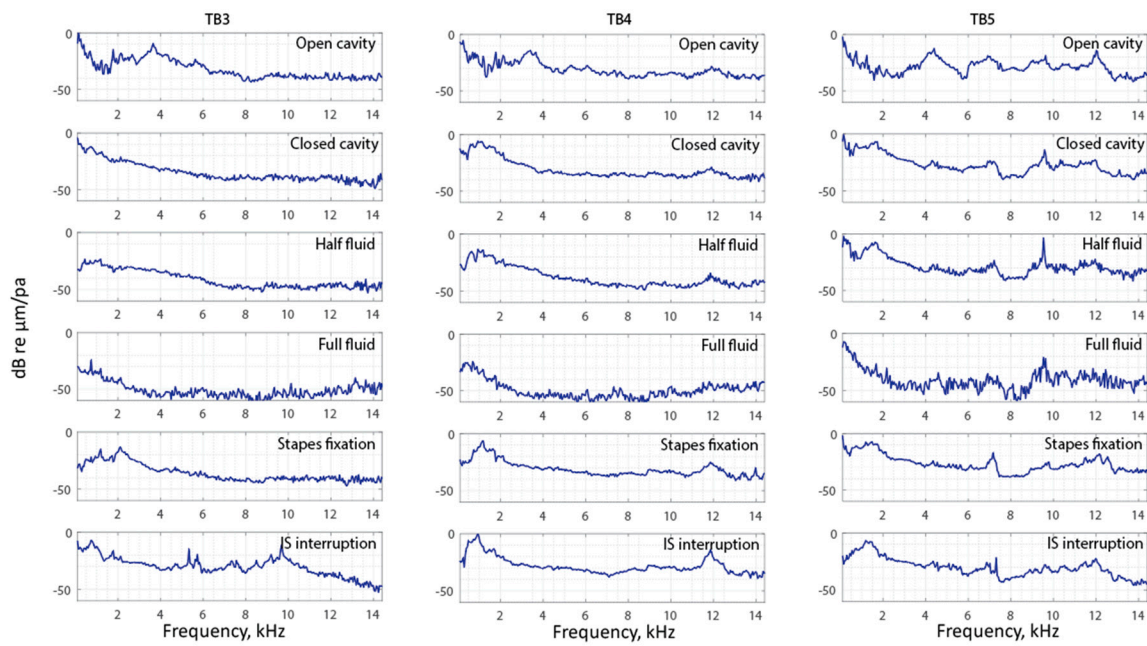


Figure 11. The complex model indicator function of TB3–5 under different conditions.

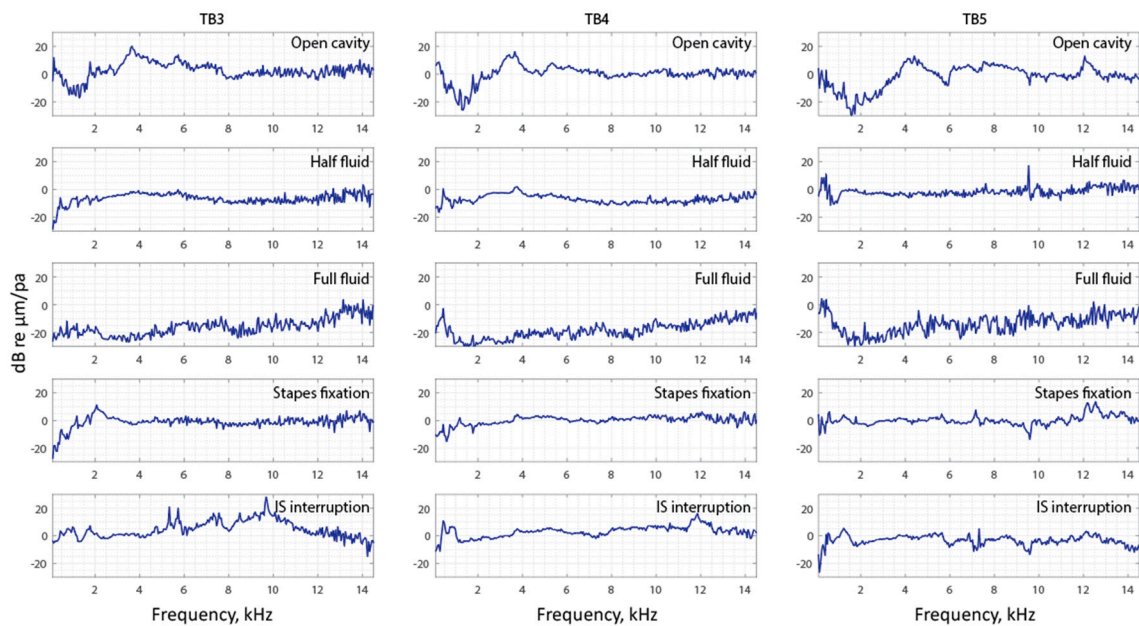


Figure 12. The complex model indicator function subtracted by the closed cavity case of TB3–5.

4. Discussion

This study provides a complete description of TM mechanics, including the 3D shape information and full-field TM surface normal vibration in both the time and frequency domains.

The shape results show that the TM shape is affected by various middle-ear manipulations. The different manipulations overall introduce a maximum shape change of less than 0.3 mm. The fluid injection pushes the TM to deform towards the ear canal side, while the IS joint interruption seems to pull the TM toward the middle-ear cavity side, which is interesting and may suggest the cochlear load produced tension on the TM. No differentiable shape change is identified for open cavity and stapes immobilization.

Displacements in the time domain show we can confidently distinguish half fluid injection and full fluid injection by checking the RMS results and the open cavity case. Fluid injections will surpass the TM motion. Opening the cavity causes the TM surface to displace more compared to the normal middle-ear cavity condition (closed cavity).

In the frequency domain, we observed trends in different CMIFs associated with different middle-ear conditions. In open cavity cases, the first significant CMIF peak appears around 4 kHz (3.7 kHz for TB3, 3.5 kHz for TB4, and 4.3 kHz for TB5). Half fluid and full fluid injections decrease the CMIF across the whole frequency range. Stapes immobilization reduces the CMIF at a lower frequency up to 2.5 kHz for TB3 and TB4 and increases it for TB5 at a higher frequency (12–14 kHz). IS joint interruption adds additional peaks to the CMIF at different frequencies.

Time domain and frequency domain analysis results can separate different middle-ear pathologies, suggesting the potential for clinical diagnosis. In the future work, we will investigate the accuracy of potential diagnostics through further experiments—identify trends in the data associated with different pathologies and test the sensitivity and selectivity of these analyses for clinical diagnosis. Artificial intelligence (AI) and data mining will be applied to automate the analysis process and assist in the separation of normal and diseased states.

Author Contributions: Conceptualization, N.M., J.J.R., C.F., J.T.C.; methodology, H.T., P.R., P.P.; software, H.T., P.R., P.P., N.M.; validation, H.T., P.P.; formal analysis, H.T.; P.P.; investigation, H.T.; resources, J.J.R., C.F., J.T.C.; data curation, H.T., writing—original draft preparation, H.T.; writing—review and editing, H.T., P.R., K.P., P.P., J.J.R., J.T.C.; visualization, H.T.; supervision, J.J.R., C.F., J.T.C.; project administration, J.J.R., C.F., J.T.C.; funding acquisition, J.J.R., C.F., J.T.C.

Funding: This work has been funded by the National Institutes of Health (NIH), National Institute on Deafness and Other Communication Disorders (NIDCD), grant number R01, DC016079.

Acknowledgments: This work is supported by the NanoEngineering, Science, and Technology (NEST) program at the Worcester Polytechnic Institute, Mechanical Engineering Department.

Conflicts of Interest: The authors declare no conflict of interest.

References

1. Rosowowski, J.J. *Outer and Middle Ears. Comparative Hearing: Mammals*; Fay, R.R., Popper, A.N., Eds.; Springer: New York, NY, USA, 1994; pp. 172–247.
2. Geisler, C.D. *From Sound to Synapse: Physiology of the Mammalian Ear*; Oxford University Press: New York, NY, USA, 1998.
3. Wang, X.; Guan, X.; Pineda, M.; Gan, R.Z. Motion of tympanic membrane in guinea pig otitis media model measured by scanning laser Doppler vibrometry. *Hear. Res.* **2016**, *339*, 184–194. [[CrossRef](#)] [[PubMed](#)]
4. Fay, J.P.; Puria, S.; Steele, C.R. The discordant eardrum. *Proc. Natl. Acad. Sci. USA* **2006**, *103*, 19743–19748. [[CrossRef](#)] [[PubMed](#)]
5. Vollandri, G.; di Puccio, F.; Forte, P.; Carmignani, C. Biomechanics of the tympanic membrane. *J. Biomech.* **2011**, *44*, 1219–1236. [[CrossRef](#)] [[PubMed](#)]
6. Cheng, T.; Dai, C.; Gan, R.Z. Viscoelastic Properties of Human Tympanic Membrane. *Ann. Biomed. Eng.* **2007**, *35*, 305–314. [[CrossRef](#)] [[PubMed](#)]
7. Fay, J.; Puria, S.; Decraemer, W.F.; Steele, C. Three approaches for estimating the elastic modulus of the tympanic membrane. *J. Biomech.* **2005**, *38*, 1807–1815. [[CrossRef](#)] [[PubMed](#)]
8. Greef, D.; Buytaert, J.A.; Aerts, J.R.; Van, L.; Dierckx, M.; Dirckx, J. Details of human middle ear morphology based on micro-CT imaging of phosphotungstic acid stained samples. *J. Morphol.* **2015**, *276*, 1025–1046. [[CrossRef](#)]
9. Van der Jeught, S.; Dirckx, J.J.J.; Aerts, J.R.M.; Bradu, A.; Podoleanu, A.G.; Buytaert, J.A.N. Full-Field Thickness Distribution of Human Tympanic Membrane Obtained with Optical Coherence Tomography. *J. Assoc. Res. Otolaryngol.* **2013**, *14*, 483–494. [[CrossRef](#)] [[PubMed](#)]
10. Aernouts, J.; Aerts, J.R.M.; Dirckx, J.J.J. Mechanical properties of human tympanic membrane in the quasi-static regime from in situ point indentation measurements. *Hear. Res.* **2012**, *290*, 45–54. [[CrossRef](#)]

11. Rosowski, J.J.; Cheng, J.T.; Ravicz, M.; Hulli, N.; Montes, M.H.; Harrington, E.; Furlong, C. Computer-assisted time-averaged holograms of the motion of the surface of the mammalian tympanic membrane with sound stimuli of 0.4–25 kHz. *Hear. Res.* **2009**, *253*, 83–96. [[CrossRef](#)]
12. Rosowski, J.J.; Hawkins, H.L.; McMullen, T.A.; Popper, A.N.; Fay, R.R. Models of External- and Middle-Ear Function. In *Auditory Computation*; Springer: New York, NY, USA, 1996; pp. 15–61.
13. Lim, D.J. Human Tympanic Membrane. *Acta Oto Laryngol.* **1970**, *70*, 176–186. [[CrossRef](#)]
14. Khaleghi, M. Development of Holographic Interferometric Methodologies for Characterization of Shape and Function of the Human Tympanic Membrane. Ph.D. Thesis, Worcester Polytechnic Institute, Worcester, MA, USA, April 2015.
15. Milazzo, M.; Fallah, E.; Carapezza, M.; Kumar, N.S.; Lei, J.H.; Olson, E.S. The path of a click stimulus from ear canal to umbo. *Hear. Res.* **2017**, *346*, 1–13. [[CrossRef](#)] [[PubMed](#)]
16. Cheng, J.T.; Aarnisalo, A.A.; Harrington, E.; Montes, S.H.; Furlong, C.; Merchant, S.N.; Rosowski, J.J. Motion of the surface of the human tympanic membrane measured with stroboscopic holography. *Hear. Res.* **2010**, *263*, 66–77. [[CrossRef](#)] [[PubMed](#)]
17. Hernández-Montes, S.; Furlong, C.; Rosowski, J.J.; Hulli, N.; Harrington, E.; Cheng, J.T.; Ravicz, M.E.; Santoyo, F.M. Optoelectronic holographic otoscope for measurement of nano-displacements in tympanic membranes. *J. Biomed. Opt.* **2009**, *14*, 034021.
18. Solís, S.M.; Hernández-Montes, M.D.; Santoyo, F.M. Tympanic membrane contour measurement with two source positions in digital holographic interferometry. *Biomed. Opt. Express* **2012**, *3*, 3203–3210. [[CrossRef](#)] [[PubMed](#)]
19. Solís, S.M.; Santoyo, F.M.; Hernández-Montes, M.D. 3D displacement measurements of the tympanic membrane with digital holographic interferometry. *Opt. Express* **2012**, *20*, 5613–5621. [[CrossRef](#)] [[PubMed](#)]
20. Rosowski, J.J.; Dobrev, I.; Khaleghi, M.; Lu, W.; Cheng, J.T.; Harrington, E.; Furlong, C. Measurements of three-dimensional shape and sound-induced motion of the chinchilla tympanic membrane. *Hear. Res.* **2013**, *301*, 44–52. [[CrossRef](#)] [[PubMed](#)]
21. Rutledge, C.; Thyden, M.; Furlong, C.; Rosowski, J.J.; Cheng, J.T. Mapping the Histology of the Human Tympanic Membrane by Spatial Domain Optical Coherence Tomography. *MEMS Nanotechnol.* **2013**, *6*, 125–129.
22. Khaleghi, M.; Furlong, C.; Cheng, J.T.; Rosowski, J.J. Characterization of Acoustically-Induced Forces of the Human Eardrum. *Mech. Biol. Syst. Mater.* **2016**, *6*, 147–154.
23. Santiago-Lona, C.V.; Hernández-Montes, M.D.; Mendoza-Santoyo, F.; Esquivel-Tejeda, J. Quantitative comparison of tympanic membrane displacements using two optical methods to recover the optical phase. *J. Mod. Opt.* **2018**, *65*, 275–286. [[CrossRef](#)]
24. Dobrev, I.; Furlong, C.; Cheng, J.T.; Rosowski, J.J. Full-field transient vibrometry of the human tympanic membrane by local phase correlation and high-speed holography. *J. Biomed. Opt.* **2014**, *19*, 96001. [[CrossRef](#)]
25. De Greef, D.; Aernouts, J.; Aerts, J.; Cheng, J.T.; Horwitz, R.; Rosowski, J.J.; Dirckx, J. Viscoelastic properties of the human tympanic membrane studied with stroboscopic holography and finite element modeling. *Hear. Res.* **2014**, *312*, 69–80. [[CrossRef](#)] [[PubMed](#)]
26. Khaleghi, M.; Guignard, J.; Furlong, C.; Rosowski, J.J. Simultaneous full-field 3-D vibrometry of the human eardrum using spatial-bandwidth multiplexed holography. *J. Biomed. Opt.* **2015**, *20*, 111202. [[CrossRef](#)] [[PubMed](#)]
27. Dobrev, I. Full-Field Vibrometry by High-Speed Digital Holography for Middle-ear Mechanics. Ph.D. Thesis, Worcester Polytechnic Institute, Worcester, MA, USA, July 2014.
28. Razavi, P.; Ravicz, M.E.; Dobrev, I.; Cheng, J.T.; Furlong, C.; Rosowski, J.J. Response of the human tympanic membrane to transient acoustic and mechanical stimuli: Preliminary results. *Hear. Res.* **2016**, *340*, 15–24. [[CrossRef](#)] [[PubMed](#)]
29. Razavi, P.; Dobrev, I.; Ravicz, M.E.; Cheng, J.T.; Furlong, C.; Rosowski, J.J. Transient Response of the Eardrum Excited by Localized Mechanical Forces. *Mech. Biol. Syst. Mater.* **2016**, *6*, 31–37.
30. Razavi, P.; Cheng, J.T.; Furlong, C.; Rosowski, J.J. High-Speed Holography for In-Vivo Measurement of Acoustically Induced Motions of Mammalian Tympanic Membrane. *Mech. Biol. Syst. Mater.* **2016**, *6*, 75–81.
31. Razavi, P.; Tang, H.; Rosowski, J.J.; Furlong, C.; Cheng, J.T. Combined high-speed holographic shape and full-field displacement measurements of tympanic membrane. *J. Biomed. Opt.* **2018**, *24*, 031008. [[CrossRef](#)] [[PubMed](#)]

32. Razavi, P. Development of High-Speed Digital Holographic Shape and Displacement Measurement Methods for Middle-Ear Mechanics In-vivo. Ph.D. Thesis, Worcester Polytechnic Institute, Worcester, MA, USA, March 2018.
33. Yamaguchi, I.; Ida, T.; Yokota, M.; Yamashita, K. Surface shape measurement by phase-shifting digital holography with dual wavelengths. *Interferom. Tech. Anal.* **2006**, *6292*, 62920V.
34. Kuwamura, S.; Yamaguchi, I. Wavelength scanning profilometry for real-time surface shape measurement. *Appl. Opt.* **1997**, *36*, 4473–4482. [[CrossRef](#)]
35. Seebacher, S.; Osten, W.; Jueptner, W.P.O. Measuring shape and deformation of small objects using digital holography. *Laser Interferom. Appl.* **1998**, *3479*, 104–116.
36. Furlong, C.; Pryputniewicz, R.J. Absolute shape measurements using high-resolution optoelectronic holography methods. *Opt. Eng.* **2000**, *39*, 216–224. [[CrossRef](#)]
37. Osten, W.; Seebacher, S.; Baumbach, T.; Jueptner, W.P.O. Absolute shape control of microcomponents using digital holography and multiwavelength contouring. *Metrol. Based Control Micro Manuf.* **2001**, *4275*, 71–85.
38. Harvey, K.C.; Myatt, C.J. External-cavity diode laser using a grazing-incidence diffraction grating. *Opt. Lett.* **1991**, *16*, 910. [[CrossRef](#)] [[PubMed](#)]
39. Kreis, T. *Handbook of Holographic Interferometry: Optical and Digital Methods*; VCH Publishers: New York, NY, USA, 2005; ISBN 978-3-527-60492-0.
40. Ghiglia, D.C.; Pritt, M.D. *Two-Dimensional Phase Unwrapping: Theory, Algorithms, and Software*; Wiley: New York, NY, USA, 1998; Volume 4.
41. Khaleghi, M.; Cheng, J.T.; Furlong, C.; Rosowski, J.J. In-plane and out-of-plane motions of the human tympanic membrane. *J. Acoust. Soc. Am.* **2016**, *139*, 104–117. [[CrossRef](#)] [[PubMed](#)]



© 2019 by the authors. Licensee MDPI, Basel, Switzerland. This article is an open access article distributed under the terms and conditions of the Creative Commons Attribution (CC BY) license (<http://creativecommons.org/licenses/by/4.0/>).

Chapter 8 Paper C: Analyses of the Tympanic Membrane Impulse Response Measured with High-Speed Holography

Overview

This paper was published in October 2021 in Hearing Research, volume 410. This paper presents new procedures to perform high-speed holographic shape and transient displacement measurements. Shape measurements show 7 of the 8 TMs have similar TMs with less than 0.3mm of variation. Displacement results show it is possible to identify the spatial differences in the amplitude and frequency of the displacement responses. Frequency and impulse response analyses are applied to the sound stimulus normalized measured motions. These analyses show significant spatial differences in the motion on the TM surfaces. Furthermore, the motion parameters are spatially averaged by the quadrants of the TM surface. These quadrant averaged parameters illustrate general quantitative similarity in the different ears. The averaged dominant frequencies and magnitudes of motion are similar to previous reports. Moreover, the spatially varied rising and decay time of the impulse response show similarity to other one-point measurements and result in newly described spatial variations in the damping ratio derived from transient stimulated TM motions and new estimates of the frequency dependence of this vital feature of TM mechanics.



Research Paper

Analyses of the Tympanic Membrane Impulse Response Measured with High-Speed Holography

H. Tang^{a,b,d,*}, P. Psota^c, J.J. Rosowski^{d,e}, C. Furlong^{a,b,d,e}, J.T. Cheng^{d,e}

^a Center for Holographic Studies and Laser Micro-mechanics (CHSLT), Worcester Polytechnic Institute, Worcester, MA United States

^b Mechanical Engineering Department, Worcester Polytechnic Institute, Worcester, MA United States

^c Faculty of Mechatronics, Informatics and Interdisciplinary Studies, Technical University of Liberec, Liberec, Czech Republic

^d Eaton-Peabody Laboratory, Massachusetts Eye and Ear Infirmary, Boston, MA United States

^e Department of Otolaryngology-Head and Neck Surgery, Harvard Medical School, Boston, MA, United States



ARTICLE INFO

Article history:

Received 4 June 2021

Revised 2 August 2021

Accepted 4 August 2021

Available online 11 August 2021

Keywords:

Tympanic membrane

Middle ear

High-speed digital holography

Frequency response function

Impulse response function

Mechanical properties

ABSTRACT

The Tympanic Membrane (TM) transforms acoustic energy to ossicular vibration. The shape and the displacement of the TM play an important role in this process. We developed a High-speed Digital Holography (HDH) system to measure the shape and transient displacements of the TM induced by acoustic clicks. The displacements were further normalized by the measured shape to derive surface normal displacements at over 100,000 points on the TM surface. Frequency and impulse response analyses were performed at each TM point, which enable us to describe 2D surface maps of four new TM mechanical parameters. From frequency domain analyses, we describe the (i) dominant frequencies of the displacement per sound pressure based on Frequency Response Function (FRF) at each surface point. From time domain analyses, we describe the (ii) rising time, (iii) exponential decay time, and the (iv) root-mean-square (rms) displacement of the TM based on Impulse Response Function (IRF) at each surface point. The resultant 2D maps show that a majority of the TM surface has a dominant frequency of around 1.5 kHz. The rising times suggest that much of the TM surface is set into motion within 50 μ s of an impulsive stimulus. The maps of the exponential decay time of the IRF illustrate spatial variations in damping, the least known TM mechanical property. The damping ratios at locations with varied dominant frequencies are quantified and compared.

© 2021 Elsevier B.V. All rights reserved.

1. Introduction

The eardrum or tympanic membrane (TM) is a thin multi-layer cone-shaped structure that separates the outer ear from the middle ear, where TM motion initiates sound transmission to the inner ear. The sound-induced motions of the TM surface are affected by its mechanical properties, shape, thickness, microstructure, and the load from the ossicular chain and inner ear (Rosowski, 1994, Geisler, 1998, Wang et al., 2016, Fay et al., 2006, Vollandri et al., 2011, Cheng et al., 2007, Fay et al., 2005, De Greef et al., 2015, Van der Jeught et al., 2013, Aernouts et al., 2012, Rosowski et al., 2009, Rosowski, 1996, Lim, 1970, Khaleghi, 2015, Milazzo et al., 2017). It has been observed that the sound-induced vibration of the TM surface is frequency dependent and the spatial patterns of the vibrations tend to change from simple to complex patterns as frequency increases (Tonndorf and Khanna, 1970, Khanna and Tonndorf, 1972, Decraemer et al., 1989, Goode et al.,

1993). To quantitatively investigate these motion patterns and better understand the function of the TM for hearing, various non-contact optical methodologies have been developed (Goode et al., 1996, Goode et al., 1994, Gan et al., 2004, Rosowski et al., 2008, Decraemer et al., 1999, de La Rochefoucauld and Olson, 2010, Cheng et al., 2010).

Our group has been studying the sound-induced motion of the TM using holography-based methodologies: we measured TM motions on cadaveric human temporal bones (TBs) at discrete frequencies using a stroboscopic holographic method. We further implemented a high-speed full field of view holographic shape and displacement measurement system that measured the TM 3D shape and responses under transient acoustic excitations (Dobrev et al., 2013, Khaleghi et al., 2014) that enabled the estimation of the TM surface normal displacements regardless of the orientation of the TM within the measurement system (Razavi et al., 2018, Tang et al., 2019). The use of transients, which include many frequencies, allowed more broad-band analyses, including frequency and impulse response computations. Recently we introduced a higher power laser and a new holographic shape mea-

* Corresponding author.

E-mail address: htang3@wpi.edu (H. Tang).

surement methodology (Razavi et al., 2018) into the system that reduced the need for sample surface preparation of the naturally non-transparent human TM (e.g., the application of paint to the imaged surface was no longer required). The system allows measurements (at each of more than 100,000 points on the TM surface) of the displacement produced by acoustic transients with 10 nanometer scale resolution and a temporal resolution of less than 20 μs (Tang et al., 2019). At those same points we can measure the TM shape (specifically the depth of the TM cone) with better than 100 μm resolution (Razavi et al., 2018).

In this paper, we present measurements of the TM shape and transient responses induced by acoustic clicks from 8 normal TM samples using our high-speed holographic system in two shape-measurement configurations. The shapes of the first 5 TM samples were obtained through a multi-wavelength method using a tunable 10 mW laser that produced a sweep of wavelengths: a combination of measurements with different wavelengths allowed the generation of synthetic optical wavelengths similar to the depth of the TM cone (Razavi et al., 2018, Tang et al., 2019, Razavi, 2018). The lower power of this tunable laser necessitated the use of reflective paint in order to provide enough reflected light from the TM surface for accurate holographic shape and displacement measurements (Razavi et al., 2018, Tang et al., 2019, Razavi, 2018). After measurements on the fifth TM sample, we introduced a 200 mW fixed-wavelength laser that did not require paint for accurate holographic measurements on the human TM samples. At the same time we introduced a new multi-angle shape measurement method: controlled changes in the angle of illumination produced changes in the interference between the reference and reflected light beams in stationary TMs that were solved to estimate the depth of the TM at each surface point (Razavi et al., 2018, Tang et al., 2019, Psota et al., 2020) with a resolution better than 100 μm . The displacement results are measured with a previously described high-speed holographic method (Tang et al., 2019). The shape information is used to compensate the variations of the sensitivity vectors of the displacement results due to near-field effects as well as compute the displacement component normal to the TM surface (Tang et al., 2019). The displacement results are further analyzed in both frequency and time domains to (a) derive the acoustic normalized frequency response function (FRF), and (b) reconstruct the impulse response (IRF) of the TM. Two-dimensional maps of the dominant frequency of the FRF function were obtained, and maps of the root mean square displacement, rising time and Exponential decay time were obtained from the IRF. The response maps are used to describe features of the mechanics of the TMs relevant to sound transduction.

2. Methods

2.1. Specimen preparation

Eight fresh human cadaveric temporal bones were used. The cartilaginous and much of the bony external ear canal were removed to better view the surface of the TM. The middle-ear cavity was opened through the facial recess to check the normality of the middle-ear ossicles, and then it was re-sealed using silastic ear-canal impression material (Westone Silicone Singles®). The inner ears remained intact and fluid filled. A 1 mm diameter, 10 cm length nylon tube sealed in the eustachian tube channel equalized static middle ear pressure with ambient pressure (Cheng et al., 2010). The lateral surface of the first 5 TMs (TB1 to 5) were sprayed with a thin layer of water-soluble white paint using a modified commercially available airbrush. To ensure the paint layer was both thin and uniform, the airbrush was set to generate the finest particles while the sample was placed >30 cm away from the airbrush. The surfaces of the last 3 TMs (TB 6

to 8) were not painted because of the increase in reflected light produced by the 200 mW laser source.

2.2. Experimental equipment and measurements

A detailed description of the high-speed displacement and multi-wavelength shape measurement equipment has already been published (Razavi et al., 2018, Tang et al., 2019). A schematic of the digital holographic system used in the multi-angle shape method is shown in Figure 1. The beam of a single wavelength (532nm) 200 mW laser source is divided into reference beam (blue) and object beam (green) by a tunable beam splitter. A mirror mounted on a piezoelectric actuator (PZT mounted mirror) modulates the length of the reference optical path by multiple wavelengths of the light. A motorized rotating mirror in the object path changes the illumination angle for shape measurements, and an expansion lens spreads the object beam to illuminate much, if not all, of the TM surface. An imaging lens collects the scattered wavefront from the object. The reflected object wavefront and the expanded reference wavefront are combined by the wedged beam splitter in front of the High-speed camera (PhotronSAZ). A speaker (SB Acoustics SB29RDNC-C000-4) provides the sound stimulus to the sample, and a piezo-electric microphone (Knowles FG-23329-P07) monitors the acoustic stimulus within 4 mm of the center of the TM. The single frequency laser described here produced significantly more incident power than the tunable laser (10 mW) used in previous shape and motion measurements (Razavi et al., 2018, Tang et al., 2019). The increased optical power increased the power reflected from the human TM and permitted shape and vibration displacement measurement without applying paint to the TM surface in the 3 TBs whose shape was measured in this manner.

2.2.1. Holographic shape measurements: Theory and implementation

We applied the previously described multi-wavelength method (Razavi et al., 2018, Tang et al., 2019) to measure the shape of painted TMs in TB1-5. Using this method, the shape of the TM, described by its relative depth at varied (x,y) , $z(x,y)$, is related to that of a flat surface with a measured optical phase difference $\Delta\gamma_c$ introduced by changing the wavelength of the illumination in the following equation:

$$z(x,y) = \frac{\Lambda}{4\pi} \Delta\gamma_c(x,y) \quad (1)$$

Where Λ is the synthetic wavelength produced by the interference of the multiple wavelengths, and x,y describe the two-dimensional surface of the camera backplane.

In TB6, 7 and 8, we applied a fixed-wavelength multi-angle method (Psota et al., 2020) to measure the relative depth of the surface of the TM, using the following equation:

$$z(x,y) = \frac{dP_m(x,y, d\theta)}{dk(x,y, d\theta)} \quad (2)$$

where $dP_m(x,y, d\theta)$ is the optical phase changes due to the change of the illumination angle $d\theta$. And $dk(x,y, d\theta)$ is the change of the sensitivity vector resulting from the $d\theta$ obtained from a flat surface sample calibration. In both depth determination techniques, a normalization technique defined the plane of the tympanic ring where $z=0$, and all estimates of $z(x,y)$ were converted to distances from that plane (Khaleghi et al., 2016).

The multi-angle measurement method was implemented by rapid, repeated measurements of the interference between the reference and reflected object beam while the angle of illumination was varied. The total measurement sequence took 500 ms; the timing of the sequence is shown in Figure 2. The sequence was built around a 500 ms duration 1.5° rotation (the sloped pink line in Figure 2) of the motorized rotation mirror. During the rotation, at ten evenly-spaced 3 ms long periods, the position of the

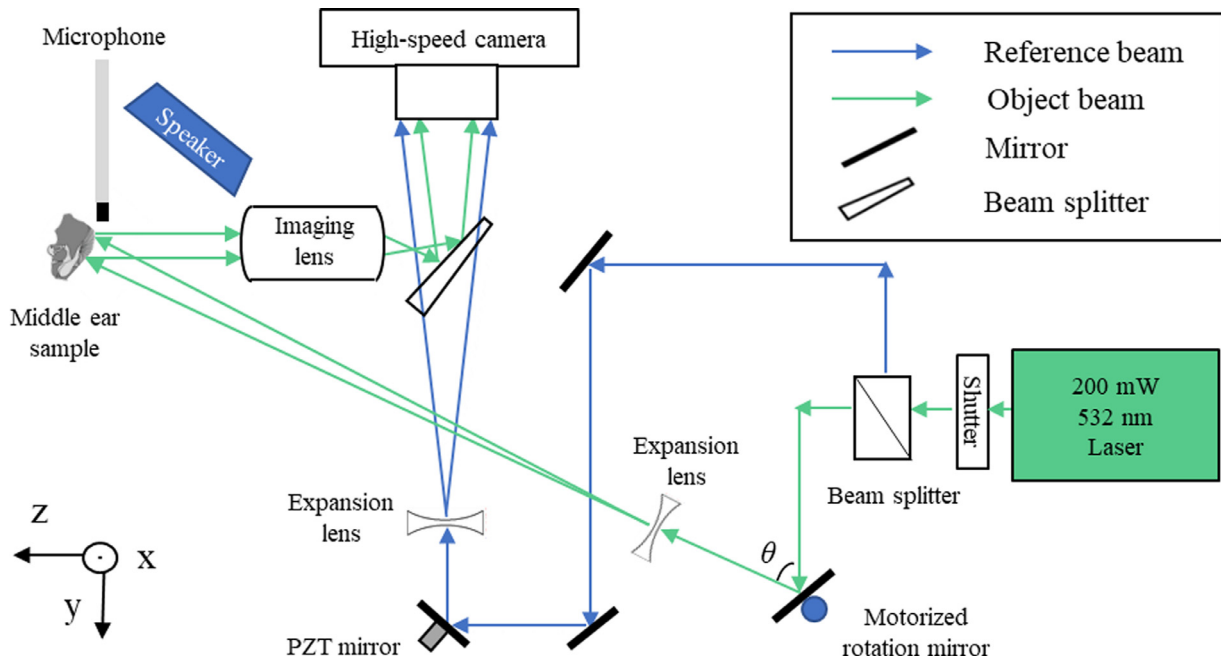


Fig. 1. Schematic of the high-speed digital holographic multi-angle shape and vibration measurement system. During the shape measurement, the illumination angle θ is altered by the motorized rotation mirror. The PZT (piezoelectric ceramic material) positioned mirror is used to shift the phase of the reference beam for shape and displacement measurement (Khaleghi et al., 2016). The middle ear sample is excited by transient click-like sounds produced by the speaker, and the resultant sound pressure near the surface of the TM is recorded by a calibrated microphone sensitive to a broad range of frequencies.

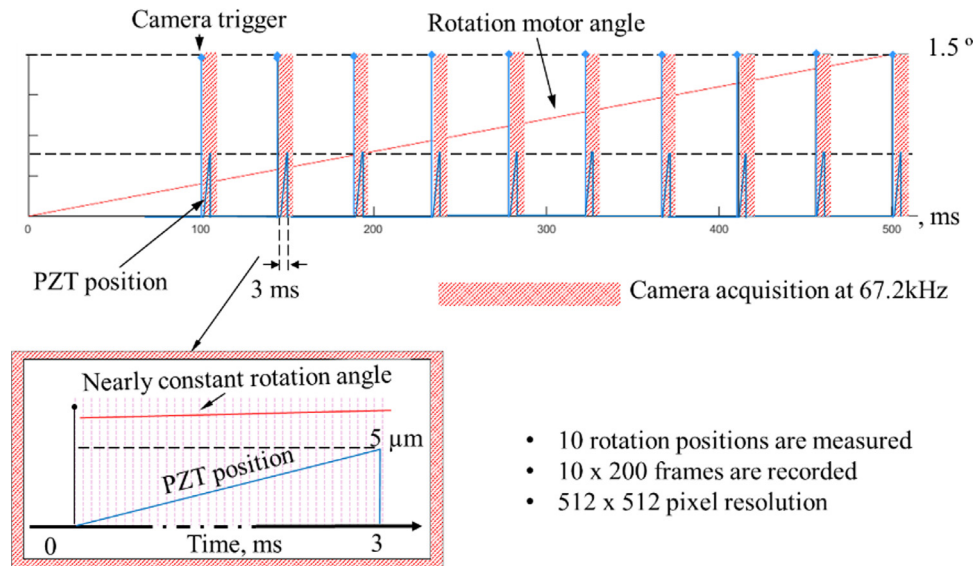


Fig. 2. The timing of a multi-angle shape measurement. Ten interference patterns are defined during a 500 ms duration 1.5° mirror rotation. Each pattern is the result of 200 camera frames captured within 3 ms when the PZT mounted mirror in the reference beam is moved from 0 to $5 \mu\text{m}$. The motion of the PZT supplies the controlled shift in the optical phase necessary to define the interference pattern at each of the 10 instances (Dobrev et al., 2013).

PZT mounted mirror was ramped from 0 to $5 \mu\text{m}$ (the small blue slopes) while the camera collected 200 frames at 67.2 kHz (the regions of pink background). Each of the ten sets of 200 ramp-associated frames defined an optical interference pattern at a different angle of rotation (Dobrev et al., 2013). These interference patterns defined the change in the optical phase at each point in the collected interferograms $dp_m(x, y, d\theta)$ and were used with Eqn 2 to define the relative depth $z(x, y)$ at each of the surface points (Psota et al., 2020). The shape measurement was performed 500 ms after the displacement measurements.

2.2.2. Displacement measurements: Theory and implementation

The generation of displacement-related- interference patterns from high-speed images collected during sound stimulation has been described previously (Dobrev et al., 2013, Razavi et al., 2018, Tang et al., 2019). Figure 3 illustrates the timing of the optical reference and motion measurements with a transient sound stimulus. Each measurement consisted of 1600 frames of continuous acquisition by the high-speed (67.2 kHz) camera – a duration of 23.8 ms. During the initial 3 ms, just prior to stimulus initiation, the PZT mounted mirror moved from 0 to $2.5 \mu\text{m}$ to provide optical phase

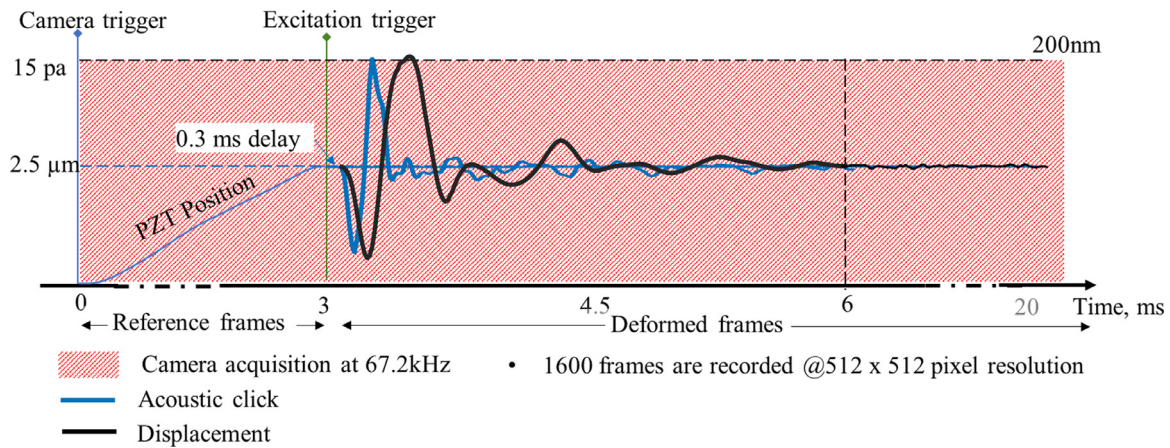


Fig. 3. The timing of the transient displacement measurement. At time 0, the PZT mirror starts to move, reaching 2.5 μm at 3 ms. The high-speed camera records the alterations in the interference between the changing reference beam and reflected light from the stationary TM to define a 90° shift in the reference phase. On completion of the reference sweep, a brief acoustic click is generated by the speaker which reaches the microphone near the TM and induces vibration of the TM after 0.3 ms, while the camera continues to gather images for another 20 ms.

shifted images for use as references in the computation of the optical phase of the deformed TM images (Razavi et al., 2018). The displacement resolution was better than 20 nm.

After the PZT motion was completed, a 50 μs square electrical pulse delivered to the speaker generated an acoustic click. The level of the pulse was chosen to result in motions that were large enough to produce a significant number of interference fringes, but small enough that the fringes were easily resolvable. About 0.3 ms after the pulse, the acoustic click propagated to the TM surface and induced a transient vibration of the TM. The TM displacement from one pixel near the center of the image is plotted in black in Figure 3. The sound-pressure stimulus measured by the microphone is plotted in blue.

2.2.3. Computation of surface normal displacements from shape and motion measurements

Previous measurements (Khaleghi et al., 2016) have demonstrated that much of the sound-induced motion of the TM can be explained by motion vectors that are normal to the TM surface. We combined our nearly coincident measurements of TM shape and displacement to derive the surface normal displacement at each measurement point. The deformation of a point $S(x, y, t)$ on the surface along the surface normal direction of the sample is described by:

$$S(x, y, t) = \frac{\Delta\phi(x, y, t)}{\mathbf{K}(x, y) \cdot \mathbf{n}(x, y)} \quad (3)$$

$\Delta\phi(x, y, t)$ is the optical phase change due to the deformation of the TM. Vector K is the sensitivity vector of the holographic system, which is calculated based on the geometry of the optical setup to compensate for the near field effect due to the close placement of the the sample and camera. The vector n is the unit surface normal vector of the sample which is obtained from the shape measurement (Khaleghi et al., 2016).

2.3. Description of the motion at each measurement point

2.3.1. Frequency response function

The frequency response function (FRF) is a quantitative representation of the output spectrum of the TM's transient motion to a broad-band acoustic stimulus like a click that can be used to characterize the broad-band dynamics of the TM. In our measurement, we measured the full-field transient displacement of the entire surface of the TM $S(x, y, t)$, which allows us to compute the

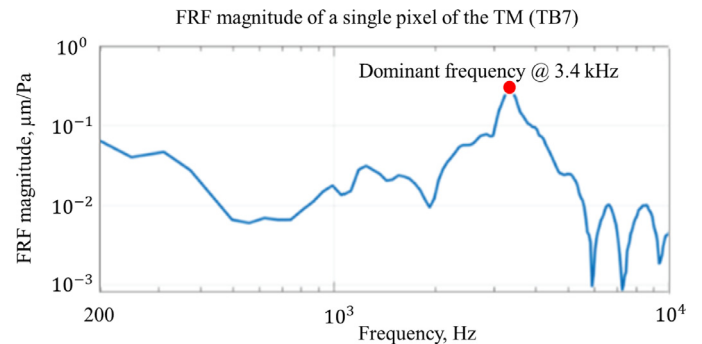


Fig. 4. The FRF magnitude of a single pixel of the TM (TB7).

FRF at all measured (x, y) points. At each point, the FRF is calculated by the ratio of Fourier transforms of the surface-normalized displacements $S(x, y, t)$ and the stimulus sound pressure $p(t)$:

$$FRF(x, y, f) = \frac{FFT(S(x, y, t))}{FFT(p(t))} \quad (4)$$

where FFT presents the Fast Fourier Transform, t is the time and f is the stimulus frequency. Figure 4 shows an example of the frequency-dependent magnitude of an FRF measured at a single point on the TM surface in TB7. The magnitude is scaled in μm/Pa. The red dot marks the Dominant Frequency, 3.4 kHz, where the magnitude of the FRF is maximum.

2.3.2. Impulse response function

The impulse response function (IRF) of the TM is obtained by taking the Inverse Fast Fourier Transformation (IFFT) of the FRF measured at each point on the TM as shown in equation (5)

$$IRF(x, y, t) = IFFT[FRF(x, y, f)] \quad (5)$$

An example of an IRF is illustrated in Figure 5. Based on the IRFs of the TM, we developed the following quantitative analyses to gain insight into TM mechanics.

2.3.2.1. Root mean square of the impulse response. The Root-mean-square of the IRF (x, y, t) at each TM location, $IRMS(x, y)$, is derived by calculating the RMS of the first 3 ms of the IRF at each location. The 3 ms threshold is based on the observation that in most cases the TM impulse response converges to zero before 3 ms.

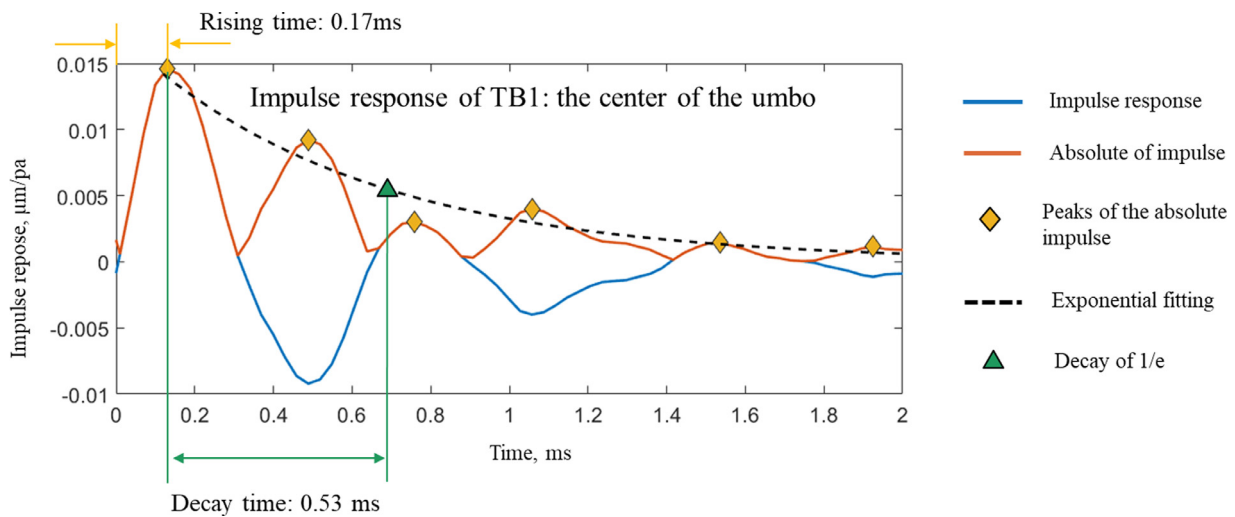


Fig. 5. Reconstructed $IRF(x,y,t)$ (in blue) of a single point at the center of the umbo in TB1. The yellow arrows at the top left of the plot describe the rising time t^R , the time to the first peak of the IRF. The orange line is the absolute value of the IRF. The peaks of the orange line (marked in orange diamonds) are fit by an exponential decay function. The green triangle and line mark the time constant of the fitted exponential decay (the exponential decay time t^D of the IRF).

2.3.2.2. Rising time of the IRF. The rising time at each TM location $t^R(x,y)$ is the time required for the $IRF(x,y,t)$ to reach the first peak (marked by the yellow arrows in Figure 5).

2.3.2.3. Exponential decay time. The exponential decay time at each TM location $t^D(x,y)$ was based on a fit of the exponential function $[a e^{bt}]$ to a series of points in time described by the successive peaks (the yellow diamonds in Figure 5). of the first 2 ms of the absolute value of the $IRF(x,y,t)$. The first peak in the series was the maximum in the $IRF(x,y,t)$. The decay time is the time ($t^D = -1/b$) when the fitted exponential reaches $1/e$ (~36.8%) of the maximum displacement.

2.4. Two-dimensional maps of the motion parameters

Our basic analysis results were two-dimensional (2D) maps of the measured and computed motion parameters. Maps of the RMS value of the raw displacements at each x and y position are illustrated on the left in Figure 8. As our camera records a square of 512×512 pixels, which included the elliptical TM area, we needed to define the edges of the TM and also identify the location of the umbo and manubrium within the square of pixels. This was done with the aid of the raw RMS displacement maps. Since the bony ear canal outside the TM surface has zero motion, the edges of the TM can be defined by the sudden drop of the RMS displacement value. Also, the umbo and manubrium are known to have smaller motions compared to most of the TM surface (Rosowski et al., 2009, Khanna and Tonndorf, 1972, Khaleghi et al., 2014, Khaleghi et al., 2016), and the outline of the umbo and manubrium can be identified by lower RMS values. Once the edges were determined and the umbo and manubrium were identified, the various measured parameters described above were then quantified on each TM surface map with a color-coded magnitude scale.

2.4.1. Spatially averaged TM response functions

To help us perform quantitative comparisons of the complex and varied 2D patterns of TM motion parameters, we also computed spatial averages of the measured parameters. To compare the total stimulus-induced motion of different TM samples, we use Eqn 6 to define the spatially averaged magnitude of the FRF at each of the spectral frequencies:

$$\text{Spatially average magnitude}(f) = \text{mean}[\text{abs}(FRF(x, y, f))] \quad (6)$$

where the *abs* function describes the magnitude of a complex argument and *mean* is the 2D averaging operator. Only points determined to be on the TM surface were included in the average. We also applied 2D-averaging to different fractions of the TM area. For example, we have defined the average of parameters in different quadrants of the TM, and over the umbo and manubrium (More details are included below).

3. Results

3.1. Shape results

The 3D shape measurement results from eight fresh cadaveric human TMs are shown in Figure 6, with a depth resolution of less than 0.15 mm. The shape results are spatially filtered via 5 by 5 pixel moving average filter to remove any discontinuities. All the results are oriented such that the manubrial axis of each TM is at 12 o'clock, and the results from right ears are flipped about the vertical axis so that the anterior TM is always on the left. The TM annulus is set at $z=0$ mm, and the medial direction is directed towards the negative z -direction. Within each plot, the spoon-shaped umbo and the more columnar manubrium are outlined in black, the red line runs along the manubrial axis, and the blue line is positioned at the center of the umbo perpendicular to the manubrial axis. All eight TMs show similar conical shapes with a depth of the umbo of about -1.5 mm, consistent with published human TM depths (Decraemer et al., 1991).

In Figure 7, the depth of the TM cone along and perpendicular to the manubrial axis are compared in the 8 TBs. (The lengths of the individual lines are limited by variations in the exposed surface of the TM.) In all 8 specimens the depth of the TM, from the highest point (often above the TM ring) to the center of the umbo, is between 1.25 and 1.75 mm. The depth profiles are generally similar in the different bones, though there are differences. For example, in the bottom plot, the depth (z) of the umbo along the anterior-posterior direction is similar in all TBs, but the distance between the umbo and the anterior rim is much smaller (2 vs 4 mm) in TB4. (This variation in TB4 is also visible in the 3D images of Figure 6). In most specimens, there is a superior-inferior asymmetry where the fraction of the superior-inferior distance (top plot) that is superior to the umbo is about 0.60. There is also anterior-posterior asymmetry, where the fraction of the anterior-posterior distance that is posterior to the manubrium umbo is about 0.55.

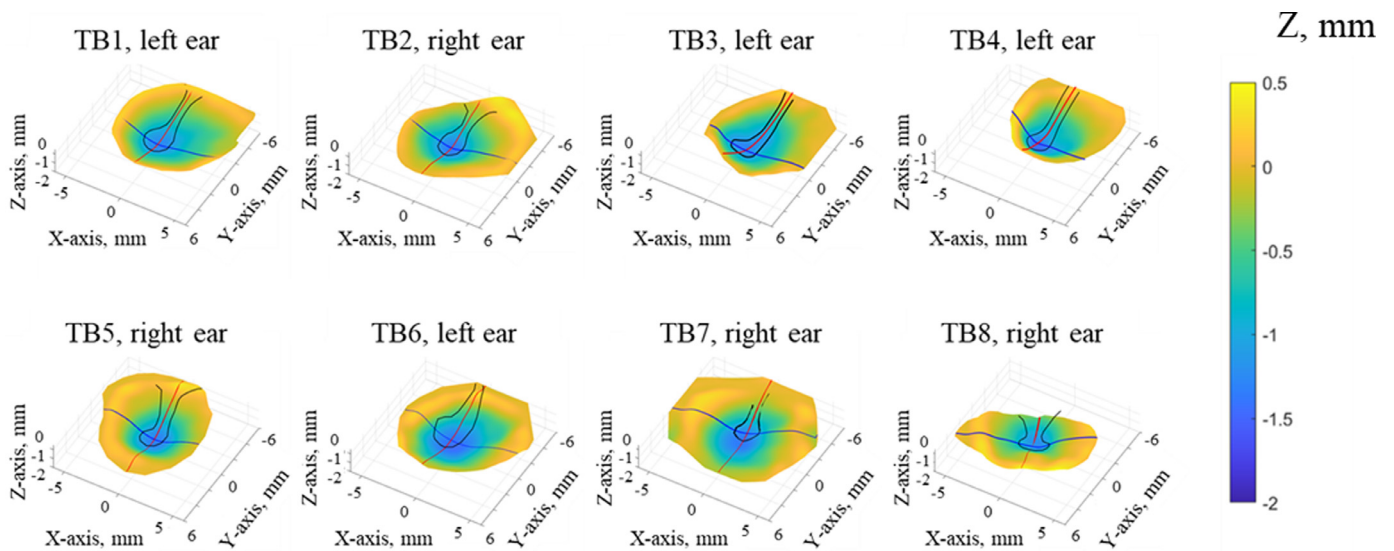


Fig. 6. Shape measurement from 8 TMs. Manubrium and umbo are outlined by the solid black line. Within each TM, a red line is plotted along the manubrial axis and a blue line perpendicular to the manubrial axis at the center of the umbo. The TM shape profiles along these two lines are compared in Figure 7.

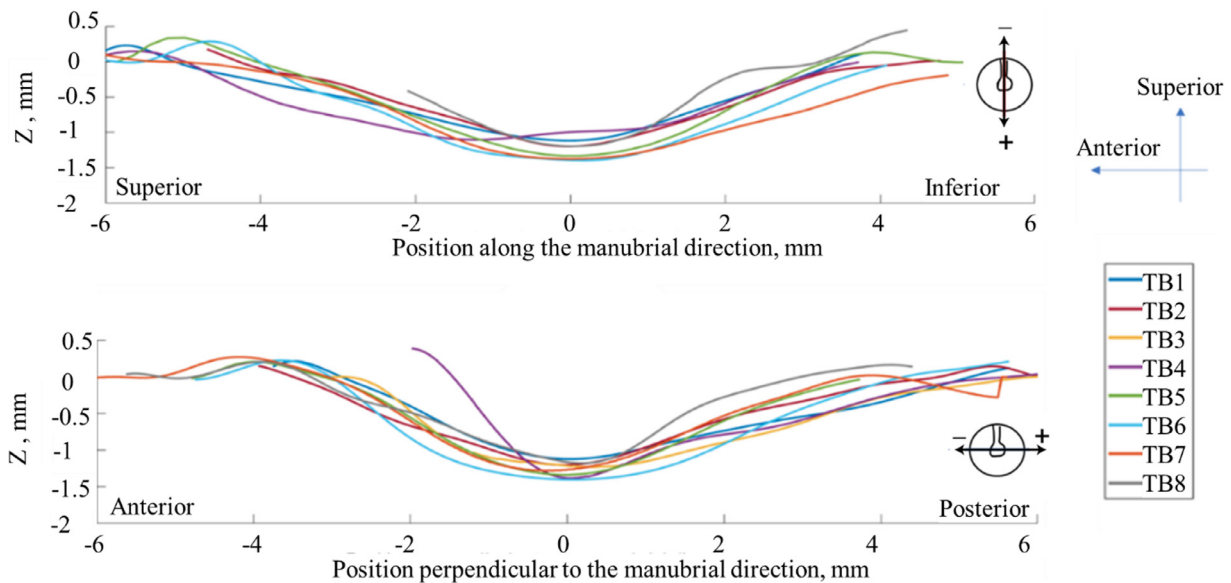


Fig. 7. The relative depth $z(x,y)$ along and perpendicular to the manubrial axis of 8 measured TBs (a) The manubrial axis from superior to inferior. (b) The anterior to the posterior axis. The center of the umbo is at position 0 on both axes.

Associated with this asymmetry is a steeper slope on the anterior side.

3.2. Displacement results

Examples of measured surface-normal displacement data $S(x,y,t)$ from TB1 and TB7 are presented in Figure 8. The left panels (i.a and ii.a) show maps of the RMS of the initial 3 ms of the raw displacement measured at all points on the surface of the two TMs. Panels i.b and ii.b show the measured microphone signals over 3 ms, and panels i.c and ii.c show the displacement waveforms at 5 different points that are marked on the RMS surface maps. The maps and the point data illustrate that the amplitude of motion varies across the TM surface in a complex manner. The point data illustrate variations in the timing of the click-induced displacements and complicated variations in the waveforms of the induced displacements at different positions on the TM surface, including differences in phase, frequency content and the time needed for

the displacement to return to zero. The maps and waveforms illustrate that the umbo and manubrium motions are of lower amplitude than much of the rest of the membrane. Comparison of the top (i.a and i.c) and bottom (ii.a and ii.c) panels demonstrate significant differences in the response of the TMs of TB1 and TB7. The displacement waveforms of TB7 (ii.c) show many more cycles of vibration within the first 3 ms compared to TB1 (i.c). While the measured displacements (maps and waveforms) are of similar amplitude, the microphone measurements display a significant difference in maximum stimulus amplitude (10 Pa for TB1 and 3 Pa for TB7).

3.3. Frequency and impulse response analysis

3.3.1. Spatially averaged frequency response functions

Equation 6 was used to define the spatially averaged FRF of the eight TMs, and the results are presented in Figure 9, with the median spatially averaged FRF plotted in solid black. Figure 9 sug-

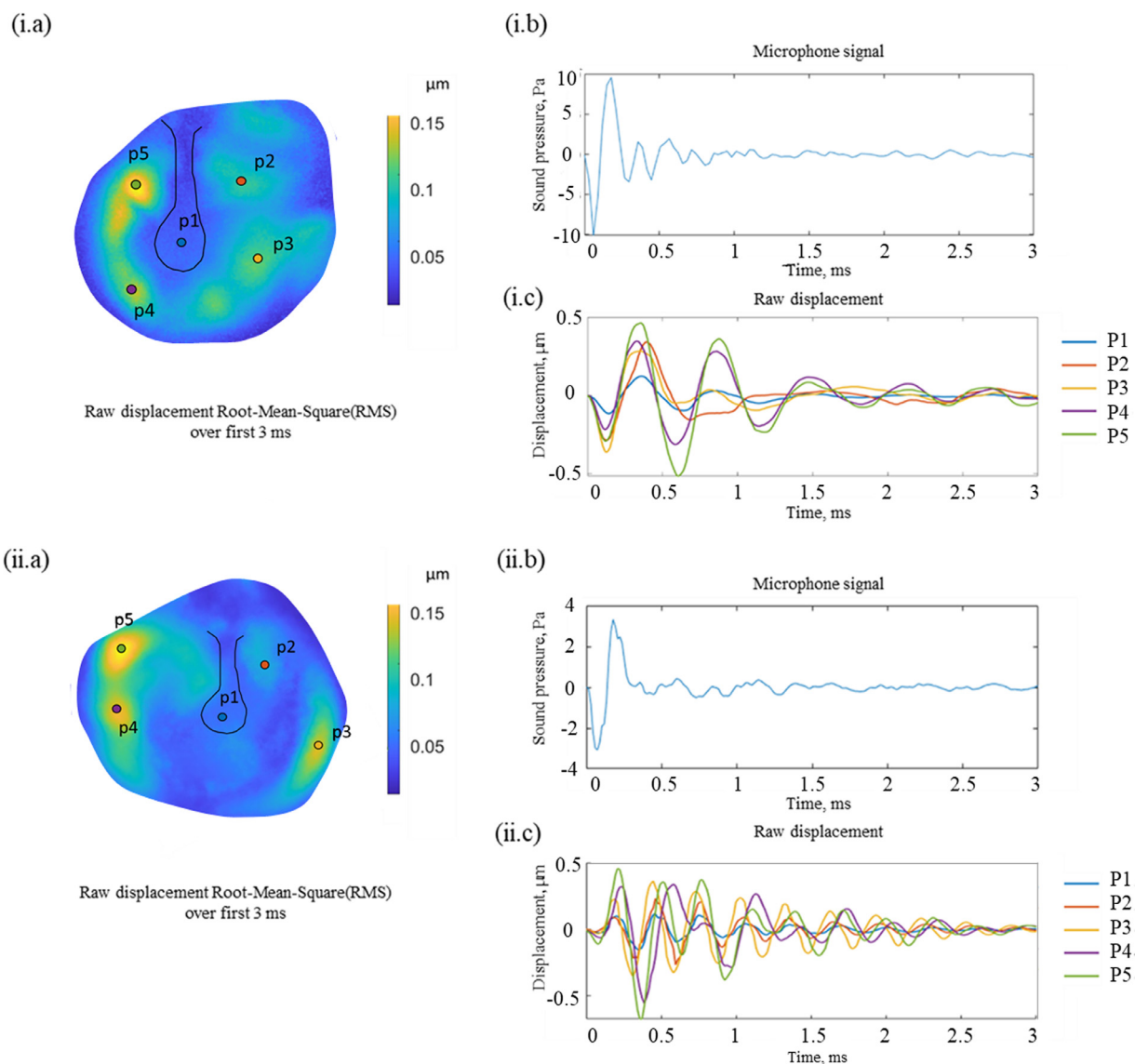


Fig. 8. Measured displacements of TB1 and TB7. The 2D maps on the left show the RMS value of the raw displacements during the first 3 ms. Panels i.b and ii.b illustrate the microphone measurement of the stimulus, and panels i.c and ii.c illustrate the measured surface normal displacement at 5 points on the TM during the 3 ms after stimulus initiation.

gests the FRF varies considerably (by more than an order of magnitude below 2 kHz) across the different bones. Such variation is consistent with large variations reported in LDV measured umbo displacement across subjects (Whittemore et al., 2004).

3.3.2. Representative results from one temporal bone

One set of complete results (the impulse responses, dominant frequencies, IRMS, t^R , t^D and the correlation coefficient of the curve fitting for the decay time calculation) of TB 1 is shown in Figure 10. The dominant frequency map (10a) suggests the umbo has a dominant frequency of 1.7 kHz. There are four areas on the surface of the TM that have dominant frequencies of less than 1.7 kHz. For the rest of the TM, the dominant frequencies are similar. Panel 10b maps the RMS of the IRF (relative to the RMS amplitude at the umbo P1); the umbo has the lowest amplitude (a relative amplitude of 1), and portions of the TM have RMS amplitudes that are 4 to 5 times larger. Panel 10c is the impulse response waveform at the umbo and at the point of maximum RMS within each quadrant. Panel 10d illustrates that the rising time (t^R) varies between 0.1 to 0.2 ms across the TM surface with a value of 0.15 at

the umbo, consistent with the rising time shown in black markers in the impulse responses plot (Panel 10c). Panel 10e shows large variations in decay time (t^D) across the TM's surface, ranging from 0.2 to 1.5 ms. The map also shows spatial clusters in the t^D value, as t^D is a parameter closely related to the mechanical properties of the membrane and the significance of these spatial variations will be discussed later. As the estimation of t^D depends on curve fitting, we also include a map of the correlation coefficient (Panel 10f) between the fit and the data demonstrating high correlations over much of the TM surface. It is worthwhile noting that some of the regions of poorer correlation ($R \sim 0.6$) correspond to regions where the RMS value of the IRF is low.

3.3.3. Grouped maps and spatially averaged responses

We now focus on the individual descriptors of our displacement data in all of the 8 bones. The initial evaluation takes the form of comparisons of the 2D maps. Such comparisons are primarily qualitative. To enable more quantitative comparisons, we used spatial averaging of the data sets to reduce the spatial patterns to a series of numbers. To maintain some of the spatial information in

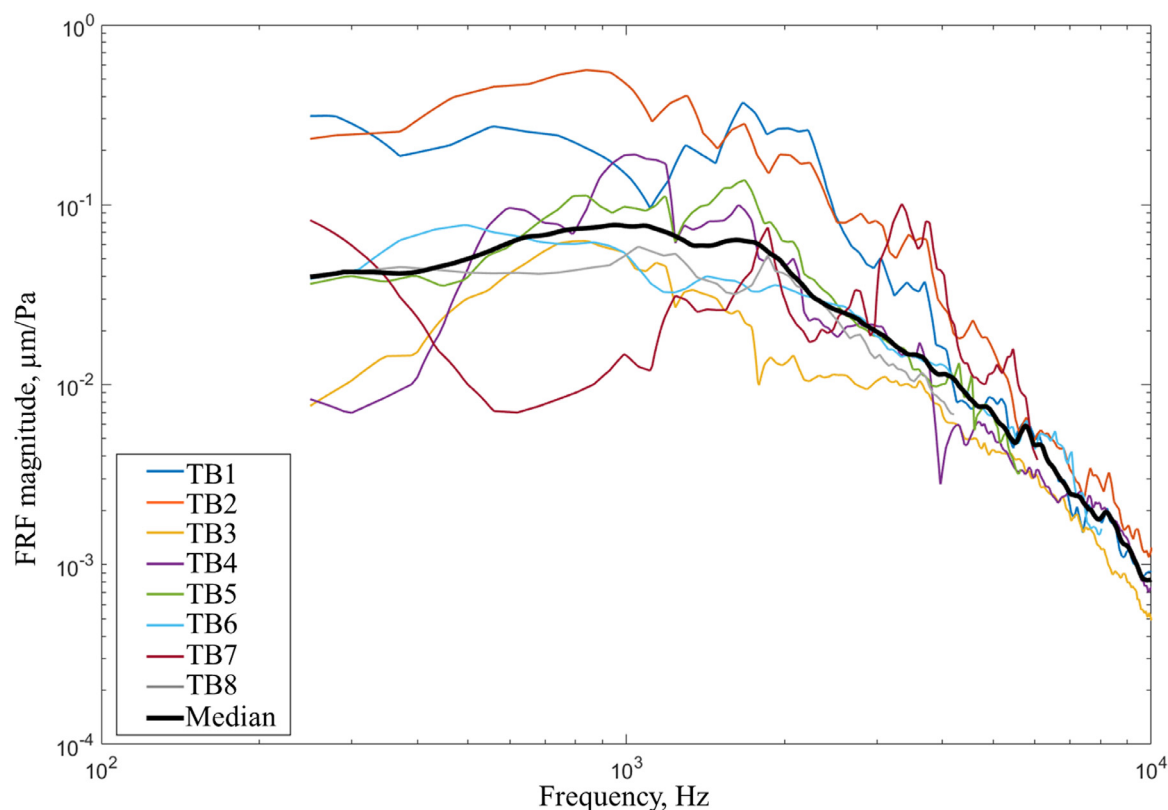


Fig. 9. Magnitude of the surface averaged FRF of 8 TMs. The median of the 8 measurements is plotted in black.

this averaging, we averaged over five separate regions of the TM, as described in the insets of the next four figures. These regions include (R1) the region posterior to the manubrium and superior to the umbo, (R2) the region posterior to the manubrium and inferior to the umbo, (R3) inferior to the umbo and anterior to the manubrium and (R4) superior to the umbo and anterior to the manubrium. A fifth region is the area defined by the spoon shape terminal region of the manubrium that includes the umbo.

3.3.3.1. Dominant frequencies and the RMS of the impulse response. Figure 11 (a) shows the maps of dominant frequency from all eight TBs. As mentioned previously, all the right ears are flipped horizontally and rotated, so the manubrium is at 12 o'clock and anterior is to the left. While TB7 shows relatively higher dominant frequencies (~ 3.6 kHz on a majority of the TM surface), the rest of the TBs have large sections where the dominant frequencies range from about 500 Hz to 2 kHz. The pattern of the dominant frequency distribution across the TM surface varies significantly across the bones. Figure 11 (b) shows the spatially averaged value of the 4 quadrants (area R1 to R4) and the manubrium and umbo of each bone. Many of the quadrant averaged dominant frequency values vary between 0.5 and 2 kHz and are reasonably approximated by the median value from the 8 TBs (the blue line in the plot). However, TB7 shows dominant frequencies that are significantly higher (between 3 and 3.5 kHz). Excluding TB7, our analysis suggests the tuning of the TM is similar across the surface of individuals and between individual TMs.

Figure 12(a) shows maps of the ratio of $IRMS(x,y)$ normalized to the umbo. In many of the specimens, we see that much of the area of the TM moves more than the umbo (relative magnitudes >1), though there are regions where the umbo normalized IRMS is less than 1 (this is particularly true in TB5 and TB8). Figure 12(b) shows the quadrant and umbo averaged values for 8 bones and their median value. These averages vary between 0.7 and 2.8. As noted

above TB5 and TB8 show average IRMS values that are smaller than the umbo (except for R3 in TB5), while the average quadrant averaged IRMS in TB1 and TB6 are some of the largest with values of 2 or larger. While the medians of the quadrant averages are relatively stable (between 1.1 and 1.6), the individual quadrant averages do vary about the median (total range of 0.7 to 2.7).

3.3.4. Rising time and decay time

Figure 13(a) shows maps of t^R , the rising time of the impulse response, and Figure 13(b) shows the quadrant and umbo spatial average values and their medians. The t^R s in TB7 are significantly shorter than those in the other TBs, and by excluding TB7 the t^R values range between 0.12 and 0.19 ms. The median value of the rising time is between 0.14 to 0.16 ms, and the umbo has a median t^R that is 0.02 to 0.03 ms longer than the 2 anterior quadrants (R3&4). Region R2 (the posterior-inferior quadrant) in TB4, 6 and 8 have t^R values larger than that at the umbo.

Figure 14 displays maps of the decay time t^D computed from the exponential curve fitting to the peaks in the IRFs along with the quadrant and umbo averaged values. The spatially averaged quadrant and umbo values from all the results range from 0.2 ms to 1.5 ms, while the median values of each area are between 0.46 to 0.6 ms. The decay times in TB4 are significantly longer than in the other ears. In quadrant R2 TB4 and TB6 have an overlapped decay time of 0.9 ms. The median t^D at the umbo is shorter than that of the quadrants, and in general, the t^D at the umbo is shorter than that observed in at least 3 of the four quadrants. Since decay time is inversely related to the damping in a system, the shorter t^D at the umbo may be related to the direct load from the cochlea and ossicles at the umbo, and any variation in the t^D across the four quadrants may be related to spatial differences in the damping within the mechanical properties of the TM itself. Maps of the correlation between the fitted exponential and the fitted data are included in Appendix A. These maps illustrate that the exponential

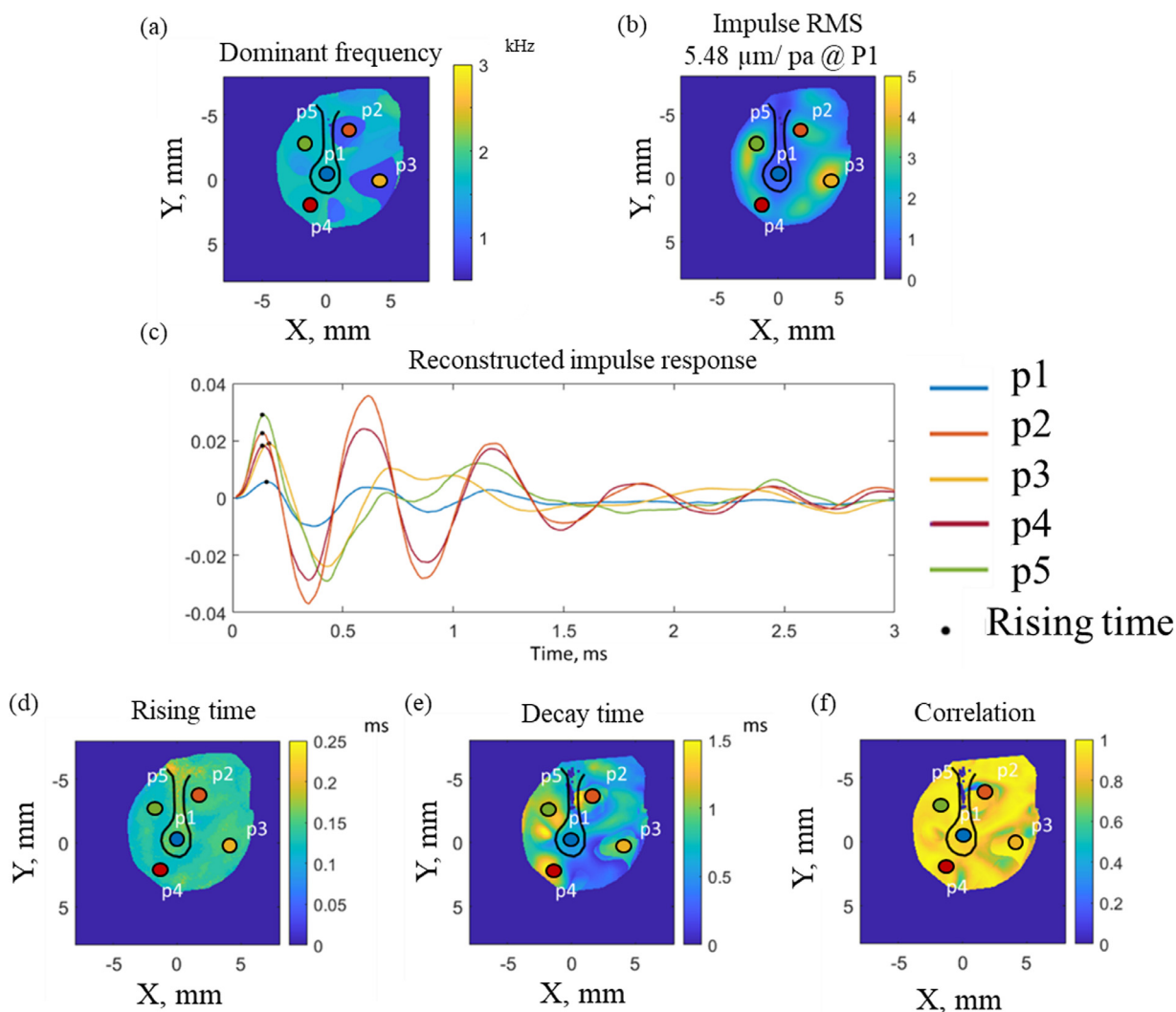


Fig. 10. Frequency and impulse analysis results of TB1:(a) dominant frequency map, (b) impulse RMS response map, the RMS values of the impulse response are normalized by their umbo value, and the colorbars show the ratio to the umbo value, (c) individual impulse responses of selected six points on the TM surface (marked by points in each of the maps). P1 is the umbo, and the other points are placed in each of the four quadrants of the TM. The dots on the IRFs mark the time to the first response maximum t^R . (d) rising time map, (e) decay time map, and (f) correlation coefficient of the decay time.

fits were highly significant $R > 0.85$ over most of the TM surface. However, there are isolated regions of the TM where the correlation value is lower. Whether the decrease in correlation is due to small motion amplitudes in those locations (as suggested from Figure 10), a need for a more complicated description (e.g. multiple exponentials) of decay time, or something else is not clear.

4. Discussion

We used a newly developed high speed holographic system to quantify both the shape and acoustic click induced full-field transient responses of the human TM within a few seconds of time. We performed frequency and impulse analysis on the measurement results to describe the function of the TM for sound transmission, with several parameters that have not been described before, including dominant frequency, rising time, and decay time.

4.1. Effect of painting the TM on the shape and displacement measurements

Our measurements were done on 5 painted and 3 unpainted TMs. To evaluate the effect of painting the TM on its response

and shape, we compare the shape measurement results and the spatially averaged FRF in the painted and unpainted samples. Figure 15(a) and (b) compare the mean and standard deviations of the depth of the TM along our two orthogonal axes. The shapes of the painted TMs are illustrated by the solid black line, and shapes of the unpainted TMs are illustrated by the dashed blue lines. The center of the umbo is set at zero along the x-axis, and the annulus of the TM is set at zero in the Y-axis. The overall shapes of the painted and unpainted TMs are similar, with a similar level of standard deviation (less than ± 0.25 mm). Please note that in Figure 15(b), the mean shape of the unpainted TMs shows a sharp increase at the position of -2 mm, because of the decreased length and much different depth of TB4 along the anterior-posterior axis (Figure 9b). The comparison suggests that the thin layer of paint applied to increase the TM's reflectivity has little effect on the measured shape.

Figure 16 compares the median and range of surface averaged magnitudes of FRF of painted and unpainted specimens. At frequencies less than 2 kHz, the unpainted median FRF is lower in magnitude. At frequencies between 3 and 7 kHz, the median spatially averaged FRF of the unpainted TMs is of higher magnitude. The small number of individuals in each group complicates sta-

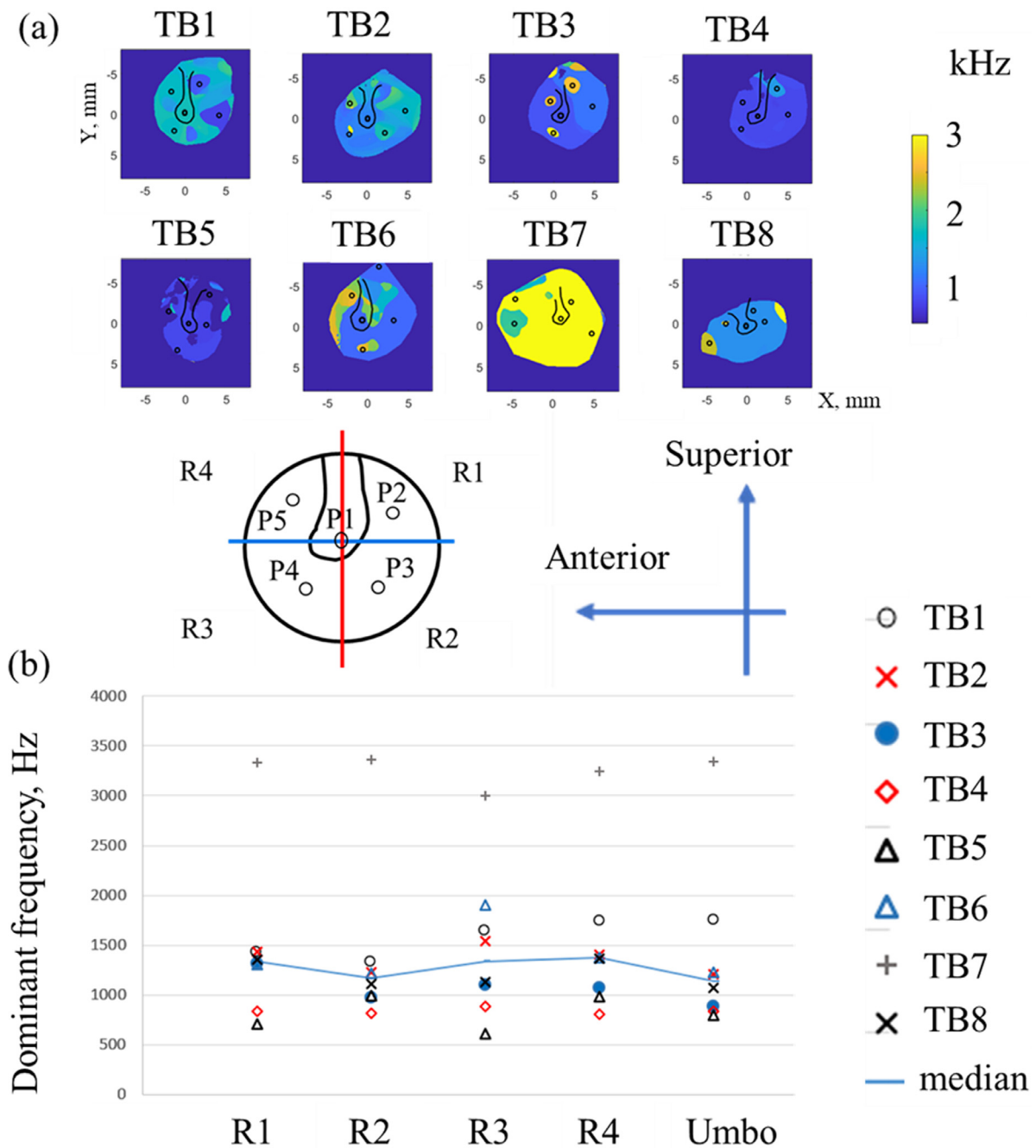


Fig. 11. (a) Dominant frequency maps of TB1 to TB8. (b) the four quadrants and umbo averaged value and their median value.

tistical analyses. However, the less than a factor of 3 (10dB) difference of the medians in the two groups is well within the ± 10 dB range of individual differences observed by (Whittemore et al., 2004) from LDV measurements.

4.2. Comparison of our shape measurements with other published results

Our shape measurements have features in common with other human TM shape measurements made in small numbers of specimens using holographic techniques, including phase-shifted holography (Khaleghi et al., 2016) and moire interferometry (Decraemer et al., 1991, Dirckx and Decraemer, 1997). All show depths of the TM cones that vary between 1.25 and 2.25 mm, with similar 8-9 mm diameters. All also show asymme-

tries in the cone shape, including larger superior fractions of the anterior-superior distance, as well as larger posterior fractions of the anterior-posterior distance. The steeper anterior slope is also in common. Similar features are observed in the shape of the TM of chinchillas (Rosowski et al., 2013) and gerbils (Von Unge et al., 1995).

4.3. Comparison of our displacement results with published umbo displacements

Figure 17 compares the mean value of 8 averaged surface FRFs and the mean value of 8 averaged umbo FRFs from our results with the mean umbo response published by Gan et al. 2004. In Gan's results, the umbo response peaks at around 1 kHz and decreases with a slope of near $-40\text{dB} / \text{decade}$ as frequency increases. Our

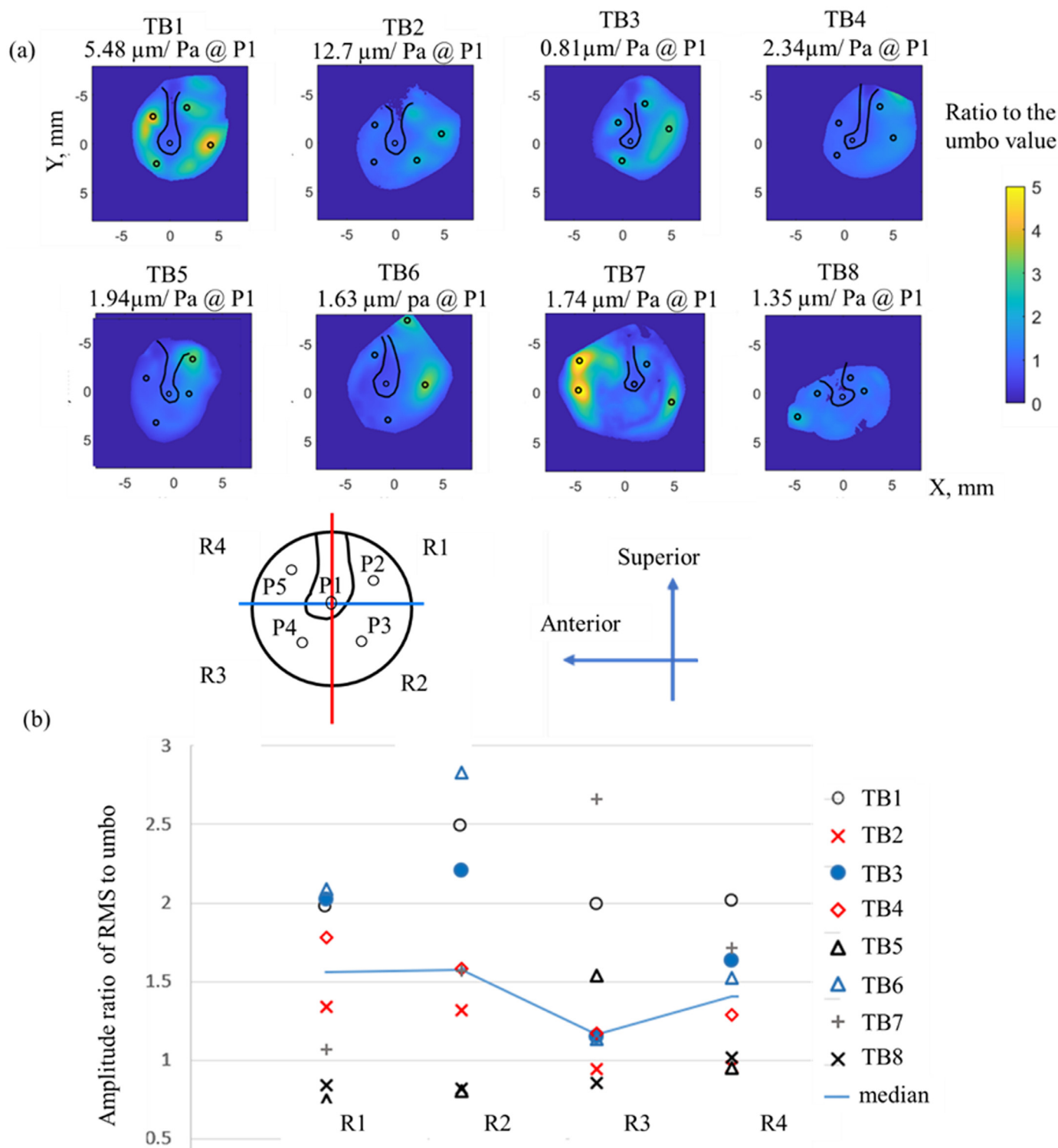


Fig. 12. (a) Amplitude ratio of the RMS of first 3 ms of the calculated impulse response. The IRMS maps are normalized by the value at the umbo, and the colorbar shows the ratio to the umbo value. (b) The four quadrant averaged values and their median.

results show the averaged surface and averaged umbo have similar decreasing trends, though the peak in our umbo and spatially averaged FRFs occur at about 1.5 kHz. Consistent with previous observations that significant sections of the TM move more than the umbo (Cheng et al., 2019), the mean of our averaged umbo FRF is generally ~20% lower in magnitude than the mean averaged surface FRF.

4.4. New insights into the role of the TM in sound transmission

The maps of the dominant frequency and the quadrant analysis of Figure 11 illustrate spatial variations and inter-specimen differences in dominant frequency where the median value is about 1.25 kHz (with TB7 as an outlier). The dominant frequency is a measure of the tuning of the TM to a broad-band stimulus, and it is a com-

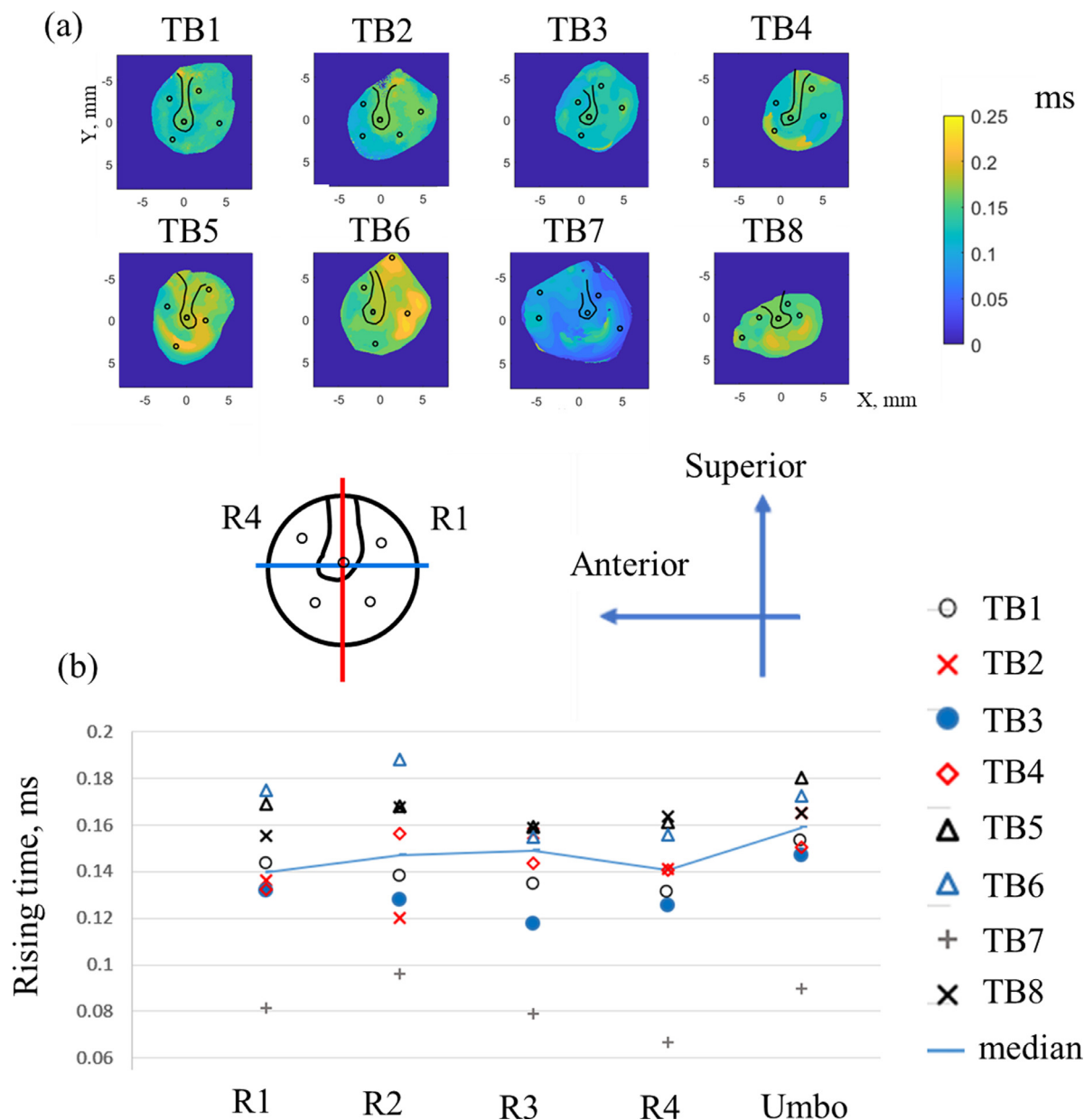


Fig. 13. (a) Maps of the rising time t^R of the reconstructed impulse response of TB1 to TB8, (b) the averaged quadrants and umbo value and their median value.

plex function of the structural features that define the localized modulus and mass of the TM as well as more generalized stiffness and mass due to the material properties of the fibers within the membrane and any tension within those fibers. The spatially varying rising and decay time of the IRF for the different TBs also address TM mechanics, where t^R describes relative delay in the growth of the response along the surface, t^D is inversely related to the magnitude of damping within the TM and the coupled ossicles and cochlea.

Maps of the rising time showed distributions with somewhat regular gradients in t^R (Figure 13a) with a small number of regions of different values. Excluding TB7, the distribution of averaged t^R on the TM surface varied from 0.12 ms to 0.20 ms (Figure 13b), where the rising time at the umbo was slightly longer than at adjacent areas with a typical time difference of 15 to 25 μ s. This difference is significantly smaller than the 83 μ s middle-ear delays described for cochlear sound pressure measurements in human temporal bone (Nakajima et al., 2009). It is, however, similar

to the delay between TM and umbo motion in the much smaller gerbil TM (Milazzo et al., 2017). (Milazzo et al., 2017) suggested that the longer rising time at the umbo can be explained by the larger mass of the umbo and manubrium compared to the localized membrane by itself, where the larger mass slows the time to maximum displacement. An alternative hypothesis is that the rising time is the result of a combination of different modal and traveling wave patterns and that the observed umbo lag is due to the superposition of multiple waves acting on the surface of the TM, some of which cancel. In such a model, the cancellation of early waves will occur less often in parts of the TM that are not centrally located.

As will be discussed more later, the decay time t^D can be related to spatial variations in the damping of the TM. Figure 14a points out multiple regions of roughly uniform t^D that are surrounded by discontinuities, as well as large variations in the t^D s observed on the TM surfaces in our sample. Some of the uniform regions coincide to regions of relatively uniform RMS displacement

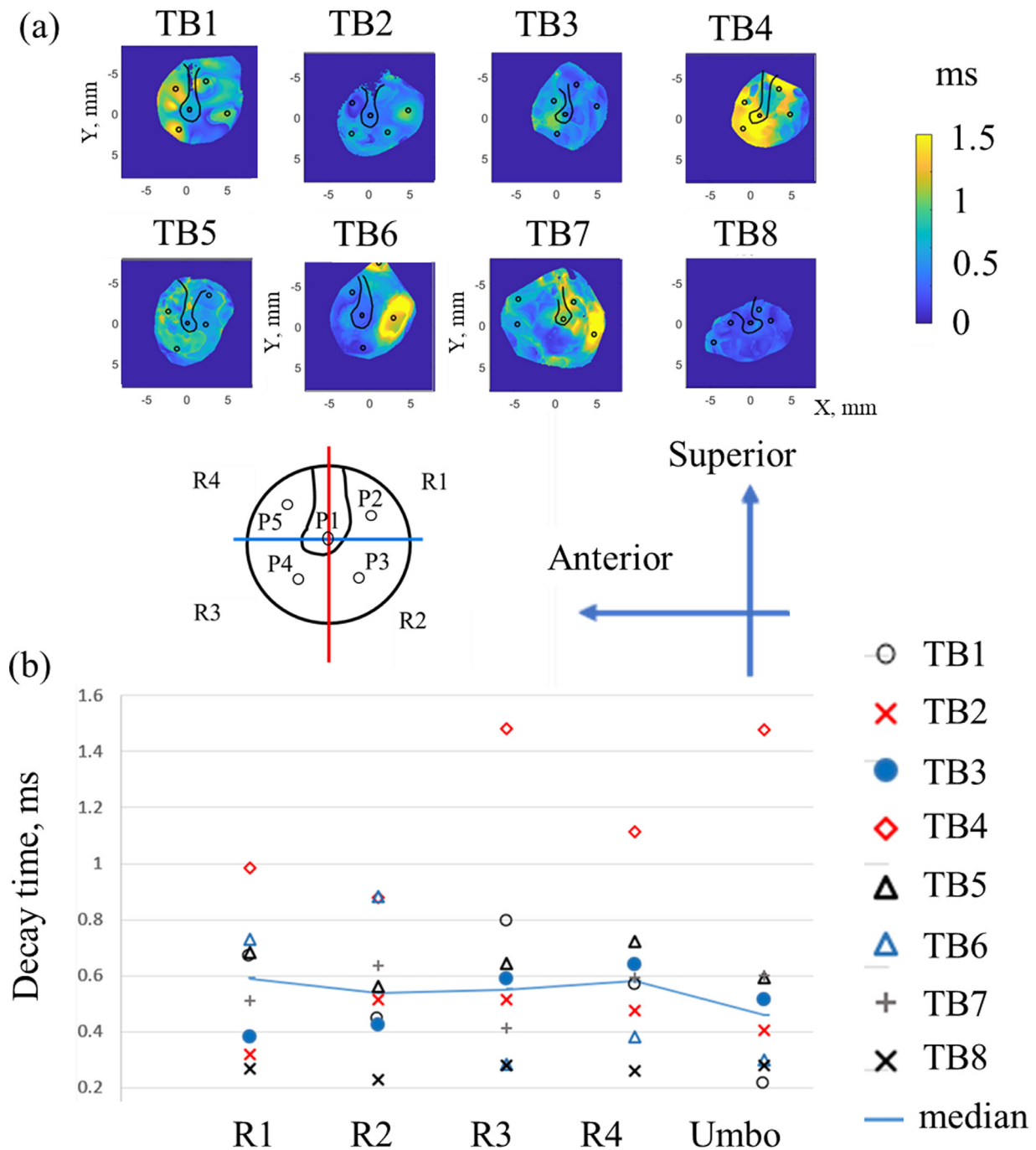


Fig. 14. (a) Maps of the decay time t^D of the impulse response, (b) the quadrant and umbo spatial averages and their median values.

(e.g. TB1, 5, and 6 in Figures 12a and 14a) and the regions of discontinuity are often marked by narrow regions where the correlation coefficient of the exponential fit that describes t^D is small, and may point to narrow regions on the TM surface where the motion is small (Figure 10 and Appendix A). The decay time of the eight specimens ranges from 0.1 ms to 2.5 ms. The longer t^D s point to regions on the surface of the TMs that oscillate more after impulsive stimulation, while shorter t^D s describe regions on the TM surface where oscillations damp out faster. We might expect that some of the shortest t^D s would be associated with the umbo and manubrium where the damping of the ossicles and cochlea should reduce the motion of the TM. However, this is not always the case (e.g. TB 4 and 7 in Figure 14a).

4.5. Estimate of damping of the TM

If we assume a simple second-order mass-spring-damping system, with the measured dominant frequency as the natural frequency of the system, the damping ratio ζ can be estimated from the following equation (Siebert, 1986):

$$\zeta = \frac{\alpha}{\omega_n} \tag{7}$$

The exponential decay rate (α) is the reciprocal of the decay time, and the natural frequency (ω_n) can be approximated by our estimate of dominant frequency. Given those definitions ζ varies across the TM's surface as an inverse function of both the domi-

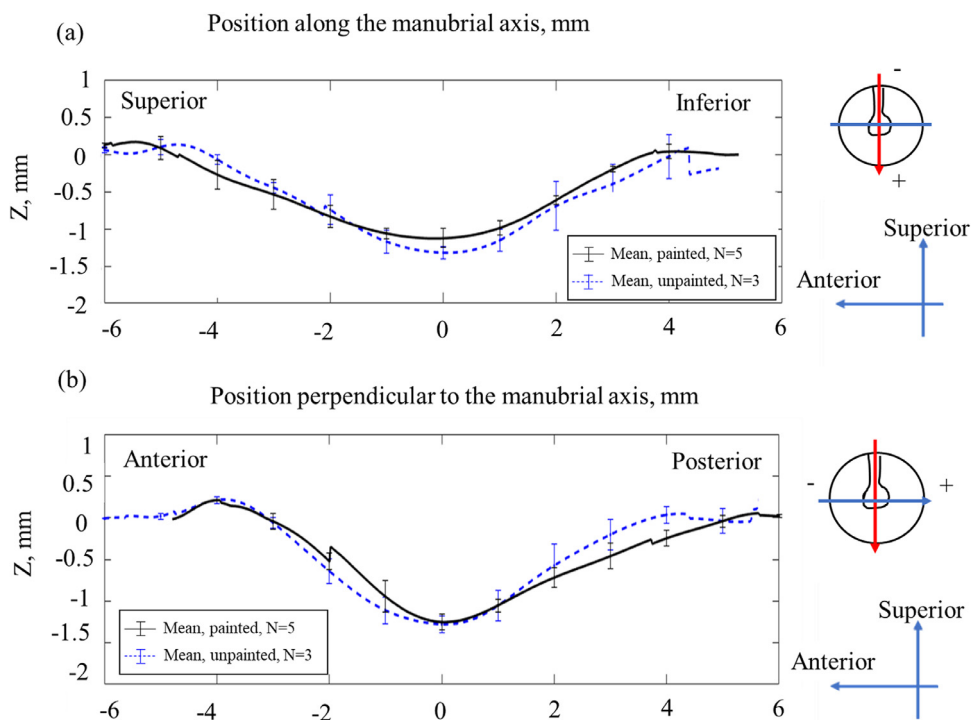


Fig. 15. Mean (\pm STD) position along and perpendicular to the manubrial axis of painted specimens (TB1 to TB5) and unpainted specimens (TB6 to TB8).

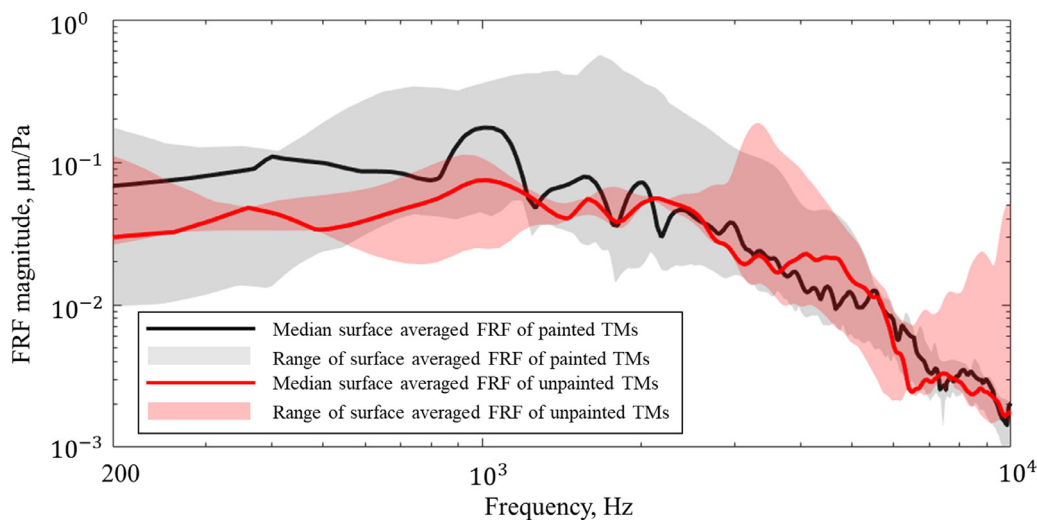


Fig. 16. Median and range of the surface averaged magnitude of FRF of painted specimens (TB1 to TB5) and unpainted specimens (TB6 to TB8).

nant frequency and decay time. Figure 18 illustrates plots of ζ as a function of the dominant frequency (from 500 to 4000 Hz) averaged over the whole TM surface of TB1-8. The spatial distribution of the dominant frequency in each bone varies, but ζ generally decreases from 0.6~0.8 with dominant frequencies < 700Hz (observed in TB1 & 5) to 0.05~0.3 with dominant frequencies > 2.1 kHz (observed in TB3, 6, 7 & 8). Note the damping ratio is derived from the TM's surface motion, but it shows the overall system damping of the middle ear system, including the damping from the mechanical property of the TM material, the ossicles, the middle ear air space and the cochlea. As the damping ratio is one of the least understood mechanical properties of the middle ear, the data of Figure 18 and its spatial distribution of the damping ratio (results are shown in Appendix B) should be of great use to middle-ear theorists and modelers. For example, while previous publications have suggested a frequency dependence in the damping ratio

(Gan et al., 2004, De Greef et al., 2014), none have demonstrated how this parameter might vary across the surface of the TM.

5. Conclusion and future works

In this paper, we describe new procedures to perform high-speed holographic shape and transient displacement measurements that are completed in a few seconds. Shape measurements show 7 of the 8 TBs have very similarly shaped TMs (except for TB 4) with less than 0.3mm of variation in TM depth vs. position. Displacement results in the time domain (Figure 8) show we can distinguish spatial differences in the amplitude and frequency of the displacement response as well as variations in the timing of the motion in different areas. We also applied frequency and impulse response analysis to the measured motions normalized by the sound stimulus. These analyses point out significant spatial dif-

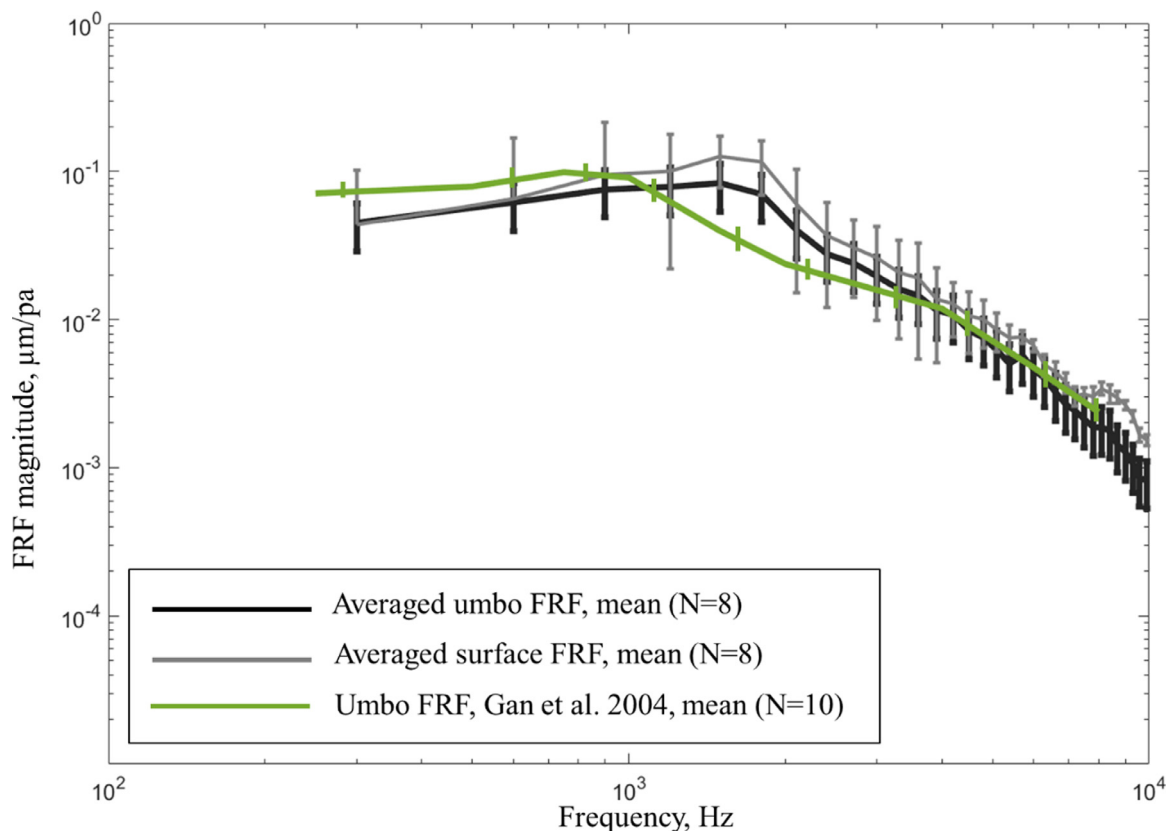


Fig. 17. Comparison of averaged umbo and surface FRFs (normalized by sound pressure) with the pressure normalized umbo motion from Gan et al. 2004 (Gan et al., 2004). Mean(\pm SE) magnitudes are plotted and compared.

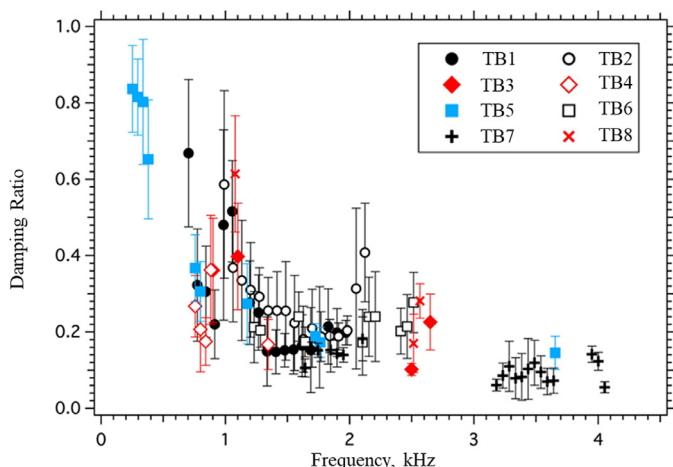


Fig. 18. Plots the mean and standard deviation of the frequency dependence of the damping ratio from all locations on the 8 individual specimens. Each plotted point is an average of the damping ratio at all (x,y) locations with identical dominant frequency in individual TBs, where the number of (x,y) locations that contribute to each plotted plot varies from a few thousand to tens of thousands.

ferences in the motion of different locations on the TM surfaces and illustrate general quantitative similarity across the quadrant averaged values in the different ears. The averaged dominant frequencies and magnitudes of motion are similar to previous reports. The rising and decay time of the impulse response show similarity to other measurements but also result in newly described spatial variations in the damping ratio derived from transient stimulated TM motions, as well as new estimates of the frequency dependence of this important feature of TM mechanics.

In the future, we will apply the same analysis method to TBs in which different pathological conditions are experimentally simulated, including fluid injection to the middle ear cavity, stapes fixation, and IS joint interruption. We hope to identify trends in the data associated with different pathologies that would suggest a clinical utility for our techniques. Artificial Intelligence (AI) and Data Mining can be applied to automate the analysis process. Engineering design to implement a holographic otoscope will be investigated to measure such motions in intact live human ears.

Author contributions

Conceptualization, J.J.R., C.F., J.T.C.; methodology, H.T., P.P.; software, H.T., P.P.; validation, H.T.; formal analysis, H.T.; investigation, H.T.; resources, J.J.R., C.F., J.T.C.; data curation, H.T., writing—original draft preparation, H.T.; writing—review and editing, H.T., P.P., C.F., J.J.R., J.T.C.; visualization, H.T.; supervision, J.J.R., C.F., J.T.C.; project administration, J.J.R., C.F., J.T.C.; funding acquisition, J.J.R., C.F., J.T.C.

Funding

This work has been funded by the National Institutes of Health (NIH), National Institute on Deafness and Other Communication Disorders (NIDCD), grant number R01, DC016079.

Declaration of Competing Interest

The authors declare no conflict of interest.

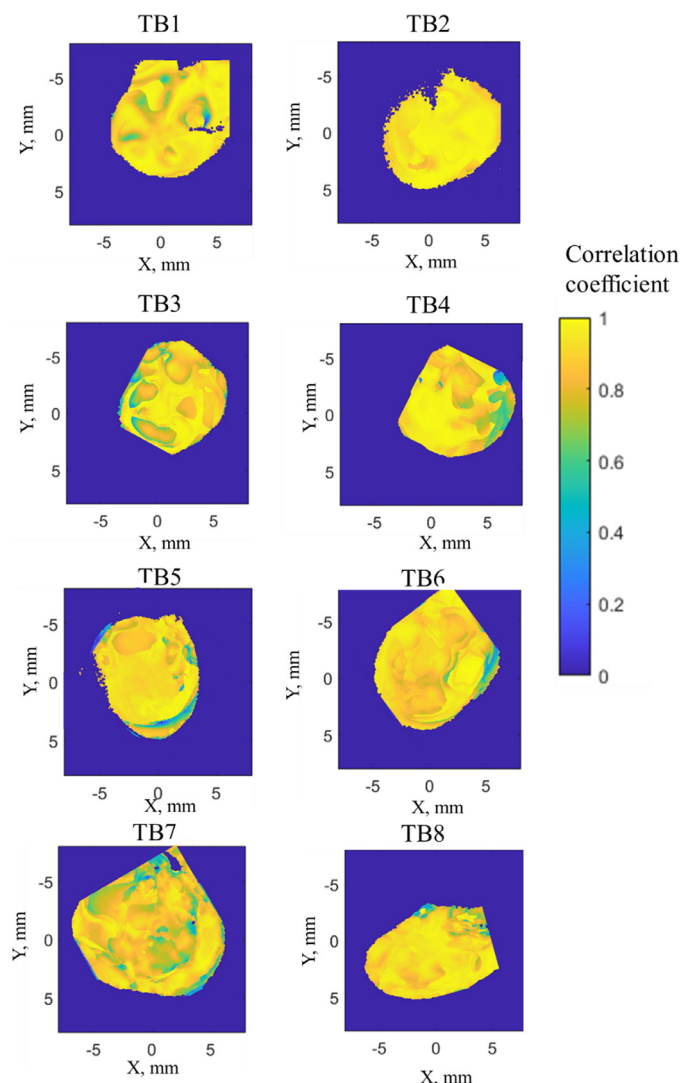


Fig. 19. Correlation coefficients of the exponential fitting for TB1- TB8 colorcoded from 0 to 1.

Acknowledgments

This work is supported by the NanoEngineering, Science, and Technology (NEST) program at the Worcester Polytechnic Institute, Mechanical Engineering Department.

Appendix A. Correlation values for exponential fitting

Figure 19

Appendix B. Damping ratio maps

Figure 20

Reference

Rosowski, J.J., 1994. Outer and Middle Ears,” in Comparative He. In: 4Fay, R.R., Popper, A.N. (Eds.), Mammals. Springer, New York, NYNew York, pp. 172–247. doi:10.1007/978-1-4612-2700-7_6.

Geisler, C.D., 1998. From sound to synapse: physiology of the mammalian ear. Oxford University Press, USA.

Wang, X., Guan, X., Pineda, M., Gan, R.Z., 2016. Motion of tympanic membrane in guinea pig otitis media model measured by scanning laser Doppler vibrometry. *Hear. Res.* 339, 184–194. doi:10.1016/j.heares.2016.07.015, Sep.

Fay, J.P., Puria, S., Steele, C.R., 2006. The discordant eardrum. *Proc. Natl. Acad. Sci.* 103 (52), 19743–19748. doi:10.1073/pnas.0603898104, Dec.

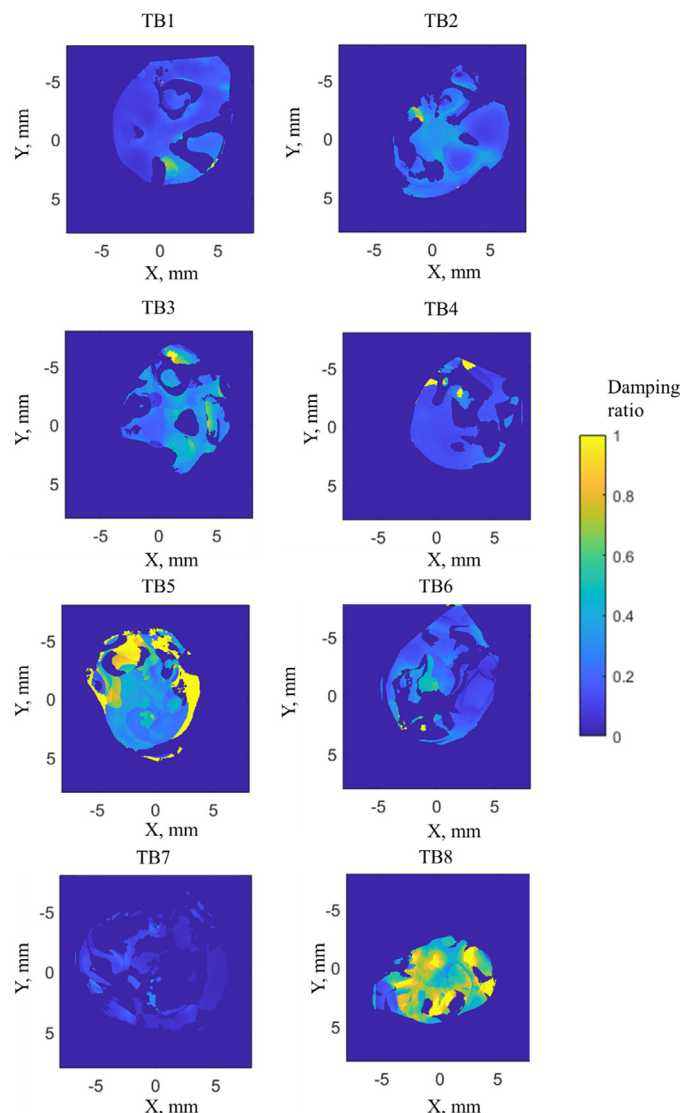


Fig. 20. Damping ratio for TB1- TB8 colorcoded from 0 to 1. TM area with correlation coefficient of the exponential fitting less than 85% are masked out.

Volandri, G., Di Puccio, F., Forte, P., Carmignani, C., 2011. Biomechanics of the tympanic membrane. *J. Biomech.* 44 (7), 1219–1236. doi:10.1016/j.jbiomech.2010.12.023, Apr.

Cheng, T., Dai, C., Gan, R.Z., 2007. Viscoelastic Properties of Human Tympanic Membrane. *Ann. Biomed. Eng.* 35 (2), 305–314. doi:10.1007/s10439-006-9227-0, Feb..

Fay, J., Puria, S., Decraemer, W.F., Steele, C., 2005. Three approaches for estimating the elastic modulus of the tympanic membrane. *J. Biomech.* 38 (9), 1807–1815.

De Greef, D., Buytaert, J.A., Aerts, J.R., Van Hoorebeke, L., Dierckx, M., Dirckx, J., 2015. Details of human middle ear morphology based on micro-CT imaging of phosphotungstic acid stained samples. *J. Morphol.* 276 (9), 1025–1046.

Van der Jeught, S., Dirckx, J.J., Aerts, J.R.M., Bradu, A., Podoleanu, A.G., Buytaert, J.A.N., 2013. Full-Field Thickness Distribution of Human Tympanic Membrane Obtained with Optical Coherence Tomography. *J. Assoc. Res. Otolaryngol.* 14 (4), 483–494. doi:10.1007/s10162-013-0394-z, Aug..

Aernouts, J., Aerts, J.R.M., Dirckx, J.J., 2012. Mechanical properties of human tympanic membrane in the quasi-static regime from in situ point indentation measurements. *Hear. Res.* 290 (1), 45–54. doi:10.1016/j.heares.2012.05.001, Aug..

Rosowski, J.J., et al., 2009. Computer-assisted time-averaged holograms of the motion of the surface of the mammalian tympanic membrane with sound stimuli of 0.4–25 kHz. *Hear. Res.* 253 (1–2), 83–96.

Rosowski, J.J., 1996. Models of external-and middle-ear function. In: *Auditory computation*. Springer, pp. 15–61.

Lim, D.J., 1970. Human tympanic membrane: an ultrastructural observation. *Acta Otolaryngol. (Stockh.)* 70 (3), 176–186.

Khaloghi, M., 2015. Development of holographic interferometric methodologies for characterization of shape and function of the human tympanic membrane Doctoral Thesis. Worcester Polytechnic Institute, Worcester MA.

- Milazzo, M., Fallah, E., Carapezza, M., Kumar, N.S., Lei, J.H., Olson, E.S., 2017. The path of a click stimulus from ear canal to umbo. *Hear. Res.* 346, 1–13. doi:10.1016/j.heares.2017.01.007, Mar..
- Tonndorf, J., Khanna, S.M., 1970. The role of the tympanic membrane in middle ear transmission. *Ann. Otol. Rhinol. Laryngol.* 79 (4), 743–753.
- Khanna, S.M., Tonndorf, J., 1972. Tympanic membrane vibrations in cats studied by time-averaged holography. *J. Acoust. Soc. Am.* 51 (6B), 1904–1920.
- Decraemer, W.F., Khanna, S.M., Funnell, W.R.J., 1989. Interferometric measurement of the amplitude and phase of tympanic membrane vibrations in cat. *Hear. Res.* 38 (1–2), 1–17.
- Goode, R.L., Ball, G., Nishihara, S., 1993. Measurement of umbo vibration in human subjects—method and possible clinical applications. *Am. J. Otol.* 14 (3), 247–251.
- Goode, R.L., Ball, G., Nishihara, S., Nakamura, K., 1996. Laser Doppler vibrometer (LDV)—a new clinical tool for the otologist. *Am. J. Otol.* 17 (6), 813–822.
- Goode, R.L., Killion, M., Nakamura, K., Nishihara, S., 1994. New knowledge about the function of the human middle ear: development of an improved analog model. *Am. J. Otol.* 15 (2), 145–154.
- Gan, R.Z., Wood, M.W., Dormer, K.J., 2004. Human middle ear transfer function measured by double laser interferometry system. *Otol. Neurotol.* 25 (4), 423–435.
- Decraemer, W., Khanna, S., Funnell, W., 1999. Vibrations at a fine grid of points on the cat tympanic membrane measured with a heterodyne interferometer. *EOS/SPIE International Symposia on Industrial Lasers and Inspection, Conference on Biomedical Laser and Metrology and Applications*, 4.
- de La Rochefoucauld, O., Olson, E.S., 2010. A sum of simple and complex motions on the eardrum and manubrium in gerbil. *Hear. Res.* 263 (1–2), 9–15.
- Cheng, J.T., et al., 2010. Motion of the surface of the human tympanic membrane measured with stroboscopic holography. *Hear. Res.* 263 (1), 66–77. doi:10.1016/j.heares.2009.12.024, May.
- Dobrev, I., Harrington, E., Cheng, T., Furlong, C., Rosowski, J., 2013. Digital holographic otoscope for measurements of the human tympanic membrane in-vivo. *Imag. Method Novel Mater. Challeng. Appl.* 3, 39–45.
- Khaleghi, M., Dobrev, I., Harrington, E., Furlong, C., Rosowski, J.J., 2014. Study of the transient response of Tympanic Membranes under acoustic excitation. In: *Mechanics of Biological Systems and Materials*, 4. Springer, pp. 1–9.
- Razavi, P., Tang, H., Rosowski, J.J., Furlong, C., Cheng, J.T., 2018. Combined high-speed holographic shape and full-field displacement measurements of tympanic membrane. *J. Biomed. Opt.* 24 (3), 031008. doi:10.1117/1.JBO.24.3.031008, Sep..
- Tang, H., et al., 2019. High-Speed Holographic Shape and Full-Field Displacement Measurements of the Tympanic Membrane in Normal and Experimentally Simulated Pathological Ears. *Appl. Sci.* 9 (14). doi:10.3390/app9142809, Art. no. 14, Jan..
- Razavi, P., 2018. Development of high-speed digital holographic shape and displacement measurement methods for middle-ear mechanics in-vivo. Dr. Diss. Diss. Years. Mar.[Online]. Available: <https://digitalcommons.wpi.edu/etd-dissertations/80> .
- Psota, P., et al., 2020. Multiple angle digital holography for the shape measurement of the unpainted tympanic membrane. *Opt. Express* 28 (17), 24614–24628. doi:10.1364/OE.398919, Aug..
- Khaleghi, M., Cheng, J.T., Furlong, C., Rosowski, J.J., 2016. In-plane and out-of-plane motions of the human tympanic membrane. *J. Acoust. Soc. Am.* 139 (1), 104–117. doi:10.1121/1.4935386, Jan..
- Decraemer, W.F., Dirckx, J.J., Funnell, W.R.J., 1991. Shape and derived geometrical parameters of the adult, human tympanic membrane measured with a phase-shift moiré interferometer. *Hear. Res.* 51 (1), 107–121.
- Dirckx, J.J., Decraemer, W.F., 1997. Optoelectronic moiré projector for real-time shape and deformation studies of the tympanic membrane. *J. Biomed. Opt.* 2 (2), 176–185.
- Rosowski, J.J., et al., 2013. Measurements of three-dimensional shape and sound-induced motion of the chinchilla tympanic membrane. *Hear. Res.* 301, 44–52.
- Von Unge, M., Decraemer, W., Dirckx, J., Bagger-Sjöbäck, D., 1995. Shape and displacement patterns of the gerbil tympanic membrane in experimental otitis media with effusion. *Hear. Res.* 82 (2), 184–196.
- Cheng, J.T., Maftoon, N., Guignard, J., Ravicz, M.E., Rosowski, J., 2019. Tympanic membrane surface motions in forward and reverse middle ear transmissions. *J. Acoust. Soc. Am.* 145 (1), 272–291.
- Nakajima, H.H., Dong, W., Olson, E.S., Merchant, S.N., Ravicz, M.E., Rosowski, J.J., 2009. Differential intracochlear sound pressure measurements in normal human temporal bones. *J. Assoc. Res. Otolaryngol.* 10 (1), 23.
- Rosowski, J.J., Nakajima, Merchant, S.N., 2008. Clinical utility of laser-Doppler vibrometer measurements in live normal and pathologic human ears. *Ear & Hearing* 29, 3–19.
- Siebert, W.M., 1986. *Circuits, Signals, and Systems*. MIT Press, USA.
- Gan, R.Z., Feng, B., Sun, Q., 2004. Three-dimensional finite element modeling of human ear for sound transmission. *Ann. Biomed. Eng.* 32 (6), 847–859.
- De Greef, D., et al., 2014. Viscoelastic properties of the human tympanic membrane studied with stroboscopic holography and finite element modeling. *Hear. Res.* 312, 69–80. doi:10.1016/j.heares.2014.03.002, Jun..
- Whittemore, K.R. Jr, Merchant, S.N., Poon, B.B., Rosowski, J.J., 2004. A normative study of tympanic membrane motion in humans using a laser Doppler vibrometer (LDV). *Hear. Res.* 187 (1–2), 85–104.

Chapter 9 Frequency and Impulse Response analyses of the Tympanic Membrane Response in Human Middle Ear with Pathologies from High-speed Holographic Measurement

This chapter is prepared as a journal paper intended to be submitted to the Journal of Hearing Research.

Abstract

We have developed a High-speed Digital Holographic (HDH) system to rapidly measure the shape and click-induced transient displacements of the human tympanic membrane (TM). Frequency and impulse response analyses of the transient vibration of the entire TM elucidate new TM mechanical parameters, including the dominant frequency, rising time, decaying time, root-mean-square (RMS) displacement and damping as they vary across the surface of the TM [1,2]. Here, we use the HDH to measure and analyze cadaveric human middle ears with experimentally induced middle-ear pathologies, including fluid injected into the middle ear cavity to mimic otitis media with effusion (OME), stapes fixation and incudo-stapedial (IS) joint interruption. We investigate the effect of these manipulations on TM function and mechanical properties and test the sensitivity and specificity of our measurements to the modelled pathologies.

Fluid behind the TM has a significant effect on the response of the TM. The spatially averaged Frequency Response Function (FRF) displays significant changes in the presence of fluid, as do more spatially localized motion measurements. Stapes fixation and IS joint interruption affect the averaged FRF mainly in the low-frequency range. The averaged motion and mechanical parameters in the four quadrants of the TM and the umbo appear differentially affected by the various middle ear manipulations, and differences in the motion parameters can be used to separate the different pathologies from each other and from normal.

9.1. Introduction

The mammalian auditory system is made up of the outer, middle and inner ear. The first ear structure that vibrates in response to sound is the tympanic membrane (TM), a multi-layer structure that separates the middle ear from the outer ear. The TM transduces the vibration of the air in the ear canal to vibrations of the middle-ear ossicles. Our understanding of TM function comes from 150 years of experimental measurements, observations and modelling. However, that understanding is incomplete. It is now clear that the motion on the TM varies across its surface and that the patterns of surface motion vary from relatively simple modal patterns at low-frequencies to more complicated patterns at middle frequencies to highly ordered multi-modal patterns at high frequencies [18-21]. The best description of this transition in complexity is by Cheng and his co-workers using stroboscopic holography [28,29]. While these observations of frequency-dependent modal patterns reveal some of the complexity and spatial dependences in the TM's response to sound, they do not describe the interactions of the TM's form and function that lead to sound conduction to the inner ear.

Our group has been improving on the holography-based methodologies used in the study of the sound-induced motion of the TM for multiple years [1,2,13,16]. The methodologies we developed improved the description of the TM's response to sound stimuli and provided quantitative evidence to distinguish between various existing TM theories. Our latest development of High-speed Digital Holography (HDH) has the spatial and temporal sensitivity to measure the full-field TM transient response to impulsive sound, thus making it possible to define and analyze the frequency and impulse response of the surface of the TM motion. Our analyses include the definition of new spatially dependent TM mechanical parameters, such as dominant frequency, rising time, decaying time, and damping, which have been described in

normal cadaveric middle ears [2]. Those measurements and analyses provide a baseline for comparisons with measurements in pathological ears.

The responses of the TM to sound are impacted by the condition of the middle ear and inner ear. Several studies have utilized Laser Doppler Vibrometry (LDV) measured umbo displacement to help diagnose middle ear diseases such as ossicular interruption or fixation and separate out semicircular canal dehiscence, an inner-ear disorder [29]. Wideband Acoustic Immittance (WAI), a measure of middle-ear input impedance based on average TM motions, is also employed as a diagnostic aid [30,31]. A significant issue with acoustic-immittance-based techniques is that they are based on the average motion of the entire TM to sound, and spatial variations in the mobility of the TM (e.g., TM regions that are hypermobile due to a poorly healed perforation, or hypomobile due to local sclerotic plaques within the TM) can mask the presence of other pathologies. Holographic measurements directly quantify the displacement of each point on the TM surface and can identify regions with defects in TM mobility. As such, holography should be very sensitive to the presence of middle-ear fluid in contact with the TM since the motion of the TM in response to high-frequency sounds is sensitive to the presence of material in contact with its surface [31].

We have published preliminary results from a limited number of cadaveric ears with experimentally induced middle ear pathologies and described several data analysis methods that differentiate various middle ear pathologies in [1,2]. In this paper, we extend our study to a large number of ears and develop and test new analyses that show promise at detecting middle ear diseases behind the intact TM.

9.2. Methods

9.2.1 Specimen Preparation and Manipulations

This study includes holographic measurements on eight fresh human cadaveric temporal bones. The details of the specimen preparation for holographic measurements can be found in our previous publication [Tang et al. 2021; Chapter 8]. Besides removing most parts of the cartilaginous and the bony ear canal to provide a clear view of most of the TM, we also opened the middle ear cavity through the facial recess to ascertain the normality of the middle ear ossicles. We then re-sealed the recess with silastic filler (Westone Silicone Singles ®). A 1 mm diameter brass tube – inserted through the eustachian tube channel to the bottom of the middle ear cavity – was used to inject saline into the middle ear cavity to mimic otitis media with effusion (OME). The lateral surface of the first five TMs was sprayed with a thin layer of water-soluble white paint using a modified commercially available airbrush, where the paint increased the light reflected from the TM and enhanced the interference between the reference and reflected light. The last three TMs were not painted because an updated laser source with increased power (200 mW) produced enough reflected light to provide well defined interference patterns when combined with the reference light beam [Tang et al., 2021].

The middle ear was positioned in a holder in a position similar to that in a seated subject with the inferior part of the TM being at the bottom of the middle ear. Initial (normal) holographic measurements of the shape and click-induced vibration of the TM in the normal middle ear were performed on each temporal bone (these control measurements have been described previously [Tang et al., 2021]). After the normal control measurements, we performed a series of manipulations that mimicked common middle ear diseases and made new measurements after each manipulation. The manipulations were performed in the following order: 1) The middle-ear cavity behind the TM was filled with saline to a level that reached halfway up the TM. The camera used

to capture the holographic images revealed the fluid level. The measurement was performed when the fluid level was stable with no leaking from the middle ea. 2) The middle-ear cavity was then fully filled with saline and the measurements were repeated. 3) We then applied ethyl cyanoacrylate (Superglue) to the footplate of the stapes to immobilize or ‘fix’ the stapes and repeated the measurements once the glue was dry. 4) Finally, the incudo-stapedial (IS) joint was interrupted with a fine knife and the measurements again repeated. Each manipulation and the corresponding measurements took about an hour; to minimize temporal bone dehydration throughout the experiment, we constantly applied an ultrasonic water mist to the specimen.

9.2.2 Data Acquisition and Analyses

We have described our data acquisition and analyses in detail in our previous publications [Tang et al., 2021; Chapter 8]. Briefly, we first recorded the shape of the TM and the full field transient displacement to acoustic clicks with our high-speed digital holography system. These measurements define the temporal variations in the motion component normal to the TM surface at over 250,000 locations on that surface with high temporal-resolution (better than 60 kHz sample rate). The recorded motion waveforms were combined with simultaneous microphone measurements of the sound pressure waveform measured within 4 mm of the TM to define the frequency response and impulse response functions (FRF and IRF) of the TM at each surface location. Observations of how the FRF and IRF (and several derived quantities) varied over the entire TM surface were compared between the normal and pathological conditions. We also computed spatial averages of the different quantities, including the full TM area and selected quadrants of the TM. The quantities derived from the FRF and IRF are graphically described in Tang et al. (2021) and include:

The **dominant frequency** is the frequency component of the FRF that has the largest magnitude at each location $DF(x,y)$.

The **Root-mean-square** of the $IRF(x,y,t)$ at each TM location, $IRMS(x,y)$, is derived by calculating the RMS of the first 3 ms of the IRF at each location. The 3 ms threshold is based on the observation that in most cases the IRF converges to zero in that time.

The **rising time** at each TM location, $t^R(x,y)$, is the time needed for the $IRF(x,y,t)$ to reach its first peak.

The **exponential decay time** at each TM location, $t^D(x,y)$, was based on a fit of the exponential function $[a e^{bt}]$ to a series of points in the time described by the successive peaks of the first 2 ms of the absolute value of the $IRF(x,y,t)$. The decay time denotes the time ($t^D = -1/b$) when the fitted exponential attains $1/e$ (~36.8%) of the maximum displacement.

9.3 Results

9.3.1 Complete data sets from two individual bones

One complete set of TB1 results is illustrated in Figure 1. Figure 1 (a) displays the TM's frequency response function averaged over the entire surface (AFRF) with different middle ear conditions. Figure 1(b) shows maps of the dominant frequency of the FRF and of the RMS of the IRF with Normal and all manipulated middle ear conditions. Figure 1(c) reveals the rising and decaying time of the TM IRF with Normal, Stapes fixation and IS joint interruption conditions. The calculation of the rising time and decaying time relies on the accurate timing of the first significant peak of the IRF, but in the fluid injection cases, the IRF is reduced by the presence of

the fluid, and the initial peak is difficult to define. Therefore, the rising time and decaying time of the fluid injection cases are not illustrated in Figure 1c. In Figures 1 (b) and (c), the manubrium is oriented at 12 o'clock, as shown in the schematic drawing in Figure 1(d). We also divided the TM surface in Figure 1(d) into four regions (R1~R4) for further analysis and comparison. A dotted line marks the fluid level behind the TM in the half-fluid injection case in the RMS map; points inferior to that line are in contact with the fluid. Below we describe the effect of individual middle ear conditions on each quantified measure:

(i) The amplitudes of the AFRF are most affected when the entire TM surface is in contact with the injected fluid. The AFRF for the full-fluid case is a factor of 3 to 10 (10 to 20 dB) lower than the Normal AFRF across the entire measured frequency range (yellow curve). The AFRF with half-fluid injection (the orange curve) is about 5~10 dB lower than Normal at frequencies above 1 kHz. The AFRF for the Normal, Stapes fixation (ST) and IS interrupted conditions are nearly indistinguishable at frequencies above 2500 Hz, but there are significant differences at lower frequencies. IS-Joint interruption (green curve) has the highest magnitude (by a factor of 2 to 3) at frequencies less than 800 Hz, where it has a peak at the lowest frequency of the set. The AFRF amplitude with Stapes fixation (purple curve) is higher than normal between 800 and 1600 Hz and is lower than the Normal case between 1650 Hz and 2350 Hz.

(ii) The dominant frequency (DF) maps indicate the manipulations generally decrease the dominant frequency. However, in the fluid injection cases, some regions show increased DF. While such a difference could be the result of air bubbles in contact with the TM, the motion amplitude displayed in the RMS maps is still reduced compared to Normal. Stapes fixation reduced the dominant frequency over most of the TM area relative to Normal and IS Joint interruption resulted in a further decrease.

(iii) The IRMS maps reveal the overall motion magnitude in the different middle ear conditions. The color scale is coded in a logarithmic scale. The reduced motions are most evident in the fluid injection cases, where the areas in contact with fluid show motions near and below the noise floor. In the half-fluid case the superior quadrants (R1 and R4) show some level of motion due to the air in the superior middle ear cavity. In the case of full-fluid, the slight movement in the R4 area is due to the presence of an air bubble (seen with endoscopy) in contact with the TM surface during the measurement. In Stapes fixation the motion of the TM is somewhat less than in the Normal condition. IS joint interruption is associated with increased umbo motion compared to the Normal condition, with a small reduction in motion of the rest of the TM.

(iv) The rising time of the umbo and manubrium is slightly longer than the immediately surrounding TM surface in the Normal, ST and IS cases, though the rising time near the edge is more similar to that at the umbo. The rising time after IS joint interruption is slightly longer than after Stapes fixation. In all cases shown in Figure 1 (c), the R1 and R2 quadrants have longer rising times than R3 and R4.

(v) The decay time maps in the manipulated cases (Stapes fixation and IS joint interruption) are somewhat different than in the Normal condition. In the ST case, the decay time increases at R1 and R2 and decreases in R3 and R4. After IS joint interruption the decay time is generally decreased compared to the Normal and Stapes fixation cases.

Figure 2 illustrates a dataset from a different bone (TB 7). The Normal AFRF (Figure 2a) has a peak around 4 kHz, which is higher than what we saw in most TMs we measured. As in other bones, the AFRF is significantly reduced in magnitude and peak frequency in the fluid injection cases. The fluid-related reduction in motion magnitude and decrease in peak frequency are also visible in DF and IRMS motion maps (Figure 2b). Stapes fixation and IS joint interruption lower

the AFRF peak and the DF but have smaller effects on the magnitude of the TM motion. Stapes fixation and IS joint interruption increased the rising and decay times for much of the TB7's TM surface when compared with that of the Normal condition. The change in decay time is complex. R1 and R2 in Stapes fixation and IS joint cases have a lower decay time. R3 and R4 in Stapes fixation case and IS joint case have a higher decaying time. The umbo area has a lower decay time in both Stapes fixation and IS interruption. In the next section we introduce a more quantitative analysis of the spatial differences in our measured quantities.

9.3.2 Quantitative comparison of motion parameters

The spatially averaged frequency response function (AFRF) amplitude spectrum averaged across all specimens is illustrated in Figure 3; the error bars show the standard error. The average AFRFs of the Normal, Stapes fixation, and IS joint interruption conditions are logarithmic averages from eight temporal bones (TB1-8). The AFRFs of the fluid injection conditions are logarithmic averages from seven temporal bones (TB1-7). Due to a leaking problem, TB8 could not hold the fluid level inside the middle ear cavity. On average, Stapes fixation (the purple line) produces a lower AFRF amplitude in the low-frequency range (200 to 1000 Hz) and a slight increase between 2000 to 3000 Hz when compared with the Normal condition. The IS joint interruption average (green line) has a peak in amplitude at around 900 Hz, where the Normal condition (blue line) has a maximum amplitude between 1000 and 2000 Hz. the IS joint interrupted case has the largest AFRF at frequencies below 900 Hz. The half-fluid case average has an AFRF amplitudes that is a factor of 2 lower than normal at frequencies above 700 Hz. The average AFRF of the full-fluid case is a factor of 3 to 10 lower than normal across the full frequency range.

We used paired t-tests to quantify the significance of the manipulation-induced changes in AFRF of the 7 or 8 temporal bones at multiple frequencies. Cases where the probability of chance

performance was 5% or lower are marked with an *. No correction was performed for repeated testing, so isolated instances of positive significance testing may be the result of random processes. The change from normal produced by the full-fluid and half-fluid injection manipulations are statistically different at all the frequencies tested in Figure 3. The change from normal produced by Stapes fixation reaches the 5% level at 1kHz, and the change produced by IS joint interruption reaches 5% significance between 5-5.5kHz.

The across specimen averages of the spatially averaged parameter values in the four quadrants (R1 through R4) and at the umbo are calculated to quantitatively compare the motion parameters among different specimens in different conditions. Figures 4-6 show the average and standard errors of the quadrant and umbo averaged DF, IRMS, rising time, decaying time, and damping ratio measured in all specimens.

Figure 4(a) displays the averaged dominant frequencies \pm standard error with the different middle ear conditions at each quadrant and umbo area. The DF of the full-fluid injection cases, with average values that range between 0.4 and 0.6 kHz, are lowest in all five plotted areas. With half level of fluid in contact with the TM surface, the dominant frequencies also are decreased relative to Normal in those regions in contact with the fluid (R2, R3, and umbo) as well the regions that are backed by air (R1 and R4). IS joint interruption decreases the dominant frequency compared to the Normal condition in all of the regions we plot. Stapes fixation reduces the motion at the umbo, and regions R1 and R4. The statistical significance of these changes in dominant frequency (and all our averaged parameters) will be left to the discussion.

Figure 4(b) shows the mean and standard errors of the area averaged Root Mean Square (RMS) of the first 3 ms of the impulse responses. As above, the plotted values are derived by first spatially averaging each individual quadrant or umbo area and then averaging the different area

values with the same middle ear conditions across all TBs. The full-fluid case has the lowest IRMS values among all calculated regions, with the standard errors being too small to visualize in most regions. In the half-fluid cases, the areas in contact with the fluid (R2, R3, and umbo) have lower RMS values, but the regions backed by middle-ear air (R1 and R4) also show reduced motion compared to normal. Stapes fixation and IS joint interruption have averaged RMS values comparable to the Normal condition; the standard errors of these three cases overlap.

Figure 5(a) plots the region averaged rising time for the following cases: Normal condition, R1, R4 and umbo areas of the half-fluid injection, Stapes fixation, and IS joint interruption. As noted earlier, it was challenging to identify the initial peak in the IRF in locations that were backed by fluid as the motion responses were small. As our rise and decay time algorithms depended on that first peak, we do not quantify these values for the full-fluid case or the inferior quadrants (R2 and R3) of the half-fluid case. The Normal condition has the shortest rise time at all locations, while the IS interruption has the longest rise time. Regions R1, R4 and the umbo area of the half-fluid injection have a longer rising time than the Normal condition even though these areas are not fully in contact with the fluid. The error bar reveals that the rising time of Stapes fixation generally overlaps the Normal and IS joint interruption cases.

Figure 5(b) illustrates the decay time based on exponential curve fitting to the IRF. The decay time is calculated for the Normal, Stapes fixed and IS interrupted conditions, along with R1, R4 and umbo from the half-fluid injection cases is calculated. Stapes fixation produces similar decay times to the Normal condition. The IS joint interruption has the longest decay times except for region R1. For R1 to R4 areas, the decaying time for the three cases have large standard errors. The Normal and Stapes fixation conditions have similar decaying times and overlapping standard errors for the umbo area. The IS joint interruption at the umbo has the largest average decay time

time with error bars separated from those around the other manipulations at R2, R3 and the umbo. The decay times in R1 and R4 areas in the half-fluid case are somewhat longer than normal, whereas the umbo in the half-fluid case has a decay time similar to normal.

Figure 6 displays the quadrants and umbo averaged damping ratio, where this ratio depends on the estimate of dominant frequency and decay time (Tang et al. 2021). In R1, R4 and at the umbo (the regions where it is measured) the damping ratio of the half-fluid case is higher than the other cases suggesting fluid increases the overall system damping even in those areas that are not fully in contact with the fluid. The damping ratio of the IS interrupted condition at the umbo is lower than the other conditions, but it is higher at R2. Stapes fixation reduced the damping ratio at R1, R2 and R3.

9.4 Discussion

9.4.1 Holography quantified TM frequency and impulse responses with different middle ear pathologies

This section presents a systematic attempt to separate the different middle conditions using the results obtained from the holographic data and the computed TM motion parameters. The fluid injection cases are the clearest cases to identify. The presence of fluid behind the TM greatly reduces the vibration of the TM. The reduced vibration motion affects the amplitude of the FRF and the IRF. Comparing AFRFs (Figure 3), full-fluid injection produces the lowest AFRF amplitude, and is clearly separable from all of the other condition between 1 kHz and 10 kHz. From

the quadrant and umbo averaged motion parameters in Figure 4, the full-fluid injection case has the lowest Dominant Frequencies and by far the lowest IRMS magnitudes. Therefore, the combination of the large reductions in AFRF, and the quadrant averaged DF and IRMS motion magnitudes are clear indicators of a middle-ear filled with fluid.

In the half-fluid case, the reductions in AFRF, Dominant Frequency and RMS vibration are smaller but still easily separable from the other conditions. While both IS joint interruption and the half-filled fluid manipulations produce similar Dominant Frequencies over most of the membrane surface, the combination of a reduced DF and RMS magnitude is distinctive to the fluid-filled cases. The half-filled case can be separated from the full-filled case by the degree of these reductions and the differences in motion between those parts of the TM backed by fluid or air. It should be noted, however, that Figure 4b suggests that the presence of fluid on some parts of the TM also affects those parts of the TM backed by air.

Figures 3 through 6 suggest that the effects of the ossicular manipulations, Stapes fixation and IS joint interruption, on the defined motion parameters tend to be smaller and more variable. Our discussion of their effects will be discussed after we introduce statistical analyses of the changes in parameter values produced by our manipulations.

9.4.2 Effects of middle ear pathologies on TM responses and parameters

We calculated the dB change from Normal of the parameters determined for the Stapes fixation, IS joint interruption and half-filled fluid manipulations, as shown in Figures 7-11. These figures show box diagrams of the distribution of the values measured in the 7 or 8 individual bones in each of the 5 areas, with the red bar displaying the average value, the blue box showing the 25th

and 75th percentile, and the black dash denoting the range. Changes in the averaged quadrant value that meet 5% and 1% statistical significance is marked with one (5%) or two (1%) *s.

Figure 7 (a) is the box diagram of the dB changes from Normal in RMS between Stapes fixation condition for the 4 quadrants and umbo in seven TM. R1, R2 and umbo have an averaged ratio below 0 meaning a decreased in RMS displacement in those regions. R2 and R3 have an averaged increased RMS displacement. Figure 7(b) displays the dB change from Normal in the RMS for the IS joint interruption for the quadrants and umbo averaged value. All the averaged ratios are positive and the ratios in R3 and umbo reach statistical significance of 5% threshold in students tests. In Figure 7 (c), box diagrams are drawn for dB change in RMS after half-fluid injection for the R1, R4 and umbo areas. R1 and umbo have negative ratios while R4 has a positive ratio. However, no statistical significance is reached to differentiate the half-fluid injection from the normal case suggesting the information in frequency domain from the averaged FRF are more sensitive in differentiating the half-fluid case

Figure 8 (a) shows a box diagram of the dB changes from Normal in DF between the Stapes fixation condition for the 4 quadrants and umbo seen in eight TMs. R1, R4, and umbo have an averaged ratio of less than 0 dB, while R2 and R3 have an averaged ratio greater than 0 dB. The 25% to 75% percentile (blue box) for all the areas reveals a variation between -4 and 3.5 dB. Figure 8(b) displays the dB change from Normal in the Dominant frequency for the IS joint interruption for the four quadrants and the umbo for eight TM measurements. The average ratios are all below 0 dB, with the R2 area having a statistical significance reaching 5 % threshold in the student t-test. This suggests a decrease occurs in dominant frequency after IS joint interruption. Such a decrease is consistent with the observation that the IS joint interruption shifts the peak amplitude of the AFRF to a lower frequency (Figure 3). In Figure 8 (c), box diagrams are drawn for dB change in

DF after half-fluid injection for the R1, R4 and umbo areas. On average the dB changes are negative as they describe reductions in DF. In area R1, our repeated value t-tests provide a significance level of 5% for the reduction from 0 dB. In area R4, the reduction in dB reaches the 1% significance level. No statistical significance was found at the umbo.

Figure 9 (a) shows the dB change from Normal in the rising time produced by Stapes fixation. The mean quadrant ratios fall between -1 and 0.8 dB, indicating the Stapes fixation and Normal conditions have similar rising times. Figure 9(b) compares the ratio of the rising time between the IS joint interruption and Normal condition. All the areas have ratios between 1.2 and 3 dB, suggesting the IS joint interruption generally enhances the rising time for all the surfaces of the TM. The IS joint Interruption case is statistically different from the Normal case in R3, R4 and umbo area; in R4 the statistical significance reaches the 1% level. Figure 9 (c) shows the box diagram of the dB change in rising time in the half-fluid condition. The averaged dB values in R1, R4 and umbo are positive, but distributions do not reach statistical significance.

Figure 10 shows box diagrams of the dB change from Normal in the decay times for the Stapes fixation, IS joint interruption and half-fluid cases. While several trends appear in the across-specimen averages. None of the changes in this figure reach statistical significance due to the relatively large variations in the response across the individuals. Figure 10(a) shows the mean ratios of the Stapes fixation to the Normal condition are greater than 0 dB in areas R1, R2, R4, and umbo. The umbo area has the largest mean ratio (around 2dB). Figure 10 (b) illustrates the mean decaying time of all surfaces of the TM is larger than Normal in the IS joint interruption condition, reaching 4 dB at the umbo. This suggests removal of the inner ear load from the TM allows the TM to vibrate for a longer time. Figure 10(c) shows the dB change in decaying time for the half-

fluid conditions. The average dB ratios of the decaying time for the TM surface in R1, R4 and umbo are between 2 and 3 dB.

Figure 11 shows the box diagram of the dB change from Normal in damping ratio for Stapes fixation, IS joint interruption and half-fluid cases. Stapes fixation leads to averages in damping that vary between -3 and +3 dB. IS joint interruption cases produces a damping ratio that is on-average less than 0 dB compared to the Normal cases. The half-fluid manipulation increases the averaged damping ratio at R1 and R4 and the umbo. However, the changes in the damping ratio from the available measurements do not reach any statistical significance.

The across specimen averaged quadrant and umbo values show that Stapes fixation tends to increase rising time and decaying time for the entire surface. IS joint interruption also tends to increase rising and decay time, where the most significant increases are seen in rise time in R3, R4 and the umbo. IS joint interruption and half-fluid cause significant decreases in dominant frequency. Summing up, the motion parameters from the frequency and impulse analysis show some degree of separation for TM pathologies. For example, low values in the RMS maps or low amplitude of the AFRF can indicate fluid behind the TM. The peak amplitude of the AFRF is at a lower frequency for Stapes fixation than that of the Normal condition. Stapes fixation leads to small increases in the rising and decaying time increase. The IS joint interruption will cause greater increases in rising time and decaying time; it also reduces the dominant frequency. This reduction of the dominant frequency is not seen in the Stapes fixation and can distinguish stapes fixation from IS joint interruption and vice versa.

9.5. Conclusion and future work

This paper presents full-field frequency and impulse responses of the human TM measured on human temporal bones with different experimental induced middle ear pathologies. The simulated pathologies include Otitis Media with Effusion, Stapes Fixation, and IS joint interruption. According to the findings, the AFRF shows significant changes when the fluid is injected into the middle cavity to simulate OME. The level of fluid inside the middle ear cavity has a different effect on the response of the TM. The stapes fixation and IS joint interruption primarily affect AFRF in a low-frequency range. We also calculated several spatially averaged motion parameters at four quadrants of the TM and the umbo and used them to help quantitatively differentiate middle ear manipulations behind the intact TM. These quadrant and umbo motion parameters analyses show trends that can separate the pathological conditions from the Normal conditions. In future studies, we will implement the same analysis method to include more TBs (over 100) in order to enrich the database. We will also develop an endoscopic configuration holographic system to measure intact ears or live human ears.

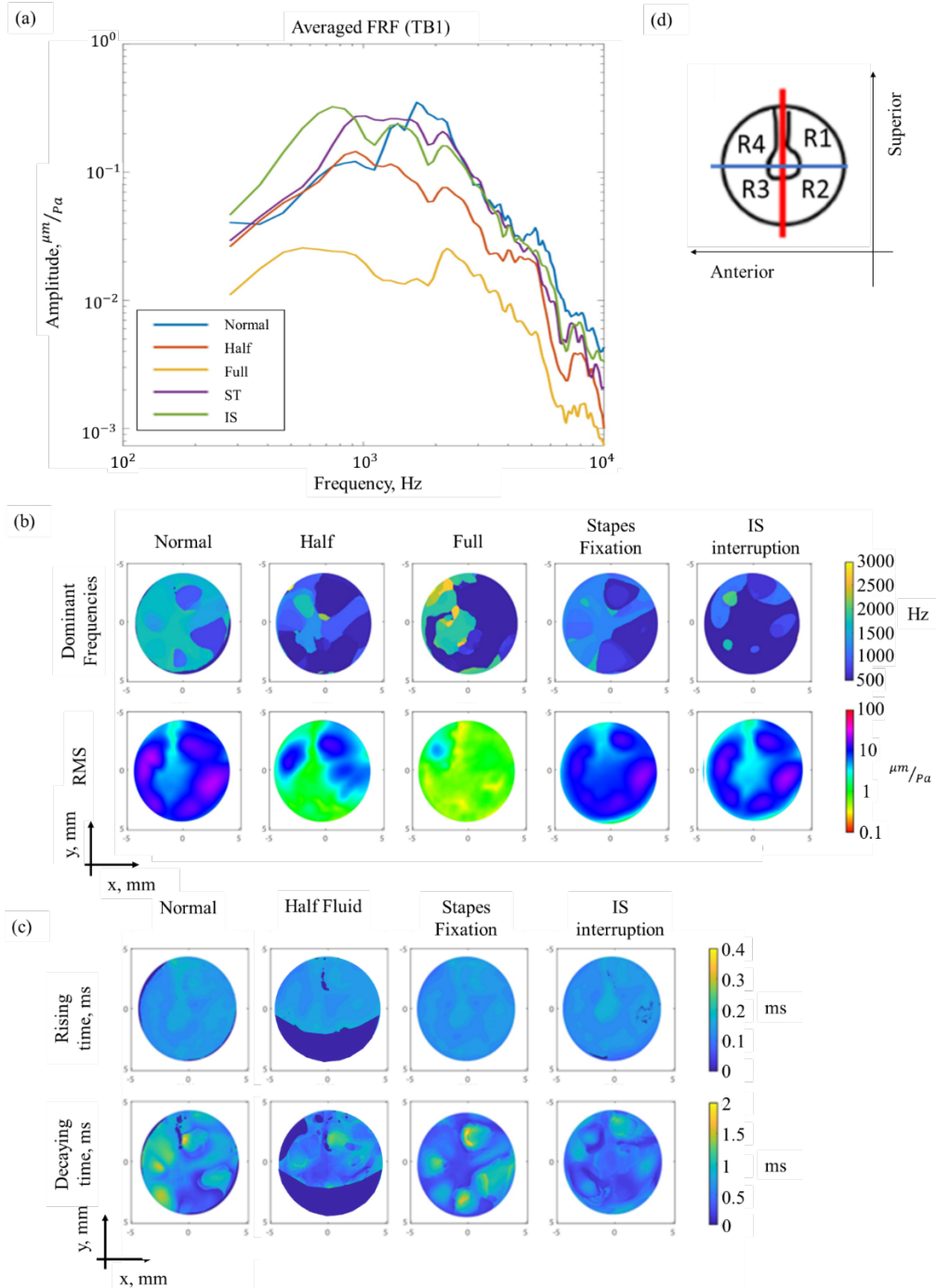


Figure 1. A complete data set of TB1: (a) Averaged FRF of the Normal, half-fluid, full-fluid, Stapes fixation and IS joint interruption cases; (b) Dominant frequencies and RMS of the IRF maps of the Normal, half-fluid, full-fluid, Stapes fixation and IS joint interruption cases; (c) Rising time and decaying time maps of the Normal, Stapes fixation and IS joint cases; and (d) the outlines of the quadrants and umbo and manubrium

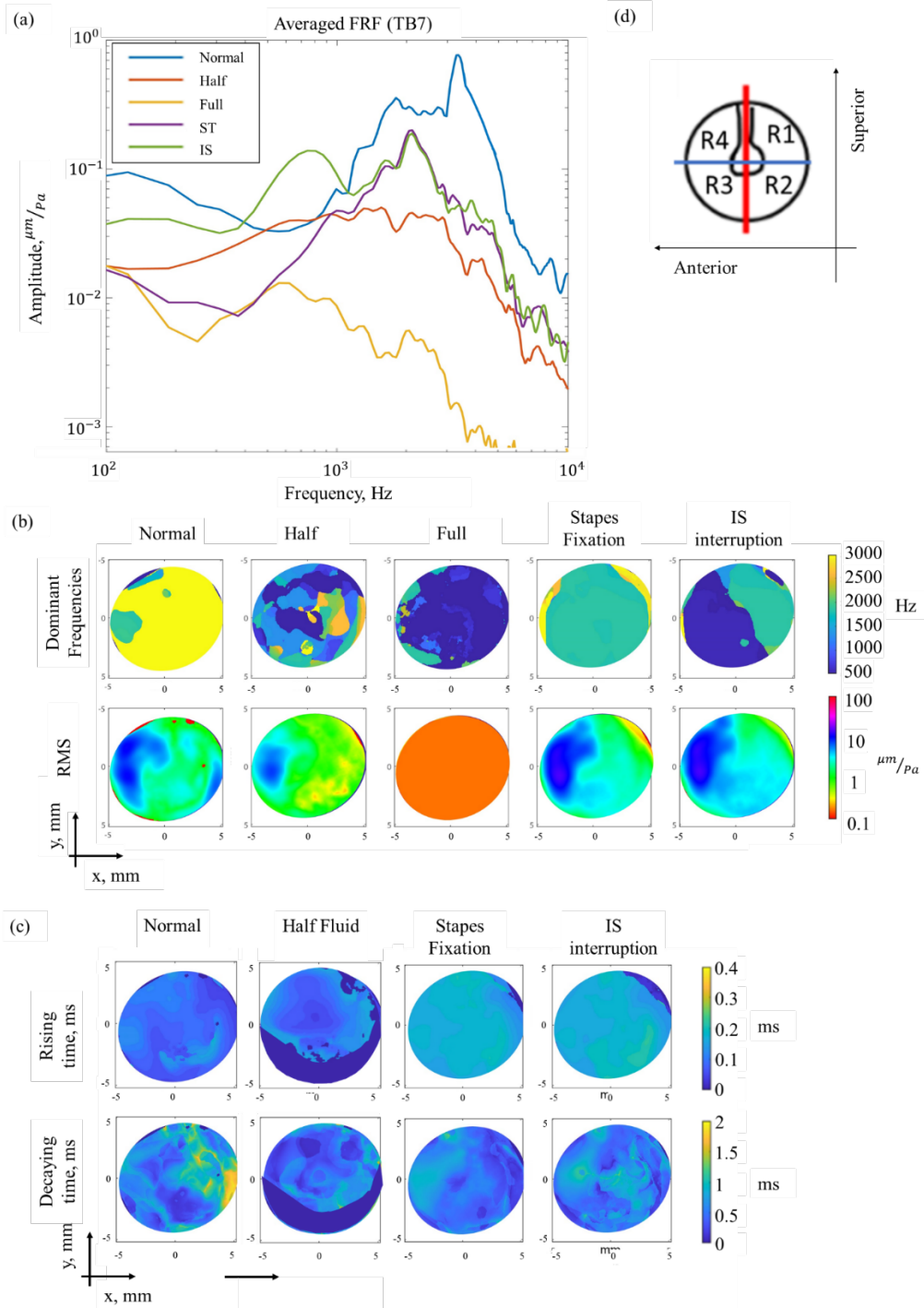


Figure 2. A complete data set of TB7: (a) Averaged FRF of the Normal, half-fluid, full-fluid, Stapes fixation and IS joint interruption cases; (b) Dominant frequencies and RMS of the IRF maps of the normal, half-fluid, full-fluid, Stapes fixation and IS joint interruption cases; (c) Rising time and decaying time maps of the Normal, Stapes fixation and IS joint cases; and (d) the outlines of the quadrants and umbo and manubrium

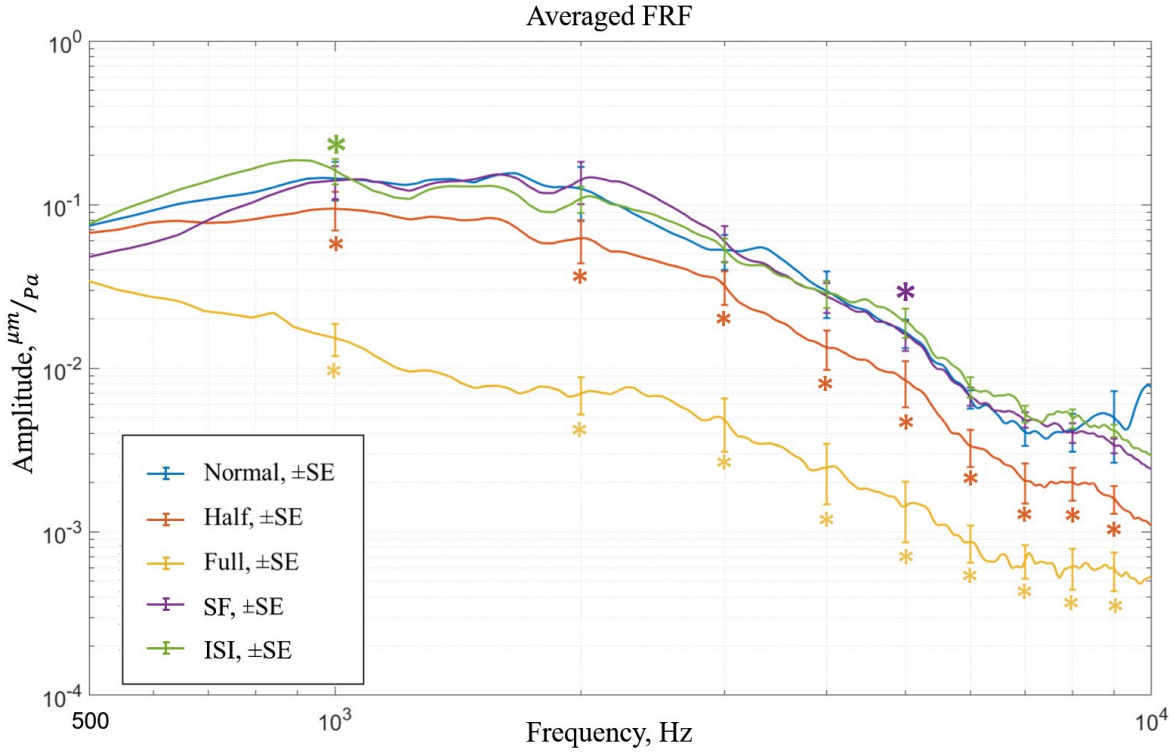


Figure 3. The averaged Frequency Response Function (FRF) amplitude spectrum with standard error. The averaged FRF for each condition was averaged spatially for each measurement and then averaged among different specimens. Manipulation-induced differences from Normal with 5% or better statistical significance are marked with asterisks.

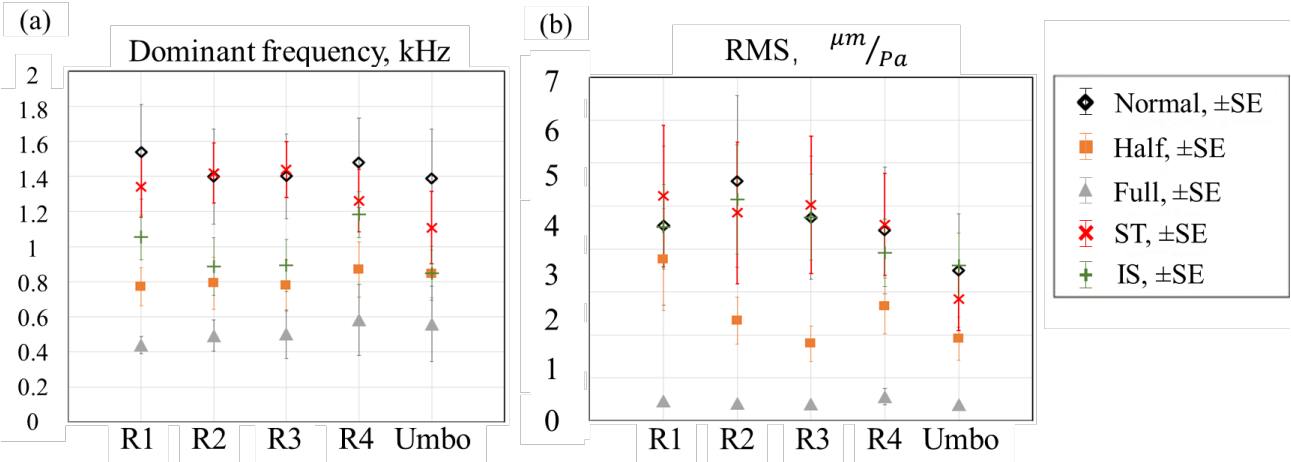


Figure 4. Mean quadrant and umbo averages of FRF dominant frequency and IR RMS amplitude with standard errors for different middle ear conditions. N=8 for Normal, ST and IS. N=7 for the fluid-filled conditions.

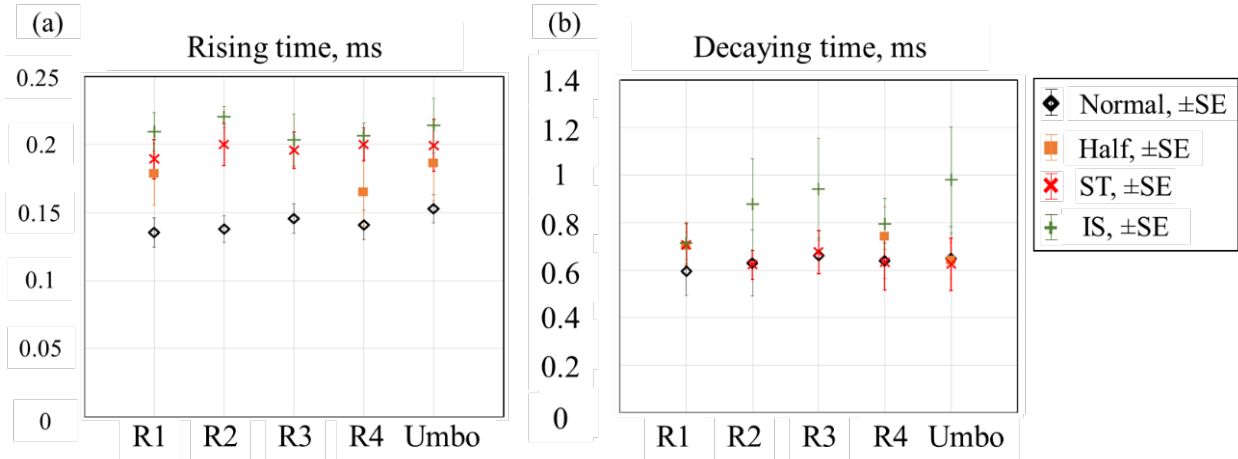


Figure 5. Mean quadrant and umbo averaged rising time and decaying time with standard errors for Normal, stapes fixation and IS joint interruption conditions.

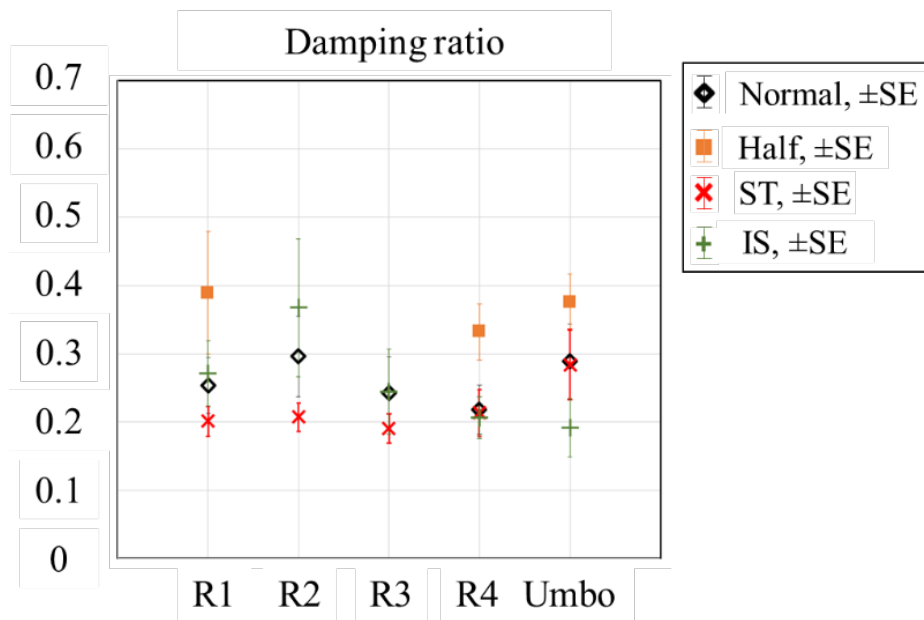


Figure 6 Mean quadrant and umbo averaged damping ratio with standard error for Normal, stapes fixation and IS joint interruption conditions.

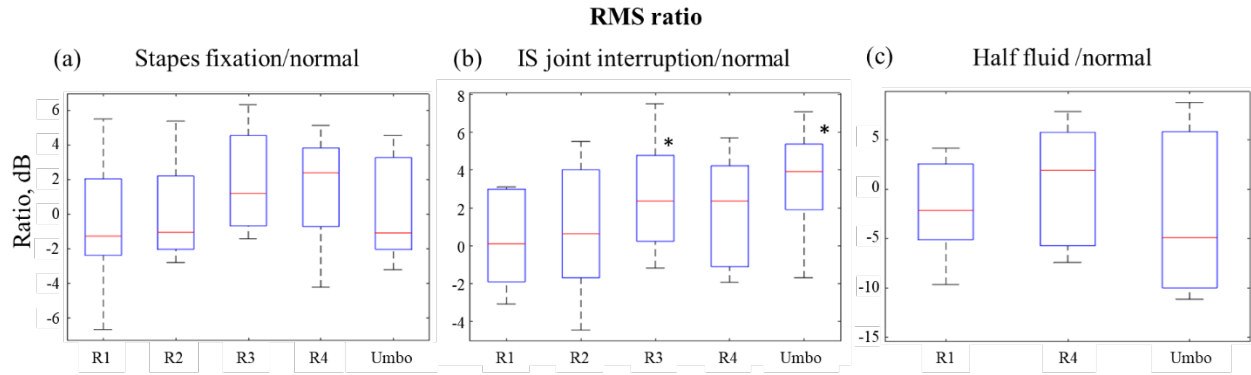


Figure 7 Comparison of the dB change in the RMS: (a) ratio between stapes fixation and Normal condition; (b) ratio between IS joint and Normal condition. (c) ratio between half-fluid and Normal condition. Changes from Normal with statistical significance level of 5% are marked with an asterisk, and two asterisks mark 1% significance.

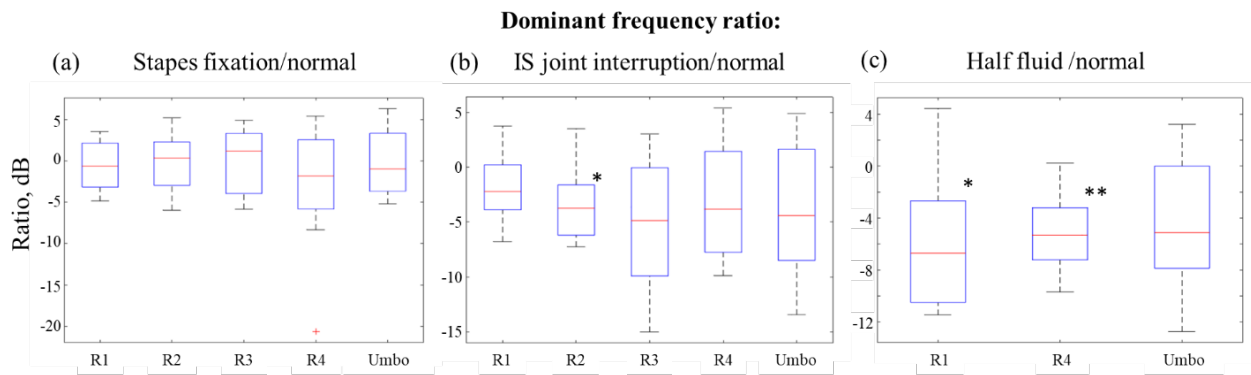


Figure 8 Comparison of the dB change in the dominant frequencies: (a) ratio between stapes fixation and Normal condition; (b) ratio between IS joint and Normal condition. (c) ratio between half-fluid and Normal condition. Changes from Normal with statistical significance level of 5% are marked with an asterisk, and two asterisks mark 1% significance.

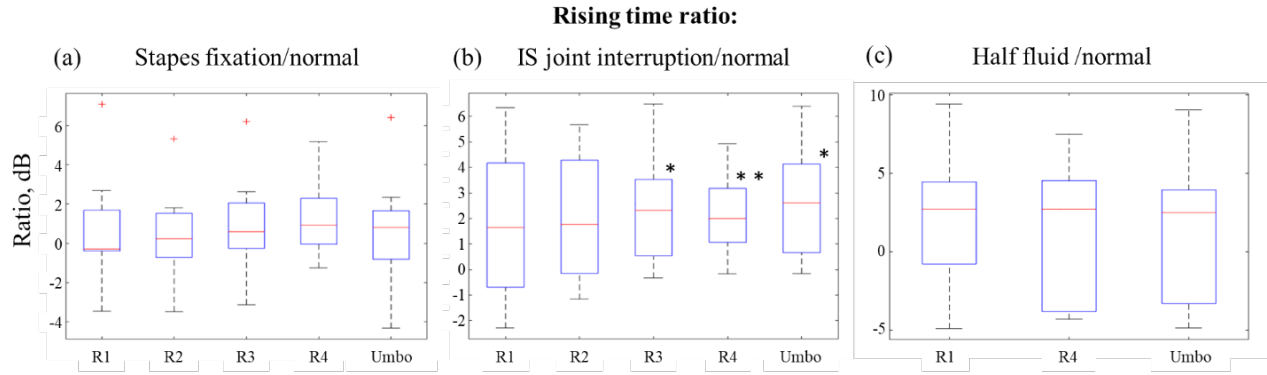


Figure 9. Comparison of the dB change in rising time: (a) ratio between stapes fixation and Normal condition; (b) ratio between IS joint and Normal. Data points with statistical significance from Normal conditions are marked asterisk. (c) ratio between half-fluid and Normal condition. One asterisk marks 5% significance, and two asterisks mark 1% significance

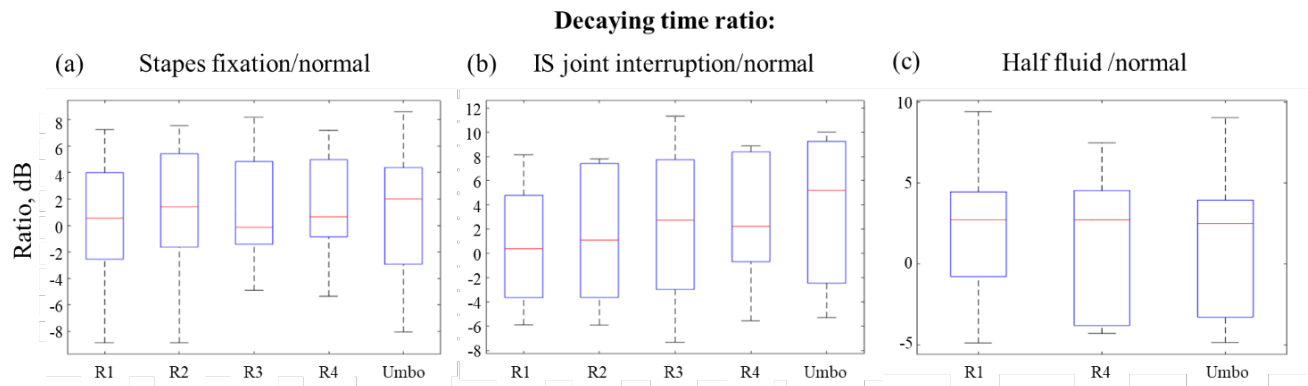


Figure 10 Comparison of the dB change in decaying time: (a) ratio between stapes fixation and Normal condition; (b) ratio between IS joint and Normal condition. (c) ratio between half-fluid and Normal condition.

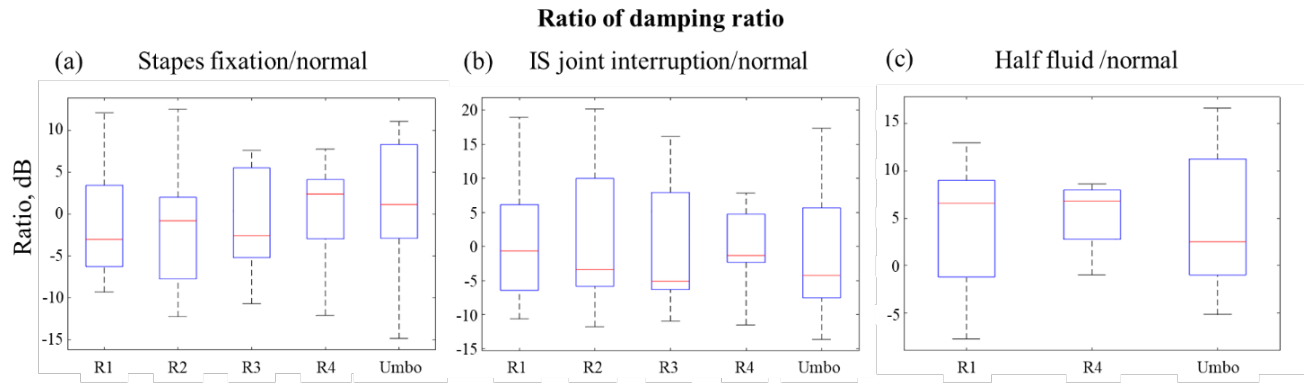


Figure 11 Comparison of the dB change in damping ratio: (a) ratio between stapes fixation and Normal condition; (b) ratio between IS joint and Normal condition. (c) ratio between half-fluid and Normal condition.

References

- [1] H. Tang, P. Razavi, K. Pooladvand, P. Psota, N. Maftoon, J. J. Rosowski, C. Furlong, J. T. Cheng, “High-Speed Holographic Shape and Full-Field Displacement Measurements of the Tympanic Membrane in Normal and Experimentally Simulated Pathological Ears,” *Appl. Sci.*, vol. 9, no. 14, Art. no. 14, Jan. 2019.
- [2] H. Tang, P. Psota, J. J. Rosowski, C. Furlong, J. T. Cheng. “Analyses of the Tympanic Membrane Impulse Response Measured with High-Speed Holography,” *Hearing Research*, Volume 410, 2021,
- [3] J. J. Rosowski, “Outer and Middle Ears,” in *Comparative Hearing: Mammals*, vol. 4, R. R. Fay and A. N. Popper, Eds. New York, NY: Springer New York, 1994, pp. 172–247. doi: 10.1007/978-1-4612-2700-7_6.
- [4] C. D. Geisler, *From sound to synapse: physiology of the mammalian ear*. Oxford University Press, USA, 1998.
- [5] X. Wang, X. Guan, M. Pineda, and R. Z. Gan, “Motion of tympanic membrane in guinea pig otitis media model measured by scanning laser Doppler vibrometry,” *Hear. Res.*, vol. 339, pp. 184–194, Sep. 2016, doi: 10.1016/j.heares.2016.07.015.
- [6] J. P. Fay, S. Puria, and C. R. Steele, “The discordant eardrum,” *Proc. Natl. Acad. Sci.*, vol. 103, no. 52, pp. 19743–19748, Dec. 2006, doi: 10.1073/pnas.0603898104.
- [7] G. Vollandri, F. Di Puccio, P. Forte, and C. Carmignani, “Biomechanics of the tympanic membrane,” *J. Biomech.*, vol. 44, no. 7, pp. 1219–1236, Apr. 2011, doi: 10.1016/j.jbiomech.2010.12.023.

[8] T. Cheng, C. Dai, and R. Z. Gan, “Viscoelastic Properties of Human Tympanic Membrane,” *Ann. Biomed. Eng.*, vol. 35, no. 2, pp. 305–314, Feb. 2007, doi: 10.1007/s10439-006-9227-0.

[9] J. Fay, S. Puria, W. F. Decraemer, and C. Steele, “Three approaches for estimating the elastic modulus of the tympanic membrane,” *J. Biomech.*, vol. 38, no. 9, pp. 1807–1815, 2005.

[10] D. De Greef, J. A. Buytaert, J. R. Aerts, L. Van Hoorebeke, M. Dierick, and J. Dirckx, “Details of human middle ear morphology based on micro-CT imaging of phosphotungstic acid stained samples,” *J. Morphol.*, vol. 276, no. 9, pp. 1025–1046, 2015.

[11] S. Van der Jeught, J. J. J. Dirckx, J. R. M. Aerts, A. Bradu, A. G. Podoleanu, and J. A. N. Buytaert, “Full-Field Thickness Distribution of Human Tympanic Membrane Obtained with Optical Coherence Tomography,” *J. Assoc. Res. Otolaryngol.*, vol. 14, no. 4, pp. 483–494, Aug. 2013, doi: 10.1007/s10162-013-0394-z.

[12] J. Aernouts, J. R. M. Aerts, and J. J. J. Dirckx, “Mechanical properties of human tympanic membrane in the quasi-static regime from in situ point indentation measurements,” *Hear. Res.*, vol. 290, no. 1, pp. 45–54, Aug. 2012, doi: 10.1016/j.heares.2012.05.001.

[13] J.J. Rosowski, J.T. Cheng, M.E. Ravicz, N. Hulli, M. Hernandez-Montes, E. Harrington, and C. Furlong, “Computer-assisted time-averaged holograms of the motion of the surface of the mammalian tympanic membrane with sound stimuli of 0.4–25 kHz,” *Hear. Res.*, vol. 253, no. 1–2, pp. 83–96, 2009.

[14] J. J. Rosowski, “Models of external-and middle-ear function,” in *Auditory computation*, Springer, 1996, pp. 15–61.

- [15] D. J. Lim, "Human tympanic membrane: an ultrastructural observation," *Acta Otolaryngol. (Stockh.)*, vol. 70, no. 3, pp. 176–186, 1970.
- [16] M. Khaleghi, "Development of holographic interferometric methodologies for characterization of shape and function of the human tympanic membrane," *Docotoral Thesis*, Worcester Polytechnic Institute, Worcester MA, 2015.
- [17] M. Milazzo, E. Fallah, M. Carapezza, N. S. Kumar, J. H. Lei, and E. S. Olson, "The path of a click stimulus from ear canal to umbo," *Hear. Res.*, vol. 346, pp. 1–13, Mar. 2017, doi: 10.1016/j.heares.2017.01.007.
- [18] J. Tonndorf and S. M. Khanna, "The role of the tympanic membrane in middle ear transmission," *Ann. Otol. Rhinol. Laryngol.*, vol. 79, no. 4, pp. 743–753, 1970.
- [19] S. M. Khanna and J. Tonndorf, "Tympanic membrane vibrations in cats studied by time-averaged holography," *J. Acoust. Soc. Am.*, vol. 51, no. 6B, pp. 1904–1920, 1972.
- [20] W. F. Decraemer, S. M. Khanna, and W. R. J. Funnell, "Interferometric measurement of the amplitude and phase of tympanic membrane vibrations in cat," *Hear. Res.*, vol. 38, no. 1–2, pp. 1–17, 1989.
- [21] R. L. Goode, G. Ball, and S. Nishihara, "Measurement of umbo vibration in human subjects—method and possible clinical applications.," *Am. J. Otol.*, vol. 14, no. 3, pp. 247–251, 1993.
- [22] R. L. Wegel and C. E. Lane. "The auditory masking of one pure tone by another and its probable relation to the dynamics of the inner ear," *Phys. Rev.* 23, 266–285 ,1924

[23] J. Zwislocki, "Some impedance measurements on normal and pathological ears," *J. Acoust. Soc. Am.* 29(12), 1312–1317, 1957.

[23] J. B. Allen, "Measurement of eardrum acoustic impedance," in *Peripheral Auditory Mechanisms*, edited by J. B. Allen, J. L. Hall, A. Hubbard, S. T. Neely, and A. Tubis (Springer-Verlag, New York), pp. 44–51, 1986.

[24] J. B. Allen, P. S. Jeng, , and H. Levitt, "Evaluating human middle ear function via an acoustic power assessment," *J. Rehabil. Res. Dev.* 42(4), 63–78, 2005

[25] J.J. Rosowski, H.H. Nakajima, J.T. Cheng, M.A. Hamadeh, and Ravicz, "Middle-ear input impedance and middle-ear sound transfer". *The Journal of the Acoustical Society of America*, 127(3), pp.1867-1867. 2010.

[26] W. R. J. Funnel, and C. A. Laszlo, "Modeling of the cat eardrum as a thin shell using the finite-element method," *J. Acoust. Soc. Am.* <https://doi.org/10.1121/1.381892> 63, 1461–1466. 1978.

[27] R. Z. Gan, B. Feng, and Quan, "Three-dimensional finite element modeling of human ear for sound transmission". *Annals of biomedical engineering*, 32(6), pp.847-859, 2004.

[28] J.T. Cheng, A.A. Aarnisalo, E. Harrington, M. del Socorro Hernandez-Montes, C. Furlong, S.N. Merchant, and J.J. Rosowski, "Motion of the surface of the human tympanic membrane measured with stroboscopic holography". *Hearing research*, 263(1-2), pp.66-77 , 2010

[29] J.J. Rosowski, H.H. Nakajima, and S.N. Merchant, “Clinical utility of laser-Doppler vibrometer measurements in live normal and pathologic human ears”. *Ear and hearing*, 29(1), p.3, 2008.

[30] BA. Prieve, M.P. Feeney, S. Stenfelt, and N. Shahnaz. “Prediction of conductive hearing loss using wideband acoustic immittance. *Ear and Hearing*”, 34, pp.54s-59s, 2013

[31] C.A. Sanford, L.L. Hunter, M.P. Feeney, and H.H. Nakajima,” Wideband acoustic immittance: tympanometric measures”. *Ear and Hearing*, 34, pp.65s-71s, 2013

[31.1]Aarnisalo AA, Cheng JT, Ravicz ME, Hulli N, Harrington EJ, Hernández-Montes MdS, Furlong C, Merchant SN, Rosowski JJ. 2009. Middle ear mechanics of cartilage tympanoplasty evaluated by laser holography and vibrometry. *Otol Neurotol*. 30(8):1209-14.

[32] P. Razavi, H. Tang, J. J. Rosowski, C. Furlong, and J. T. Cheng, “Combined high-speed holographic shape and full-field displacement measurements of tympanic membrane,” *J. Biomed. Opt.*, vol. 24, no. 3, p. 031008, Sep. 2018, doi: 10.1117/1.JBO.24.3.031008.

[33] H. Tang, P. Razavi, N. Maftoon, J.J. Rosowski, C. Furlong, and J.T. Cheng, “Comparative Modal Analysis of the Tympanic Membrane Mechanics Between Normal and Experimentally Simulated Pathological Ears”. In *Mechanics of Biological Systems and Materials & Micro-and Nanomechanics, Volume 4* (pp. 63-71). Springer, Cham, 2020

[34] I. Dobrev, E. Harrington, T. Cheng, C. Furlong, and J. Rosowski, “Digital holographic otoscope for measurements of the human tympanic membrane in-vivo,” in *Imaging Methods for Novel Materials and Challenging Applications, Volume 3*, Springer, 2013, pp. 39–45.

[35] M. Khaleghi, I. Dobrev, E. Harrington, C. Furlong, and J. J. Rosowski, “Study of the transient response of Tympanic Membranes under acoustic excitation,” in *Mechanics of Biological Systems and Materials*, Volume 4, Springer, 2014, pp. 1–9.

[36] P. Razavi, H. Tang, J. J. Rosowski, C. Furlong, and J. T. Cheng, “Combined high-speed holographic shape and full-field displacement measurements of tympanic membrane,” *J. Biomed. Opt.*, vol. 24, no. 3, p. 031008, Sep. 2018, doi: 10.1117/1.JBO.24.3.031008.

Chapter 10 Tympanic Membrane Shape and Impulse Response Measured with High-Speed Holography in Live Chinchilla Ear with Otitis Media with Effusion

This chapter presents the results of the high-speed digital holographic (HDH) measurement of the shape and impulse response of the TM in live chinchillas with Otitis media with Effusion (OME).

Background and method of animal study

Otitis Media with Effusion (OME) is a common middle ear disease in children, causing hearing loss and learning disability (Bluestone et al., 1998, Cunningham et al., 1993, Hunter et al., 1994, Roberts et al., 2004). Several mechanisms have been proposed for OME-associated hearing loss, including viscous damping of middle ear motions, reduction of middle-ear air space, static-middle-ear-pressure-induced changes in the tympanic membrane (TM) shape and compliance, and increased TM thickness and stiffness due to chronic inflammation (Fulghum et al., 1994, Gaihede et al., 1997, Guan et al., 2014, von Unge et al., 1994). However, the frequency dependence of the hearing loss and the effect of fluid levels remain unclear. Furthermore, most mechanical measurements of middle ear responses with OME are either based on surface averages like middle-ear admittance (Prieve et al. 2013) or on single-point laser measurements either at the umbo or the stapes (Rosowski et al., 2013). However, changes in umbo displacement or admittance do not fully explain the hearing loss in a clinical population (Dai et al., 2007), and do not permit any spatial separation of the effects of effusion on part, but not all, of the TM.

In this study, HDH was used to measure the TM surface motion in six female adult chinchillas, weighing between 500 and 900g. This animal study is reviewed and approved by the

Massachusetts Eye and Ear(MEE) Institutional Animal Care and Use Committee(animal study protocol # 2021N000024). The left middle ear of each animal was injected with lipopolysaccharide (LPS, 0.3ml, 100 μ g/ml, of *Klebsiella pneumonia*, Sigma) to induce OME; the right ear served as the control ear. LPS is a sterile construct of the major component of the outer membrane of gram-negative bacteria. Studies have demonstrated that inoculation of the middle ear with LPS induces long-term middle ear effusions (Ohashi et al, 1988).

Before the LPS inoculation, baseline hearing response studies were performed in both ears. The auditory brainstem response (ABR) is an auditory-evoked potential extracted from ongoing electrical activity in the brain and recorded via electrodes placed on the scalp (Hecox et al., 1974). Similarly, distortion product otoacoustic emission tests (DPOAE) reflect outer hair cell integrity and cochlear function (White et al. 2005, Shera et al., 2002, Dolan et al., 1985, Yoshida et al., 2000). These hearing tests were repeated 5 days after the inoculation just prior to the HDH measurements. In between, the condition of both middle ears was monitored daily via an endoscope. Endoscope images of the left ear and right ear taken 5 days after the LPS injection, are shown in Figure 10.1. In those images, the reaction to the LPS in the left ear can be seen as a yellow- or red- colored fluid mixed with air bubbles. After the second round of DPOAE and ABR measurements the external ear of the chinchilla was surgically removed to more fully expose the TM, which was then painted with a reflective paint (titanium dioxide). HDH then recorded the shape and the click-induced transient displacement of the surface of TM. Frequency and impulse analyses were used to compare the TM mechanics of the OME and control ears.

We first use the HDH to measure the shape of the exposed TM using the multi-angle method described in Chapter 5 The measurements defined the relative depth of the TM at each x, y location on its surface. We investigated whether the presence of OME affected the shape by

quantifying and comparing the TM depth on along axes: One that ran through the center of the manubrium, and a second that was perpendicular to the first and included the umbo in the center of the TM (**Chapter 8**).

After the shape measurements, we made multiple HDH measurements of the displacement of the TM induced by click-like acoustic transients (as described in Chapter 8). The repeated measurements were often made with different stimulus levels (± 10 dB). The combination of HDH shape and motion measurements allowed us to compute the surface normal motion at each location on the TM surface. The Frequency Response Function at each surface point, $FRF(x,y,f)$, was defined by the ratio of the FFT of the surface normal displacement at each surface location and the FFT of the simultaneously measured stimulus sound pressure waveform measured within 3 mm of the TM. The FRF at each pixel is averaged among the multiple measurements in the same ear. The inverse FFT of the averaged $FRF(x,y,f)$ is then calculated to define the Impulse response Function at each surface point, $IRF(x,y,t)$ (Chapters 5 and 8). After defining the FRF and the IRF the following motion parameters were used to quantify the motion of the TM in the OME and the control ears:

- (1) The **averaged frequency response function** (AFRF) was calculated by averaging the amplitude of the $FRF(x,y,f)$ from each pixel coordinate on the surface of the TM.
- (2) The **dominant frequency**, $DF(x,y)$, of the frequency response at each location on the TM is defined as the frequency component of the $FRF(x,y,f)$ with the highest magnitude
- (3) The **root-mean-square** of the $IRF(x,y,t)$ at each TM location, $IRMS(x,y)$, was derived by calculating the RMS of the first 3 ms of the IRF at each location. The 3 ms threshold is based on the observation that the TM impulse response converges to zero after 3 ms in most cases.

- (4) The **rising time** at each TM location $t^R(x,y)$ denotes the time needed for the $IRF(x,y,t)$ to reach the first peak.
- (5) The **exponential decay time** at each TM location $t^D(x,y)$ was based on a fit of the exponential function $[a e^{bt}]$ to a series of points in the time described by the successive peaks of the first 2 ms of the absolute value of the $IRF(x,y,t)$. The decay time denotes the time ($t^D = -1/b$) when the fitted exponential attains $1/e$ (~36.8%) of the maximum displacement.
- (6) The **damping ratio** as described in Chapter 5 is computed as the reciprocal of the product of the exponential decay time and the dominant frequency (scaled in radians/s):

$$\zeta(x,y) = \frac{1}{\omega_{DF}(x,y) t^D(x,y)} .$$

As we described in Chapter 7 and 8, we used spatial averages of the above motion parameters across distinct regions of the TM to quantify these parameters for comparisons across the different ears. Because it was not possible to expose the entire TM of the live chinchillas to the HDH system without opening the middle ear or damaging the TM, the exposure of the TM surface was limited, and there was little optical access to the inferior part of the TM. Therefore, we divided the TM surface into three areas: superior-anterior, superior-posterior, and umbo areas..

Measurement results

Figure 10.2 compares the shape profile of the OME-infected left ear (blue) and normal right ear (red). The shape profiles of the manubrial position are shown in the left panels, and the shape profiles of the position perpendicular to the manubrium across the center of the umbo are shown in the right panels in each image set. The manubrial positions of the normal and OME-infected ears are compared by aligning the superior end of the manubrial at the tympanic ring to the zero position, with the superior facing to the Figure's left. From the comparison, it can be

concluded that the manubrial positions of the normal and OME-infected ears are similar and little affected by the fluid behind the TM.

The shape profiles perpendicular to the manubrium were defined once the manubrium and tympanic ring were aligned to the zero-shape position. The posterior side of the shape-profile perpendicular to the manubrium is aligned to the left of Figure 10.2. Animals #1 and #2 had a similar perpendicular shape profiles in the Normal and OME ears. The posterior side of Animal #3 was higher in the normal ear, while the posterior sides of Animals #4 and #5 were higher in the OME-infected ear. The OME-infected ear of Animal #6 had a much steeper slope on the posterior side compared with the normal ear.

Figure 10.3 shows AFRFs from repeated displacement measurements in both ears (the Normal ear and the OME ear) in each experimental animal. The repeated measurements (two-per-ear in Animal #1, three-per-ear in the other five animals), were made with somewhat varied excitation levels, and were then normalized by the sound pressure to generate the FRFs at each location on the visible TM surface. The AFRF is the average of the FRF(x,y) over all visible x and y positions. Since the input excitations level normalizes the FRFs, the AFRF from repeated measurements with different stimulus levels should have similar amplitude and frequency dependence. All the measurements except for those from both ears of Animal #6 show high repeatability with the repeated AFRFs plotted on top of each other. The AFRFs of the normal ears had a dominant peak at around 0.8–2 kHz, with a peak magnitude between 3 and 0.3 μm per pascal of sound pressure. Two of the OME ears (Animal# 2 & 4) had peaks at lower frequencies than the normal ear, three (1,3 &5) had peaks at higher frequencies than the normal ear. Two OME ears (2 & 6) had peak magnitudes considerably lower than the normal ear. The other OME ears showed peaks in AFRF that were similar to those observed in the Normal ears. We conclude that AFRF is

not a good indicator of the presence of OME. This conclusion is similar to others' conclusions regarding the limited utility of acoustic admittance (another average surface measurement) in detecting ears that are only partially filled with effusions (Reference).

Associated with the endoscopic changes we see in the OME ears are elevations in two measures of hearing function, ABR and DPOAE. Figure 10.3(b) compares the changes in threshold sound pressure, the lowest sound pressure where a response occurs, that occurred between the start of the study and 5 days after LPS inoculation, in the Normal and OME ears. The figure plots the average threshold change (\pm standard deviation) across the 6 Normal and 6 OME ears. The untreated Normal ears (orange curves) shows little change in these hearing thresholds. In the OME ears (blue curves) the ABR threshold increased by 15 to 30 dB over the 0.5 to 16 kHz frequency range, and the DPOAE threshold increased by 10 to 40 dB. The standard deviations around these measurements clearly separate the increased thresholds of the OME ears from the unchanged thresholds of the Normal ears.

How do the endoscopic difference and changes in hearing threshold compare to the holographic motion measurements? Figure 10.4 shows surface maps of the $IRMS(x,y)$ displacement calculated from the $IRF(x,y,t)$ defined by one of the motion measurements. The OME ear was always the left ear, and the posterior side of the OME ear is to the left. In the right-sided Normal ears, posterior is to the right. The measurements in the Normal ears show patterns of high and low motion magnitude that vary between individuals, with the magnitude of the motion of the manubrium and umbo on the lower end. Both the variation between individuals and low motion of the manubrium have been seen in Normal cadaveric human ears (Chapter 6, 7 & 8). In the OME ears five of the six (#1,2,4,5,6) show less motion on the posterior sides of the TM with a reduction in the complexity of the motion pattern. Please note that due to the limitation of the

TM exposure and the observation angle, the view of the posterior and anterior sides for the left and right ears are not symmetric.

The dominant frequency maps (DF(x,y); Figure 10.5) show different patterns in the normal and OME-infected ears. For Animal #1 in Figure 10.5, the manubrium area of the normal ear had a lower dominant frequency than the OME-infected ear. In the anterior and posterior sides, the OME-infected ear had a lower dominant frequency where the TM was in contact with the fluid. For Animals #2, #3, and #4, the normal ear had overall higher dominant frequencies compared with the OME-infected ear in the manubrial and its surrounding area. The manubrium of the OME-infected ear in Animal 6 had a larger dominant frequency than the normal ear, while the rest of the TM surface had a similar dominant frequency. For Animal #6, the normal ear had a smaller dominant frequency in the manubrium area and posterior side of the TM.

Figure 10.6 illustrates maps of the rising time of the impulse responses $t_R(x,y)$ in the OME and normal ears. In the OME ears the rising time tends to be longer than in the normal ear. The posterior sides of the OME ears (where fluid tends to accumulate) in Animals #1, 2, 4, 5, and 6 had longer rising times. The OME-infected ears of Animals #3 and #5 had increased rising time in the manubrium and its surrounding areas, while the normal ear had decreased rising time in the manubrium and its surrounding areas. The longer the rising time for the TM to reach the maximum displacement, the harder it is for the TM to move consistent with a potential hearing loss.

Figure 10.7 shows maps of the impulse response decay time $t_D(x,y)$ in the OME-infected ears and normal ears. A shorter decay time means the motions on the TM damp out more quickly and should be associated with smaller RMS motion magnitudes. Figure 10.8 shows that the TM's overall decaying time is in the range of 1–5 ms. The deep blue areas with 0 decay time are regions where the exponential fit to the decaying wave form was poor. The computed decay times varies

widely along the TM surface in both the normal and OME ears. The OME-infected ear of Animal #1 had a shorter decaying time in the manubrium area than the normal ear. The OME-infected ears of Animals #2 and #3 had a shorter decaying time in the manubrium area and anterior area than the normal ear. The OME-infected ear of Animal #4 had a shorter decaying time in the anterior area than the normal ear. The OME-infected ears of Animals #5 and #6 had a shorter decaying time in the posterior and manubrium area than the normal ear. Maps of the damping ratio maps derived from the dominant frequency and the decaying time indicate the damping of the entire TM surface (Figure 10.8). This damping ratio only considers the under-damping condition, and the damping ratio over 1 is masked out in the damping ratio maps. Based on the colormap, it can be concluded that the damping ratios of the normal ear in Animals #2,#3,#4, and #5 are overall smaller than the OME-infected ear. In Animal #1, the posterior side has a lower damping ratio than the manubrium. The manubrium has a higher damping ratio than both the anterior and posterior sides in the normal ear. In Animal #6, the manubrium area has a larger damping ratio than the rest of the TM. The larger damping ratio may be attributed to the loading from the inner ear.

To quantify the motion parameters in the OME-infected and normal ear, the surface of the TM was divided into three areas: posterior side, manubrium, and anterior side (see the inset in Figure 10.9), where the region in contact with OME is the posterior half of the OME ear. The motion parameters in each ear (6 OME and 6 normal) were averaged over the three areas, and then these area-averaged motion parameters were then averaged for the 6 individual OME and normal ears, as shown in Figure 10.9. Student t-tests were used to estimate the statistical significance of differences in the motion parameters between the OME and normal ears. In the Figure, one asterisk marks a 5% significance level and two asterisks mark 1% or better significance. The averaged dominant frequencies (Figure 10.9(a)) of the OME-infected ears were lower than the normal ear

in all three areas. The average difference (1.2 kHz in the normal ear vs 1 kHz in OME) was largest along the manubrium, where the standard deviations in the DF of the OME-infected and normal ears are separated without overlap, and the t-test predicted a 5% significance, which suggests the dominant frequency at the manubrium is sensitive to the difference between OME-infected ear and normal ear.

Figure 10.9(b) demonstrates the averaged IRMS values of the OME-infected ears are smaller than the normal ear at all three areas. The variation in RMS magnitude in the normal ears is larger than the OME-infected ear. The largest difference ($0.7 \mu\text{m}/\text{Pa}$ in normals vs. $0.5 \mu\text{m}/\text{Pa}$ in OME ears) occurs in the posterior region (where fluid is most visible in the OME ear) and has a predicted significance of better than 5%.

Figure 10.9(c) shows the area averaged rising time of the in the three area of the OME and normal ears. The averaged rising time of the anterior side (with no visible fluid) of the OME-infected ear was slightly smaller than the normal ear, while the averaged rising time of the posterior and manubrium areas of the OME-infected ear were higher than the normal ear. The difference on the posterior side (0.18 ms in the normal ears and 0.25 ms in OME ears) reached 5% significance.

The decaying time comparison in Figure 10.9(d) shows that on average, the normal ear has a higher average decaying time than the OME-infected ears. While we see the largest OME to Normal difference in decay time (1.13 ms normal vs 1.05 ms in OME ears) in the Anterior section (the region with no visible fluid in the endoscopic images), we also see significant variations in decay time between the different normal ears, and none of the observed difference in Figure 10.9 (d) reach statistical significance.

Figure 10.9(e) shows the averaged damping ratio of the normal and OME-infected ears. The normal ears' damping ratios are lower than the normal ears, and the standard deviation of the

damping ratio in posterior side show good separation between the two middle-ear conditions (a damping ratio of 0.8 in the normal ears and 0.125 in the OME ears) reaching a t-test significance threshold of 1%. These differences suggest the presence of OME increase the damping measured on the TM surface.

Discussion and Conclusion

Our pre and post inoculation endoscopy and hearing tests (Figures 10.1 and 10.2) demonstrate the LPS induced middle ear effusions in the inoculated left ear of the six experimental animals, with no visible cross-contamination to the right ear. The presence of the OME on the left side and the lack of effusion on the right is consistent with the hearing tests that showed 10 to 20 dB elevations in ABR thresholds and 20 to 40 dB elevations in DPOAE thresholds in the OME ears with little change in thresholds in the control ears.

Our observations of the TM's shape in the OME and Normal ears point to little differences in shape along the manubrial axis. Perhaps the bony manubrium adds support to the TM and helps maintain its shape in the presence of effusion. The shape comparison along the perpendicular axis reveals a more complicated story, with the ears from animals 1&2 showing little difference along the perpendicular, animal #3 shows a more acute shape in the Normal ear, and animals 4&5 show more acute shapes in the OME ear. The incomplete view of the TM surface is a complication in these comparisons as our positioning algorithm depends on defining a location along the rim of the help align our coordinate system. In our views, we usually can define such a location along the manubrial projection, but its more difficult along the perpendicular projection.

While the spatial average of the FRF defines one frequency dependent description of TM motion that is easily compared across individuals and different conditions, the loss of spatial variation leads to decreased ability to separate the TM responses in our data set. Figure 10.3

suggests that the presence of effusion leads to differences in the AFRF function, but it also points out significant variations in the AFRFs of the Normal and OME ears. Large variations in other average measurements of TM motion, e.g., acoustic immittance and reflectance, have led to poor sensitivity in the identification of ears that are partially filled with effusions, such as the six animals here (Tang et al., 2021, Prieve et al., 2013).

The maps of motion magnitude and motion parameters maintains spatial variations in these measures, but the complications in the observed patterns of motion (Figure 10.XX), make quantitative comparisons difficult. Our use of partial area averages maintains some of the spatial differences while still simplifying quantitative comparisons. The across area differences in the motion parameters plotted in Figure 10, demonstrate that such an analysis can lead to the identification of significant differences in different areas of the moving TM, these include OME associated decreases in dominant frequency and RMS displacement magnitude, as well as increases in rising time and damping ratio. All of these changes are consistent with spatially dependent OME associated reductions in the mobility of the TM.

To conclude, our high-speed holography measurements show significant changes in TM's mechanical parameters and impulse response in the OME-infected ear, where we also saw significant difference in hearing function in the same OME ears. The motion parameter maps show their spatial variations, and the area's averaged motion parameter provides a more quantitative way of differentiating the OME-infected ear from the normal ear. In the future, an endoscopic instrument using observation and illumination holographic fibers can be designed along with a tunable laser for illumination. The tunable laser source will allow the shape measurement without the need for triangulation volume and increase the dynamic range for displacement measurement. In the current state, the comparison of the motion parameters are between the modified ear and

controlled ear. With the holographic endoscope and a tunable laser, one could measure the shape and motion of the TM through the ear canal. Thus, it will be possible to perform holographic measurement before/ after the LPS injection to assess the changes of the frequency and impulse analysis motion parameters. These changes of the motion parameters can be better compared against the ABR and DPOAE measurements.

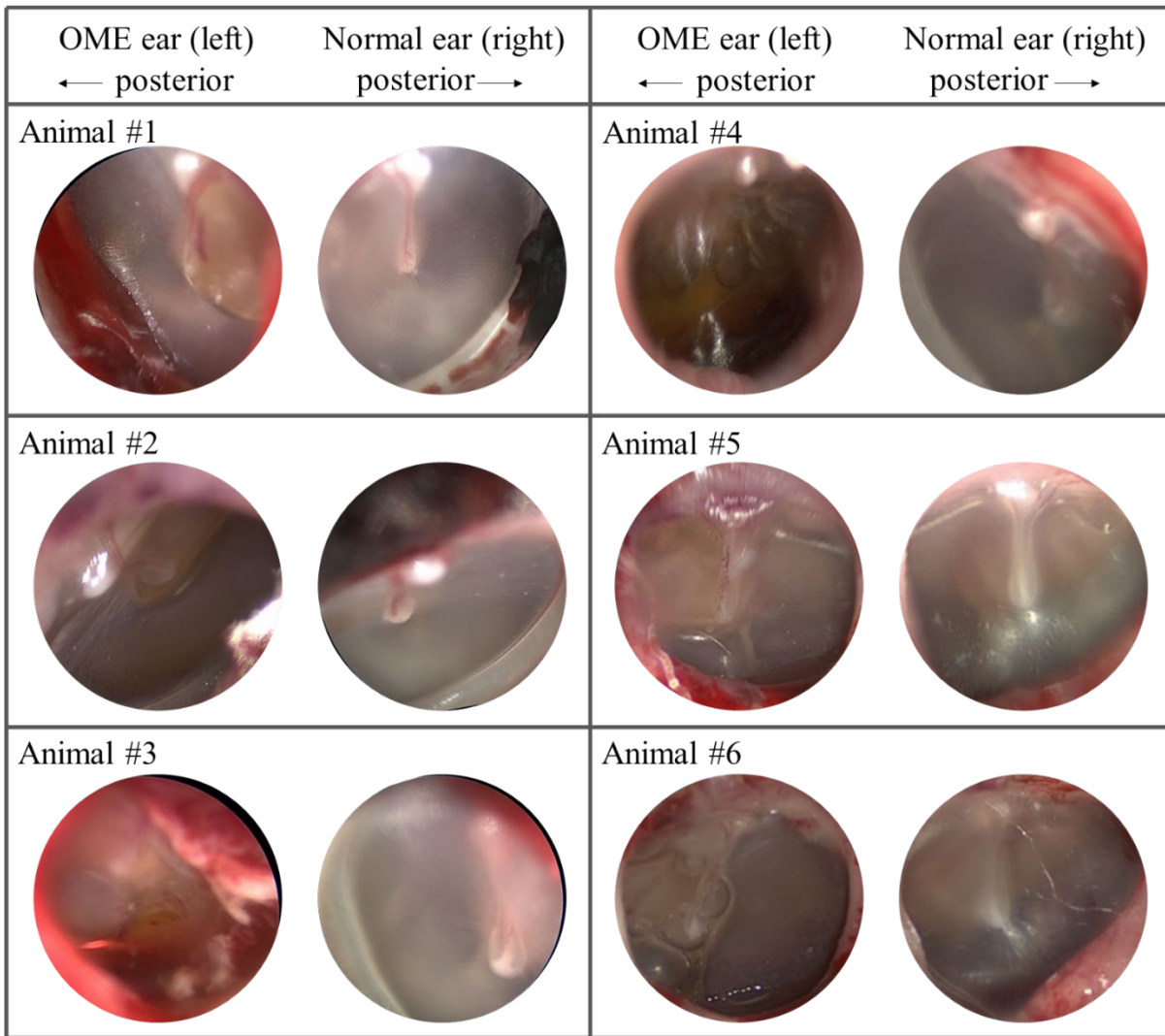


Figure 10.1. Endoscopic images of the TM in six animals. The images were gathered 5 days after inoculation of the left middle ear. The left side of each panel shows the TM of the LPS injected ear; the right side of each panel shows the TM of the control ear. The manubrium and umbo are oriented approximately in the 12 o'clock direction. The LPS injected ears contain yellow or reddish fluid behind the drum (usually behind the posterior TM) with bubbles

sometimes visible (e.g. animal 4 & 6). The TMs of the controlled ears are free of fluid, and the definition of the manubrium and umbo is clear.

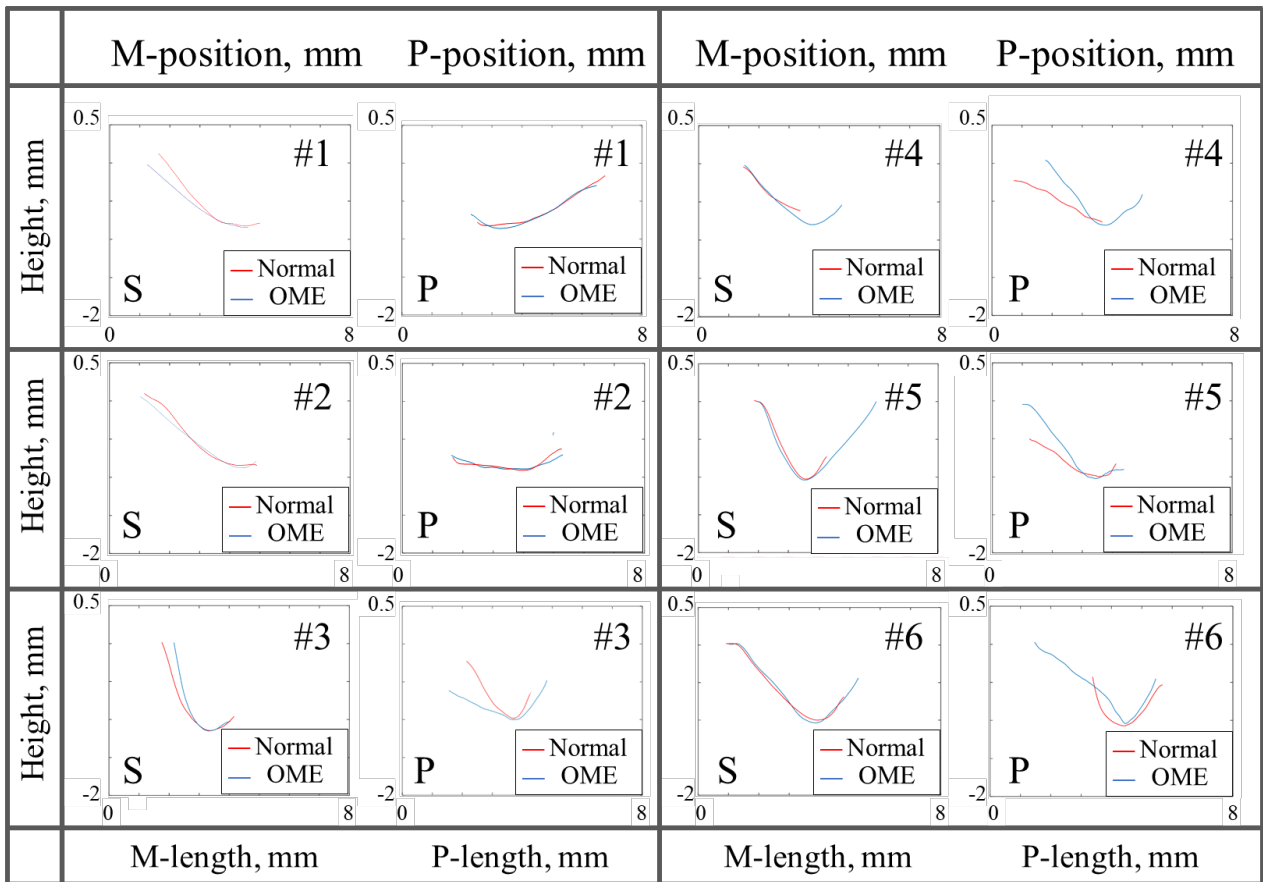
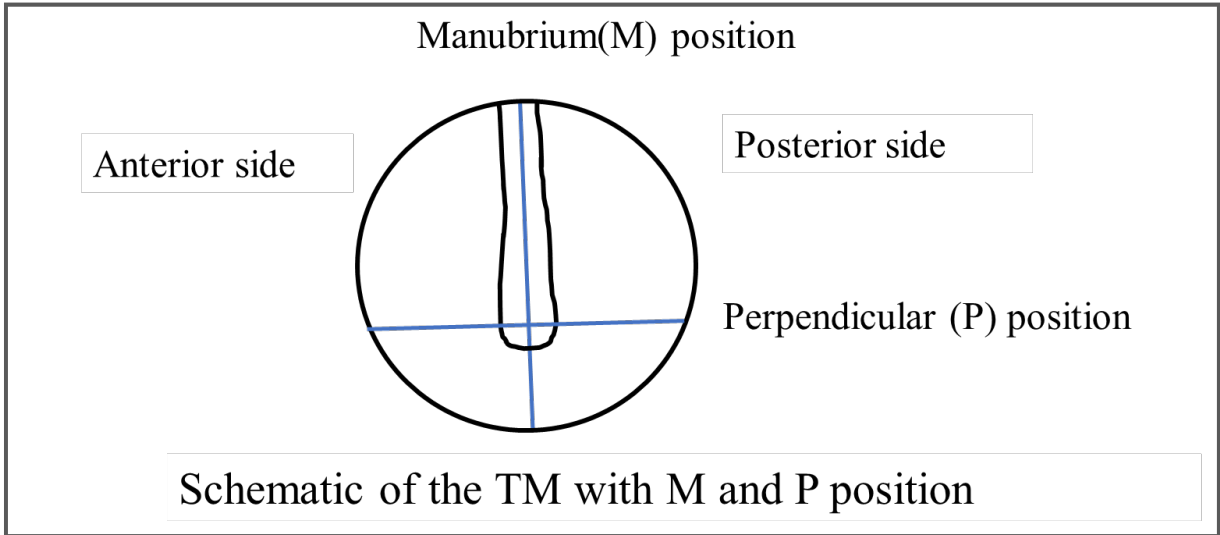


Figure 10.2. The TM height along a Manubrial diameter (M-length) and Perpendicular diameter (P-length) compared between LPS injected ears and controlled ears for Animal #1 to #6. S marks the superior side of the TM and P marks the posterior side of the TM.

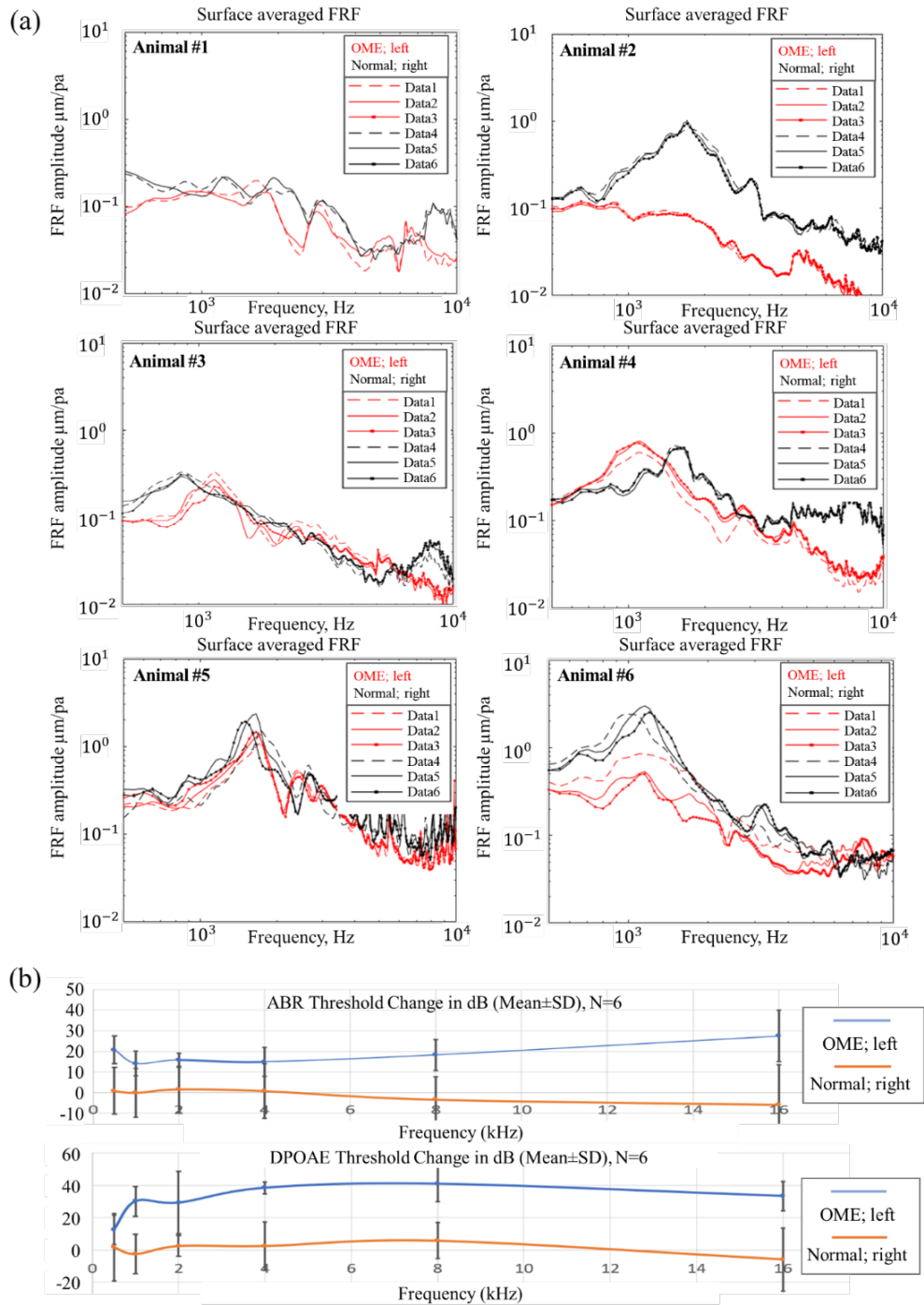


Figure 10.3. (a): The averaged frequency response functions (AFRF) of LPS injection ears are shown in red and controlled (normal) ears are shown in black. Different line type indicates the measurements were taken with different excitation levels. (b): The change of the ABR and DPOAE thresholds before and after 5 days of LPS injection of left ear and right ear. The LPS was only injected into the left ear, and the right ear remained untouched as a control measurement.

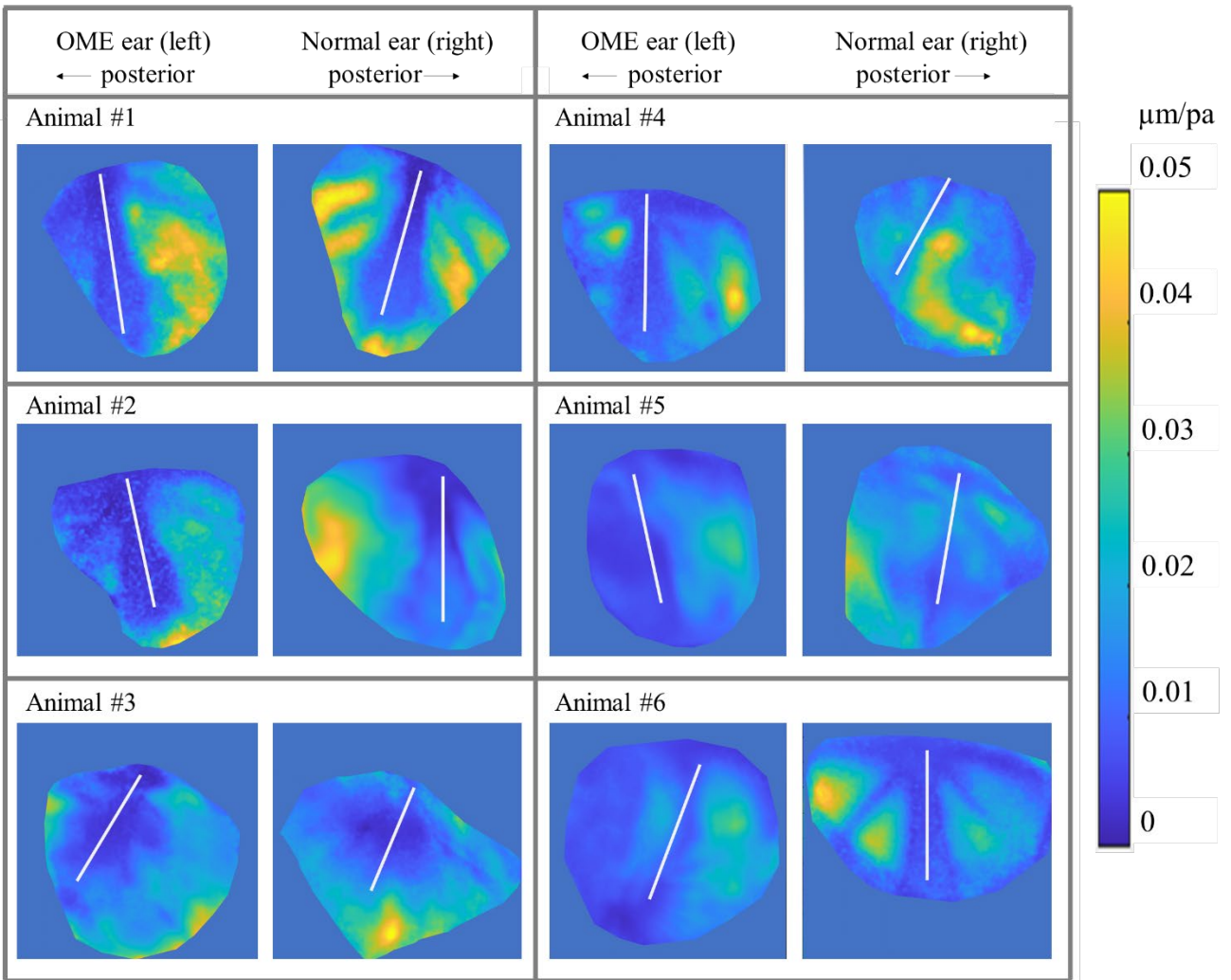


Figure 10. 4. The maps of IRMS, the RMS of the impulse response. The LPS injected ears are on the left of each panel, and the normal ears are on the right. In each ear the manubrium is aligned in the 12 o'clock direction with the umbo at the bottom of the manubrium. White line marks the center of the umbo to the superior most end of the manubrium.

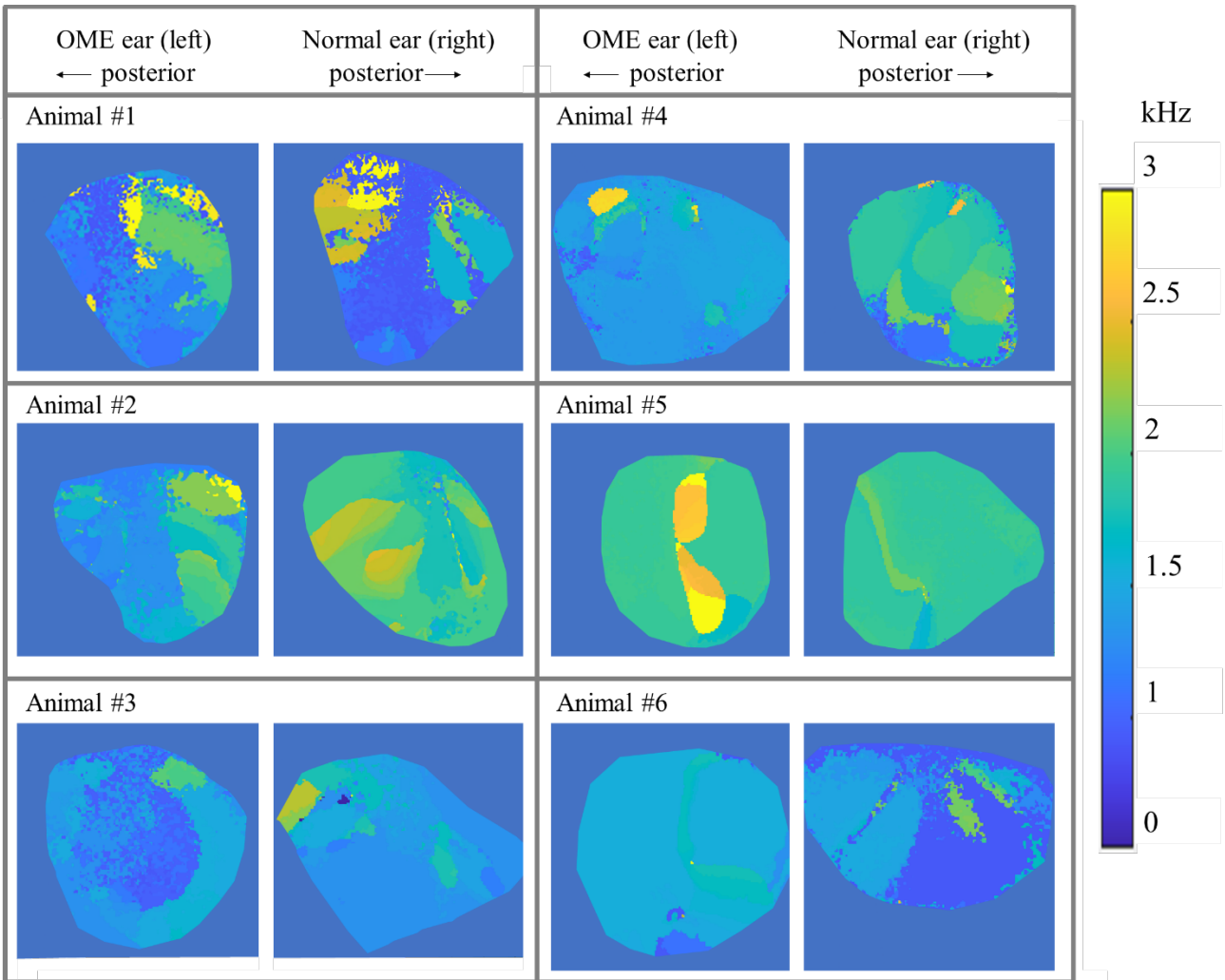


Figure 10.6. Maps of the dominant frequencies of OME with LPS injected ears and normal ears. The left ears are injected with the LPS, and the right ears are measured as a control. The dominant frequencies are determined by locating the frequency with the maximum FRF amplitude in the frequency domain. The dominant frequency maps show a large variation between 500 Hz to 3 kHz.

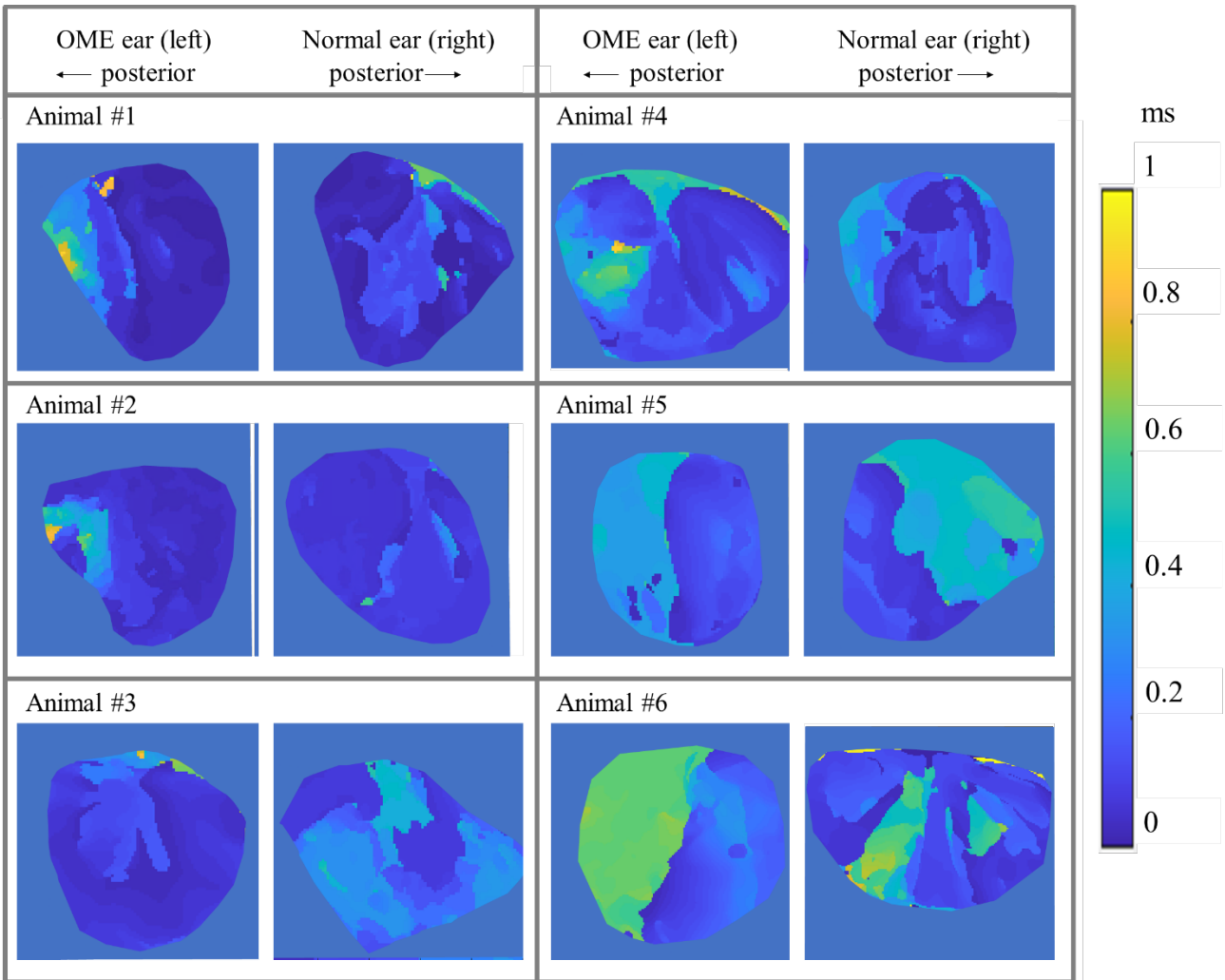


Figure 10.7. Maps of the Rising time of the OME with LPS injected ears (left) and normal (right) ears. The manubrium are aligned in the 12 o'clock direction, and the posterior directions are marked respectively for each side of the ears. The rising time is calculated from the impulse response function, and it is the time for each TM point to travel to its maximum displacement.

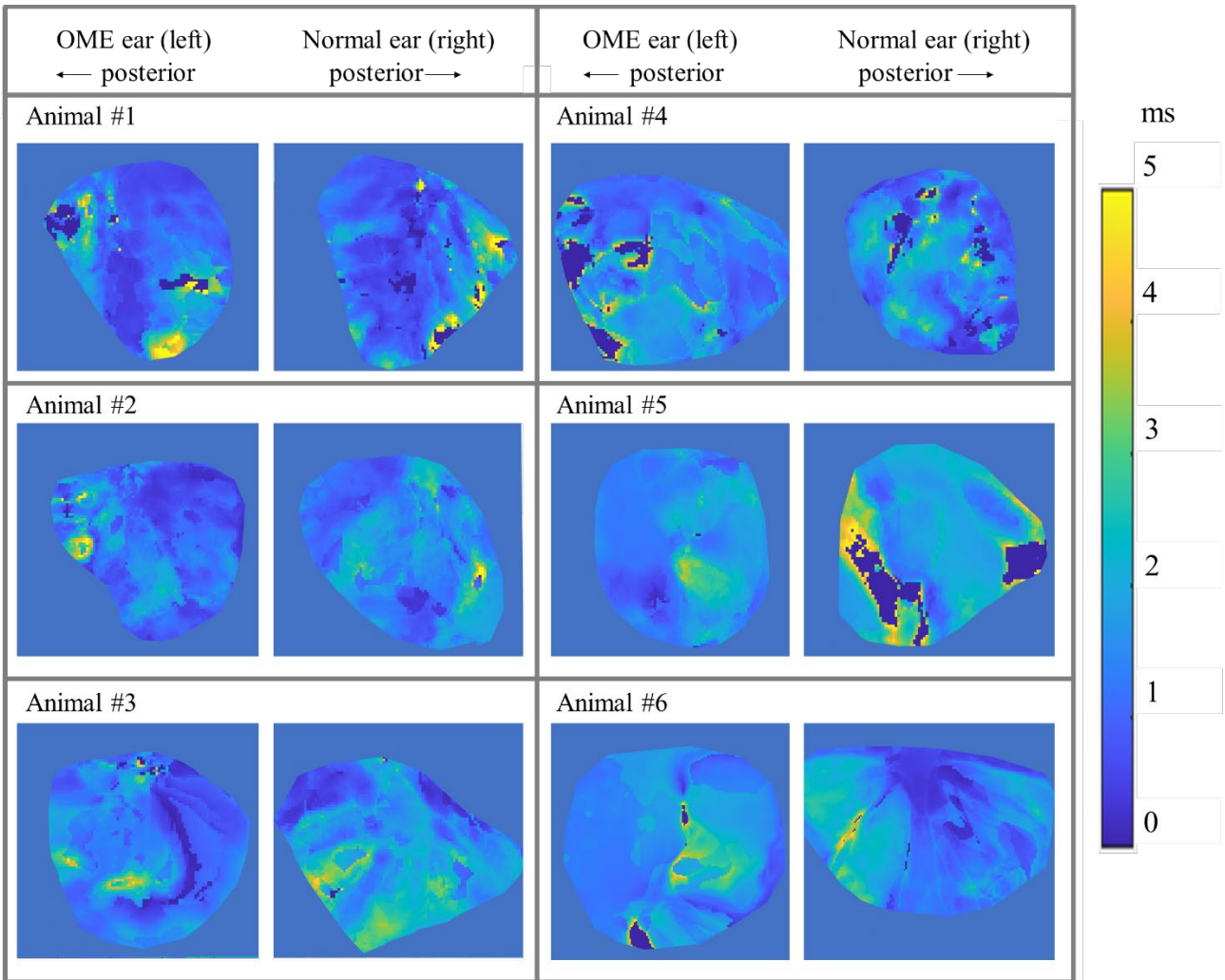


Figure 10.8. Maps of the Decaying time of the OME with LPS injected ears (left) and normal (right) ears with manubrium orientated at 12 o'clock. The decaying time suggests how fast the TM surface will damp out the surface vibration, and it is related to the estimation of the damping of the mechanical properties.

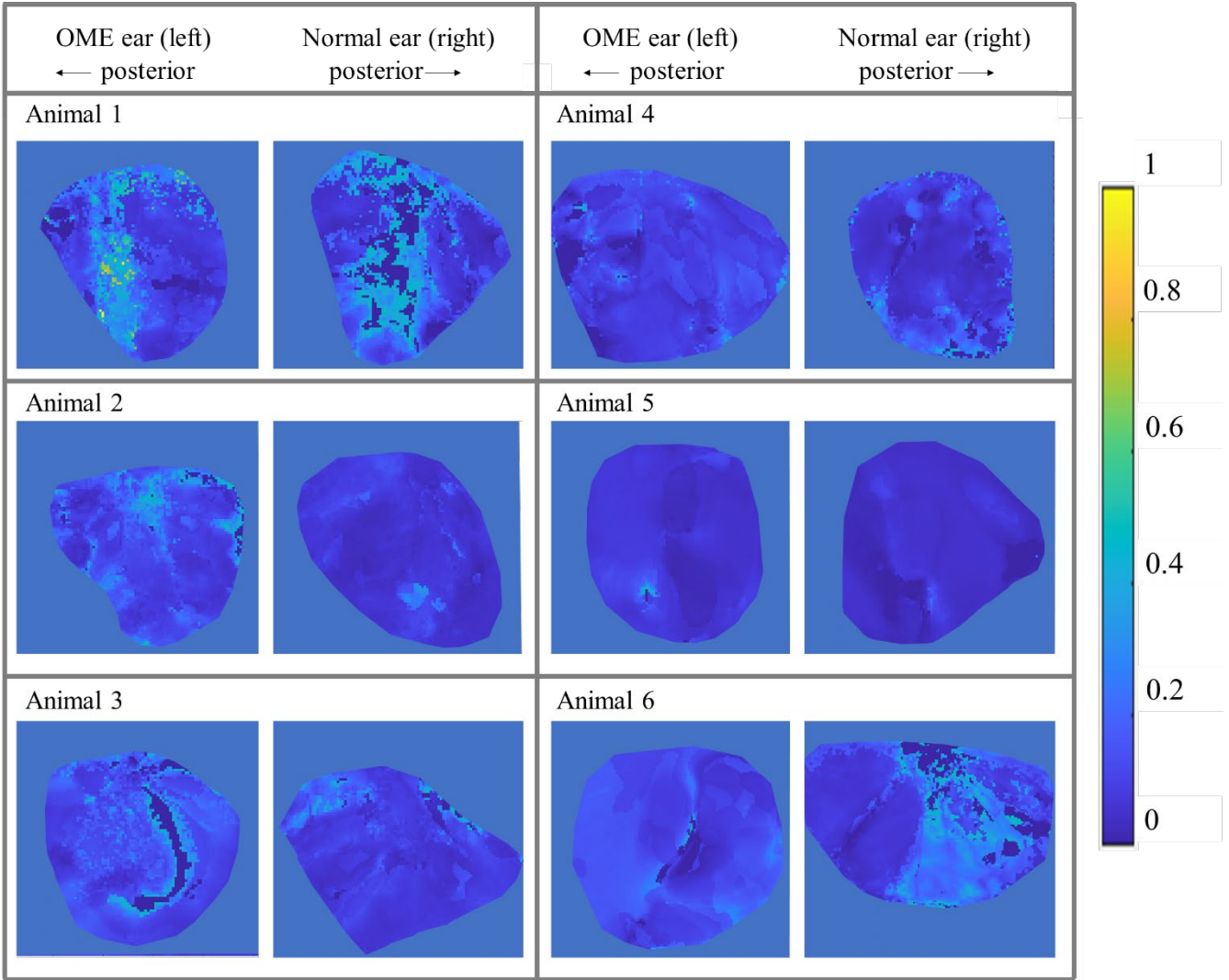


Figure 10.9. Maps of the damping ratio of the LPS injected ears in the left panel and normal ear in the right panel. The damping ratio is estimated based on the dominant frequencies and decaying time of each measured point on the TM. The damping ratio calculated here is the middle ear's system damping, including the effect from the middle cavity and the loads from the inner ear.

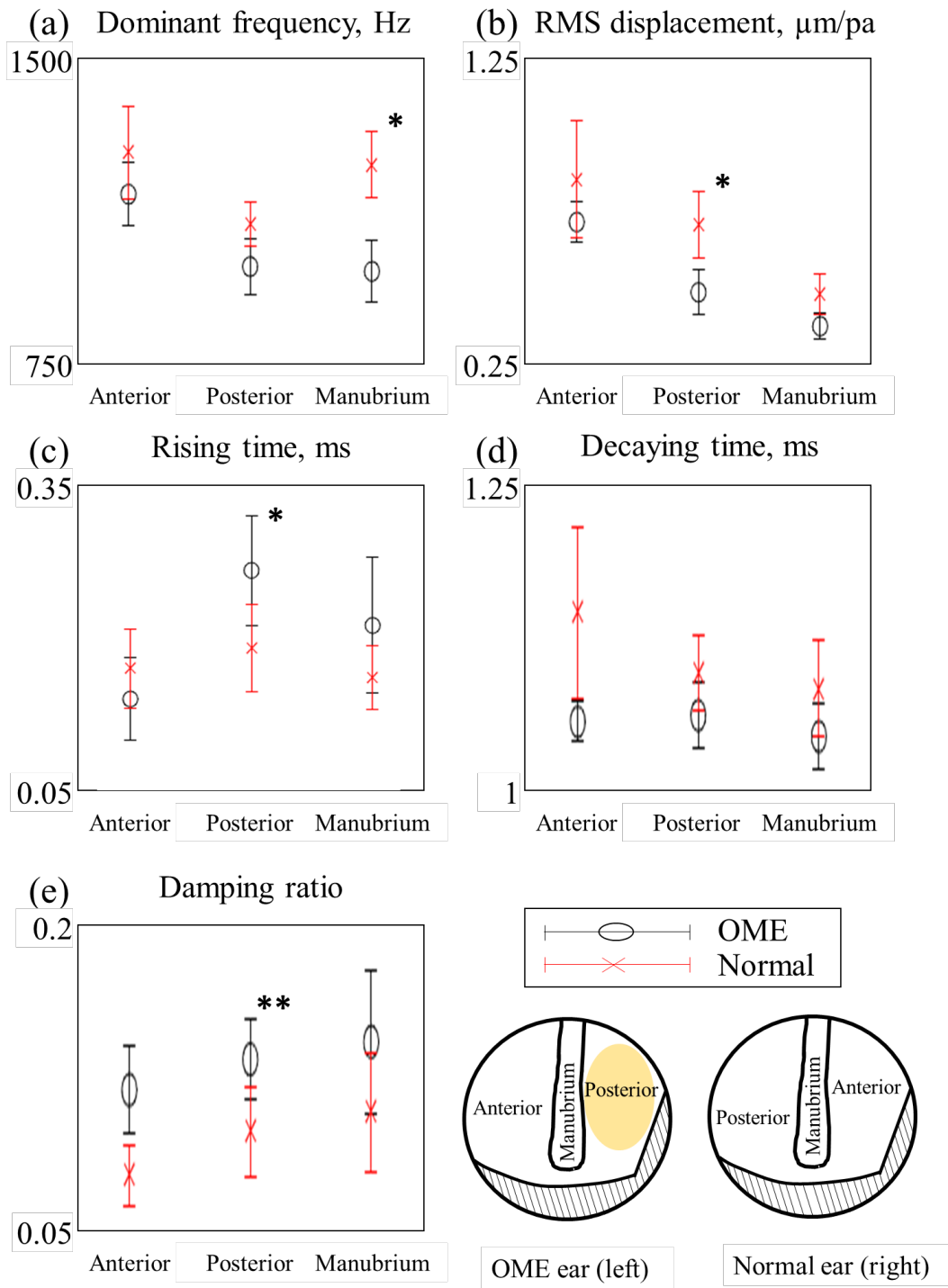


Figure 10.10. The areas averaged motion parameters for anterior, posterior, and manubrium areas: (a) dominant frequencies, (b) RMS of the impulse response, (c) rising time, (d) decaying time, and (e) damping ratio. The averaged motion parameters of LPS injected (OME) ears, and their standard deviations are shown in black, while the control ears(normal) data are red.

Chapter 11 Conclusions and Future Work

We have developed laser holographic interferometry and fringe projection systems to quantify shape and sound-induced motions of the mammalian TMs for investigations of middle ear mechanics and pathologies. 3D shape and transient sound-induced motion of live animal TM have been characterized using these new holographic systems with a spatial resolution of more than one million points on the surface of the TM and a temporal resolution of >65 kHz for impulsive acoustic stimuli. Sound-induced motion measurements are combined with shape measurements to characterize surface normal sound-induced motion components. The motion and shape measurements are performed within a fraction of a sound to minimize the time-varying factors of biological samples. Furthermore, the measurement results are analyzed in the frequency domain to extract meaningful motion parameters to describe the TM's characters and provide information for middle ear diseases diagnosis.

The newly developed shape measurement method using a miniaturized fringe projection system with a MEMS mirror was compared with two multi-wavelength and multi-angle methods. For the shape measurement, even though the multi-wavelength method performs best on measuring well-illuminated surfaces (i.e., NIST gauge), the measurement quality largely depends on how much light is captured by the high-speed camera. The Fringe projection method is faster in terms of data processing time, and it utilizes the illumination power more efficient by single line projection. However, the fringe projection and multi-angle methods require triangulation volume, causing challenges to measurements on live intact ears.

Frequency and impulse response analyzes are applied to study the human TM with different experimentally introduced middle ear conditions. Displacement data in the time domain show we can distinguish the presence of fluid inside the middle ear cavity. We observed different trends of

CMIFs and AFRFs associated with different middle ear conditions in the frequency domain. We also proposed different motion parameters derived from the frequency and impulse analysis to describe the TM mechanics. Those motion parameters are then averaged based on the locations of the TM surface to study the statistical significance of those parameters in differencing the middle ear conditions. Those measurements and analyzes are applied to study the live chinchilla ear with Otitis Media with Effusion.

To conclude, our high-speed holography measurements show significant changes in TM's mechanical parameters and impulse response in the OME-infected ear, consistent with the ABR and DPOAE measurements with a much short measurement time and additional shape information for diagnosis from the high-speed holographic measurements. The results are correlated to hearing losses in these ears. The holographic measurements' analyses show the spatial variations of the different motion parameters. The averaged motion parameter from different regions of the TM provides a more quantitative way of differentiating the OME-infected ear from the normal ear.

A general conclusion is that TMs with fluid-filled middle ear cavities have 10 – 20 dB smaller frequency responses. Preliminary impulse response analysis suggests that the response of the TM with stapes fixation often has a slight increase in rising time and decaying time along as a result of more stiffness in the ossicles. TM with IS joint interruption will also cause the rising time and decaying time to increase, but the increases are more significant than the case of stapes fixation. Moreover, the IS joint interruption can be distinguished from the stapes fixation because the IS joint interruption also reduces the dominant frequency for the entire surface of the TM.

The developments in optical mythologies and the data analysis method will lead to new findings in hearing research and encourage the development of new techniques in optics, lasers, and imaging systems for clinical applications. The next phase of this project is to measure the TM

response under blast-like sound and make the holographic system suitable for live subjects without surgically removing the ear canal.

The following should be considered as future work and a road map.

11.1 Increase the dynamic range of the holography displacement measurement:

The TM will deform much more, reaching sub-millimeter scale under high-intensity sound from the blast-like excitation, and the current holographic system does not have the measurement range. Hence, one approach utilizing two laser sources are proposed below in **Figure 11.1**

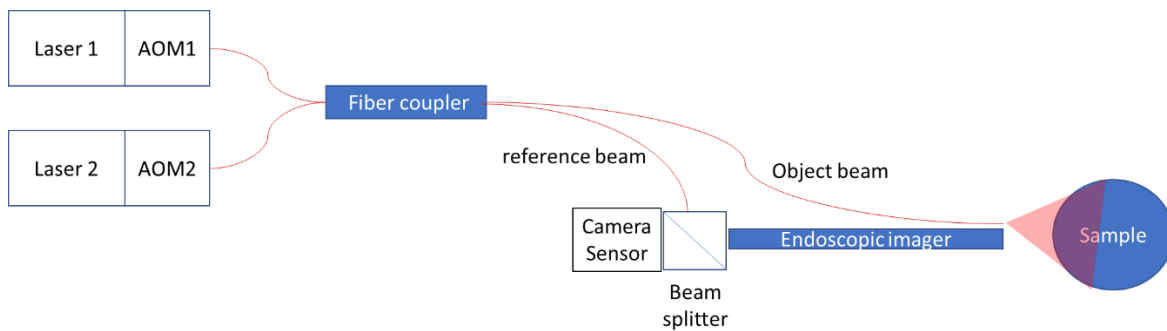


Figure 11.1 Proposed schematic of the holographic system to measure larger deformations of the TM under blast-like excitation. Two lasers are used as coherent light sources. The wavelength of each laser should be carefully chosen to generate a desired synthetic wavelength. At least one wavelength-tunable laser is preferred to increase the flexibility of the synthetic wavelength range.

In the Proposed schematic shown in Figure 11.1, Laser 1 is preferable a wavelength-tunable laser, and Laser 2 is a single frequency laser with its wavelength within the range of the tunable laser. AOM 1 and AOM 2 are acousto-optic modulators to switch the laser illumination. Laser beams are coupled into optical fibers for easy manipulation and space-saving. A fiber coupler combines the two laser sources into the same optical path and divides them into an object

beam and a reference beam. And an endoscopic imager is used to observe the sample through the ear canal. And a beam splitter is placed between the camera sensor and endoscopic imager to combine the object beam and reference beam allowing interference. Phase shifting is not included in this schematic. One can add a PZT mounted mirror between the reference beam and the beam splitter for temporal phase shifting. Or a camera sensor with a pixelated polarizing filter can be used for spatial phase shifting.

Before the measurement, the wavelength of the tunable laser is selected so that the synthetic wavelength of Laser 1 and Laser 2 is suitable for the range of the target's deformation. The AOMs alternate the illumination between the two lasers for each camera frame during the measurement. Each pair of the camera frames generates a hologram of the synthetic wavelength allowing the system to measure the surface deformations of the sample with the measuring range dominated by the synthetic wavelength.

11.2 Full-field 3D Force measurements:

In terms of force measurements, previous studies have shown that force measurements should be improved significantly so that instead of having the measurements at a few points with a rigid tip MEMS force sensor, a 2D grid of points on the surface of the TM should be measured simultaneously. Therefore, it requires a newly designed force sensor that is able to scan all those points for the full-field sound-induced force of the TM. Furthermore, the newly designed force sensor should measure 1D sound-induced force along the surface normal direction and be able to measure the tangential direction. To achieve such goal, nano 3D printing technology can be applied in the design and implementation of such force sensors.

11.3 Improve the design of the shock tube for blast delivery

The work presented in this dissertation is focused on the TM response to the sound pressure within normal conversation level. We are also interested in investigating of the TM response to large or blast-like sound. That information will provide valuable information to understand hearing loss due to exposure of loud sound or improve hearing protection devices. In the past, we have designed, constructed, and characterized an acoustic loading apparatus to deliver a known and controlled transient acoustic force, representative of a blast, enabling accurate and repeatable investigations on the mechanics of the TM at high loading rates. However, the output of the blast tube was not strong enough to rupture postmortem human TM. To increase the amount of energy received by the sample, the TM had to be positioned in very close vicinity to the output of the Tube, blocking the optical path of the measurement system. An improved version of the shock tube should be implemented that allows a clear optical path for the holographic system to image the measured object and is able to protect the experiment apparatus from the high energy generated by the shock tube.

References

- Lin, F. R., J. K. Niparko, and L. Ferrucci (2011) "Hearing loss prevalence in the United States." *Archives of internal medicine* 171, no. 20: 1851-1853.
- Lim, D. J. (1970) "Human tympanic membrane: an ultrastructural observation." *Acta oto-laryngologica* 70, no. 3: 176-186.
- Kawabata, I., and H. Ishii (1971) "Fiber Arrangement in the Tympanic Membrane: Scanning Electron Microscope Observations." *Acta oto-laryngologica* 72, no. 1-6: 243-254.
- Hofmeyr, L. (2021) "3D-Printed titanium ossicular chain reconstruction—Hype or reality?." *Medical Chronicle* 2021, no. 1: 14-16.
- Rosowski, J. J., S. Stenfelt and D. Lilly (2013). An overview of wideband immittance measurements, techniques and terminology: You say absorbance, I say reflectance. *Ear Hear*, 34, 9S-16S.
- Hunter, L. L, B. A. Prieve, J. Kei and Sanford (2013). Pediatric application of wideband acoustic immittance measures. *Ear Hear*, 34, 36s-42s.
- Nakajima, H. H, D. V. Pisano, C. Rösli, M. A. Hamade, G. Merchant, L. Mafoud, C. Furlong, J. J. Rosowski, and Merchant (2012). Comparison of ear-canal reflectance and umbo velocity in patients with conductive hearing loss: A preliminary study. *Ear Hear*, 33, 35-43.

- Foth, H., C. Huthoff, M. Brenner, S. Färber, N. Stasche, A. Baker-Schreyer, and K. Hörmann (1996) "Measuring the motions in the human middle ear by Laser Doppler Vibrometry." *Optics and lasers in engineering* 25, no. 4-5: 289-301.
- de La Rochefoucauld, O., and E. S. Olson (2010) "A sum of simple and complex motions on the eardrum and manubrium in gerbil." *Hearing research* 263, no. 1-2: 9-15.
- Rosowski, J. J., R. P. Mehta, and S. N. Merchant (2003) "Diagnostic utility of laser-Doppler vibrometry in conductive hearing loss with normal tympanic membrane." *Otology & neurotology: official publication of the American Otological Society, American Neurotology Society [and] European Academy of Otology and Neurotology* 24, no. 2: 165.
- Decraemer, W. F., O. de La Rochefoucauld, W. R. J. Funnell, and E. S. Olson (2014) "Three-dimensional vibration of the malleus and incus in the living gerbil." *Journal of the Association for Research in Otolaryngology* 15, no. 4: 483-510.
- Zhang, X., X. Guan, D. Nakmali, V. Palan, M. Pineda, and R. Z. Gan (2014) "Experimental and modeling study of human tympanic membrane motion in the presence of middle ear liquid." *Journal of the Association for Research in Otolaryngology* 15, no. 6: 867-881.
- Salman, M., (2012) "Continuous scanning laser doppler vibrometry for synchronized array measurements: applications to non-contact sensing of human body vibrations." PhD diss., Georgia Institute of Technology.

- Huber, A. M., C. Schwab, T. Linder, S. J. Stoeckli, M. Ferrazzinin, N. Dillier and U. Fisch (2001). "Evaluation of eardrum laser doppler interferometry as a diagnostic tool," *The Laryngoscope*, 111, 501-507.
- Whittimore, K. R., S. N. Merchant, B. B. Poon, and J. J. Rosowski (2004). A normative study of tympanic membrane motion in humans using a laser Doppler vibrometer (LDV). *Hear Res*, 187, 85-104.
- Khanna, S. M., and J. Tonndorf (1972) "Tympanic membrane vibrations in cats studied by time-averaged holography." *The Journal of the Acoustical Society of America* 51, no. 6B: 1904-1920.
- Rosowski, J. J., J. T. Cheng, M. E. Ravicz, N. Hulli, M. Hernandez-Montes, E. Harrington, and C. Furlong (2009) "Computer-assisted time-averaged holograms of the motion of the surface of the mammalian tympanic membrane with sound stimuli of 0.4–25 kHz." *Hearing research* 253, no. 1-2: 83-96.
- Cheng, J. T., A. A. Aarnisalo, E. Harrington, M. del Socorro Hernandez-Montes, C. Furlong, S. N. Merchant, and J. J. Rosowski (2010) "Motion of the surface of the human tympanic membrane measured with stroboscopic holography." *Hearing research* 263, no. 1-2: 66-77.
- Cheng, J. T., M. Hamade, S. N. Merchant, J. J. Rosowski, E. Harrington, and C. Furlong (2013) "Wave motion on the surface of the human tympanic membrane: holographic measurement and modeling analysis." *The Journal of the Acoustical Society of America* 133, no. 2: 918-937.

- Rosowski, J. J., I. Dobrev, M. Khaleghi, W. Lu, J. T. Cheng, E. Harrington, and C. Furlong (2013) "Measurements of three-dimensional shape and sound-induced motion of the chinchilla tympanic membrane." *Hearing research* 301: 44-52.
- Mota, C., S. Danti, D. D'Alessandro, L. Trombi, C. Ricci, D. Puppi, D. Dinucci (2015) "Multiscale fabrication of biomimetic scaffolds for tympanic membrane tissue engineering." *Biofabrication* 7, no. 2: 025005.
- Zhang, Q., L. Liu, Q. Yong, J. Deng, and W. Cao (2015) "Intralesional injection of adipose-derived stem cells reduces hypertrophic scarring in a rabbit ear model." *Stem cell research & therapy* 6, no. 1: 1-11.
- Fay, J., S. Puria, W. F. Decraemer, and C. Steele (2005) "Three approaches for estimating the elastic modulus of the tympanic membrane." *Journal of biomechanics* 38, no. 9: 1807-1815.
- Fay, J. P., S. Puria, and C. R. Steele(2006) "The discordant eardrum." *Proceedings of the National Academy of Sciences* 103, no. 52: 19743-19748.
- Cohen, M. S., L. D. Landegger, E.D. Kozin, and D. J. Lee (2016) "Pediatric endoscopic ear surgery in clinical practice: lessons learned and early outcomes." *The Laryngoscope* 126, no. 3: 732-738.
- Gan, R. Z., B. Feng, and Q. Sun (2004) "Three-dimensional finite element modeling of human ear for sound transmission." *Annals of biomedical engineering* 32, no. 6: 847-859.
- Zwislocki, J. "Analysis of the middle-ear function. Part I: input impedance (1962)" *The journal of the Acoustical Society of America* 34, no. 9B: 1514-1523.

- Martínez-Lera, P., J. D. Greef, and M. Tournour (2015) "A Finite Element Strategy to Compute Aerodynamic Sound with Lighthill's Analogy." In *Proceedings of the 22nd International Congress on Sound and Vibration, International Inst. of Acoustics and Vibration*, Florence, Italy, pp. 1-8.
- Funnell, W. J. Robert, and A. L. Charles (1978) "Modeling of the cat eardrum as a thin shell using the finite-element method." *The Journal of the Acoustical Society of America* 63, no. 5: 1461-1467.
- Rosowski, J. J & Merchant, S. N (1995). "Mechanical and acoustic analysis of middle ear reconstruction". *Am J Otol*, 16, 486-497.
- Voss, S. E, J. J. Rosowski, S. N. Merchant and W. T. Peake (2001). "Middle-ear function with tympanic membrane perforations". II. A simple model. *J Acoust Soc Am*, 110, 1445-1452.
- Price, G. Richard, and J. T. Kalb (1998) "Modeling the effect of a hearing protector on the waveform of intense impulses." *The Journal of the Acoustical Society of America* 103, no. 5: 2878-2878.
- Price, G. R and J. T. Kalb (1991). Insight into hazard from intense impulses from a mathematical model of the ear. *J. Acoust. Soc. Am.*, 90, 219-227.
- Zagadou, B., P. Chan, K. Ho, and D. Shelley (2016). "Impulse noise injury prediction based on cochlear energy," *Hear Res.* 342, 23–38.

- Gan, R. Z., D. Nakmali, X. D. Ji, K. Leckness, and Z. Yokell (2016) "Mechanical damage of tympanic membrane in relation to impulse pressure waveform—a study in chinchillas." *Hearing research* 340: 25-34.
- Rabbitt, R. D., and M. H. Holmes (1986) "A fibrous dynamic continuum model of the tympanic membrane." *The Journal of the Acoustical Society of America* 80, no. 6: 1716-1728.
- Wang, X., and R. Z. Gan. (2016) "3D finite element model of the chinchilla ear for characterizing middle ear functions." *Biomechanics and modeling in mechanobiology* 15, no. 5: 1263-1277.
- Dobrev, I., C. Furlong, J. T. Cheng, and J. J. Rosowski (2014) "Full-field transient vibrometry of the human tympanic membrane by local phase correlation and high-speed holography." *Journal of biomedical optics* 19, no. 9: 096001.
- Razavi, P., J. T. Cheng, C. Furlong, and J. J. Rosowski (2017) "High-speed holography for in-vivo measurement of acoustically induced motions of mammalian tympanic membrane." In *Mechanics of Biological Systems and Materials*, Volume 6, pp. 75-81. Springer, Cham.
- Buunen T. J. F. (1981). "Laser-Doppler velocity meter applied to tympanic membrane vibrations in cat". *J. Acoust. Soc. Am.*, 69, 744-750.
- Chang E. W., J. T. Cheng, C. Rööslı, J. B. Kobler, J. J. Rosowski , S. H. Yun (2013). Simultaneous 3D imaging of sound-induced motions of the tympanic membrane and middle ear ossicles. *Hear Res*, 304, 49-56.

- Maru, K., K. Kobayashi, and Y. Fujii (2010) "Multi-point differential laser Doppler velocimeter using arrayed waveguide gratings with small wavelength sensitivity." *Optics Express* 18, no. 1: 301-308.
- Ehrhardt, D. A., M. S. Allen, S. Yang, and T. J. Beberniss. (2017) "Full-field linear and nonlinear measurements using continuous-scan laser doppler vibrometry and high speed three-dimensional digital image correlation." *Mechanical Systems and Signal Processing* 86: 82-97.
- Tonndorf, J., and S. M. Khanna (1972) "Tympanic-membrane vibrations in human cadaver ears studied by time-averaged holography." *The Journal of the Acoustical Society of America* 52, no. 4B: 1221-1233.
- Dancer, A. L., R. B. Franke, P. Smigielski, F. Albe, and H. Fagot (1975) "Holographic interferometry applied to the investigation of tympanic-membrane displacements in guinea pig ears subjected to acoustic impulses." *The Journal of the Acoustical Society of America* 58, no. 1: 223-228.
- Dobrev, I., C. Furlong, J. T. Cheng, and J. J. Rosowski (2015) "Optimization of a lensless digital holographic otoscope system for transient measurements of the human tympanic membrane." *Experimental mechanics* 55, no. 2: 459-470.
- Khaleghi, M., J. Guignard, C. Furlong, and J. J. Rosowski (2015) "Simultaneous full-field 3-D vibrometry of the human eardrum using spatial-bandwidth multiplexed holography." *Journal of biomedical optics* 20, no. 11: 111202.
- Dobrev, I. "Full-field vibrometry by high-speed digital holography for middle-ear mechanics." PhD diss., Worcester Polytechnic Institute, 2014.

- Razavi, Payam, Haimi Tang, John J. Rosowski, Cosme Furlong, and Jeffrey T. Cheng. "Combined high-speed holographic shape and full-field displacement measurements of tympanic membrane." *Journal of Biomedical Optics* 24, no. 3 (2018): 031008.
- Schnars, Ulf, Claas Falldorf, John Watson, and Werner Jüptner. "Digital holography." In *Digital Holography and Wavefront Sensing*, pp. 39-68. Springer, Berlin, Heidelberg, 2015.
- Kreis, Thomas M. "Frequency analysis of digital holography." *Optical Engineering* 41, no. 4 (2002): 771-778.
- Wykes, C., and R. Jones. "Advances In Optical Metrology Of Complex Objects." In *Max Born Centenary Conf*, vol. 369, pp. 200-206. SPIE, 1983.
- Schmitt, Douglas R., and R. W. Hunt. "Optimization of fringe pattern calculation with direct correlations in speckle interferometry." *Applied Optics* 36, no. 34 (1997): 8848-8857.
- Psota, Pavel, Haimi Tang, Koohyar Pooladvand, Cosme Furlong, John J. Rosowski, Jeffrey T. Cheng, and Vít Lédl. "Multiple angle digital holography for the shape measurement of the unpainted tympanic membrane." *Optics Express* 28, no. 17 (2020): 24614-24628.
- Su, Wei-Hung. "Color-encoded fringe projection for 3D shape measurements." *Optics Express* 15, no. 20 (2007): 13167-13181.

- Xu, Y., S. Jia, Qi. Bao, H. Chen, and J. Yang (2014) "Recovery of absolute height from wrapped phase maps for fringe projection profilometry." *Optics express* 22, no. 14: 16819-16828.
- Bally, G. von. (1979) "Otological investigations in living man using holographic interferometry." In *Holography in Medicine and Biology*, pp. 198-205. Springer, Berlin, Heidelberg,
- Ogura, Y., Y. Masuda, M. Miki, T. Takeda, S. Watanabe, T. Ogawara, S. Shibata, T. Uyemura, and Y. Yamamoto. (1979) "Vibration analysis of the human skull and auditory ossicles by holographic interferometry." *In Holography in Medicine and Biology*, pp. 218-222. Springer, Berlin, Heidelberg,
- Bally, G. von. "Holography in medicine and biology-state of the art and the problem of increasing militarization." *Optical Metrology* (1987): 441-458.
- Ogura, Y., Y. Masuda, M. Miki, T. Uyemura, and Y. Yamamoto. (1979) "Application of holographic interferometry to the study of hearing mechanism." *In 13th Intl Congress on High Speed Photography and Photonics*, vol. 189, pp. 772-775. SPIE.
- Uyemura, T., N. Yokoyama, Y. Ohba, Y. Yamamoto, Y. Ogura, T. Takeda, T. Ogawara, and S. Kawakami (1983) "Development Of Pulse Holo-Camera For Observation Of Vibration Of Human Eardrum." *In 15th Intl Congress on High Speed Photography and Photonics*, vol. 348, pp. 666-669. SPIE.
- Koike, T., H. Wada, and T. Kobayashi (2002) "Modeling of the human middle ear using the finite-element method." *The Journal of the Acoustical Society of America* 111, no. 3: 1306-1317.

- Solís, S. Muñoz, F. Mendoza Santoyo, and M. del Socorro Hernández-Montes (2012) "3D displacement measurements of the tympanic membrane with digital holographic interferometry." *Optics express* 20, no. 5: 5613-5621.
- Dirckx, J. J. J, and W. F. Decraemer (1997) "Optoelectronic moiré projector for real-time shape and deformation studies of the tympanic membrane." *Journal of Biomedical Optics* 2, no. 2: 176-185.
- Liang, J., K. D. Smith, H. Lu, T. W. Seale, and R. Z. Gan (2018) "Mechanical properties of the Papio anubis tympanic membrane: Change significantly from infancy to adulthood." *Hearing research* 370: 143-154.
- Liang, M., H. Xiong, Y. Cai, Y. Chen, Z. Zhang, S. Chen, Y. Xu, Y. Ou, H. Yang, and Y. Zheng (2016) "Effect of the combination of balloon Eustachian tuboplasty and tympanic paracentesis on intractable chronic otitis media with effusion." *American Journal of Otolaryngology* 37, no. 5: 442-446.
- Estrada, J. C., M. Servin, and J. Vargas (2012) "2D simultaneous phase unwrapping and filtering: A review and comparison." *Optics and Lasers in Engineering* 50, no. 8: 1026-1029.
- Yost, W. (2006) "A. Fundamentals of Hearing: An Introduction". 5th edn. (New York: Academic Press.
- Fastl, H. and E. Zwicker(2007) "Information processing in the auditory system. in Psychoacoustics" Berlin, Heidelberg: Springer, 10.1007/978-3-540-68888-4_3.

- Vollandri, G. et al. (2011). “Biomechanics of the tympanic membrane”. *Journal of Biomechanics* 44, 1219-1236
- Rosowski, J. J. (1994) “Outer and middle ears”. in *Comparative Hearing: Mammals* New York: Springer, 172-247. 10.1007/978-1-4612-2700-7_6.
- Geisler, C. D.(1998) “From Sound to Synapse: Physiology of the Mammalian Ear”. New York: Oxford University Press,.
- Lim, D. J. (1995) “Structure and function of the tympanic membrane: a review”. *Acta Oto-Rhino-Laryngologica Belgica* 49, 101-115.
- De Greef, D. et al. (2015) “Details of human middle ear morphology based on micro-CT imaging of phosphotungstic acid stained samples”. *Journal of Morphology* 276, 1025-1046
- van der Jeught, S. et al. (2013) “Full-field thickness distribution of human tympanic membrane obtained with optical coherence tomography”. *Journal of the Association for Research in Otolaryngology* 14, 483-494 <https://doi.org/10.1007/s10162-013-0394-z>.
- Aernouts, J., J. R. M. Aerts and J. J. J. Dirckx (2012) “Mechanical properties of human tympanic membrane in the quasi-static regime from in situ point indentation measurements.” *Heari'ng Research* 290, 45-54.
- Rosowski, J. J. (1996) “Models of external- and middle-ear function. in *Auditory Computation*” (eds Hawkins H.L. et al.) (New York: Springer, , 15-61.

- Wang, X. L. et al. (2016) "Motion of tympanic membrane in guinea pig otitis media model measured by scanning laser Doppler vibrometry". *Hearing Research* 339, 184-194 <https://doi.org/10.1016/j.heares.2016.07.015>.
- Aernouts, J. et al. (2010) "Elastic characterization of membranes with a complex shape using point indentation measurements and inverse modelling." *International Journal of Engineering Science* 48.6
- Cheng, T., C. Dai, and R. Z. Gan. (2007) "Viscoelastic properties of human tympanic membrane." *Annals of Biomedical Engineering* 35, no. 2: 305-314.
- Milazzo, M. et al. (2017) "The path of a click stimulus from ear canal to umbo". *Hearing Research* 346, 1-13 <https://doi.org/10.1016/j.heares.2017.01.007>.
- Kakue, T., R. Yonesaka, T. Tahara, Y. Awatsuji, K. Nishio, S. Ura, T. Kubota, and O. Matoba. (2011) "High-speed phase imaging by parallel phase-shifting digital holography." *Optics letters* 36, no. 21: 4131-4133.
- Fuller, P. W. W. (2009) "An introduction to high speed photography and photonics". *The Imaging Science Journal* 57, 293-302.
- Goode, R. L., G. Ball, S. Nishihara, and K. Nakamura. (1996) "Laser Doppler vibrometer (LDV)--a new clinical tool for the otologist." *The American journal of otology* 17, no. 6: 813-822.
- Goode, R. L. et al. (1994) "New knowledge about the function of the human middle ear: development of an improved analog model". *The American Journal of Otology* 15, 145-154.

- Gan, R. Z., M. W. Wood, and K. J. Dormer. (2004) "Human middle ear transfer function measured by double laser interferometry system." *Otology & Neurotology* 25, no. 4: 423-435.
- Rosowski, J. J., H. H. Nakajima, and S. N. Merchant. (2008)"Clinical utility of laser-Doppler vibrometer measurements in live normal and pathologic human ears." *Ear and hearing* 29, no. 1: 3.
- Decraemer, W. F., S. M. Khanna, and W. R. J. Funnell. (1999) "Vibrations at a fine grid of points on the cat tympanic membrane measured with a heterodyne interferometer." In EOS/SPIE International Symposia on Industrial Lasers and Inspection, *Conference on Biomedical Laser and Metrology and Applications*, pp. 1-4.
- Kim, S., R. D. Frisina, F. M. Mapes, E. D. Hickman, and D. Robert Frisina (2006) "Effect of age on binaural speech intelligibility in normal hearing adults." *Speech Communication* 48, no. 6: 591-597.
- Desoer, C., and Y. Wang. (1980) "On the generalized Nyquist stability criterion." *IEEE Transactions on Automatic Control* 25, no. 2: 187-196.
- Dobrev, I., C. Furlong, J. J. Rosowski, and J. T. Cheng. (2015) "High-speed digital holography for transient response of the human Tympanic Membrane." In *Advancement of Optical Methods in Experimental Mechanics, Volume 3*, pp. 337-342. Springer, Cham.
- Tang, H., P. Razavi, K. Pooladvand, P. Psota, N. Maftoon, J. J. Rosowski, C. Furlong, and J. T. Cheng (2019) "High-speed holographic shape and full-field displacement measurements of the tympanic membrane in normal and experimentally simulated pathological ears." *Applied Sciences* 9, no. 14: 2809.

- Tang, H., P. Psota, J. J. Rosowski, C. Furlong, and J. T. Cheng (2021) "Analyses of the Tympanic Membrane Impulse Response Measured with High-Speed Holography." *Hearing research* 410: 108335.
- Tang, H., P. Psota, J. J. Rosowski, J. T. Cheng, and C. Furlong (2021) "High speed Holographic Shape and Vibration Measurement of the Semi-transparent Tympanic Membrane." *In Mechanics of Biological Systems and Materials & Micro-and Nanomechanics & Research Applications*, pp. 67-71. Springer, Cham.
- Jones, R., and C. Wykes (1989) "Holographic and speckle interferometry". No. 6. Cambridge university press.
- Kreis, T. (2006) "Handbook of holographic interferometry: optical and digital methods". John Wiley & Sons,
- Razavi, P. (2018) "Development of high-speed digital holographic shape and displacement measurement methods for middle-ear mechanics in-vivo." PhD diss., Worcester Polytechnic Institute.
- De Greef, D., J. Buytaert, J. RM Aerts, L. V. Hoorebeke, M. Dierick, and J. Dirckx. (2015) "Details of human middle ear morphology based on micro-CT imaging of phosphotungstic acid stained samples." *Journal of morphology* 276, no. 9: 1025-1046.
- Khaleghi, M. (2015) "Development of holographic interferometric methodologies for characterization of shape and function of the human tympanic membrane." PhD diss., Worcester Polytechnic Institute.

- del Socorro Hernández-Montes, M., C. Furlong, J. J. Rosowski, N. Hulli, E. Harrington, J. T. Cheng, M. E. Ravicz, and F. Mendoza-Santoyo. (2009) "Optoelectronic holographic otoscope for measurement of nano-displacements in tympanic membranes." *Journal of biomedical optics* 14, no. 3: 034023.
- Solís, S. M., M. S. Hernández-Montes, and F. M. Santoyo (2012) "Tympanic membrane contour measurement with two source positions in digital holographic interferometry." *Biomedical optics express* 3, no. 12: 3203-3210.
- Rutledge, C., M. Thyden, C. Furlong, J. J. Rosowski, and J. Tao Cheng (2013) "Mapping the histology of the human tympanic membrane by spatial domain optical coherence tomography." *In MEMS and Nanotechnology*, Volume 6, pp. 125-129. Springer, New York, NY.
- Khaleghi, M., C. Furlong, J. Tao Cheng, and J. J. Rosowski (2016) "Characterization of acoustically-induced forces of the human eardrum." *In Mechanics of Biological Systems and Materials*, Volume 6, pp. 147-154. Springer, Cham.
- Santiago-Lona, C. V., M. S. Hernández-Montes, F. Mendoza-Santoyo, and J. Esquivel-Tejeda (2018) "Quantitative comparison of tympanic membrane displacements using two optical methods to recover the optical phase." *Journal of Modern Optics* 65, no. 3: 275-286.
- De Greef, D., J. Aernouts, J. Aerts, J. T. Cheng, R. Horwitz, J. J. Rosowski, and J. J. J. Dirckx. (2014) "Viscoelastic properties of the human tympanic membrane studied with stroboscopic holography and finite element modeling." *Hearing research* 312: 69-80.

- Razavi, P., M. E. Ravicz, I. Dobrev, J. Tao Cheng, C. Furlong, and J. J. Rosowski (2016) "Response of the human tympanic membrane to transient acoustic and mechanical stimuli: Preliminary results." *Hearing research* 340: 15-24.
- Razavi, P., I. Dobrev, M. E. Ravicz, J. Tao Cheng, C. Furlong, and J. J. Rosowski (2016) "Transient response of the eardrum excited by localized mechanical forces." In *Mechanics of Biological Systems and Materials*, Volume 6, pp. 31-37. Springer, Cham.
- Khaleghi, M., J. T. Cheng, C. Furlong, and J. J. Rosowski. (2016) "In-plane and out-of-plane motions of the human tympanic membrane." *The Journal of the Acoustical Society of America* 139, no. 1: 104-117.
- Decraemer, W. F., J. J. J. Dirckx, and W. R. J. Funnell (1991) "Shape and derived geometrical parameters of the adult, human tympanic membrane measured with a phase-shift moire interferometer." *Hearing research* 51, no. 1: 107-121.
- Yamaguchi, I., T. Ida, M. Yokota, and K. Yamashita (2006) "Surface shape measurement by phase-shifting digital holography with a wavelength shift." *Applied optics* 45, no. 29: 7610-7616.
- Kuwamura, S., and I. Yamaguchi (1997) "Wavelength scanning profilometry for real-time surface shape measurement." *Applied optics* 36, no. 19: 4473-4482.
- Seebacher, S., W. Osten, and W. P. Jueptner (1998) "Measuring shape and deformation of small objects using digital holography." In *Laser Interferometry IX: Applications*, vol. 3479, pp. 104-115.

- Furlong, C., and R. J. Pryputniewicz (2000) "Absolute shape measurements using high-resolution optoelectronic holography methods." *Optical Engineering* 39, no. 1: 216-223.
- Osten, W., S. Seebacher, T. Baumbach, and W. P. Jueptner (2001) "Absolute shape control of microcomponents using digital holography and multiwavelength contouring." In *Metrology-Based Control for Micro-Manufacturing*, vol. 4275, pp. 71-84.
- Ghiglia, D. C., and M. D. Pritt. (1998) "Two-dimensional phase unwrapping: theory, algorithms, and software." A Wiley Interscience Publication.
- Rosowski, J. J. (1996) "Models of external-and middle-ear function." In *Auditory computation*, pp. 15-61. Springer, New York, NY.
- Tonndorf, J., and S. M. Khanna (1970) "The role of the tympanic membrane in middle ear transmission." *Annals of Otology, Rhinology & Laryngology* 79, no. 4: 743-753.
- Khanna, S. M., and J. Tonndorf (1972) "Tympanic membrane vibrations in cats studied by time-averaged holography." *Journal of the Acoustical Society of America* 51, no. 6B: 1904-1920.
- Decraemer, W. F., S. M. Khanna, and W. Robert J. Funnell (1989) "Interferometric measurement of the amplitude and phase of tympanic membrane vibrations in cat." *Hearing research* 38, no. 1-2: 1-17.
- Goode, R. L., G. Ball, and S. Nishihara (1993) "Measurement of umbo vibration in human subjects--method and possible clinical applications." *American journal of otology* 14, no. 3: 247-251.

- Khaleghi, M., I. Dobrev, E. Harrington, C. Furlong, and J. J. Rosowski (2014) "Study of the transient response of Tympanic Membranes under acoustic excitation." In *Mechanics of Biological Systems and Materials*, Volume 4, pp. 1-9. Springer, Cham.
- Von Unge, M., W. F. Decraemer, J. J. Dirckx, and D. Bagger-Sjöbäck (1995) "Shape and displacement patterns of the gerbil tympanic membrane in experimental otitis media with effusion." *Hearing research* 82, no. 2: 184-196.
- Cheng, J. T., N. Maftoon, J. Guignard, M. E. Ravicz, and J. Rosowski (2019) "Tympanic membrane surface motions in forward and reverse middle ear transmissions." *Journal of the Acoustical Society of America* 145, no. 1: 272-291.
- Nakajima, H. H., W. Dong, E. S. Olson, S. N. Merchant, M. E. Ravicz, and J. J. Rosowski (2009) "Differential intracochlear sound pressure measurements in normal human temporal bones." *Journal of the Association for Research in Otolaryngology* 10, no. 1: 23-36.
- Wegel, R. L. F., and C. E. Lane (1924) "The auditory masking of one pure tone by another and its probable relation to the dynamics of the inner ear." *Physical review* 23, no. 2: 266.
- Zwislocki, J. (1957) "Some impedance measurements on normal and pathological ears." *The Journal of the Acoustical Society of America* 29, no. 12: 1312-1317.
- Allen, J. B. (1986) "Measurement of eardrum acoustic impedance." In *Peripheral auditory mechanisms*, pp. 44-51. Springer, Berlin, Heidelberg.

- Allen, J. B., P. S. Jeng, and H. Levitt (2005) "Evaluation of human middle ear function via an acoustic power assessment." *Journal of Rehabilitation Research & Development* 42.
- Rosowski, J. J., H. H. Nakajima, J. T. Cheng, M. A. Hamadeh, and M. E. Ravicz (2010) "Middle-ear input impedance and middle-ear sound transfer." *The Journal of the Acoustical Society of America* 127, no. 3: 1867-1867.
- Funnell, W. R. J., and C. A. Laszlo (1978) "Modeling of the cat eardrum as a thin shell using the finite-element method." *The Journal of the Acoustical Society of America* 63, no. 5: 1461-1467.
- Prieve, B. A., M. P. Feeney, S. Stenfelt, and N. Shahnaz (2013) "Prediction of conductive hearing loss using wideband acoustic immittance." *Ear and Hearing* 34: 54s-59s.
- Sanford, C. A., L. L. Hunter, M. P. Feeney, and H. H. Nakajima (2013) "Wideband acoustic immittance: Tympanometric measures." *Ear and Hearing* 34: 65s-71s.
- Aarnisalo, A. A., J. T. Cheng, M. E. Ravicz, N. Hulli, E. J. Harrington, M. S. Hernandez-Montes, C. Furlong, S. N. Merchant, and J. J. Rosowski (2009) "Middle ear mechanics of cartilage tympanoplasty evaluated by laser holography and vibrometry." *Otology & neurotology: official publication of the American Otological Society, American Neurotology Society and European Academy of Otology and Neurotology* 30, no. 8: 1209.
- Tang, H., P. Razavi, N. Maftoon, J. J. Rosowski, C. Furlong, and J. T. Cheng (2020) "Comparative Modal Analysis of the Tympanic Membrane Mechanics Between Normal

and Experimentally Simulated Pathological Ears." In *Mechanics of Biological Systems and Materials & Micro-and Nanomechanics*, Volume 4, pp. 63-71. Springer, Cham.

- Dobrev, I., E. J. Harrington, T. Cheng, C. Furlong, and J. J. Rosowski (2013) "Digital holographic otoscope for measurements of the human tympanic membrane in-vivo." In *Imaging Methods for Novel Materials and Challenging Applications*, Volume 3, pp. 39-45. Springer, New York, NY.
- Bluestone, CD (1998). Epidemiology and pathogenesis of chronic suppurative otitis media: Implications for prevention and treatment. *Int J. Pediatr Otorhinolaryngol*, 42, 207-23.
- Cunningham, MJ & Eavey, RJ (1993). Otitis media with effusion. In: NADOL, J. J. & SCHUKNECHT, H. (eds.) *Surgery of the ear and temporal bone*. New York: Raven Press.
- Hunter, L.L., Margolis, R.H. & Giebink, G.S. (1994). Identification of hearing loss in children with otitis media. *Ann Otol Rhinol Laryngol*, 103, 59-64.
- Roberts, JE, Rosenfeld, RM & Zeisel, SA (2004). Otitis media and speech and language: A meta-analysis of prospective studies. *Pediatrics*, 113, 238-48.
- Fulghum, RS, Chole, RA, Brinn, JE & Branigan, AE (1987). Mongolian gerbil Tympanic membrane: Normal and with induced otitis media. *Arch Otolaryngol Head Neck Surg*, 113, 521-525.
- Gaihede, M, Lildholt, T & Lundig, J (1997). Sequelae of secretory otitis media: Changes in middle ear biomechanics. *Acta Otolaryngol*, 117, 382-389.
- Guan, X, Y, Chenm & Gan, RZ (2014). Factors affecting loss of tympanic membrane mobility in acute otitis media model of chinchilla. *Hear Res*, 309, 136-46.
- von Unge, M. & Bagger-Sjöbäck (1994). Tympanic membrane changes in experimental otitis media with effusion. *Am J Otolaryngol*, 15, 663-669.

- J.J. Rosowski, H.H. Nakajima, and S.N. Merchant(2008), “Clinical utility of laser-Doppler vibrometer measurements in live normal and pathologic human ears”. *Ear and hearing*, 29(1), p.3.
- Dai, C, Wood, MW & Gan, RZ (2007). Tympanometry and laser Doppler interferometry measurements on otitis media with effusion model in human temporal bones. *Otol Neurotol*, 28, 551-8.
- Ohashi, Y , Nakai, Y, Ikeoka, H, Esaki, Y, Ikeoka, H, Kato, S & Kato, M (1988). Experimental otitis media with effusion induced by lipopolysaccharide from *Klebsiella pneumoniae*: mucociliary pathology of the middle ear. *Am J Otolaryngol*, 9, 83-9.
- Hecox, K & Galambos, R (1974). Brain stem auditory evoked responses in human infants and adults. *Arch Otolaryngol*, 99, 30-33.
- Ruth, R, Dey-Sigman, S & Mills, J (1985). Neonatal ABR screening. *The Hearing Journal*, 38, 15-20.
- Zheng, QY, Johnson, KR & Erway, LC (1999). Assessment of hearing in 80 inbred strains of mice by ABR threshold analyses. *Hear Res*, 130, 94-107.
- Yoshida, A, Hequembourg, SJ, Atencio, CA, Rosowski, JJ & Liberman, MC (2000). Acoustic injury in mice: 129/SvEv is exceptionally resistant to noise-induced hearing loss. *Hearing Research*, 141, 97-106.
- White, KR, Vohr, BR, Meyer, S, Widen, JE, Johnson, JL, Gravel, JS, James, M, Kennalley, T, Maxon, AB, Spivak, L, Sullivan-Mahoney, M & Weirather, Y (2005). A multisite study to examine the efficacy of the otoacoustic emission/automated auditory brainstem response newborn hearing screening protocol: Research design and results of the study. *Am J Audiol*, 14, S186-99.

- Shera, CA, Guinan, JJ Jr. & Oxenham, AJ (2002). Revised estimates of human cochlear tuning from otoacoustic and behavioral measurements. *PNAS*, 99, 3318-3323.
- Dolan, TG & Abbas, PJ (1985). Changes in the 2f1-f2 acoustic emission and whole-nerve response following sound exposure: Long-term effects. *J. Acoust. Soc. Am.*, 77, 1475-1483.
- Yoshida, A, Hequembourg, SJ, Atencio, CA, Rosowski, JJ & Liberman, MC 2000. Acoustic injury in mice: 129/SvEv is exceptionally resistant to noise-induced hearing loss. *Hearing Research*, 141, 97-106.
- Prieve, BA, Vander Werff, K, Preston, JL & Georgantas, L (2013). Identification of conductive hearing loss in young infants using tympanometry and wideband reflectance. *Ear Hear*, 34, 168-78.
- BA. Prieve, M.P. Feeney, S. Stenfelt, and N. Shahnaz (2013). “Prediction of conductive hearing loss using wideband acoustic immittance. *Ear and Hearing*”, 34, pp.54s-59s,